



# Super- and subradiance in a dilute cloud of cold atoms

Michelle Oliveira de Araujo

► **To cite this version:**

Michelle Oliveira de Araujo. Super- and subradiance in a dilute cloud of cold atoms. Atomic Physics [physics.atom-ph]. Université Côte d'Azur, 2018. English. NNT : 2018AZUR4200 . tel-02102832

**HAL Id: tel-02102832**

**<https://tel.archives-ouvertes.fr/tel-02102832>**

Submitted on 17 Apr 2019

**HAL** is a multi-disciplinary open access archive for the deposit and dissemination of scientific research documents, whether they are published or not. The documents may come from teaching and research institutions in France or abroad, or from public or private research centers.

L'archive ouverte pluridisciplinaire **HAL**, est destinée au dépôt et à la diffusion de documents scientifiques de niveau recherche, publiés ou non, émanant des établissements d'enseignement et de recherche français ou étrangers, des laboratoires publics ou privés.



$$\rho \left( \frac{\partial v}{\partial t} + v \cdot \nabla v \right) = -\nabla p + \nabla \cdot T + f$$

$$e^{i\pi} + 1 = 0$$

# THÈSE DE DOCTORAT

Super- et sous-radiance dans un nuage dilué  
d'atomes froids

**Michelle OLIVEIRA DE ARAÚJO**

Institut de Physique de Nice

**Présentée en vue de l'obtention  
du grade de docteur en physique  
de l'Université Côte d'Azur**  
**Dirigée par :** Robin Kaiser  
**Soutenue le :** 11 Décembre 2018

**Devant le jury, composé de :**  
Romain Bachelard, maître de conférences,  
Universidade Federal de São Carlos  
Jérôme Beugnon, maître de conférences, Uni-  
versité Pierre et Marie Curie  
Fabrice Mortessagne, professeur, Université  
Côte d'Azur  
Leticia Tarruell, chargée de recherche, The  
Barcelona Institute of Science and Technology  
Jook Walraven, professeur émérite, University  
of Amsterdam



# Super- et sous-radiance dans un nuage dilué d'atomes froids

Jury :

Rapporteurs

Jérôme Beugnon, maître de conférences, Université Pierre et Marie Curie

Leticia Tarruell, chargée de recherche, The Barcelona Institute of Science and Technology

Examineurs

Romain Bachelard, maître de conférences, Universidade Federal de São Carlos

Fabrice Mortessagne, professeur, Université Côte d'Azur

Jook Walraven, professeur émérite, University of Amsterdam



# Résumé

## Super- et sous-radiance dans un nuage dilué d'atomes froids

Le problème de l'interaction de  $N$  atomes avec un faisceau laser et les modes du vide peut donner lieu à de nombreux phénomènes intéressants concernant l'émission spontanée de la lumière et sa propagation dans l'échantillon. Les effets coopératifs, par exemple, tels que la super- et la sous-radiance, sont des effets liés à la cohérence créée entre les atomes lorsqu'un photon est émis spontanément par un seul atome excité. La super-radiance peut être définie comme le renforcement de l'émission spontanée due à une interférence constructive de la lumière diffusée. Son homologue, la sous-radiance, est le piégeage d'une partie de la lumière restante en raison d'interférences destructives.

Dans les atomes froids, certains travaux théoriques antérieurs prédisent et caractérisent ces deux effets coopératifs dans un nuage atomique large et dilué, dans le régime des faibles intensités et à grands désaccords du laser incident. Le modèle théorique est un modèle de dipôles couplés pour atomes à deux niveaux pilotés par un champ de faible intensité et dans l'approche scalaire. L'expérience consiste à mesurer les taux de décroissance super- et sous-radiants à partir de l'intensité temporelle émise après la coupure du laser incident en régime stationnaire. Notre schéma expérimental consiste en un piège magneto-optique d'atomes de rubidium 87 à grandes épaisseurs optiques à résonance. Un faisceau sonde excite les atomes proche de la raie  $D_2$ . L'intensité émise est détectée par un détecteur de photons uniques dépourvu d'afterpulsing et une procédure d'étalonnage nous permet de déterminer l'épaisseur optique résonante du nuage et sa température.

Dans ce travail, nous rapportons l'observation expérimentale de la super- et sous-radiance dans un grand nuage d'atomes froids. Pour la sous-radiance, le résultat principal est l'évolution linéaire du temps caractéristique avec l'épaisseur optique résonante du nuage et son indépendance du désaccord. Pour la super-radiance, on observe la super-radiance en dehors de la direction vers l'avant. Nous vérifions la validité de nos interprétations avec les prédictions du modèle de dipôles couplés. Finalement, nous discutons l'interaction entre la sous-radiance et le piégeage de radiation, ainsi que des prévisions théoriques concernant: la configuration d'un nuage phasé, pour contrôler l'émission de l'amplitude sous-radiante; et les effets de température, où la sous-radiance s'avère robuste dans une large gamme de températures.

**Mot clés :** physique atomique, atomes froids, effets coopératifs, super-radiance, sous-

radiance, piégeage de radiation.

# Abstract

## Super- and subradiance in a dilute cloud of cold atoms

The problem of the interaction of  $N$  atoms with a laser beam and vacuum modes can give rise to many interesting phenomena concerning the spontaneous emission of light and its propagation in the medium. The cooperative effects, for example, such as super- and subradiance, are effects related to the coherence created between the atoms when a photon is emitted spontaneously by a single excited atom. Superradiance can be defined as the enhancement of the spontaneous emission due to constructive interference of the scattered light. Its counterpart, subradiance, is the trapping of some remaining light due to destructive interference.

In cold atoms, some previous theoretical works predict and characterize these two cooperative effects in a large and diluted atomic cloud, in the regime of low intensities and large detunings of the incident laser. The theoretical model is a coupled-dipole model for two-level atoms driven by a low-intensity field and in the scalar approach. The experiment consists in measuring the super- and subradiant decay rates from the temporal emitted intensity after the switch off of the incident laser in the steady state. Our experimental setup consists in a magneto-optical trap of rubidium 87 atoms at large resonant optical thicknesses. A probe beam excites the atoms close to the  $D_2$  line. The intensity emitted is detected by a single photon detector with no afterpulsing and a calibration procedure allows us to determine the resonant optical thickness of the cloud and its temperature.

In this work, we report the experimental observation of super- and subradiance in a large cloud of cold atoms. For subradiance, the main result is the linear evolution of the characteristic time with the resonant optical thickness of the cloud and its independence of the detuning. For superradiance, we observe superradiance out of the forward direction. We verify the validity of our interpretations with the predictions of the coupled-dipole model. Finally, we discuss the interplay of subradiance and radiation trapping, as well as theoretical predictions for: a setup of a phased cloud, to control the subradiant amplitude emission; and temperature effects, where subradiance is shown to be robust in a large range of temperatures.

**Keywords:** atomic physics, cold atoms, cooperative effects, superradiance, subradiance, radiation trapping.



# Contents

<b>Introduction</b>	<b>1</b>
Cooperative effects in cold atoms . . . . .	3
Content of this thesis . . . . .	4
<b>1 The coupled-dipole model for two-level atoms in the scalar approach</b>	<b>7</b>
1.1 The coupled-dipole model in the scalar approximation . . . . .	7
1.1.1 Overview . . . . .	7
1.1.2 Setting the equations . . . . .	11
1.1.3 Solving the equations for the coefficients . . . . .	13
1.2 The detected fluorescence . . . . .	17
1.2.1 The total emitted intensity . . . . .	18
1.2.2 Intensity in a given direction from the incident light . . . . .	22
1.3 Simulation methods . . . . .	23
1.3.1 Impact of the exclusion condition . . . . .	27
1.3.2 Emission diagram and off-axis superradiance . . . . .	27
1.3.3 Temporal decay rate . . . . .	28
1.4 Conclusions of this chapter . . . . .	30
<b>2 Subradiance in cold atoms</b>	<b>31</b>
2.1 Numerical results . . . . .	31
2.1.1 Scaling with $b_0$ . . . . .	32
2.1.2 Subradiance at resonance and for several detection directions . . . . .	33
2.1.3 Subradiance and temperature . . . . .	35
2.2 Experimental setup . . . . .	36
2.2.1 Basics about magneto-optical traps (MOTs) . . . . .	36
2.2.2 General description of our MOT setup . . . . .	38
2.2.3 Setup for the probe beam . . . . .	40
2.2.4 Cloud preparation and data acquisition procedure . . . . .	43
2.2.5 Absorption imaging . . . . .	45
2.2.6 Time of flight (TOF) . . . . .	47
2.2.7 Calibration of $b_0$ . . . . .	48
2.3 Experimental results . . . . .	51
2.3.1 Detected intensities with $b_0$ and $\Delta$ . . . . .	51

2.3.2	Subradiant decay rates <i>versus</i> $b_0$ . . . . .	52
2.3.3	Subradiant decay rates <i>versus</i> laser intensity . . . . .	52
2.3.4	Possibility of radiation trapping in the subradiance data . . . . .	54
2.4	Conclusions of this chapter . . . . .	56
<b>3</b>	<b>Superradiance in cold atoms</b> . . . . .	<b>57</b>
3.1	Numerical results . . . . .	57
3.1.1	Off-axis superradiance . . . . .	58
3.1.2	Scaling with $b_0$ . . . . .	59
3.1.3	Superradiance at resonance and for several detection directions . . . . .	60
3.2	Experimental setup . . . . .	62
3.2.1	Setup for the probe beam . . . . .	62
3.3	Experimental results . . . . .	64
3.3.1	Fit procedure . . . . .	64
3.3.2	Superradiant decay rates <i>versus</i> $b_0$ . . . . .	66
3.3.3	Superradiant decay rates <i>versus</i> laser intensity . . . . .	67
3.3.4	Superradiant decay rates for small $b_0$ . . . . .	68
3.4	Conclusions of this chapter . . . . .	68
<b>4</b>	<b>Radiation trapping and subradiance</b> . . . . .	<b>71</b>
4.1	Radiation trapping in cold atoms . . . . .	72
4.1.1	Overview . . . . .	72
4.1.2	Theory . . . . .	74
4.2	Simulation methods with the small beam setup . . . . .	78
4.2.1	Coupled-dipole model . . . . .	78
4.2.2	Random walk model . . . . .	79
4.3	Numerical results . . . . .	80
4.3.1	Emitted intensities <i>versus</i> time . . . . .	80
4.3.2	Decay rates <i>versus</i> $b$ . . . . .	82
4.3.3	Comparison with the large beam setup . . . . .	83
4.3.4	Effects of temperature and laser spectrum . . . . .	83
4.4	Experimental setup . . . . .	85
4.4.1	New laser source . . . . .	85
4.4.2	Optimization of the dark MOT phase . . . . .	88
4.4.3	Setup of the probe beam . . . . .	89
4.5	Experimental results . . . . .	91
4.5.1	Data for large beam . . . . .	91
4.5.2	Data for small beam . . . . .	92
4.5.3	Attempt to decrease the temperature of the cloud . . . . .	94
4.6	Conclusions of this chapter . . . . .	96
<b>5</b>	<b>Phased cloud and temperature effects</b> . . . . .	<b>97</b>
5.1	Excitation with a phased cloud . . . . .	98
5.1.1	Description . . . . .	98
5.1.2	Simulation methods . . . . .	99

5.1.3	Numerical results . . . . .	99
5.2	Temperature effects . . . . .	103
5.2.1	The coupled-dipole model with temperature . . . . .	103
5.2.2	The ballistic model . . . . .	103
5.2.3	The harmonic oscillator model . . . . .	105
5.2.4	Simulations methods . . . . .	107
5.2.5	Numerical results . . . . .	108
5.3	Conclusions of this chapter . . . . .	109
<b>Conclusion</b>		<b>111</b>
	Perspectives . . . . .	112
	Publications . . . . .	112
<b>Annex</b>		<b>115</b>
<b>Bibliography</b>		<b>119</b>



# Introduction

It is known that physics had seen an important development since the last centuries, when a large step was done from classical physics (classical mechanics, electromagnetism and thermodynamics) to modern physics (relativity and quantum mechanics). While relativity describes phenomena in huge macroscopic scale dominated by the speed of light and astronomical distances, quantum mechanics deals with the microscopic world, dominated by atoms, ions, molecules and their dual nature, as well as light and its dual nature. A throwback to the end 19th/early 20th centuries brings us to the introduction of new physical concepts about the structure of matter and light: the atom seen as bounded electrons occupying discrete energy levels, by E. Rutherford and N. Bohr; the concept of quantum, or photon, introduced by M. Planck and A. Einstein to explain the blackbody radiation and the photoelectric effect, respectively; the wave nature of matter introduced by L. de Broglie; the E. Schrödinger's wave equation for matter and its numerous applications to microscopic systems, with particles trapped or moving freely in several types of potential energies. Contemporary research in Physics is mainly based on these concepts, and several fields are substantially based on light-matter interaction on a microscopic scale. Some examples are: atomic physics [Foot 2005], which deals with the arrangement of the electrons in the atomic energy levels when interacting with photons and other particles; laser physics [Siegman 1986], which studies the laser light and how it is produced in a cavity with a gain medium; and quantum optics [Scully 1997, Mandel 1995], which studies phenomena related with the quantization of the electromagnetic field introduced by P. Dirac.

Interaction processes between atoms and photons are not only responsible for phenomena at the microscopic scale: in fact, one of the main goals in physics is to extend applications and predictions in microscopic scale to explain and understand macroscopic phenomena. One of these macroscopic phenomena is propagation of light in matter. Described mainly in classical electrodynamics [Jackson 1998] and optics [Hecht 2002], the main assumption is to consider the medium as homogeneous and continuous, and hence the problem is reduced to solving the Helmholtz equation and finding the features of the light propagation and modifications in the medium properties as susceptibility and refractive index. On the other hand, E. Rutherford studied the scattering of alpha particles by a metallic sheet by considering the latter as a single scatterer. Here, a more realistic picture is to consider the granularity of the medium, i.e., to see it directly as a set of point-like particles spread out in space, what is called a *disordered medium*, like stars, clouds, fog, smoke, or even a piece of paper. The disordered medium is the real situation

between the idealizations of a homogeneous medium and a single-scatterer medium (Fig. 1).

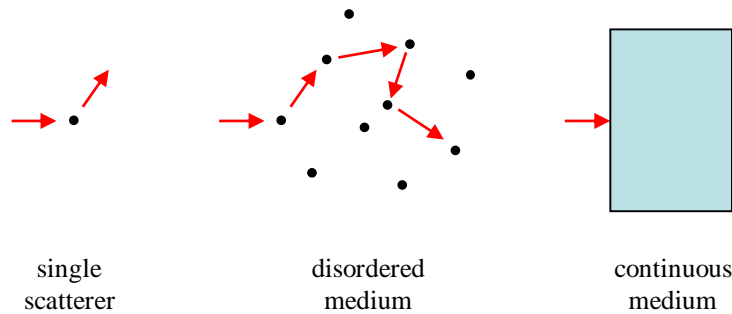


**Figure 1:** Propagation of light (red arrow) in matter. **Left:** A medium composed by a single scatterer. **Center:** A disordered medium. **Right:** A continuous medium.

Disordered media is a good assumption to study light scattering in crystals and gas-like or vapor-like media. The interactions between the atoms and photons modify the external and internal dynamics of the latter, since a photon carries momentum, energy and angular momentum and these quantities are transmitted to the atom [Cohen-Tannoudji 1992]. As introduced by A. Einstein, and later detailed by I. Rabi, V. Weisskopf and E. Wigner, a photon interacts with an atom under three processes: absorption (absorption of a photon from a low to an upper energy level), stimulated emission (emission of a photon from a upper level to a lower level induced by an incoming photon), and spontaneous emission (emission of a photon from a upper to a lower level spontaneously). These processes allowed the building of the laser, a source of coherent and monochromatic light, by C. Townes and A. Schawlow in 1960. Its achievement allowed a large development of several experiments, in many research areas, and several types of laser are available, like dye lasers, He-Ne, Ti:sapphire and semiconductors lasers. Later, in the 1980 – 1990s, the development of techniques on cooling and trapping atoms by using radiation pressure force allowed the production of atomic samples at very low temperatures [Metcalf 1999], like clouds of *cold atoms* and Bose-Einstein condensates, thanks to the magnetic and/or dipole traps.

The propagation of light in disordered media can be studied from standard experiments in atomic physics, where the medium is a vapor of atoms, and the light is obtained from a laser source, like semiconductor lasers. Semiconductor lasers provide laser light at high powers and at tunable frequencies, and alkaline atoms like sodium, potassium, rubidium and cesium are the main candidates for the vapor sample due to its simple structure of a single optically active electron in the valence shell.<sup>1</sup> In a hot vapor, all atoms have a velocity and move, which introduces Doppler effect and collisions. However, since its experimental achievement, cold atoms have become a powerful tool because of its low temperatures (few  $\mu\text{K}$ , few nK) and tunable properties, like temperature, size, shape, and density.

<sup>1</sup> Experiments with earth-alkaline atoms, like calcium and strontium, are also carried out in many research groups.

## Cooperative effects in cold atoms

Light propagation in a disordered medium can be seen as a sequence of absorption and spontaneous emission performed by a photon when encountering an atom in the medium. Absorption, stimulated emission and spontaneous emission lead the system to an equilibrium state, or a *steady state*, where the medium emits light called *fluorescence*. Phenomena like Rayleigh scattering, Mie scattering, Compton scattering and Raman scattering depend on how close the light frequency is compared to the atomic resonance frequency [Cohen-Tannoudji 1992], as well as the size of the particles with respect to the light wavelength. The light emitted by the medium contains features of the physical phenomenon taking place in the medium, when the photons are being scattered. The results obtained from the problem of a single atom interacting with light and vacuum modes [Griffiths 2005] are also valid for a set of  $N$  independent particles and, if the incoming light is suddenly extinguished, the excited atoms in the medium decay by spontaneous emission. The emitted fluorescence  $I(t)$  is isotropic and proportional to  $I(t) \propto \exp(-\Gamma t)$  [see Fig. 2(a)] where  $\Gamma = 1/\tau_0$  gives the timescale related with the excited state.

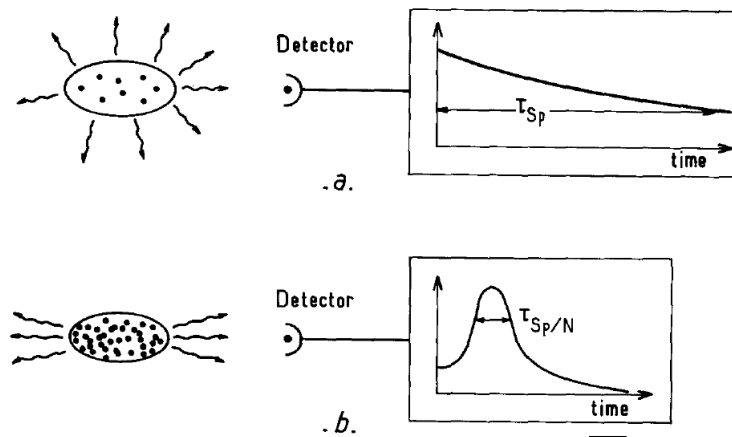


**Figure 2:** Fluorescence emitted by a medium composed of (a) independent scatterers and (b) dependent scatterers. Extracted from [Gross 1982].

In 1954, R. Dicke [Dicke 1954] proposed for the first time the interaction of light with a system where all the atoms can interact themselves, by defining a wavefunction for the whole system, like in a system of identical particles in quantum mechanics. Symmetrical and anti-symmetrical states can be defined, and several posterior works [Gross 1982] showed that, in the case of a sample size  $R$  very small compared with the light wavelength  $\lambda$ , i.e.,  $R \ll \lambda$ , the spontaneous emitted light is modified to be *directional* (non-isotropic), and to decay with a *very fast* decay rate compared with the natural atomic decay rate  $\Gamma$  [see Fig. 2(b)]. This is true even if there is only one atom in the excited state, as shown later by [Scully 2006]. This phenomenon was named *superradiance*, or *superfluorescence*, and the emitted light depends on how close the atoms are (which determines the strength of the *coherence* created between them), as well as the number of atoms  $N$  and the sample geometry.

A lot of work on superradiance was performed in the 1970–1980s, both experimentally and theoretically [Gross 1982], focusing mainly in small pencil-shape samples and inverted systems (many atoms in the excited state). However, the condition  $R \ll \lambda$  is very hard to

achieve experimentally, so in 2006, M. O. Scully *et al.* [Scully 2006] proposed the *single-photon superradiance*, i.e., a single resonant photon (obtained from, e.g., parametric down conversion) excites a *large sample*, i.e.,  $R > \lambda$ , of  $N$  atoms at random positions  $\vec{r}_j$ . In this work, the assumption is that one of the atoms is excited in a such way that the whole system is in the state

$$|\Psi(\vec{r}, t)\rangle = \frac{1}{\sqrt{N}} \sum_{j=1}^N e^{i\vec{k}_0 \cdot \vec{r}_j} |j\rangle$$

where  $|j\rangle$  denotes the atom  $j$  at the excited state,  $j = 1, \dots, N$ ,  $k_0 = 2\pi/\lambda$ , summed to all possibilities of excited atoms, with position-dependent phase  $e^{i\vec{k}_0 \cdot \vec{r}_j}$  and divided by the same probability  $1/\sqrt{N}$ . The spontaneous decay of this state is shown to be at the same direction of the incident photon, i.e., in the *forward direction*, with a rate  $\Gamma_{\text{sup}}$  which depends on the size  $R$  and number of atoms  $N$  in the sample as  $\Gamma_{\text{sup}} \propto N\Gamma/(k_0 R)^2$  [Svidzinsky 2008c].

Since then, several theoretical works were performed concerning single-photon superradiance, using several theoretical approaches [Eberly 2006, Mazets 2007, Das 2008]. In 2010, P. W. Courteille *et al.* [Courteille 2010] proposed a theoretical model for describing superradiance. A cloud of cold atoms is an ideal example of disordered system for experiments, with  $N$  identical atoms at random positions, and the excitation by a single photon can be achieved by a far detuned laser beam at weak intensities, called *linear optics regime*. Moreover, a large range of detunings can be covered, and not only resonant as studied in the previous work. This model is a model of *coupled dipoles*, i.e., the atoms are considered as dipoles driven by a monochromatic electric field. It was proposed originally to describe the *cooperative radiation pressure force*, and the experimental observation of this latter by T. Bienaimé *et al.* [Bienaimé 2010] provided an evidence that *cooperative effects* can take place in a cloud of cold atoms.

A direct evidence of superradiance in cold atoms is the experimental observation of a fast decay in the emitted intensity. In 2012, T. Bienaimé *et al.* [Bienaimé 2012] showed numerically that, besides a superradiant emission, characterized by a fast decay rate  $\Gamma_{\text{sup}} > \Gamma$  at early times, observed in emitted intensities, a *subradiant* emission is also observed, characterized by a slow decay rate  $\Gamma_{\text{sub}} < \Gamma$  at late times (see Fig. 3). Both decay rates scale with the parameter  $b_0 \propto N/(k_0 R)^2$ , called resonant optical thickness, i.e., these cooperative effects depend only on the medium properties.

## Content of this thesis

The aim of this thesis is to present an experimental study of super- and subradiance in a dilute cloud of cold atoms, as well as the interplay of subradiance with radiation trapping. The main focus is the understanding of the phenomena with the predictions of the coupled-dipole model.

Super- and subradiance are two examples of cooperative effects, due to the coherence created by the atoms in the medium when interacting with a laser beam and vacuum modes. Our experimental study is based in the predictions of references [Courteille 2010] and [Bienaimé 2012], although we also intend to discuss improvements on the simulations

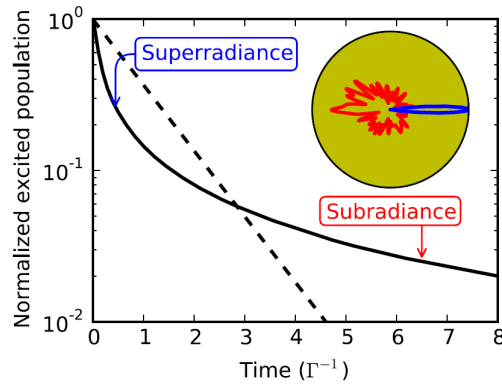


**Figure 3:** Decay of the population of the excited state as a function of time for 2000 atoms (full line), and comparison with the emission of a single atom (dashed line). Extracted from [Bienaimé 2012].

methods and to present new and complete numerical results. Concerning subradiance, the focus is the observation of a slow decay in a cloud of  $N$  atoms. Concerning superradiance, the focus is on *off-axis superradiance*, i.e., the observation of a fast decay out of the direction of the incident laser. In addition, we discuss the interplay of subradiance and *radiation trapping*, where this latter is the random walk performed by the photon when scattered several times by neglecting interference effects. All experiments were performed using a magneto-optical trap (MOT) of  $^{87}\text{Rb}$  atoms already available in our laboratory.

This thesis is organized as follows. In Chapter 1 we present the standard model of coupled dipoles, for two-level atoms, single excitations (linear optics regime) and scalar approach (valid for dilute media, i.e., low densities). We discuss the response of the system due to the atom-light interactions and then we derive analytical equations for the emitted intensity by the sample, as well as some numerical predictions. Then, we discuss the main results obtained in this thesis: subradiance, in Chapter 2; superradiance, in Chapter 3; and subradiance *versus* radiation trapping, in Chapter 4. In each one, we present the main predictions from the coupled-dipole model, the experimental setup designed for the measurements, and the experimental results and discussion. In Chapter 5, we discuss numerical results with the coupled-dipole model by taking into account phase shifts in the incoming field and temperature effects. Finally, we point out the main conclusions and perspectives for future works.



# The coupled-dipole model for two-level atoms in the scalar approach

The main problem treated in this thesis is super- and subradiance in cold atoms, and it involves physical concepts on light propagation and light-matter interaction. We detect super- and subradiance from the light emitted spontaneously by a cloud of atoms after interacting with an incident laser beam. The emitted light depends on how the atoms in the cloud interact with the incident radiation field. In this chapter, we present the theoretical model for these interactions, which is the coupled-dipole model, whose main goal is to describe the general features and the relevant processes about the arising of super- and subradiance, as well as the set of parameters for detecting them from the emitted fluorescence.

This chapter is divided in four sections. In section 1.1, we present the coupled-dipole model for our physical system and its many approaches for deriving and solving the equations for the dipole dynamics. In section 1.2, we define the detected intensity emitted by the atoms and then we derive analytical expressions for the total emitted intensity and the intensity detected in a given direction. In section 1.3, we discuss the simulations methods for implementing the coupled-dipole model numerically, in order to perform a theoretical study of super- and subradiance. Finally, in section 1.4, we point out the main conclusions of this chapter.

## 1.1 The coupled-dipole model in the scalar approximation

### 1.1.1 Overview

Maybe the most used theoretical model in order to describe cooperativity in cold atoms is the *coupled-dipole model*, which describes  $N$  identical atoms interacting with a monochromatic electric field and the vacuum modes (see Fig. 1.1). The atoms are treated as dipoles, which oscillate when interacting with the electric field, and a set of coupled differential equations is obtained for the oscillation amplitudes of the atoms. From them, we obtain analytical equations for the emitted intensity.<sup>1</sup> The emitted fluorescence

---

<sup>1</sup> In this thesis the term “fluorescence” is used with the meaning of “emitted (or detected) intensity”.

contains signatures of cooperativity, and simulations can be implemented in order to study and extract cooperative decay rates from the fluorescence, by varying the parameters of the atomic sample, like density and optical thickness.

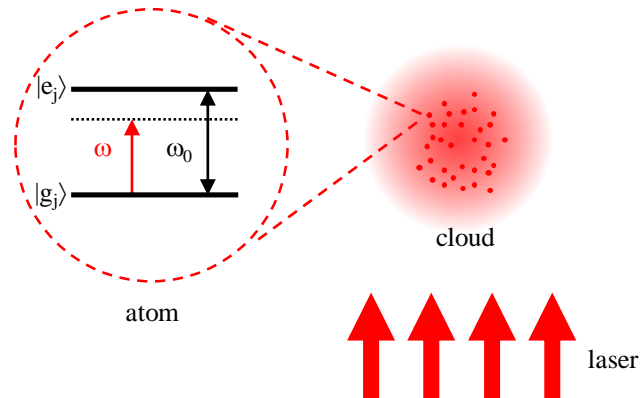


**Figure 1.1:** The physical system. An atomic cloud is considered as a set of  $N$  identical atoms, interacting with a laser beam and the vacuum modes. The laser is modeled as a monochromatic electric field and the atoms are modeled as two-level systems, where, for any atom  $j$ ,  $|g_j\rangle$  is the ground state and  $|e_j\rangle$  is the excited state, with energies  $E_g$  and  $E_e$ , respectively. The atomic resonance frequency is defined as  $\omega_0 = (E_e - E_g)/\hbar$ , and the laser frequency is  $\omega$ .

When interacting with a coherent radiation field, we will show in this chapter that the amplitudes of the atoms evolve in time according to the *coupled-dipole equations*, given in Eq. 1.15 and rewritten below:

$$\dot{\beta}_j = \left( i\Delta - \frac{\Gamma}{2} \right) \beta_j - \frac{i\Omega}{2} e^{i\vec{k}_0 \cdot \vec{r}_j} - \frac{\Gamma}{2} \sum_{j' \neq j} \frac{\exp(ik_0 r_{jj'})}{ik_0 r_{jj'}} \beta_{j'}$$

These equations are a system of  $N$  coupled first order linear differential equations for  $\beta_j(t)$ , where  $j = 1, \dots, N$ . They assume motionless atoms, low density for the atomic sample (dilute media), interaction with a weak field (linear optics) with constant polarization (scalar approximation). Different approaches can be used for their derivation, as well as different solving methods. Physical operators like the radiation pressure force and the detected intensity can be expressed as functions of the  $\beta_j$  obeying these equations [Courteille 2010]. In many works the geometry of the atomic distribution is taken as a slab or a Gaussian sphere, in both theory and experiments. Some cooperative phenomena arising from these equations are: a forward emission lobe [Rehler 1971, Bienaimé 2011a], superradiance [Rehler 1971, Roof 2016], subradiance [Bienaimé 2012], cooperative Lamb shift [Scully 2009, Bienaimé 2011a], cooperative radiation pressure force [Bienaimé 2010, Bux 2010, Bender 2010, Bienaimé 2014, Bachelard 2016], cooperative Mie scattering [Bender 2010, Bachelard 2012], coherent multiple scattering [Chabé 2014], coherent backscattering [Chabé 2014, Rouabah 2014].

T. Bienaimé PhD thesis [Bienaimé 2011b] discusses different ways of deriving and solving the coupled-dipole equations. For the derivation, we have the following approaches:

- *Classical approach:* The atoms and the laser field are treated classically, i.e., the

field is a sinusoidal monochromatic plane wave and the atoms have a single electron which oscillates as a classical harmonic oscillator [Svidzinsky 2010]. The  $\beta_j$  are the position amplitudes of each electron.

- *Semi-classical approach in the Schrödinger picture:* The atoms are treated as two-level systems and the coherent field is treated classically [Courteille 2010]. A wave function is written as a superposition of the atom-field eigenstates, where its coefficients, the  $\beta_j$ , are calculated from the Schrödinger equation, under the Markov and Weisskopf-Wigner approximation [Scully 1997]. The  $\beta_j$ s are the amplitudes of the projection in the excited state, and the sum of their square absolute value,  $\sum_{j=1}^N |\beta_j|^2$ , is related to the time evolution of the atomic excited states.
- *Semi-classical approach in the Heisenberg picture:* The Hamiltonian of the system and other operators, like the annihilation operator, evolve in time according to the Heisenberg equation [Bienaimé 2011a]. The Markov approximation is also assumed in this approach. Physical observables like the emitted intensity can be evaluated from the Heisenberg equation.
- *The master-equation approach:* The vacuum is considered as a reservoir of electromagnetic modes and interacts with the two-level atoms and the laser field [Fleischhauer 1999]. A reduced density operator is defined and its time-evolution equation is written in the density matrix formalism [Bienaimé 2013].

For the different solving methods, we can mention: a *analytic solution*, which includes the *timed-Dicke approximation* and the *continuous medium approximation*; and a *numerical solution*, which includes the *steady state solution* and the *time dependent solution*, described below:

- *The timed-Dicke approximation:* A change of basis is done for the  $N$  single excited states, in order to have one symmetrical state, which is superradiant, and  $N - 1$  anti-symmetrical states, which are subradiant [Svidzinsky 2008c, Bienaimé 2013]. Then, the population of the subradiant states is neglected. The  $\beta_j$  are replaced by the coefficient for the superradiant state, yielding to a single coupled-dipole equation which analytic solution in the steady state. Also, the expressions for the physical observables in the timed-Dicke approximation can be written analytically.
- *Continuous medium approximation:* The atomic sample is considered as a continuous medium and the  $\beta_j$  are replaced by a scalar function  $\beta(\vec{r}, t)$ , which transforms the coupled-dipole equations into a single integral equation [Bachelard 2011]. This approach was considered as main solving method by M. O. Scully *et al.* and R. Friedberg, J. T. Manassah *et al.* in several works [Svidzinsky 2009, Manassah 2012], and was shown to be reasonable for large optical thicknesses and large sample sizes [Bachelard 2011, Bienaimé 2010]. More recently, the continuous approach was shown to describe the scaling of super- and subradiance with the resonant optical thickness as well in dilute samples [Cottier 2018]. The continuous approach can be extended to include special features in the medium, like quantum statistic for bosons

in several works from J. Ruostekoski's and A. Browaeys' groups [Morice 1995, Jennewein 2018].

- *Solution for the steady state:* The  $\beta_j$  are seen as the elements of a column vector and the coupled-dipole equations are written in a matricial form [Svidzinsky 2008b, Guerin 2017b]. The matricial equation is diagonalized and solved by using the eigenvalue method, such that we find the probability of occupation of each excited state. Another approach is to calculate the eigenvalues and eigenstates of the system from the diagonalization of an *effective Hamiltonian* [Bellando 2014].
- *Time dependent solution:* The coupled-dipole equations are a many-body problem and have no analytical solution, except when  $N = 2$ , i.e., two interacting atoms. Therefore, the more direct way to solve them is by using numerical methods for differential equations, like the fourth order Runge-Kutta method.

As already mentioned, the derivation of the coupled-dipole equations is done under specific assumptions and approximations about the physical system: motionless atoms, dilute cloud, weak excitations, non-degenerate atoms. However, more general assumptions with less approximations have been studied:

- *Dense samples.* If the atoms are close enough to each other, e.g., like in dense samples, the polarization of the scattered field cannot be neglected, so near-field effects take place and the  $\beta_j$ s should be calculated in the vectorial approximation [Bellando 2014, Stephen 1964, Lehmberg 1970, Milonni 1974]. This is equivalent to taking into account the degeneracy of the excited states in the two-level atoms, like the transition  $|J_g = 0, m_g = 0\rangle \rightarrow |J_e = 1, m_e = -1, 0, 1\rangle$  [Bellando 2014, Milonni 1974]. Also, as the atoms are closer, interactions between them may occur, like van der Waals interactions [Gross 1982], collisions, and quantum statistics for bosons [Morice 1995]. Recent works show that high densities also lead to: red frequency shifts and line broadening [Pellegrino 2014, Bromley 2016, Jennewein 2016], absence of cooperative Lamb shift and Lorentz-Lorenz shift [Jenkins 2016], blue frequency shifts and deviations in the Lorentzian wings in bi-dimensional samples [Chomaz 2012, Corman 2017].
- *Sample geometry.* The geometry of the sample has a big impact on the magnitude and signal of the cooperative Lamb shift [Friedberg 2010].
- *Ordered atomic positions.* If the atoms are not randomly distributed, e.g., forming a periodical array, the decay rates and emitted intensity change [Feng 2014]. In the case of an optical lattice, cooperative phenomena like photonic band gaps arises [Schilke 2011, Samoylova 2014].
- *Strong excitation.* If the incoming radiation field is at strong intensities, nonlinear effects take place, because more than a single excitation will be produced in the cloud. The emitted light is distorted when propagating through the sample [Gross 1982]. New effects are predicted to arise, like cooperative blockade [Ott 2013], asymmetry of the Mollow triplet [Ott 2013, Pucci 2017], additional sidebands in the Mollow triplet [Pucci 2017].

- *Atomic motion.* If the particles move, Doppler effects reduce drastically the cooperative effects [Bienaimé 2012]. This will be discussed in detail in Chapter 5. Recently, the observation of a superradiant flash was reported for a cloud with considerable atomic motion [Kwong 2014].
- *Phase of the incident field.* Variations in the spatial phase of the incident laser beam make the atoms experience a different incident phase. If each atom sees a random detuning, the subradiant states are predicted to become hybrid, with features of extended states and Anderson localized states [Biella 2013]. If an inhomogeneous magnetic field is applied in order to induce Zeeman shifts in the atoms, a deviation in the emission lobe is predicted to occur [Máximo 2014]. If half of the cloud is excited by a incoming laser with a phase shift of  $\pi$  compared to the other half, subradiance may be enhanced (to be discussed in Chapter 5).
- *Atomic degeneracy and multilevel schemes.* If the atomic two levels are degenerated, line broadening may arise [Sutherland 2017]. Degeneracy was also considered in schemes with multilevel atoms in other theoretical models to study superradiance [de Oliveira 2014] and “subradiance echo” [Pavolini 1985].

### 1.1.2 Setting the equations

In this section we will use the semi-classical treatment in the Schrödinger picture to discuss the coupled-dipole model. To fix the ideas, we start by defining the physical variables of the physical system (see Fig. 1.1):

- *Atoms:* a set of  $N$  two-level atoms with two non-degenerate states: a ground state  $|g_j\rangle$  and an excited state  $|e_j\rangle$ , where  $j = 1, \dots, N$  denotes the  $j$ -th atom. Each atom has a natural frequency  $\omega_0$ , decay rate  $\Gamma$  and lifetime  $\tau_0 = 1/\Gamma$ . They do not move and are distributed in random positions  $\vec{r}_j$  in space.
- *Laser:* a monochromatic plane wave with constant polarization vector  $\hat{e}$  (linear polarization), amplitude  $\vec{E}_0 = E_0\hat{e}$ , wavelength  $\lambda$ , wavevector  $\vec{k}_0$  of magnitude  $k_0 = 2\pi/\lambda$ , and frequency  $\omega$ . Its electrical field is given by

$$\vec{E}(\vec{r}, t) = \frac{1}{2}E_0\hat{e} \left[ e^{i(\vec{k}_0 \cdot \vec{r} - \omega t)} + c.c. \right] \quad (1.1)$$

- *Vacuum:* a quantized electromagnetic field of amplitude  $\vec{E}_V(\vec{r}, t)$  defined by the Fock states  $\{|0_{\vec{k}}\rangle, |1_{\vec{k}}\rangle, \dots\}$  in the mode  $\vec{k}$  and polarization  $\hat{e}_{\vec{k}}$ , where  $\vec{k}$  is the wave vector, and frequency  $\omega_k$ , given by

$$\vec{E}_V(\vec{r}, t) = i \sum_{\vec{k}} \sqrt{\frac{\hbar\omega_k}{2\epsilon_0 V_{\text{ph}}}} \hat{e}_{\vec{k}} \left[ a_{\vec{k}} e^{i(\vec{k} \cdot \vec{r} - \omega_k t)} + h.c. \right] \quad (1.2)$$

where  $V_{\text{ph}}$  is the photon quantization volume.

The Hamiltonian for the system can be written as

$$H = H_A + H_V + H_{AL} + H_{AV} \quad (1.3)$$

with

$$H_A = -\frac{\hbar\Delta}{2} \sum_j |e_j\rangle \langle e_j| - |g_j\rangle \langle g_j| \quad (1.4a)$$

$$H_V = \sum_{\vec{k}} \hbar\omega_k a_k^\dagger a_k \quad (1.4b)$$

$$H_{AL} = \frac{\hbar\Omega}{2} \sum_j \left[ \sigma_j e^{-i(\vec{k}_0 \cdot \vec{r}_j - \Delta t)} + h.c. \right] \quad (1.4c)$$

$$H_{AV} = \hbar \sum_j \sum_{\vec{k}} g_k (\sigma_j e^{-i\omega_0 t} + h.c.) \left( a_k e^{i(\vec{k} \cdot \vec{r}_j - \omega_k t)} + h.c. \right) \quad (1.4d)$$

where we simplified the notation  $\sum_j = \sum_{j=1}^N$ .  $\vec{d}$  is the dipole matrix element,  $\Omega = \vec{d} \cdot \hat{\epsilon} E_0 / \hbar$  is the Rabi frequency,  $g_{\vec{k}} = \vec{d} \cdot \hat{\epsilon}_{\vec{k}} \sqrt{\omega_k / 2\hbar\epsilon_0 V_{\text{ph}}}$  is the quantum Rabi frequency, i.e., the single photon coupling strength,  $\sigma_j = |g_j\rangle \langle e_j|$  is the atomic operator,  $\Delta = \omega - \omega_0$  is the laser detuning, and  $\Delta_k = \omega_k - \omega_0$  is the vacuum field detuning.  $H_A$  is the atomic Hamiltonian;  $H_V$  is the Hamiltonian for the vacuum modes;  $H_{AL}$  represents the interaction between the atoms and the laser; and  $H_{AV}$  represents the interaction between the atoms and the vacuum.

Some important comments can be done here:

- $H_A$  can be written as  $H_A = \sum_j H_j$  with  $H_j = -(\hbar\Delta)/2 (|e_j\rangle \langle e_j| - |g_j\rangle \langle g_j|)$ , i.e.,  $H_A$  is the sum of the Hamiltonians for single atoms. The same can be done for  $H_{AL}$  and  $H_{AV}$ , in a such way that if  $N = 1$  we recover the interaction of a single atom with the monochromatic field and vacuum modes, treated in standard quantum mechanics textbooks [[Griffiths 2005](#), [Cohen-Tannoudji 1992](#), [Foot 2005](#), [Scully 1997](#), [Berman 2008](#), [Mollow 1969](#)]. The obtained results can be extended for  $N$  *independent* atoms. On the other hand, in the coupled dipole model, the  $N$  atoms are “dependent”, in the sense that we consider that they can see each other and interact.
- $H_{AL}$  is written in the rotating-wave approximation (RWA) [[Cohen-Tannoudji 1992](#)], and  $H_A$  and  $H_{AL}$  are written in the rotating frame. However, we do not do the RWA for  $H_{AV}$ , which allows virtual-photon exchanges. This is because, beyond the cooperative Lamb shift, virtual photons contribute for a correct description of the subradiant amplitudes and decay rates [[Friedberg 2008a](#), [Svidzinsky 2008a](#), [Friedberg 2008b](#), [Svidzinsky 2009](#), [Svidzinsky 2010](#)]. Another approach with virtual photons is discussed in [[Li 2012](#), [Li 2013](#)].

Now, following [[Svidzinsky 2010](#)], we consider that there are the following possible states for the atom-light-vacuum interaction:

- The state  $|G, 0_{\vec{k}}\rangle \equiv |g_1, \dots, g_j, \dots, g_N\rangle |0_{\vec{k}}\rangle$ , where all atoms are in the ground state and there is no photon; the  $N$  states  $|j, 0_{\vec{k}}\rangle \equiv |g_1, \dots, e_j, \dots, g_N\rangle |0_{\vec{k}}\rangle$ , where the atom  $j$  is in the excited state and no photon (absorption). There are  $N$  excited states because we do not know which atom is in the excited state, so there are  $N$  possibilities. This is equivalent to consider that the atoms are a system of identical particles.
- The state  $|G, 1_{\vec{k}}\rangle \equiv |g_1, \dots, g_j, \dots, g_N\rangle |1_{\vec{k}}\rangle$ , where all atoms are in the ground state and one photon in the mode  $\vec{k}$  is present (emission).
- The state  $|pq, 1_{\vec{k}}\rangle \equiv |g_1, \dots, e_p, \dots, e_q, \dots, g_N\rangle |1_{\vec{k}}\rangle$ , which stands for two excited atoms and a photon in the mode  $\vec{k}$  (virtual photon exchanges).

Thus, the wavefunction  $|\Psi(t)\rangle$  of the system is

$$|\Psi(t)\rangle = \alpha(t) |G, 0_{\vec{k}}\rangle + \sum_j \beta_j(t) |j, 0_{\vec{k}}\rangle + \sum_{\vec{k}} \gamma_{\vec{k}}(t) |G, 1_{\vec{k}}\rangle + \sum_{p < q} \sum_{\vec{k}} \alpha_{pq, \vec{k}}(t) |pq, 1_{\vec{k}}\rangle \quad (1.5)$$

with  $\alpha_{pq, \vec{k}} = \alpha_{qp, \vec{k}}$ . Note that this ansatz of  $|\Psi(t)\rangle$  restricts ourselves to the limit of single excitations, or linear-optics regime, which can also be expressed by the condition

$$s(\Delta) = \frac{I/I_s}{1 + 4\Delta^2/\Gamma^2} \ll 1 \quad (1.6)$$

where  $s(\Delta)$  is the saturation parameter [Foot 2005], with  $I_s$  the saturation intensity and  $I = (2\Omega^2/\Gamma^2)I_s$  is the laser field intensity.

By replacing  $|\Psi(t)\rangle$  in the Schrödinger equation  $H|\Psi\rangle = i\hbar\partial|\Psi\rangle/\partial t$ , with  $H$  in Eqs. 1.4, and projecting the result in each one of the four allowed states of the system, we obtain the time evolution for the coefficients  $\alpha(t)$ ,  $\beta_j(t)$ ,  $\gamma_{\vec{k}}(t)$  and  $\alpha_{pq, \vec{k}}(t)$  [Svidzinsky 2010]:

$$\dot{\alpha} = -\frac{i\Omega}{2} \sum_j \beta_j e^{-i(\vec{k}_0 \cdot \vec{r}_j - \Delta t)} \quad (1.7a)$$

$$\begin{aligned} \dot{\beta}_j &= -\frac{i\Omega}{2} \alpha e^{i(\vec{k}_0 \cdot \vec{r}_j - \Delta t)} - i \sum_{\vec{k}} g_{\vec{k}} \gamma_{\vec{k}} e^{i(\vec{k} \cdot \vec{r}_j - i\Delta_k t)} - \\ &\quad - i \sum_{j' \neq j} \sum_{\vec{k}} g_{\vec{k}} \alpha_{jj', \vec{k}} e^{i[\vec{k} \cdot \vec{r}_{j'} - (\omega + \omega_k)t]} \end{aligned} \quad (1.7b)$$

$$\dot{\gamma}_{\vec{k}} = -ig_{\vec{k}} \sum_j \beta_j e^{-i(\vec{k} \cdot \vec{r}_j - \Delta_k t)} \quad (1.7c)$$

$$\dot{\alpha}_{pq, \vec{k}} = -ig_{\vec{k}} e^{i(\omega_k + \omega_0)t} \left( \beta_p e^{-i\vec{k} \cdot \vec{r}_q} + \beta_q e^{-i\vec{k} \cdot \vec{r}_p} \right) \quad (1.7d)$$

### 1.1.3 Solving the equations for the coefficients

Equations 1.7 are a system of coupled differential equations, and they have to be solved. The initial conditions are  $\alpha(0) = 1$  and  $\beta_j(0) = \gamma_{\vec{k}}(0) = \alpha_{pq, \vec{k}} = 0$ , i.e., initially the atoms are in the ground state when they interact with the incident laser field and vacuum modes.

As we will discuss in section 1.3, we are interested in studying the temporal dynamics, from the decay of each one of the single-atom excited states  $|j\rangle$ , so we solve Eqs. 1.7 for  $\beta_j(t)$ .

For Eq. 1.7a,  $\alpha(t) \approx 1$  is a good approximation because we are in the regime of weak excitations (a general approach is to substitute Eq. 1.7a in Eq. 1.7b; see [Ott 2013]). For Eqs. 1.7c and 1.7d, we integrate under the initial conditions, which gives

$$\gamma_{\vec{k}}(t) = -ig_{\vec{k}} \int_0^t \sum_j \beta_j(t') e^{-i\vec{k}\cdot\vec{r}_j} e^{-\Delta_k t'} dt' \quad (1.8)$$

$$\alpha_{pq,\vec{k}}(t) = -ig_{\vec{k}} \int_0^t e^{i(\omega_k+\omega_0)t'} \left[ \beta_p(t') e^{-i\vec{k}\cdot\vec{r}_q} + \beta_q(t') e^{-i\vec{k}\cdot\vec{r}_p} \right] dt' \quad (1.9)$$

Replacing  $\alpha = 1$  and Eqs. 1.8 and 1.9 in Eq. 1.7b, we get rid of the degrees of freedom of the field and we obtain the time evolution for  $\beta_j$  only:

$$\begin{aligned} \dot{\beta}_j &= -\frac{i\Omega}{2} e^{i(\vec{k}_0\cdot\vec{r}_j-\Delta t)} - \sum_{\vec{k}} |g_{\vec{k}}|^2 \sum_{j'} e^{i\vec{k}\cdot(\vec{r}_j-\vec{r}_{j'})} \int_0^t \beta_{j'}(t') e^{-i\Delta_k(t-t')} dt' - \\ &- \sum_{j' \neq j} \sum_{\vec{k}} |g_{\vec{k}}|^2 \left[ \sum_{j' \neq j} e^{-i\vec{k}\cdot(\vec{r}_j-\vec{r}_{j'})} \int_0^t \beta_{j'}(t') e^{-i(\omega_k+\omega_0)(t-t')} dt' - \right. \\ &\left. - (N-1) \int_0^t \beta_j(t') e^{-i(\omega_k+\omega_0)(t-t')} dt' \right] \end{aligned} \quad (1.10)$$

The evaluation of the integral terms in Eq. 1.10 is done under three important approximations:

- *The scalar approximation.* This ignores near fields and polarizations, so only long-range interactions are taken into account in describing the strength of the dipole-dipole interactions with respect to the distances between the atoms. Hence,  $\vec{d}\cdot\hat{\epsilon} = d$  and  $\hat{\epsilon}_{\vec{k}} = \hat{\epsilon}$ , which give  $\Omega = dE_0/\hbar$ ,  $\vec{d}\cdot\hat{\epsilon}_{\vec{k}} = d$  and  $g_{\vec{k}} = g_k = d\sqrt{\omega_k/2\hbar\epsilon_0 V_{\text{ph}}}$  in Eq. 1.10 [Lehmberg 1970]. As we will see soon, the scalar approximation yields to dipole-dipole interactions proportional to

$$V_{jj'} \propto \frac{1}{k_0 r_{jj'}} \quad (1.11)$$

where  $r_{jj'}$  is the distance between to any atoms  $j$  and  $j'$ . If one does not do the scalar approximation, we have thus the *vectorial approximation* [Lehmberg 1970, Milonni 1974, Bellando 2014] and it yields to dipole-dipole interactions with angular terms and distances proportional to  $1/(k_0 r_{jj'})$ ,  $1/(k_0 r_{jj'})^2$  and  $1/(k_0 r_{jj'})^3$  [Bellando de Castro 2013]. It is possible to show that the quadratic and cubic distance terms can be neglected for large  $r_{jj'}$ , which is true for dilute (low density) samples.

- *Retardation terms:* The retardation in the emitted fields is neglected, so  $t \gg |\vec{r}_j - \vec{r}_{j'}|/c$ . A discussion with retarded time for two atoms can be found in [Milonni 1974].

- *The Markov approximation.* This assumes a large timescale compared to the response of the physical system, i.e.,  $t \gg 1/\omega_0$ . Thus,  $\beta_j(t')$  is assumed to vary slowly and it comes out of the integrals. Also, the upper integration limit is set as  $t \rightarrow \infty$ .

Under the scalar and Markov approximations, we go to the continuum limit for the modes  $\vec{k}$ , i.e.,  $\sum_{\vec{k}} \rightarrow \frac{V_{\text{ph}}}{(2\pi)^3} \int d^3\vec{k}$ , and the integrals are solved by using the Cauchy principal value method. The calculations are detailed in [Svidzinsky 2010] and the result is finally the *coupled-dipole equations*:

$$\dot{\beta}_j = -\frac{i\Omega}{2} e^{i(\vec{k}_0 \cdot \vec{r}_j - \Delta t)} - \frac{\Gamma}{2} \sum_{j'} \frac{e^{ik_0 r_{jj'}}}{ik_0 r_{jj'}} \beta_{j'} \quad (1.12)$$

where  $r_{jj'} \equiv |\vec{r}_j - \vec{r}_{j'}|$  is the distance between the atoms  $j$  and  $j'$  and the natural decay rate  $\Gamma$  has been defined as

$$\Gamma \equiv \frac{d^2 k_0^3}{2\pi \hbar \epsilon_0} \quad (1.13)$$

The term  $V_{jj'} = \frac{e^{ik_0 r_{jj'}}}{ik_0 r_{jj'}}$  represents the interactions between the atoms, which are the first correction that arises under the approximations and assumptions already discussed. They are long-range interactions, which are small for two atoms but are summed up for the whole set of atoms.

Eq. 1.12 can be rewritten as

$$\dot{\beta}_j = i\Delta\beta_j - \frac{i\Omega}{2} e^{i\vec{k}_0 \cdot \vec{r}_j} - \frac{\Gamma}{2} \sum_{j'} \frac{e^{ik_0 r_{jj'}}}{ik_0 r_{jj'}} \beta_{j'} \quad (1.14)$$

by means of the change  $\beta_j \rightarrow \beta_j e^{-i\Delta t}$  and  $\dot{\beta}_j \rightarrow (\dot{\beta}_j - i\Delta\beta_j)e^{-i\Delta t}$ , which is to write  $\beta_j$  in the rotating frame. One can show [Svidzinsky 2010] that this equation can be rewritten as

$$\dot{\beta}_j = \left( i\Delta - \frac{\Gamma}{2} \right) \beta_j - \frac{i\Omega}{2} e^{i\vec{k}_0 \cdot \vec{r}_j} - \frac{\Gamma}{2} \sum_{j' \neq j} \frac{e^{ik_0 r_{jj'}}}{ik_0 r_{jj'}} \beta_{j'} \quad (1.15)$$

Eqs. 1.15 tells us how the dipole amplitudes evolve in time. The first term is the decay for a single atom, the second term is due to the interaction with the incident laser and the third term is the dipole-dipole interaction, i.e., the field radiated by the other atoms  $j'$  onto the atom  $j$ . For a single atom, i.e.,  $N = 1$ , and hence the third term is absent, which yields to the standard time evolution for a single atom.

## Effective Hamiltonian

It is possible to set the wavefunction of the system directly as (c.f. Eq. 1.5)

$$|\Psi(t)\rangle = \alpha(t) |G\rangle + \sum_j \beta_j(t) |j\rangle \quad (1.16)$$

i.e., without the degrees of freedom of the field. However, to obtain Eqs. 1.15, the Hamiltonian has to be replaced by an *effective Hamiltonian* [Bienaimé 2013], shown to be

$$H_{\text{eff}} = \frac{\hbar\Omega}{2} \sum_j \left[ \sigma_j e^{-i(\vec{k}_0 \cdot \vec{r}_j - \Delta t)} + c.c. \right] - \hbar\Delta \sum_j \sigma_j^\dagger \sigma_j - \frac{\hbar\Gamma}{2} \sum_{j,j'} V_{jj'} \sigma_j^\dagger \sigma_{j'} \quad (1.17)$$

and hence  $H_{\text{eff}} |\Psi\rangle = i\hbar \partial |\Psi\rangle / \partial t$ .

### Timed-Dicke approximation

It is possible to solve the coupled-dipole equations analytically by means of the *timed-Dicke approximation* [Courteille 2010]. A change of basis is done for the  $N$  excited states, from the basis  $\{|j\rangle\}$  to the basis  $\{|TD\rangle, |s_1\rangle, |s_2\rangle, \dots, |s_{N-1}\rangle\}$ , where  $|TD\rangle$  is the super-radiant state

$$|TD\rangle = \frac{1}{\sqrt{N}} \sum_{j=0}^l e^{i\vec{k}_0 \cdot \vec{r}_j} |j\rangle \quad (1.18)$$

known also as the *timed-Dicke state* [Scully 2006], and the  $N-1$  states  $|s_l\rangle$ ,  $l = 1, \dots, N-1$ , are the subradiant states, defined by [Bienaimé 2011b, Scully 2007]

$$|s_l\rangle = \frac{1}{\sqrt{l(l+1)}} \left( \sum_{j=1}^l e^{i\vec{k}_0 \cdot \vec{r}_j} |j\rangle - l e^{i\vec{k}_0 \cdot \vec{r}_{l+1}} |l+1\rangle \right) \quad (1.19)$$

Note that  $|TD\rangle$  is a symmetric combination of  $|j\rangle$ , while the  $|s_l\rangle$ s are anti-symmetric combinations of  $|j\rangle$ .

Hence, the wavefunction  $|\Psi(t)\rangle$  in the new basis reads

$$|\Psi(t)\rangle = \alpha(t) |G\rangle + \beta_{\text{TD}}(t) |TD\rangle + \sum_{l=1}^{N-1} c_l(t) |s_l\rangle \quad (1.20)$$

and then we make  $c_l(t) = 0$ , i.e., we neglect the population of the subradiant states. Thus, the timed Dicke approximation assures that the system is equivalent to say that the atomic system is at the state  $|TD\rangle$ , i.e., one excited atom, with phase  $e^{i\vec{k}_0 \cdot \vec{r}_j}$ , summed to all the  $N$  atoms with equal probability  $1/\sqrt{N}$ , as if the atomic cloud was excited originally by a single photon at resonance, as originally proposed by [Scully 2006].

The assumption  $c_l(t) = 0$  is equivalent to neglect the Fano coupling [Fano 1961], which states that:

*If two physical systems (the superradiant state  $|TD\rangle$  and all the subradiant states  $|s_l\rangle$ ) are coupled each one with the vacuum, they also are coupled to each other. Therefore, there is a transfer of population between them.*

Neglecting the Fano coupling means that  $|TD\rangle$  decays directly to the ground state  $|G\rangle$ . This is true for samples whose size  $R$  is  $R \ll \lambda$ , as discussed initially by R. Dicke

[Dicke 1954], and for large samples  $R > \lambda$  in the far detuning limit [Courteille 2010, Bienaimé 2013].

The comparison with the wavefunctions in Eqs. 1.20 and 1.5 leads to

$$\beta_j = \frac{1}{\sqrt{N}} \beta_{\text{TD}} e^{i\vec{k}_0 \cdot \vec{r}_j} \quad (1.21)$$

which is the timed-Dicke approximation defined in [Courteille 2010]. Moreover, if we assume that the  $N$  atoms are distributed spatially in a Gaussian sphere of RMS radius  $R$  (which is approximately the case in our experimental cold atoms clouds), the timed-Dicke state decays from the steady state with a decay rate in the forward direction [Courteille 2010]

$$\Gamma_N = \left(1 + \frac{b_0}{12}\right) \Gamma \quad (1.22)$$

where  $b_0 = 3N/(k_0 R)^2$  is the resonant optical thickness for a Gaussian sphere (to be discussed in section 1.3).

Simulations show that the coupled-dipole equations converge to the timed-Dicke approximation only when  $b(\Delta) < 1$  [Bienaimé 2013], where  $b(\Delta) = b_0/(1 + 4\Delta^2/\Gamma^2)$  is the optical thickness of the sample for a spherical Gaussian distribution (see section 1.3). The condition  $b(\Delta) < 1$  can be achieved for large detunings of the incident laser beam.

## 1.2 The detected fluorescence

From the coupled-dipole equations, Eq. 1.15, we can derive analytic expressions for the detected intensity. As we will discuss in section 1.3, cooperative signatures of the atom-field interactions are extracted from the emitted intensity, after the atoms interact with the laser for some time and the latter is switched off.

According to the photodetection theory [Mandel 1995], the intensity emitted by the atoms detected in a given position  $\vec{r}$  from the center of mass of the atomic distribution and at time  $t$  is defined by

$$I(\vec{r}, t) = 2c\epsilon_0 \langle E^\dagger E \rangle \quad (1.23)$$

where  $E$  is the electric field given in Eq. 1.2. The photon annihilation operator  $a_k(t)$  can be calculated in the Heisenberg picture from the Heisenberg equation. It can be shown [Bienaimé 2011a] that in the far-field limit

$$E(\vec{r}, t) \approx -i \frac{dk_0^2}{4\pi\epsilon_0} \frac{e^{-i\omega_0(t-r/c)}}{r} \sum_j e^{-ik_0 \hat{r} \cdot \vec{r}_j} \beta_j(t) \quad (1.24)$$

where the unit vector  $\hat{r}$  defines the detection direction, from the cloud center of mass to the detector.

Inserting Eq. 1.24 in Eq. 1.23, we obtain the intensity collected by a photodetector (see Fig. 1.2):

$$I(\vec{r}, t) = \frac{d^2\omega^4}{8\pi^2 c^3 \epsilon_0 r^2} \left| \sum_j e^{-ik_0 \hat{r} \cdot \vec{r}_j} \beta_j \right|^2 = \frac{d^2\omega^4}{8\pi^2 c^3 \epsilon_0 r^2} \sum_j \sum_{j'} e^{-ik_0 \hat{r} \cdot (\vec{r}_j - \vec{r}_{j'})} \beta_j \beta_{j'}^* \quad (1.25)$$

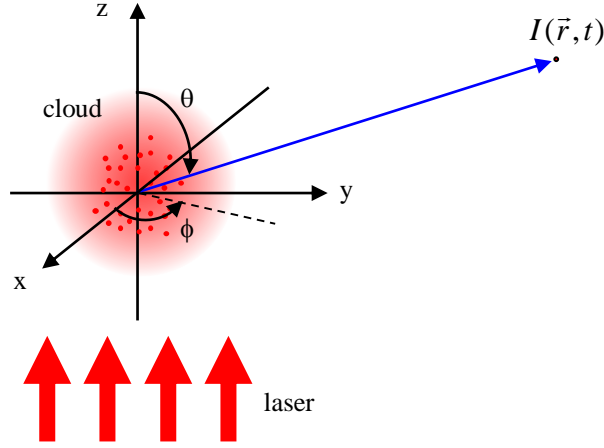


**Figure 1.2:** The detected intensity  $I(\vec{r}, t)$  emitted by a cloud of atoms excited by an incident beam, detected in a point  $\vec{r}$  of the space in a instant  $t$ .  $I(\vec{r}, t)$  is given by Eq. 1.25 (definition) and Eqs. 1.34 and 1.35 (in spherical coordinates), i.e.,  $I(\theta, \phi, t)$  and  $I(\theta, t)$ , this last one integrated in  $\phi$  due to the symmetry of the cloud with respect to the laser the laser axis, fixed at the  $z$  direction.

### 1.2.1 The total emitted intensity

The total emitted power  $P(t)$  is the power measured in the whole space, in all directions. It corresponds to a spherical detector surrounding the atoms. By definition,  $P(t) = \int I(\vec{r}, t) dA$ , where  $dA$  is the differential area element.

It is convenient to write  $I(\vec{r}, t)$  in spherical coordinates,  $\{r, \theta, \phi\}$ <sup>2</sup>, so  $I(\vec{r}, t) = I(r, \theta, \phi, t)$  and  $dA = r^2 \sin \theta d\theta d\phi$ , giving

$$P(t) = r^2 \int_0^\pi \int_0^{2\pi} I(r, \theta, \phi, t) \sin \theta d\theta d\phi \quad (1.26)$$

By substituting Eq. 1.25, the terms  $r^2$  vanish and we have

$$P(t) = \frac{d^2\omega^4}{8\pi^2 c^3 \epsilon_0} \int_0^\pi \int_0^{2\pi} \left| \sum_j e^{-ik_0 \hat{r} \cdot \vec{r}_j} \beta_j(t) \right|^2 \sin \theta d\theta d\phi \quad (1.27)$$

The double integral can be calculated analytically, which leads to

$$P(t) = \frac{d^2\omega^4}{8\pi^2 c^3 \epsilon_0} \times 4\pi \sum_j \sum_{j'} \frac{\sin(k_0 r_{jj'})}{k_0 r_{jj'}} \beta_j(t) \beta_{j'}^*(t) \quad (1.28)$$

However, it is possible to prove that  $P(t)$  is also equal to

<sup>2</sup> In this definition of spherical coordinates,  $r$  is the radial coordinate (from 0 to infinite),  $\phi$  is the azimuth angle (from 0 to  $2\pi$ , laying on the  $xy$  plane) and  $\theta$  is the polar angle (from 0 to  $\pi$ , from the  $z$  axis). See Fig. 1.2.

$$P(t) = -\hbar\omega \frac{d}{dt} \sum_j |\beta_j(t)|^2 \quad (1.29)$$

after the extinction of the incident field. In words: *the total emitted power is proportional to the derivative of the excited state population* once the laser is switched off. We provide a proof of Eq. 1.29 below.

### Proof

The starting point is the definition of total emitted power in Eq. 1.27, which can be rewritten as

$$P(t) = \frac{d^2\omega^4}{8\pi^2 c^3 \epsilon_0} \int_0^\pi \int_0^{2\pi} \sum_j \sum_{j'} e^{-ik_0 \hat{r} \cdot (\vec{r}_j - \vec{r}_{j'})} \beta_j(t) \beta_{j'}^*(t) \sin \theta \, d\theta \, d\phi$$

and the integral

$$I_a = \int_0^\pi \int_0^{2\pi} \sum_j \sum_{j'} e^{-ik_0 \hat{r} \cdot (\vec{r}_j - \vec{r}_{j'})} \beta_j(t) \beta_{j'}^*(t) \sin \theta \, d\theta \, d\phi$$

should be solved. As already pointed, it is exact.

To see that, we choose a coordinate frame where  $\hat{r} \cdot (\vec{r}_j - \vec{r}_{j'}) = r_{jj'} \cos \theta$  [Jackson 1998], we have

$$\begin{aligned} I_a &= \sum_j \sum_{j'} \beta_j(t) \beta_{j'}^*(t) \int_0^{2\pi} d\phi \int_0^\pi e^{-ik_0 r_{jj'} \cos \theta} \sin \theta \, d\theta = \\ &= 2\pi \sum_j \sum_{j'} \beta_j(t) \beta_{j'}^*(t) \int_{-1}^1 e^{-ik_0 r_{jj'} u} \, du = \\ &= 2\pi \sum_j \sum_{j'} \frac{2 \sin(k_0 r_{jj'})}{k_0 r_{jj'}} \beta_j(t) \beta_{j'}^*(t) \end{aligned} \quad (1.30)$$

exactly as in Eq. 1.28 and [Bienaimé 2014]. This is valid for all  $\beta_j(t)$ , in all instants  $t$ .

Now we will show that the derivative  $I_b = \frac{d}{dt} \sum_j |\beta_j(t)|^2$  is also equal to Eq. 1.30 when  $\Omega = 0$ . To do so, we start by expanding the summation

$$\begin{aligned} I_b &= \frac{d}{dt} \sum_j |\beta_j(t)|^2 = \frac{d}{dt} \sum_j \sum_{j'} \beta_j \beta_{j'}^* \delta_{jj'} = \sum_j \sum_{j'} \delta_{jj'} \frac{d}{dt} (\beta_j \beta_{j'}^*) = \\ &= \sum_j \sum_{j'} \delta_{jj'} \left( \dot{\beta}_j \beta_{j'}^* + \beta_j \dot{\beta}_{j'}^* \right) \end{aligned}$$

and then we use the coupled-dipole equations, Eq. 1.14, to replace the two derivatives in the parenthesis. When the laser is switched off,  $\Omega = 0$ , so

$$\dot{\beta}_j = i\Delta\beta_j - \frac{\Gamma}{2} \sum_{j'} V_{jj'} \beta_{j'}$$

with  $V_{jj'} = \frac{e^{ik_0 r_{jj'}}}{ik_0 r_{jj'}}$ . Changing  $j \rightarrow j'$  and taking the conjugate in both sides, we have

$$\dot{\beta}_{j'}^* = -i\Delta\beta_{j'}^* - \frac{\Gamma}{2} \sum_j V_{jj'}^* \beta_j^*$$

(note that  $V_{jj'} = V_{j'j}$  and we also have changed  $j' \rightarrow j$  in the last term because  $j$  is a sum index).

Thus: (we do  $j \rightarrow m$ ,  $j' \rightarrow n$ ; the terms in  $\Delta$  vanish)

$$\begin{aligned} I_b &= \sum_j \sum_{j'} \delta_{jj'} \left( \left[ i\Delta\beta_j - \frac{\Gamma}{2} \sum_m V_{jm} \beta_m \right] \beta_{j'}^* + \beta_j \left[ -i\Delta\beta_{j'}^* - \frac{\Gamma}{2} \sum_n V_{nj'}^* \beta_n^* \right] \right) = \\ &= \sum_j \sum_{j'} \delta_{jj'} \left( i\Delta\beta_j \beta_{j'}^* - \frac{\Gamma}{2} \sum_m V_{jm} \beta_m \beta_{j'}^* - i\Delta\beta_j \beta_{j'}^* - \frac{\Gamma}{2} \sum_n V_{nj'}^* \beta_j \beta_n^* \right) = \\ &= -\frac{\Gamma}{2} \sum_j \sum_{j'} \delta_{jj'} \left( \sum_m V_{jm} \beta_m \beta_{j'}^* + \sum_n V_{nj'}^* \beta_j \beta_n^* \right) \end{aligned}$$

Now we use the property of the Kronecker delta to do  $\sum_j \delta_{jj'} V_{jm} = V_{j'm}$  and  $\sum_{j'} \delta_{jj'} V_{nj'}^* = V_{nj}^*$ . So

$$I_b = -\frac{\Gamma}{2} \sum_j \left( \sum_{j'} \sum_n V_{j'm} \beta_m \beta_{j'}^* + \sum_j \sum_n V_{nj}^* \beta_j \beta_n^* \right)$$

and from it we have (we undo  $m \rightarrow j$ ,  $n \rightarrow j'$ )

$$I_b = -\frac{\Gamma}{2} \sum_j \sum_{j'} (V_{jj'} + V_{jj'}^*) \beta_j \beta_{j'}^*$$

Finally, we use the definition of  $V_{jj'}$  to get

$$I_b = -\Gamma \sum_j \sum_{j'} \frac{\sin(k_0 r_{jj'})}{k_0 r_{jj'}} \beta_j \beta_{j'}^* \quad (1.31)$$

exactly as in Eqs. 1.30.

Therefore,

$$\sum_j \sum_{j'} \frac{\sin(k_0 r_{jj'})}{k_0 r_{jj'}} \beta_j \beta_{j'}^* = -\frac{1}{\Gamma} \frac{d}{dt} \sum_j |\beta_j(t)|^2$$

and by substituting the equation above in Eq. 1.28, as well as the definition of  $\Gamma$  in Eq. 1.13, we obtain

$$P(t) = -\frac{d^2\omega^4}{8\pi^2c^3\epsilon_0} 4\pi \frac{2\pi\hbar\epsilon_0c^3}{d^2\omega^3} \frac{d}{dt} \sum_j |\beta_j(t)|^2 = -\hbar\omega \frac{d}{dt} \sum_j |\beta_j(t)|^2$$

exactly as in 1.29. *Q.E.D.*

If  $\Omega \neq 0$ , we can do a similar calculation to obtain

$$P(t) \propto -\frac{d}{dt} \sum_j |\beta_j(t)|^2 + \frac{i\Omega}{2} \sum_j \left( e^{-i\vec{k}_0 \cdot \vec{r}_j} \beta_j - c.c. \right) \quad (1.32)$$

which is valid for all  $t$  and  $\Omega$ , both before and after the switch off of the incident field.

### Total power for a single atom

For pedagogical purposes, we can write the total emitted power and the  $\beta_j$  equations for a single atom, i.e.,  $N = 1$ . With one atom, Eqs. 1.23 and 1.15 turn into

$$\begin{aligned} I(\vec{r}, t) &= \frac{d^2\omega^4}{8\pi^2c^3\epsilon_0r^2} |e^{-i\vec{k}_0 \cdot \vec{r}} \beta|^2 = \frac{d^2\omega^4}{8\pi^2c^3\epsilon_0r^2} |\beta|^2 \\ \dot{\beta} &= \left( i\Delta - \frac{\Gamma}{2} \right) \beta - \frac{i\Omega}{2} e^{i\vec{k}_0 \cdot \vec{r}} \end{aligned}$$

since  $V_{jj'} = 0$  for a single atom. The total power is

$$P(t) = r^2 \int_0^{2\pi} \int_0^\pi \frac{d^2\omega^4}{8\pi^2c^3\epsilon_0r^2} |\beta(t)|^2 \sin\theta d\theta d\phi = \frac{d^2\omega^4}{8\pi^2c^3\epsilon_0} 4\pi |\beta(t)|^2 = \hbar\omega\Gamma |\beta(t)|^2$$

as in Eq. 1.28.

When the incoming field is switched off, we have

$$\dot{\beta} = \left( i\Delta - \frac{\Gamma}{2} \right) \Rightarrow \beta(t) = \beta(0) e^{i\Delta t} e^{-\Gamma t/2}$$

providing an analytical solution for the single atom case, and  $t = 0$  is the instant where the field is switched off. From it, we have  $|\beta(t)|^2 = |\beta(0)|^2 e^{-\Gamma t}$  and

$$\frac{d}{dt} |\beta|^2 = -\Gamma |\beta|^2 \Rightarrow |\beta|^2 = -\frac{1}{\Gamma} \frac{d}{dt} |\beta|^2$$

Replacing this last equation in the total power, we have

$$P(t) = -\hbar\omega \frac{d}{dt} |\beta|^2$$

as in Eq. 1.29.

For the steady state,  $\dot{\beta} = 0$ , so  $\beta \rightarrow \beta_0$  and hence

$$0 = \left( i\Delta - \frac{\Gamma}{2} \right) \beta_0 - \frac{i\Omega}{2} e^{i\vec{k}_0 \cdot \vec{r}} \Rightarrow \beta_0 = \frac{i\Omega/2}{i\Delta - \Gamma/2} e^{i\vec{k}_0 \cdot \vec{r}} \Rightarrow |\beta_0|^2 = \frac{\Omega^2/4}{\Delta^2 + \Gamma^2/4}$$

This is exactly the population of the excited state for the single atom, in the steady state and in linear regime [Berman 2008]. Hence, the emitted fluorescence in the steady state is  $P = \hbar\omega\Gamma|\beta_0|^2$ .

### 1.2.2 Intensity in a given direction from the incident light

The intensity measured in a given position of space is indeed given by Eq. 1.25, since it comes from photodetection theory as already discussed. By expanding  $\vec{r}_j - \vec{r}_{j'} = (x_j - x_{j'}, y_j - y_{j'}, z_j - z_{j'}) = (x_{jj'}, y_{jj'}, z_{jj'})$  and using spherical coordinates like in Fig. 1.2, we have  $\hat{r} = (\sin\theta \cos\phi, \sin\theta \sin\phi, \cos\theta)$ , so the intensity detected in a direction  $\{\theta, \phi\}$  is

$$I(r, \theta, \phi, t) = \frac{d^2\omega^4}{8\pi^2 c^3 \epsilon_0 r^2} \sum_j \sum_{j'} \beta_j(t) \beta_{j'}^*(t) e^{-ik_0(x_{jj'} \sin\theta \cos\phi + y_{jj'} \sin\theta \sin\phi + z_{jj'} \cos\theta)} \quad (1.33)$$

In the following we drop the prefactor  $1/r^2$  for the intensities. The main reason for that is that all theoretical and experimental intensities presented in this thesis will be normalized by its steady-state value, so all constants cancel and we have only the dependency in the summations. Formally, we can define a power  $P(\theta, \phi, t) = r^2 I(r, \theta, \phi, t)$  and then calculate  $P(\theta, \phi, t)$ ; however, when normalized,  $P(\theta, \phi, t) \propto I(r, \theta, \phi, t) \propto$  summation. We will also use the word ‘‘intensity’’ even if it means power.

Therefore, we have the detected intensity in spherical coordinates as

$$I(\theta, \phi, t) \propto \sum_j \sum_{j'} \beta_j(t) \beta_{j'}^*(t) e^{-ik_0(x_{jj'} \sin\theta \cos\phi + y_{jj'} \sin\theta \sin\phi + z_{jj'} \cos\theta)} \quad (1.34)$$

For spherical Gaussian distributions, and averaging the positions along the azimuthal angle  $\phi$ , the atomic cloud is symmetric with respect to the incident laser axis, so we can do an integration to remove one of the two angular dependencies. By setting the incident laser beam along the  $z$ -axis of a Cartesian coordinate frame whose origin is in the center of mass of the atomic cloud (see Fig. 1.2), we have  $\vec{k}_0$  parallel to the  $z$ -axis, i.e.,  $\vec{k}_0 = k_0 \hat{z}$ . Thus, the system cloud-laser is symmetric to  $z$  and, in spherical coordinates, it is symmetric along the coordinate  $\phi$ . The coordinate  $\theta$  becomes the angle between the detector and the laser direction. Therefore, the detected intensity is the intensity at the position  $\theta$  for all directions  $\phi$ , so we integrate on  $\phi$ :

$$I(\theta, t) = \int_0^{2\pi} I(\theta, \phi, t) d\phi = \sum_j \sum_{j'} \beta_j(t) \beta_{j'}^*(t) \int_0^{2\pi} e^{-ik_0(x_{jj'} \sin\theta \cos\phi + y_{jj'} \sin\theta \sin\phi + z_{jj'} \cos\theta)} d\phi \quad (1.35)$$

with  $\theta \in [0, \pi]$ , where  $\theta = 0$  is the forward direction and  $\theta = \pi$  is the backward direction.

The integral in Eq. 1.35 has an analytic solution. We rewrite it as

$$I(\theta, t) \propto \sum_j \sum_{j'} \beta_j(t) \beta_{j'}^*(t) e^{-ik_0 z_{jj'} \cos \theta} \int_0^{2\pi} e^{-ik_0 \sin \theta (x_{jj'} \cos \phi + y_{jj'} \sin \phi)} d\phi \quad (1.36)$$

and then we use the identity

$$\int_0^{2\pi} e^{i(a \cos \phi + b \sin \phi)} d\phi = 2\pi J_0(\sqrt{a^2 + b^2}) \quad (1.37)$$

where  $J_0(x)$  is the zero order Bessel function of first kind. In our case,  $a = -k_0 \sin \theta x_{jj'}$  and  $b = -k_0 \sin \theta y_{jj'}$ , which gives

$$I(\theta, t) \propto 2\pi \sum_j \sum_{j'} \beta_j(t) \beta_{j'}^*(t) e^{-ik_0 z_{jj'} \cos \theta} J_0\left(k_0 |\sin \theta| \sqrt{x_{jj'}^2 + y_{jj'}^2}\right) \quad (1.38)$$

It is important to point out that Eqs. 1.34 and 1.35 are equivalent in the sense that both give the detected intensity in a given angle  $\theta$  (Eq. 1.35 is just an integration of Eq. 1.34 over  $\phi$ ). In the other hand, Eq. 1.27 is the power integrated over all the space, so it washes out the spatial features of the emitted light.

### 1.3 Simulation methods

The equations for the emitted intensity  $I(\theta, t)$  and for the coefficients  $\beta_j(t)$  were derived with the initial condition that the atoms are in the ground state and no photon is present. The interactions of the atoms with the incoming field and the vacuum modes drive the system into a steady state after some time [Bux 2010], so the  $\beta_j(t)$ s tend to a constant value and by assumption at most one atom is in the excited state. Then, the incident field is suddenly switched off, allowing the excited state to decay. We are interested in the temporal dynamics of the system, i.e., in how the excited atom emits spontaneously light [see Fig. 1.5(b)]. Contrary to the naive picture where the emitted light is  $I(t) \propto e^{-\Gamma t}$ , the presence of the other  $N - 1$  atoms modifies the emitted intensity in a such way that  $I(t)$  has features of fast and slow decays, defined as *super-* and *subradiance*, respectively [Bienaimé 2012]. The fast decay, i.e., superradiance, takes place immediately after the switch off, whereas the slow decay, i.e., subradiance, takes place after a long time after the switch off. Superradiance corresponds to the emission of most part of the light, whereas subradiance corresponds to a late emission of some trapped light in the atomic sample. Superradiance is due to constructive interference of the emitted light from the dipole oscillations, whereas subradiance is related to destructive interference of the scattered light. Decay rates  $\Gamma_{\text{sup}}$  and  $\Gamma_{\text{sub}}$  can be associated with super- and subradiance, respectively, in a such way that  $\Gamma_{\text{sup}} > \Gamma$  and  $\Gamma_{\text{sub}} < \Gamma$  and they depend on the atomic distribution.

We can perform simulations and characterize the decay dynamics of the physical system. The main numerical results will be presented in the following chapters, however some of results will be discussed in this section, as well as the procedure for evaluation.

The simulations consist in generating emitted intensities by means of Eqs. 1.29, 1.34 and 1.35, with the  $\beta_j$  obeying Eq. 1.15. The incident laser was set along the  $z$  axis,

so  $e^{i\vec{k}_0 \cdot \vec{r}_j} = e^{ik_0 z_j}$  in the second term of Eq. 1.15, and the spherical coordinates  $\{\theta, \phi\}$  are defined in Fig. 1.2. For the emitted intensity, an exponential fit  $y(t) = A \exp(-Bt)$  is done in an appropriate interval, in order to extract the super- and subradiant decay amplitudes  $A = \{A_{\text{sup}}, A_{\text{sub}}\}$  and rates  $B = \{\Gamma_{\text{sup}}, \Gamma_{\text{sub}}\}$ , respectively. For superradiance, the fit interval is chosen just after the switch off. For subradiance, the fit interval is set for long times after the switch off.

Equations 1.15 contain the parameters of the physical system: the laser detuning  $\Delta$ , the Rabi amplitude  $\Omega$ , the atom number  $N$  and the atomic positions  $\vec{r}_j$ , distributed under a given spatial geometry. Concerning  $\Omega$ , its value can be any value, since all equations were derived under the assumption  $s \ll 1$ . In our experiments the atomic sample is a Gaussian cloud, a cloud of atoms whose density is described by a Gaussian function, so we consider a spherical Gaussian cloud characterized by the parameters atom number  $N$ , RMS radius  $k_0 R$ , density

$$n_0 \lambda^3 = \frac{(2\pi)^{3/2} N}{(k_0 R)^3} \quad (1.39)$$

and resonant optical thickness  $b_0 \propto N/(k_0 R)^2$ . The scalar approximation of the coupled-dipole model yields a  $b_0$  defined as [Bellando de Castro 2013]

$$b_0 = \frac{2N}{(k_0 R)^2} \quad (1.40)$$

known as *scalar definition*, whereas the vectorial approximation of the coupled-dipole model yields a  $b_0$  defined as

$$b_0 = \frac{3N}{(k_0 R)^2} \quad (1.41)$$

i.e., a factor of three instead of two, known as the *vectorial definition*. In the experiments, the measured  $b_0$  is defined as

$$b_0 = g \frac{3N}{(k_0 R)^2} \quad (1.42)$$

where  $g$  is a constant which depends on the degeneracy of the two levels in the atom species, since pure two-level atoms are not the standard situation in experiments. In this thesis,  $g = 7/15$ , which stands for the atom  $^{87}\text{Rb}$  in a equal statistical mixture of Zeeman sublevels for the ground state.

Another parameter for the cloud is the optical thickness

$$b(\Delta) = \frac{b_0}{1 + 4\Delta^2/\Gamma^2} \quad (1.43)$$

The reader is referred to Chapter 2, subsection 2.2.5, for the derivation of  $b_0$ ,  $b(\Delta)$  and  $n_0 \lambda^3$ . In this thesis, we use mainly Eq. 1.40 in the numerical results and Eq. 1.42 for the experimental results, although we sometimes use Eq. 1.41 for both numerical

and experimental results in order to have a direct comparison. The definition of  $b_0$  is mentioned in all figure captions in this manuscript.

Typical experimental values for the atomic cloud parameters are  $N \sim 10^9$ ,  $R \sim 10^{-3}$  m and  $k_0 \sim 10^6$  m $^{-1}$ , which lead to  $b_0 \sim 10 - 100$  and  $n_0\lambda^3 \sim 10^{-2}$ . However, it is very hard to simulate a cloud with large  $N$  in the computers, due to limitation in software and running time, so we set  $N \sim 10^{3-4}$  and  $b_0 \sim 10$ , which makes  $n_0\lambda^3 \sim 1 - 10$ . In the experiments  $n_0\lambda^3 \ll 1$ , so we are well in the dilute cloud regime. However, in the simulations the density is  $10^{2-3}$  times higher and possible density effects must be checked.

The positions  $\vec{r}_j = (x_j, y_j, z_j)$  for all atoms are set randomly from a spherical Gaussian distribution for a given  $k_0R$ . However, when setting randomly the positions, pairs of atoms may occur, i.e., two atoms may be close to each other. It can be shown [DeVoe 1996, Bienaimé 2011b] that the super- and subradiant decay rates  $\Gamma_+$  and  $\Gamma_-$ , respectively, for an interacting pair separated by the distance  $r_{12}$ , are equal to

$$\Gamma_{\pm} = \Gamma \left[ 1 \pm \frac{\sin(k_0 r_{12})}{k_0 r_{12}} \right] \quad (1.44)$$

i.e., pairs cause enhancement of super- and subradiance. As in our experiments the cloud is dilute, we look for cooperative effects due to the  $N$  atoms as a whole. It can be shown from Eq. 1.44 that  $\Gamma_{\pm} \rightarrow \Gamma$  when the distance between the two atoms become  $k_0 r_{12} \gtrsim \pi$ , i.e, absence of pair effects, so we remove the pairs in the simulation by imposing an exclusion distance condition as follows: if the distance between the atoms  $j$  and  $j'$  is  $k_0 r_{jj'} < 3$ , one of the two atoms has its position changed. This condition is verified until it is fulfilled for all atoms.

In the experiments, the incident laser light is a pulse of duration  $\Delta t_{\text{pulse}}$  enough large for the system to reach a steady state, so  $\Delta t_{\text{pulse}} \gg \tau_0$ . Experiments with short excitations were performed and superradiance and cooperative Lamb shift were observed [Roof 2016], and a numerical study about angular distribution of superradiance with also dependence on the pulse duration is discussed in [Kuraptsev 2017]. In our simulations, no effect due to the pulse duration was observed, as shown in Fig. 1.3. We set  $\Delta t_{\text{pulse}} = 100\tau_0$  in most of our simulations, although smaller values like  $\Delta t_{\text{pulse}} = 50\tau_0$  and  $\Delta t_{\text{pulse}} = 25\tau_0$  were also set.

The laser switch off is the abrupt extinction of the pulse intensity. Therefore, the laser excitation is set as a step function defined by

$$\Omega(t) = \begin{cases} \Gamma, & \text{if } t < \Delta t_{\text{pulse}} \\ 0, & \text{if } t \geq \Delta t_{\text{pulse}} \end{cases} \quad (1.45)$$

where  $\Omega = \Gamma$  when the laser is on and  $\Omega = 0$  when it is off.

For  $\Delta$ , we allow  $\Delta \sim 0 - 10\Gamma$  to accomplish interactions both on resonance and far from resonance. Then, Eqs. 1.15 are solved numerically by means of the fourth order Runge-Kutta method. As the intensities might present speckles and spurious oscillations, the calculation is repeated for different configurations of the atomic positions, and then the intensity is averaged over the total number of configurations. This is also because in the experiment the detector indeed measures an average intensity in time. We have set

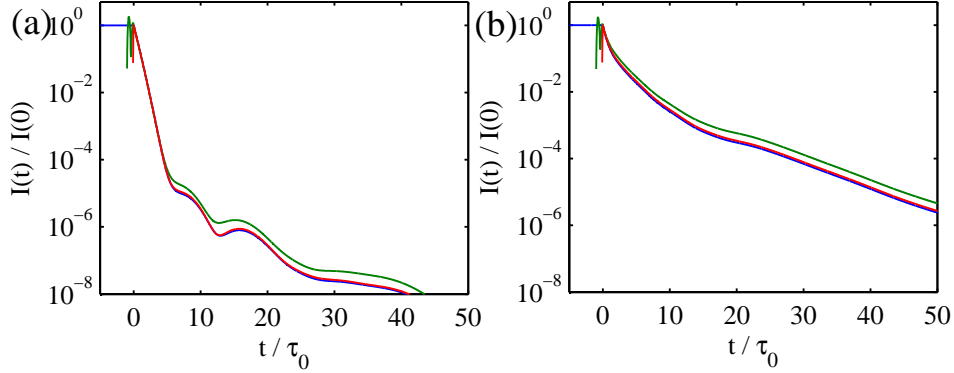


**Figure 1.3:** Emitted intensity  $I(\theta, t)$  at (a)  $\theta = 0^\circ$  and (b)  $\theta = 45^\circ$ , for the pulse durations  $\Delta t_{\text{pulse}} = 100\tau_0$  (blue),  $\Delta t_{\text{pulse}} = \tau_0$  (green) and  $\Delta t_{\text{pulse}} = 0.1\tau_0$  (red). Parameters:  $\Delta = 10\Gamma$ ,  $n_0\lambda^3 = 4.7$  and  $b_0 = 11.3$  ( $N = 633$  and  $k_0R = 11.3$ ), for a single configuration of the atomic positions.

between 50 and 100 realizations on the atomic positions in all calculations described in this thesis.

In summary, we have the following algorithm for the procedure described above, implemented in the programming language MATLAB and following the steps below:

- To define a value for  $\Delta$ ,  $b_0$ ,  $n_0\lambda^3$  and then to calculate the corresponding  $N$  and  $k_0R$ ;
- To set randomly the positions of all the  $N$  atoms under a Gaussian distribution of RMS radius  $k_0R$ ;
- To check the exclusion distance condition for each atom and to change randomly the position of one of the atoms in the pair, by using the Gaussian distribution previously defined. As some atoms will have their positions changed, the net effect is an increase in the value of  $k_0R$ ;
- To calculate the new  $k_0R$  from its definition, i.e., the definition of RMS average,

$$k_0R = \sqrt{\sum_j \frac{(k_0x_j)^2}{N} + \sum_j \frac{(k_0y_j)^2}{N} + \sum_j \frac{(k_0z_j)^2}{N}}$$

and to recalculate  $b_0$  and  $n_0\lambda^3$ , which will decrease;

- To substitute the positions,  $\Delta$  and  $\Omega$  in the coupled-dipole equations and to solve numerically for a given vector time  $t \geq 0$ , where  $t = 0$  is the initial time and  $t = \Delta t_{\text{pulse}} > 0$  is the instant of the switch off. Later  $t$  is redefined as  $t \rightarrow t - \Delta t_{\text{pulse}}$  in order to have  $t = 0$  as the instant of the switch off. The solutions are  $N$  functions  $\beta_j(t)$ ;
- To substitute the  $\beta_j(t)$  and the positions previously set in the intensities equations, for each  $t$ ;

- To repeat the procedure with new atomic positions. This generates new emitted intensities, and the final intensity is the arithmetic mean of all generated intensities. Then, we normalize it by its steady value, set as the value of the intensity immediately before the switch off;
- To define a fit interval and to extract the decay rates  $\Gamma_{\text{sup}}$  and  $\Gamma_{\text{sub}}$ .

In the following we present qualitative results and interpretations from the simulations with the coupled-dipole model.

### 1.3.1 Impact of the exclusion condition

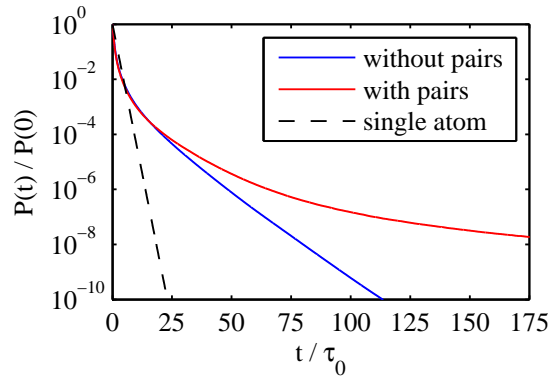


**Figure 1.4:** Comparison between the total fluorescence with and without atomic pairs. Parameters:  $b_0 = 3N/(k_0R)^2 = 11.3$ ,  $n_0\lambda^3 = 4.6$  ( $N = 633$  and  $k_0R = 11.3$ ),  $\Delta = 10\Gamma$ , over 100 configurations on the atomic positions.

A comparison between the emission with and without atomic pairs is shown in Fig. 1.4. The fluorescence  $P(t)/P(0)$  is the total emitted fluorescence in Eq. 1.29, normalized by its maximum value and plotted in log scale. The cloud without pairs (blue) was generated from initial  $b_0 = 3N/(k_0R)^2 = 15.0$  and  $n_0\lambda^3 = 7.0$ , which gives  $N = 633$  and  $k_0R = 11.3$ . After the exclusion distance condition is fulfilled,  $k_0R$  increased to 12.9, however, the atomic distribution remains Gaussian with a good approximation. The increasing of  $k_0R$  gives recalculated  $b_0 = 11.3$  and  $n_0\lambda^3 = 4.6$ . We checked that  $\sim 50\%$  of the atoms had their positions changed. This number increases for high densities and might introduce correlations (i.e., equal distances and ordered pattern) in the positions, so we also perform calculations at low densities, to be discussed in the next chapters. The cloud with pairs (red) was generated from the final values of  $b_0$  and  $n_0\lambda^3$ , without the exclusion condition. We also plot the single-atom decay,  $P(t) \sim \exp(-\Gamma t)$  (dashed line; see subsection 1.2.1). The main difference between the curves is the amplitude for times  $t \gg \tau_0$ , i.e., where subradiance takes place. The subradiant amplitude, which can be seen as the curve level for fixed  $t$ , is larger for the red curve than for the blue curve. This means that the presence of pairs increases the contribution of the subradiant states.

### 1.3.2 Emission diagram and off-axis superradiance

Figure 1.5(a) shows the emission diagram in logarithm scale and in the steady state, i.e.,  $I(\theta, t)$  for  $t \gg \tau_0$ . This is equivalent to solve the coupled-dipole equations for  $\dot{\beta}_j = 0$ .

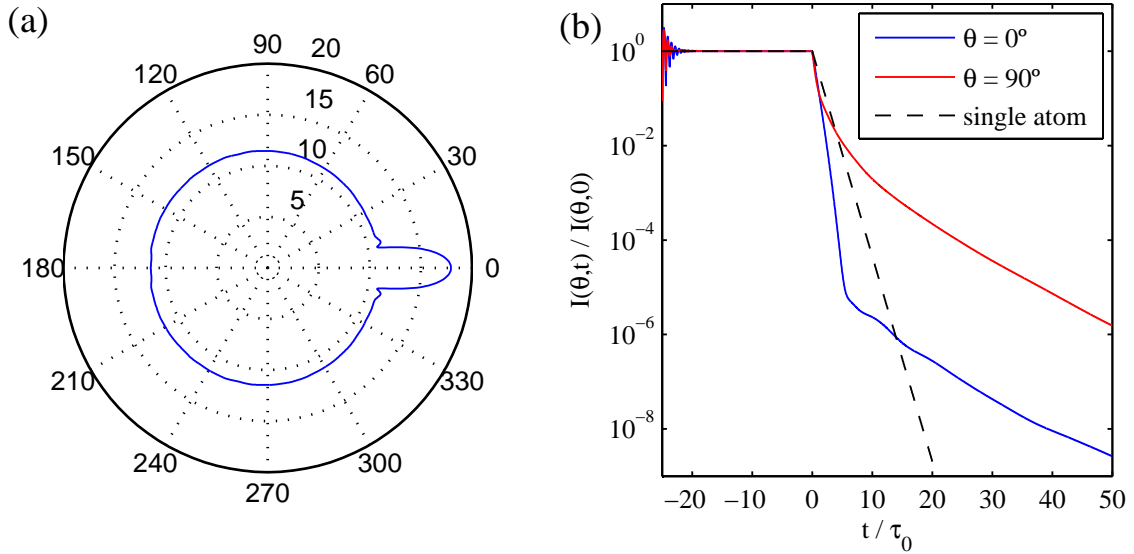


**Figure 1.5:** (a) Emission diagram calculated from Eq. 1.35 in the steady state, i.e., with Eq. 1.15 for  $\dot{\beta}_j = 0$ . For better visualization, the blue curve is the logarithm of  $I(\theta)$  times  $10^5$ . Parameters:  $b_0 = 3N/(k_0R)^2 = 11.3$ ,  $n_0\lambda^3 = 4.6$  ( $N = 633$  and  $k_0R = 11.3$ ),  $\Delta = 10\Gamma$ , averaged over 50 configurations on the atomic positions. (b) Emitted intensities calculated from Eq. 1.35 for  $\theta = 0^\circ$  (blue) and  $90^\circ$  (red), for the same parameters in (a). The dashed line is the decay for a single atom.

The main feature of the emission diagram is a forward lobe, i.e., a strong intensity in the direction of the incident laser ( $\theta \sim 0$ ). Such lobe is discussed extensively in the literature of superradiance [Rehler 1971, Bienaimé 2011a] and more recently in [Rouabah 2014]. For the directions outside the lobe ( $\theta \neq 0$ ), the emission is mainly isotropic.

Figure 1.5(b) illustrates emitted intensities  $I(\theta, t)$  in log scale for  $\theta = 0^\circ$  and  $\theta = 45^\circ$ , for different  $b_0$  and  $\Delta = 10\Gamma$ . By comparing the intensities with the decay for the single atom, we see that they show super- and subradiance, which is verified by the slopes of the emitted intensities, respectively faster and slower than the single-atom slope  $\Gamma$ . Moreover, the curves show superradiance out of the forward direction. This is what we call “off-axis superradiance”, i.e., superradiance detected from an intensity out of the driving laser axis ( $\theta \neq 0$ ). We checked that intensity curves evaluated for different angles  $\theta \neq 0$  are similar. We will discuss more detailed in Chapter 3 that intensities calculated and measured on- and off-axis give different superradiant decay rates  $\Gamma_{\text{sup}}$ , but the same subradiant decay rate  $\Gamma_{\text{sub}}$ .

### 1.3.3 Temporal decay rate

As already discussed, we use a fit procedure to extract the super- and subradiant decay rates. However, another method is to calculate the instantaneous decay rate  $\Gamma(t)$ , i.e., the *temporal decay rate*, calculated from the emitted intensity  $I(t)$  from the ansatz

$$I(t) \propto e^{-\Gamma(t)t} \quad (1.46)$$

i.e, we assume that the emitted curve is an exponential with instantaneous decay rate  $\Gamma(t)$ . From it, by taking the logarithm and the derivative in both sides, we “isolate”  $\Gamma(t)$  as

$$\Gamma(t) = -\frac{d}{dt} \ln I(t) \quad (1.47)$$

Figure 1.6 shows the result of Eq. 1.47 for a decay after the switch off, where the intensity is the total power  $P(t)$  from Eq. 1.29. Values  $\Gamma(t)/\Gamma > 1$  denote superradiance, while  $\Gamma(t)/\Gamma < 1$  denotes subradiance. We see that  $\Gamma(t)$  remains evolving even for very long times after the switch off, like  $t \sim 100\tau_0$ , becoming constant only for  $t \geq 600\tau_0$ . In amplitude, this corresponds to  $P(t)/P(0) \sim 10^{-28}$ , which is out of the limit for any realistic experiment (we will discuss in Chapter 2 that subradiance was measured for amplitudes  $\sim 10^{-4}$ , which corresponds to times between  $t \sim 200$  and  $400\tau_0$ ). However, we can still see  $\Gamma(t)/\Gamma < 1$  for lower times, although it does not correspond to a purely exponential decay in the system.

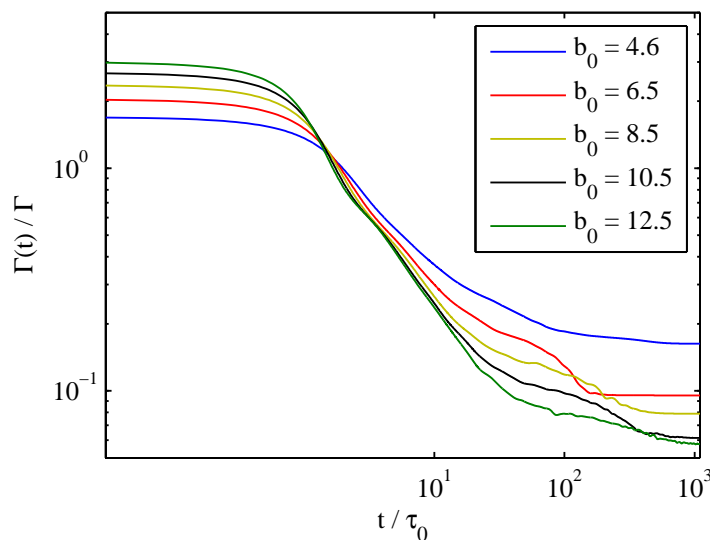


**Figure 1.6:** Temporal decay rates  $\Gamma(t)$  for different values of  $b_0$ , calculated from Eqs. 1.47 and 1.29 for varying  $b_0 = 2N/(k_0R)^2$  at constant  $n_0\lambda^3$  and  $\Delta$ . Parameters:  $n_0\lambda^3 = 4.6$ ,  $\Delta = 10\Gamma$ , averaged over 100 configurations on the atomic positions.

The results plotted for several  $b_0$  show that the cooperativity is stronger as  $b_0$  increases, i.e, the larger  $b_0$ , the stronger cooperativity is, represented by an increase of  $\Gamma(t)$  for  $t \sim 0$  (enhancement of superradiance) and a decrease of  $\Gamma(t)$  for  $t \geq \tau_0$  (enhancement of subradiance). Physically, as cooperative effects are due to the interactions of all atoms in the sample and their positions, larger  $b_0$  implies in large  $N$  and/or small  $k_0R$ . For a single atom,  $b_0 \rightarrow 0$ , since  $k_0R \rightarrow \infty$ .

In our simulations,  $b_0$  was varied by varying  $N$  and  $k_0R$  simultaneously. In our experiment (to be discussed from Chapter 2),  $b_0$  was varied by varying  $k_0R$  for constant (and sometimes decreasing)  $N$ . Two clouds with different  $N$  and  $k_0R$  but same  $b_0$  present the same strength in cooperativity. Indeed, it has been discussed in [Guerin 2017a] that, among the cloud parameters  $\{N, k_0R\}$  and their combinations  $N/(k_0R)^2 \propto b_0$  and

$N/(k_0R)^3 \propto n_0\lambda^3$ , for a given detuning and geometry, the combination  $N/(k_0R)^2 \propto b_0$  is the only good parameter to investigate cooperativity. In Chapters 2 and 3, we will present scaling laws for the super- and subradiant decay rates with respect to  $b_0$ , as well as its observations in the experiments performed in this work.

## 1.4 Conclusions of this chapter

We have discussed the coupled-dipole model in the scalar approximation for cooperativity in cold atoms. Super- and subradiance will be the subject of discussion in the following chapters, specially in Chapters 2 and 3, where theoretical and experimental results for the decay rates will be presented with respect to the parameters of the system. In Chapters 4 and 5, super- and subradiance will be investigated besides radiation trapping, temperature effects and an excitation with a phase shift in the incident laser.

## Subradiance in cold atoms

In this chapter, we discuss the results obtained in subradiance. The results include numerical predictions, a full description of our experimental setup, the experimental results and the overall discussion.

Since R. Dicke's proposition about super- and subradiance [Dicke 1954], superradiance was studied extensively in several kind of media and approximations [Gross 1982, Scully 2006, Bienaimé 2013], but subradiance remained not studied experimentally due to, maybe, experimental difficulties for its detection. In experiments, only two works report the observation of subradiance: a late subradiant pulse emitted by Ga atoms in a three-level scheme [Pavolini 1985], where the subradiant is induced by a superradiant decay to a lower level; and the measurement of the subradiant decay rate for two ions [DeVoe 1996]. In the case of a system of  $N \gg 2$  atoms, it was discussed in Chapter 1 that the model of coupled dipoles for cold atoms predicts subradiance as a late decay in the emitted intensity, with a rate  $\Gamma_{\text{sub}}$  smaller than the natural decay rate  $\Gamma$ . The observation of subradiance in a large cloud of cold atoms is the subject of this chapter, and its detection at very low amplitudes was achieved thanks to a good extinction and fall time in our driving laser beam, as well as a hybrid photomultiplier to provide a clear detection.

This chapter is divided in four sections. In section 2.1, we present the main theoretical predictions on the subradiant decay rates with the parameters of the system. In section 2.2, we discuss the complete experimental setup available in our laboratory, the techniques for preparing and characterizing the atomic sample, the experimental procedure for performing the measurements and the probe beam setup to measure subradiance. In section 2.3, we demonstrate the experimental results on subradiance. Finally, in section 2.4, we point out the main conclusions of this chapter.

### 2.1 Numerical results

A numerical study on subradiance was firstly presented in [Bienaimé 2012], where predictions for the subradiant decay rates  $\Gamma_{\text{sub}}$  in cold atoms were obtained with several parameters of the system. However, in this work we have improved the simulation methods since we added, for instance, an exclusion condition and the calculation of intensities that depend on the detection direction (see Chapter 1). Also, we extended the simulation procedure for the superradiant decay rates (to be discussed in Chapter 3), a truncated

plane wave that excites the atoms (Chapter 4) and the inclusion of temperature and phase effects (Chapter 5), so this work provides a more complete understanding.

Our study on subradiance was performed by using the equations predicted by the coupled-dipole model, discussed in Chapter 1, with the simulation procedure described in section 1.3. We extract the subradiant decay rates  $\Gamma_{\text{sub}}$  and its corresponding time  $\tau_{\text{sub}} = 1/\Gamma_{\text{sub}}$  by means of an exponential fit  $y(t) = A_{\text{sub}} e^{-\Gamma_{\text{sub}} t}$  in the emitted intensity in a range where a slow decay is observed compared to the single atom decay. The atomic cloud is considered as a Gaussian sphere with RMS size  $k_0 R$  and atom number  $N$ , and also density  $n_0 \lambda^3$  (Eq. 1.39), resonant optical thickness  $b_0 \propto N/(k_0 R)^2$  (Eq. 1.40, 1.41 or 1.42) and optical thickness  $b(\Delta)$  (Eq. 1.43). The emitted intensity depends on the coefficients  $\beta_j(t)$  given by Eqs. 1.15 and can be the total emitted power  $P(t)$  (Eq. 1.29) or the intensity detected in a given direction  $I(\theta, \phi, t)$  (Eq. 1.34) or  $I(\theta, t)$  (Eq. 1.35). Eq. 1.35 is an integration of Eq. 1.34, obtained from symmetry of the cloud with respect to the incident laser axis.

In our experiment, the detector was placed at an angle of  $\theta = 35^\circ$  from the incident laser direction, so we investigate subradiance calculated with  $I(\theta, t)$ . We have checked that  $\Gamma_{\text{sub}}$  extracted from  $I(\theta, t)$  is similar to those extracted from  $I(\theta, \phi, t)$  and  $P(t)$ . The parameters for the simulations are  $b_0$  (cloud),  $n_0 \lambda^3$  (cloud), the laser detuning  $\Delta$  (laser) and  $\theta$  (detection position).  $\theta$  is varied to include directions in and out of the incident axis. Also, the simulations are performed mainly at large detunings (i.e.,  $\Delta \gg \Gamma$ ), in order to have  $b(\Delta) < 1$  and thus to assure single scattering and the timed-Dicke state. Also, we have performed simulations at resonance and other detection directions for a full understanding.

### 2.1.1 Scaling with $b_0$

The main prediction of the coupled-dipole model for subradiance is a linear scaling of  $\tau_{\text{sub}}$  with  $b_0$ , displayed in Fig. 2.1. Fig. 2.1(a) shows emitted intensities  $I(\theta, t)$  for several  $b_0$ , for constant  $n_0 \lambda^3$  and detuning fixed at  $\Delta = 10\Gamma$ , calculated at  $\theta = 45^\circ$ , i.e., close to the position where the detector is placed in the experiment. The red curves are exponential fits in the interval  $I(\theta, t)/I(\theta, 0) \in [10^{-4}, 10^{-3}]$ , in order to extract  $\tau_{\text{sub}}$ . This interval was chosen based on experimental data, where we have observed subradiance in amplitudes  $\sim 10^{-4}$  (see Fig. 2.17).

Figure 2.1(b) shows the result of the fits,  $\tau_{\text{sub}}$  versus  $b_0$ . We set several  $n_0 \lambda^3$  to see whether the density plays a role (as discussed in section 1.3, the values of  $n_0 \lambda^3$  in the simulations are much higher compared to the experimental ones  $n_0 \lambda^3 \sim 10^{-2}$ ). We see a linear scaling of  $\tau_{\text{sub}}$  with  $b_0$ , as suggested in [Bienaimé 2012], and the density has practically no effect in these subradiance data. Also,  $\tau_{\text{sub}}$  increases with  $b_0$ , i.e., cooperative effects are strong for high atom number and/or small sample sizes. About the fit range, we have checked that, by choosing a fit range smaller in amplitude, e.g., for  $I(\theta, t)/I(\theta, 0) \in [10^{-8}, 10^{-6}]$ , the results are similar.

A linear fit  $\tau_{\text{sub}}/\tau_0 = (1 + c b_0)$  gives  $c = 0.54$  for all the numerical data and  $c = 0.53$  for the data at  $n_0 \lambda^3 = 0.5, 0.9$  and  $2.5$  (low densities), with  $b_0$  given in the scalar definition (Eq. 1.40). By converting  $b_0$  to the vectorial definition (Eq. 1.41), we get  $c = 0.35$ . In the experiment, we have found  $c = 0.80$  with  $b_0$  in the vectorial definition [see Fig. 2.18(a)].

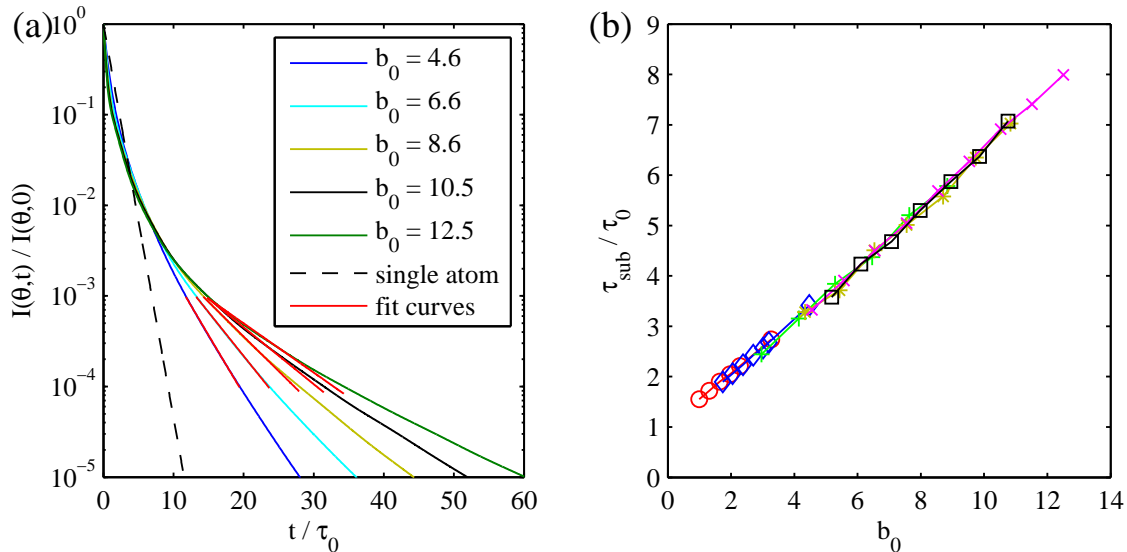


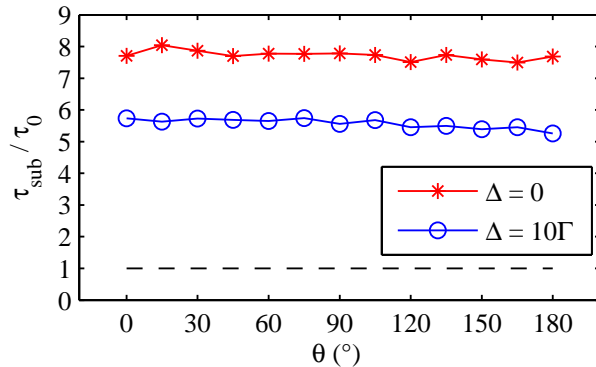
**Figure 2.1:** (a) Emitted intensities for several  $b_0 = 2N/(k_0R)^2$ , for  $n_0\lambda^3 = 4.6$  and  $\Delta = 10\Gamma$ . The emitted intensity was calculated from Eq. 1.35 for  $\theta = 45^\circ$ . The red curves are exponential fits in the interval  $I(\theta, t) \in [10^{-4}, 10^{-3}]I(\theta, 0)$ . (b) Subradiant decay rates  $\tau_{\text{sub}}$  as a function of  $b_0 = 2N/(k_0R)^2$ , for  $\Delta = 10\Gamma$  and  $n_0\lambda^3 = 0.5$  (red circles), 0.9 (blue diamonds), 2.5 (green crosses), 3.7 (yellow asterisks), 4.6 (magenta X), 5.3 (black squares). The decay rates were obtained from fits in the same interval as those in (a). Data averaged over 100 configurations on the atomic positions.

As discussed in next section, the atom used in the experiment,  $^{87}\text{Rb}$ , is not a pure two-level system: it is degenerated in hyperfine levels, so we should not expect an agreement with the theoretical and experimental data.

### 2.1.2 Subradiance at resonance and for several detection directions

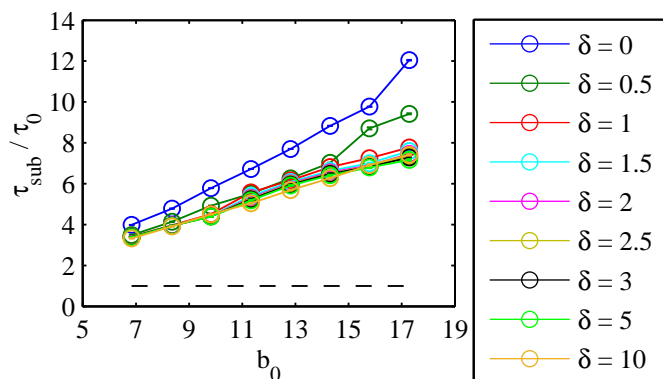
In order to investigate the subradiant decay at resonance and for different directions, we plot in Fig. 2.2  $\tau_{\text{sub}}$  as a function of  $\theta$ , for constant  $n_0\lambda^3$  and  $b_0$ , on- and off-resonance (red and blue data, respectively), extracted from  $I(\theta, t)$  by varying the detection angles. We see that  $\tau_{\text{sub}}$  is constant for both  $\theta \approx 0$  (forward emission, presence of an intensity lobe) and  $\theta \neq 0$  (directions out of the incident laser, where our detector is placed); hence, the subradiant decay rates are mainly isotropic. With respect to the detuning dependence,  $\tau_{\text{sub}}$  for  $\Delta = 10\Gamma$  is different of the ones for  $\Delta = 0$  by a factor of  $\simeq 25\%$ . This may be due to radiation trapping and will be discussed in Chapter 4. Now one cannot know if subradiance survives at resonance: the  $\tau_{\text{sub}}$  at  $\Delta = 0$  may be due to radiation trapping only.

Figure 2.3 shows  $\tau_{\text{sub}}$  as a function of  $b_0$  for several detunings of the incident laser beam. This figure is similar to what will be discussed in the experimental results. At resonance, i.e., for  $\Delta = 0$ ,  $\tau_{\text{sub}}$  is larger than the values for  $\Delta \neq 0$ , as in Fig. 2.2. For  $\Delta \neq 0$ , even for slight  $\Delta$ , all curves practically collapse, showing that subradiance is independent of the detuning.



**Figure 2.2:** Angular dependence of  $\tau_{\text{sub}}$  for  $\Delta = 0$  (red) and  $\Delta = 10\Gamma$  (blue). The dashed line is the time decay rate for a single atom. The fit interval is the same as in Fig. 2.1. Parameters:  $b_0 = 2N/(k_0R)^2 = 8.55$ ,  $n_0\lambda^3 = 4.6$  ( $N = 921$ ,  $k_0R = 14.7$ ), averaged over 100 configurations of the atomic positions.

A linear fit  $\tau_{\text{sub}}/\tau_0 = (1 + cb_0)$  for the data for  $\delta \geq 1$  yields to  $c \simeq 0.37$  for  $b_0$  in the vectorial definition. By converting  $b_0$  to the scalar definition to compare with the fit for the data in Fig. 2.1(b), we obtain  $c = 0.37 \times 3/2 = 0.56$ , which is practically equal to  $c = 0.54$  found from Fig. 2.1(b).



**Figure 2.3:** Subradiant decay rates  $\tau_{\text{sub}}$  as a function of the resonant optical thickness  $b_0 = 3N/(k_0R)^2$ , for several detunings  $\delta = \Delta/\Gamma$ . The value of  $\tau_{\text{sub}}$  were extracted from normalized intensities  $I(\theta, t)$  at  $\theta = 45^\circ$ , in the interval  $I(\theta, t)/I(\theta, 0) \in [10^{-4}, 10^{-3}]$ . Parameters:  $n_0\lambda^3 = 4.6$ , averaged over 50 realizations for the first five data (smaller  $b_0$ ) and 10 realizations for the three last data (larger  $b_0$ ).

Figure 2.4 displays the data in Fig. 2.3 as a function of  $\Delta$ , for constant  $b_0$ . Panel (a) displays the emitted intensities for several detunings, and the respective fit curves in red. We see that the fit slopes are practically the same. However, their amplitudes are higher for  $\Delta \sim 0$ . Panels (b) and (c) show, respectively,  $\tau_{\text{sub}}$  and  $A_{\text{sub}}$  extracted from (a) and plotted as a function of  $\Delta$ . In (b), as already discussed in Figs. 2.2 and 2.3, the values of  $\tau_{\text{sub}}$  are the same except for  $\Delta \simeq 0$ . In (c),  $A_{\text{sub}}$  decreases when  $\Delta$  increases, but it tends to a constant value of  $\sim 10^{-2}$ , showing that subradiance should be observed at very low amplitudes.

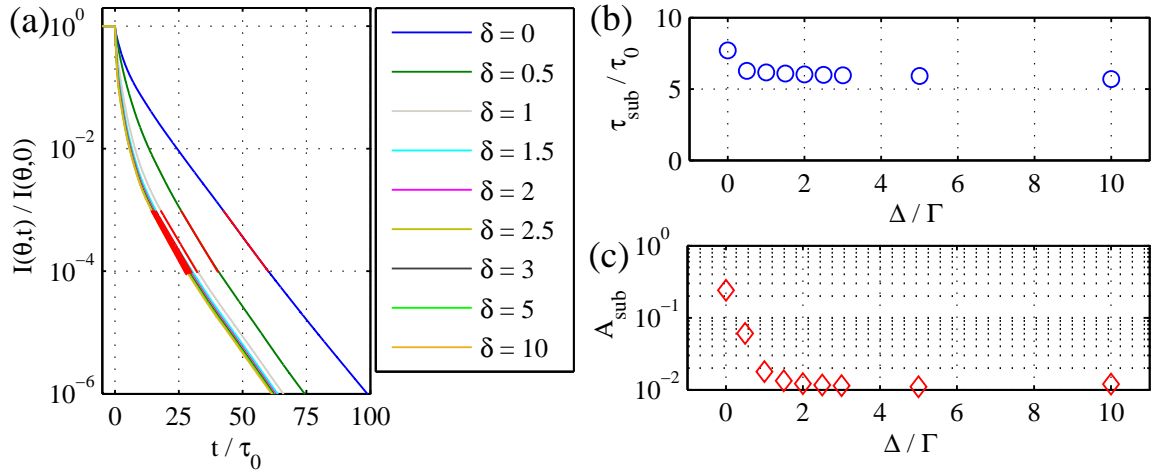


**Figure 2.4:** (a) Intensities and subradiant fits calculated at  $\theta = 45^\circ$ , for several detunings  $\delta = \Delta/\Gamma$  at constant  $n_0\lambda^3 = 4.6$ ,  $b_0 = 3N/(k_0R)^2 = 12.8$ , averaged over 50 realizations. (b) Subradiant decay rates  $\tau_{\text{sub}}$  and (c) subradiant amplitudes  $A_{\text{sub}}$  extracted from the fits in (a), plotted as a function of  $\delta$ .

### 2.1.3 Subradiance and temperature

As already discussed in Chapter 1, in our theoretical model it is assumed that the atoms do not move, which implies temperature  $T = 0$ . However, in the experiments the actual temperature is in the order of some  $\mu\text{K}$ . In our MOT setup, as discussed in the next section, we have  $T \sim 50 \mu\text{K}$ . Temperature means atomic motion, i.e., a gas where the atoms move at random directions. Thus, the atomic positions change in time and it is not evident from the coupled-dipole model if cooperative effects will remain detectable and observable. Also, the atomic velocity causes a shift in the laser detuning  $\Delta$  (Doppler shift) in the atomic frame. *Frequency redistribution* may occur, i.e., a photon may have its frequency even and even shifted as long as it is scattered (absorbed and emitted) by one or more atoms in the cloud.

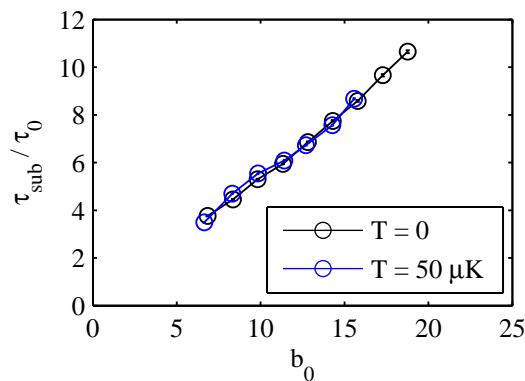


**Figure 2.5:** Subradiant decay rates  $\tau_{\text{sub}}$  as a function of the optical thickness  $b_0 = 3N/(k_0R)^2$  at  $\Delta = 20\Gamma$ , for temperatures  $T = 0$  and  $T = 50 \mu\text{K}$ .  $\tau_{\text{sub}}$  were extracted from the total emitted power  $P(t)$ . Parameters:  $n_0\lambda^3 = 4.6$ , averaged over 20 configurations on the atomic positions.

In order to investigate the impact of temperature in  $\tau_{\text{sub}}$ , Fig. 2.5 shows  $\tau_{\text{sub}}$  versus  $b_0$

for zero and 50  $\mu\text{K}$ . We see that both data collapse into a single curve, so Doppler effects and frequency redistribution do not suppress subradiance. Details about the simulations with temperature are discussed in Chapter 5, as well as a full numerical study about cooperativity with temperature. The reader is referred to Fig. 5.9 for a plot of  $\tau_{\text{sub}}$  with  $b_0$  for other values of temperatures.

The main conclusions of this numerical data are that subradiance is a robust slow decay with large detuning, small temperatures and detection direction. Subradiance depends mainly on  $b_0$ , and the non-zero temperature should not limit the experiment. In the following section, we will discuss the experimental setup developed in our laboratory.

## 2.2 Experimental setup

### 2.2.1 Basics about magneto-optical traps (MOTs)

In order to produce a sample of cold and neutral atoms at low temperatures, we have in our laboratory a *magneto-optical trap* (MOT). The MOT is an experimental apparatus in order to cool and trap atoms from a warm gas or vapor, from room temperature to very low temperatures, close to the absolute zero [Foot 2005, Metcalf 1999] [see Fig. 2.6(a)]. Since its theoretical proposition and experimental achieving, which led to the 1997 Nobel Prize in Physics to S. Chu, C. Cohen-Tannoudji and W. D. Phillips for the developing of techniques for cooling and trapping atoms, the MOT has become a powerful tool to produce experimentally cold and neutral atomic samples. Cold samples produced by a MOT are subject of several research fields and interests. Also, the MOT is the first step to produce samples even colder, like degenerate gases, Bose-Einstein condensates and optical lattices. The MOT consists in a set of three pairs of identical counter-propagating laser beams along the three spatial directions and a inhomogeneous magnetic field produced by two identical circular coils set in the called anti-Helmholtz configuration.

The physical principle behind cooling atoms is the interactions between the atoms and the photons from the laser, by absorption and spontaneous emission. Due to the fact that a photon carries momentum, energy and angular momentum, all these quantities are transferred to the atom because of the conservation laws. These interactions lead to light forces, like radiation pressure force and dipole forces. It can be shown [Foot 2005] that, for two-level atoms with degenerated excited states at small atomic velocities  $\vec{v}$  and small Zeeman shifts induced by the inhomogeneous magnetic field, the force seen by the atoms in the MOT is equal to

$$\vec{F} = -\beta\vec{v} - \kappa\vec{r} \quad (2.1)$$

where the first term comes from the six laser beams and reduces the velocity of the atoms (each pair of beams reduces a component of the velocity), and the second term comes from the gradient of magnetic field (magnetic field per unit of distance) and the circular polarization of the six laser beams. In Eq. 2.1, the first term is a friction force, responsible for the cooling, where the atoms have their velocity reduced after several absorption and spontaneous emission events, and achieve a *molasses phase*. The second term is a restoring force, responsible for trapping, due to the Zeeman shifts in the excited state and the

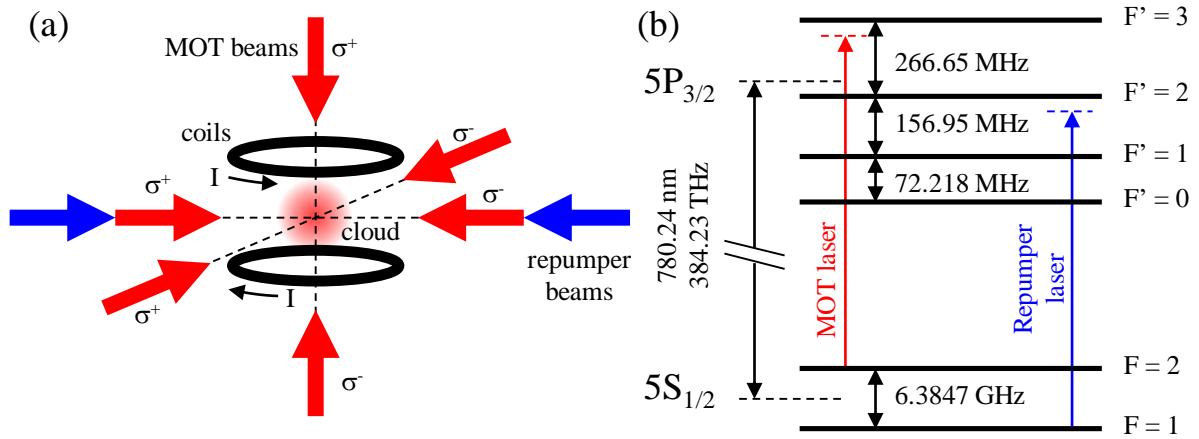


**Figure 2.6:** The  $^{87}\text{Rb}$  MOT in our laboratory. (a) Six laser beams are set in the three independent directions of the space. All the beams are identical in size, intensity, size, spatial profile, negative detuning  $\Delta_{\text{MOT}} < 0$  and have right and left circular polarizations for each counter-propagating pair. Two identical circular coils are placed in the anti-Helmholtz configuration, i.e., the sense of the driving current  $I$  is in opposite directions. This generates a linear position-dependent magnetic field from the center of the system. There is also a pair of repumper beams. (b) The  $^{87}\text{Rb}$   $D_2$  line and the laser beams. The MOT laser beams are set close to the transition  $F = 2 \rightarrow F' = 3$  and the repumper laser beams, at the transition  $F = 1 \rightarrow F' = 2$ .

circular polarization, which selects the transitions for the absorbed photon. Thus, the total force acts as a damped harmonic oscillator and drives the atoms to the center of the six-beams-magnetic-field configuration. The constant  $\beta$  depends on the intensity  $I_{\text{MOT}}$  and the detuning  $\Delta_{\text{MOT}}$  of the six beams, and we must have the condition  $\Delta_{\text{MOT}} < 0$  in order to have  $\beta > 0$  and to obtain a friction force. The constant  $\kappa$  is proportional to  $\beta$  and to the magnetic gradient, and the choice of opposite circular polarizations for each beam pair yields to the functional form of the second term of Eq. 2.1.

As already mentioned, the atom used in our experiments is the  $^{87}\text{Rb}$ , which is an alkali element, very reactive with air and water, solid at room temperature and found in Earth in a natural mixture with the isotope  $^{85}\text{Rb}$ , in quantities equal to 72% of  $^{85}\text{Rb}$  and 28% of  $^{87}\text{Rb}$ . We consider transitions in its  $D_2$  line [see Fig. 2.6(b)], i.e., its single optically active electron is excited from the ground level  $5S_{1/2}$  (valence level) to the excited level  $5P_{3/2}$  (second allowed excited level). As  $^{87}\text{Rb}$  has a non-zero nuclear spin  $I = 3/2$ , its ground level is split in two hyperfine states  $F = 1, 2$ , and the excited level is split in four hyperfine states  $F' = 0, 1, 2, 3$ . The MOT laser beams are set in the transition  $F = 2 \rightarrow F' = 3$  for two reasons: it is *closed*, i.e., once in the state  $F' = 3$ , the atom decays only to  $F = 2$  (the decay  $F' = 3 \rightarrow F = 1$  is not allowed according to the dipole selection rules); and has *the largest probability to occur* among the transitions from  $F = 2$  to  $F' = 1, 2, 3$ . However, there is a non-zero probability of excitation of the state  $F' = 2$  and consequently an eventual decay to  $F = 1$ , which does not interact with the MOT beams. In order to recover the atoms in this latter, a second laser called *repumper* [see Fig. 2.6(a)] is set at the transition  $F = 1 \rightarrow F' = 2$ . Thus the atoms go back to the state  $F' = 2$  and can decay to  $F = 2$ , restarting the cooling and trapping cycle.

Some data about the  $^{87}\text{Rb}$   $D_2$  line are [Steck 2001]: resonance wavelength  $\lambda = 780$  nm, natural lifetime  $\tau_0 = 26$  ns, natural decay rate  $\Gamma = 2\pi \times 6.066$  MHz, saturation intensity  $I_s = 1.7$  mW/cm<sup>2</sup>.

### 2.2.2 General description of our MOT setup

When this PhD thesis started, the experimental setup was already available in the laboratory [Lucioni 2008, Bienaimé 2011b, Bellando de Castro 2013]. A description of the whole setup is the subject of this and the next four subsections. The reader can find full schemes of the experimental setup in Annex and should refer to them when necessary.

The main equipment in our MOT setup are:

- *MOT laser*: This laser source provides the MOT six laser beams and also the *probe beam*, used to perform the measurements and for the *absorption imaging technique* (to be discussed in section 2.2.5). It is a distributed feedback laser (DFB) placed inside a homemade transparent box for providing electric current and temperature regulation by means of the Peltier effect. Also, the six laser beams are arranged in a setup of independent beams with one pair in the vertical plane and two pairs in the horizontal plane of the optical table [see Fig. 2.6(a)]. Each beam has a waist size 2.8 cm [Bienaimé 2011b], power  $\sim 40$  mW and detuning  $\Delta_{MOT} = -4\Gamma$ . This laser source is not perfectly monochromatic and has a linewidth of  $\Delta\omega \sim 3$  MHz.
- *Repumper laser*: This laser source is also a DFB laser, also placed in a transparent box with current and temperature controls similar to the DFB installed for the MOT laser. In our experiment, the repumper beams are set as one counter-propagating beam pair, superposed to one of the horizontal MOT beam pairs [see Fig. 2.6(a)]. Each repumper beam has a power of 5.5 mW and detuning  $\Delta_{REP} = -\Gamma$ . They are initially linearly polarized but become circular polarized after passing through the  $\lambda/4$  waveplates placed in the MOT six beams setup for generating circular polarization.
- *Vacuum system*: It consists of a vertical cylinder, with a cubic glass cell on the top and a Rb reservoir at the bottom. The glass chamber has sides 10 cm and it is the main chamber where the cold cloud is produced. The reservoir contains Rb in a mixture of the isotopes  $^{85}\text{Rb}$  and  $^{87}\text{Rb}$ , at solid and vapor phases. A valve controls the amount of vapor for the chamber, and an ionic pump from Varian VacIon Plus 20, model Diode 27 L·s<sup>-1</sup>, provides a vacuum of  $\sim 10^{-9}$  mbar. This vacuum pressure is estimated from the MOT loading time, i.e., the time necessary to produce the cold atoms when the six beams and magnetic field are turned on [Arpornthip 2012].
- *Coils for the magnetic field*: The two main coils have a diameter of 26 cm and are powered by a current source from TDK-Lambda. The current is equal to 4 A and provides a field of  $\sim 12$  G/cm at the center of the vacuum chamber [Bienaimé 2011b]. Also, compensation coils are set in the three spatial directions to cancel the Earth's magnetic field.

Like in standard atomic physics experiments, we use a locking system in order to stabilize the frequency of the emitted laser beam, which usually is unstable due to mechanic

and thermal fluctuations in the laboratory room. Our locking systems consist in a homemade proportional-integrator (PI) controller (i.e., a PID controller without the derivative part), where the input signal is the  $^{87}\text{Rb}$  saturated absorption spectrum [Foot 2005]. Also, as in standard MOT experiments, we use acousto-optic modulators (AOMs) to modify the frequency and intensity of the laser beams at different points of the optical table. AOMs are devices which diffract light by means of the acousto-optical effect, and are driven by a sinusoidal voltage generated by electronic devices called voltage-controlled oscillators (VCOs). The amplitude and frequency of the sinusoidal voltage control, respectively, the intensity and frequency of the diffracted light by the AOM.

A scheme of our laser setup is represented in Fig. 2.7. The MOT laser [panels (a) and (c)] is locked at the crossover transition  $F = 2 \rightarrow F' = 2, 3$ , i.e., in the middle-frequency between the states  $F' = 2$  and  $F' = 3$ . Then, an AOM set in the double-pass configuration [McCarron 2007] shifts the frequency of the +1 order beam of  $2 \times 100$  MHz. This AOM was aligned to favor mainly negative detunings for the probe beam in the range from  $+2\Gamma$  to  $-12\Gamma$ . It is followed by a tapered amplifier (TA) from Sacher, which increases the laser output power to  $\sim 1$  W. Then, an AOM in single-pass configuration is set such as its  $-1$  order beam goes to the MOT and its zero order beam goes to the probe beam. The frequency shift of the  $-1$  order beam is equal to  $-66$  MHz. This beam passes through a spatial filter with a pinhole, in order to get a clean transverse mode for the laser beam, and then it is split in the six laser beams for the MOT chamber.

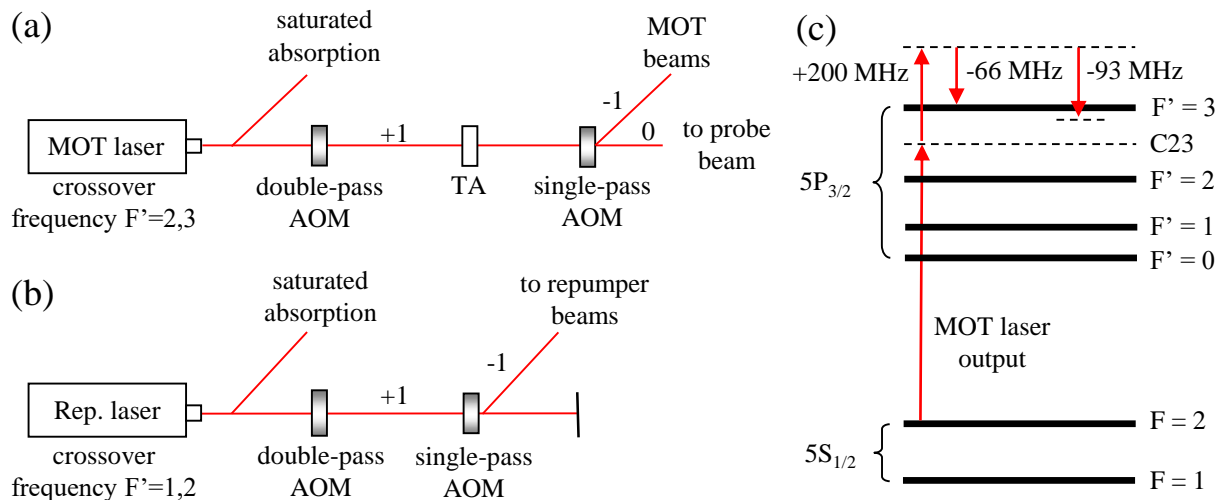


**Figure 2.7:** Simplified scheme of our experimental setup in our laboratory, showing the laser sources and the AOMs setup. (a) The MOT laser setup, which provides the MOT beams and the probe beam. (b) The repumper laser setup, which provides the repumper beams. (c) Scheme for the transitions in the  $^{87}\text{Rb}$   $D_2$  line for the MOT laser. C23 is the crossover frequency between the levels  $F' = 2$  and  $F' = 3$ .  $+200$  MHz is the shift frequency from the double-pass AOM,  $-66$  MHz is the frequency shift from the single-pass AOM, and  $-93$  MHz is the frequency shift from the AOM in the probe beam setup (see subsection 2.2.3).

The setup for the repumper laser is similar to the MOT laser setup [see Fig. 2.7(b)]. A saturated absorption spectroscopy spectrum is the input of another homemade PI controller, which locks the laser at the crossover transition  $F = 1 \rightarrow F' = 1, 2$ . Then, a

double-pass AOM followed by a single-pass AOM shift the frequency of the +1 and -1 order beams, respectively, in order to reach the state  $F' = 2$ . The -1 order beam goes into a monomode optical fiber in order to obtain a clean Gaussian beam. Then, it is split in the two repumper beams and reaches the MOT chamber.

Finally, the experimental setup and the time sequence for performing the experiments are controlled by TTL and analogical signals generated by a data-acquisition card, whose input is controlled by a graphical interface of a program written in the software MATLAB. After receiving the input parameters set by the user (e.g., frequency and intensities for the laser beams, time duration of probe beams and MOT loading), the program code generates a data matrix which is sent to the data-acquisition card from National Instruments, model PCI-6723. The outputs of this card are connected to the two AOMs of the MOT laser setup, to the current source of the MOT coils, to the AOM with focused beam in the probe beam setup (see subsection 2.2.3) and to a CCD camera used in the absorption imaging technique (see subsection 2.2.5). The double-pass AOM has its frequency modified, which modifies the detuning for the probe beam. The single-pass AOM has its voltage amplitude modified, which modifies the intensity of the -1 order beam and consequently the power of the MOT beams. Finally, the AOM in the probe beam setup has its -1 order turned on or off, which controls if the probe beam will be on or off.

### 2.2.3 Setup for the probe beam

The probe beam is the laser beam used for performing the experimental measurements (in this work, subradiance, superradiance and radiation trapping) and the absorption imaging technique (to be discussed in subsection 2.2.5). Its experimental setup is implemented and modified according to the specific features of the experiment to be performed and investigated.

For the subradiance experiment, as subradiance is the emission of light at very low amplitudes and late times, characterized by slow decay rates  $\tau_{\text{sub}} > \tau_0$ , it is important to have a good extinction and a fast enough fall time after the probe beam is switched off. This is because, like in the simulations, in the experiment the driving laser is a square wave pulse, but its extinction and ratio (which are ideal in the simulations, i.e., a perfect square wave) must be as good as possible. In order to achieve these two requirements, the setup was chosen to be two AOMs in series with a focused beam.

The probe beam setup for subradiance is shown in Fig. 2.8(a). The two AOMs are connected to a function generator from Agilent, model 33220A, which generates square pulses. A setup with a strongly focused beam inside an AOM is a technique to obtain a fast fall time at the pulse edge, because the switch off of the probe beam is the switch off of the -1 order beam, and this becomes faster if the beam is focused in the AOM. Thus, the focusing lens, whose focal distance is 150 mm, was chosen in order to find the best trade-off between a fast extinction, a reasonable diffraction efficacy, and the ability to separate the different diffraction orders.

To obtain the good extinction in amplitude, the AOM with focused beam is connected to two switches and another AOM is placed before, in such a way that one of the AOMs has its switch connections inverted in order to provide the timing in Fig. 2.8(b): when

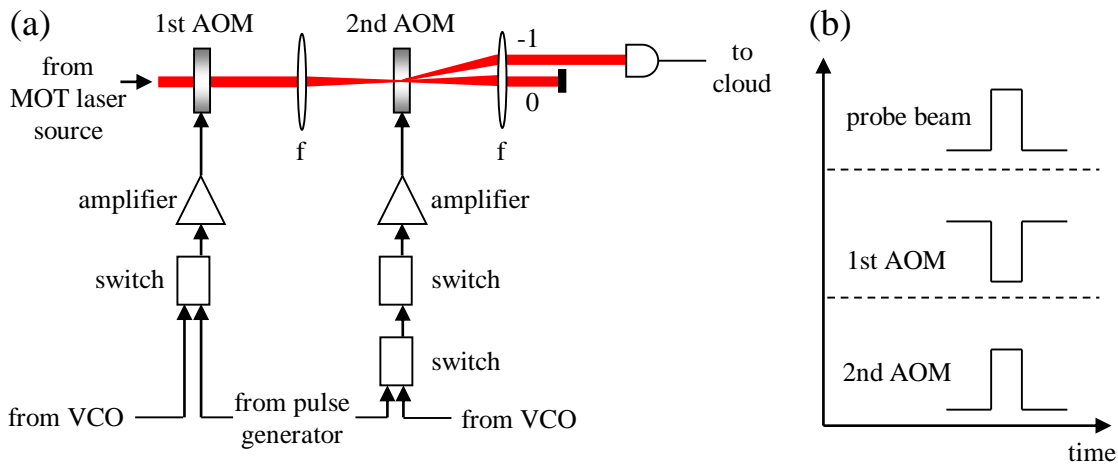


**Figure 2.8:** Probe beam setup for the subradiance experiment. **(a)** AOMs in series connected to a pulse generator, VCOs, switches and amplifiers. The lenses have focal distance  $f = 150$  mm. The  $-1$  order beam enters into a monomode optical fiber towards the atoms. **(b)** Timing of the AOMs. The probe beam is a squared pulse with maximum and minimum amplitudes, and the two AOMs are connected in such a way that, at the maximum amplitude, the first AOM is off and the second is on [exactly as in (a)], and at the minimum amplitude, the first AOM is on (diffraction) and the second is off (no  $-1$  order going into the optical fiber).

one AOM is on, i.e., diffracts, the other is off, i.e., does not diffract, and vice-versa.<sup>1</sup> As mentioned in the last subsection, the diffracted beam by the AOM depends both on the frequency and the amplitude of the sinusoidal voltage provided by the VCO and, after passing through a switch, the amplitude is reduced by a factor  $x$ . When the first AOM is off, the second AOM is on [setup shown in Fig. 2.8(a)], thus the probe beam is on (maximum intensity) and excites the atoms. However, after the probe beam is extinguished (minimum intensity), the first AOM diffracts, which reduces the input intensity for the second AOM, and the second AOM does not diffract, which in theory means no light to the cloud but in fact means light at very low intensity (this low intensity would be larger if the first AOM was off). The two switches in the second AOM reduce this low intensity by a factor of  $x^2$ , and therefore a good extinction is achieved.

The  $-1$  order beam after the second AOM has a frequency shift of  $-93$  MHz [see Fig. 2.7(c)]. Then, it is collimated by a lens of focal distance  $f = 150$  mm and passes through two waveplates of  $\lambda/4$  and  $\lambda/2$  [not represented in Fig. 2.8(a)], whose purpose is to assure linear polarization for the input of the monomode polarization-maintaining fiber placed after. The optical fiber assures a clean Gaussian beam for the atoms.

After the monomode optical fiber, a small part of the probe beam is deviated to a photodetector connected to an oscilloscope (we label it as *femto PD*, from the manufacturer's name, for the following discussions), in order to monitor the pulse amplitudes during the measurements (ideally they should remain constant during the data acquisition, but in practice small drifts may occur). Then, the probe beam reaches the atoms in the MOT chamber (see Fig. 2.9). The waist size of the probe beam is 5.7 mm, which is enough to

<sup>1</sup> The inverted connections is because we use the *zero order* of the first AOM as the input for the second AOM. Another possibility of arrangement is to use the  $-1$  order of the first AOM as the input for the second AOM, and then the switches would not be inverted.

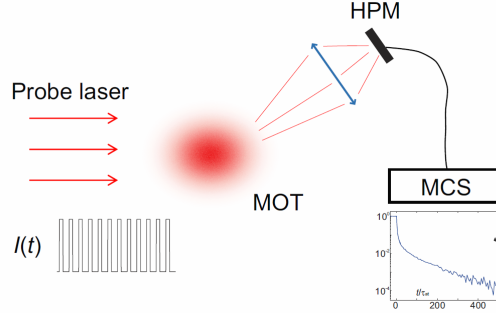


**Figure 2.9:** Scheme of the probe beam, atomic cloud and hybrid photomultiplier (HPM). Not represented: two standard photodetectors connected to an oscilloscope in order to measure the pulses and fluorescence levels. In this thesis, they are labeled as *Femto PD* and *MOT PD*, respectively.

excite the whole cloud, whose RMS size is of order of  $\sim 1$  mm.

The detector used in our measurements is a hybrid photomultiplier (HPM) from Hamamatsu, model R10467U-50 MOD. The motivation for buying and setting this detector is to avoid afterpulsing, i.e., spurious detection events after the switch off of the lasers, specially for low amplitudes, which is the main requirement for performing the subradiance experiment. Before the purchase of the HPM, several other detectors were tested, but with no success (see Fig. 2.10).

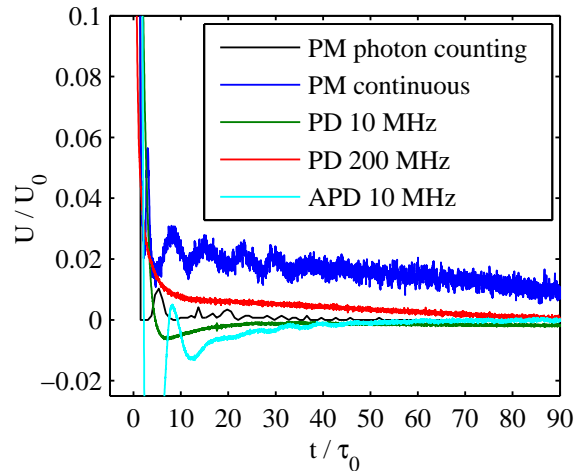


**Figure 2.10:** Extinction of several types of detectors: photon counting photomultiplier (black), continuous photomultiplier (blue), photodiode of bandwidth 10 MHz (green), photodiode of bandwidth 200 MHz (red), and avalanche photodiode of bandwidth 10 MHz (cyan). The signal is normalized to the steady state value  $U_0$ .

The HPM was set in an angle of  $\theta \approx 35^\circ$  from the probe laser direction. Also, a standard photodetector (not represented in Fig. 2.9; we label it as *MOT PD* for following discussions) was set and connected to a oscilloscope in order to measure the fluorescence amplitudes for the calibration procedure (to be discussed in subsection 2.2.7). A setup with lenses and iris is placed between the cloud and the HPM in order to better collect the fluorescence. A shutter was also set to protect the HPM when the MOT lasers are on. All the HPM system is covered by a black cardboard box in order to avoid excess of

light from the whole setup and laboratory room. Also, black cardboards are set on the optical table to cover the main optics and to avoid excess of scattered laser light.

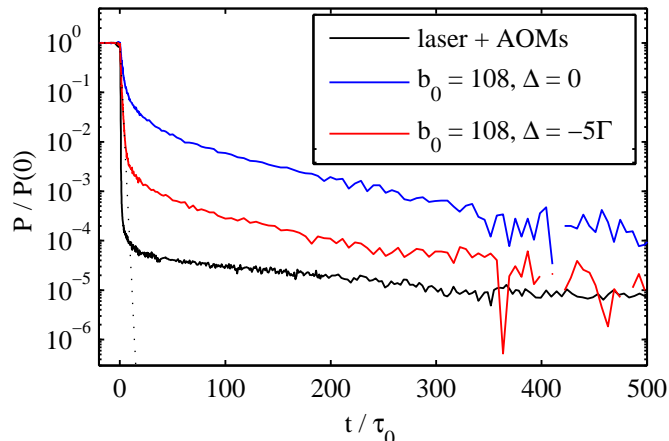


**Figure 2.11:** Probe beam extinction (black) and comparison with two atomic fluorescences, for  $b_0 = 108$  and  $\Delta = 0$  (blue) and  $\Delta = -5\Gamma$  (red), measured by the HPM, after the probe beam setup for subradiance. The black dotted line is the single atom decay. All the data are normalized by their steady value.

Figure 2.11 shows the normalized extinction of the probe beam after the AOMs outputs (black) and the comparison with two fluorescences emitted by the cold atoms. All the signals were recorded with the HPM. It was obtained a fall time of  $\sim 15$  ns in the edge of the pulses, obtained from an exponential fit in amplitude between 10% and 90% of the initial value. We also see that the extinction level is better than  $10^{-4}$ . The comparison with two fluorescences, recorded at  $\Delta = 0$  and  $\Delta = -5\Gamma$ , shows that the fluorescence level is well above of the extinction level. Also, the comparison with the single atom decay shows that a slow decay is indeed observed at late times, i.e., subradiance.

## 2.2.4 Cloud preparation and data acquisition procedure

The preparation of the atomic cloud sample inside the vacuum chamber and the experimental sequence for the data acquisition obey the following steps:

- *MOT loading.* From the vapor at room temperature, the six laser beams, the two repumper beams and the magnetic field are turned on during a time  $t_{\text{load}}$ , in order to charge the MOT. The value of  $t_{\text{load}}$  is 50–60 ms for the measurements,  $\sim 500$  ms for the  $b_0$  calibration (see subsection 2.2.7) and 2–4 s for the absorption imaging cycle. As already mentioned, the MOT and repumper beams have a detuning of  $-4\Gamma$  and  $-\Gamma$ , respectively. They are set at their maximum intensities, which corresponds to a power of 40 mW for each MOT beam and 5.5 mW for each repumper beam.
- *Dark MOT.* During 30 ms, the intensity of the repumper beams is reduced to 37% of its maximum value and the MOT lasers detuning is changed to  $-5\Gamma$ , in order to make the atoms go to the *dark MOT phase* [Ketterle 1993]. In this phase, due to the weak repumper beams, the atoms accumulate in the ground level  $F = 1$  and do not interact with the cooling beams anymore. This reduces the repulsion between

the atoms due to multiple scattering and excited-state collisions, which leads to an increase of the cloud density and a decrease of the temperature.

- *Extinction of the magnetic field.* At this phase the MOT beams, the repumper beams and the magnetic field are turned off, leading the cloud to a free expansion. We set 1.0 ms for the extinction of the magnetic field.
- *Optical hyperfine pumping.* During 0.5 ms, the repumper beams are turned on at maximum intensity to make the atoms go back to the state  $F = 2$ , since they went to the state  $F = 1$  at the dark MOT phase.
- *Data acquisition or absorption imaging.* As the MOT beams and magnetic field were turned off, the cloud falls due to gravity and expands ballistically. During the cloud expansion, the probe beam is turned on to perform either the data acquisition (to be discussed in this subsection) or the absorption imaging (subsection 2.2.5).

The extinction of the magnetic field is displayed in Fig. 2.12. Panel (a) shows the magnitude of the magnetic field  $B$  at the center of the MOT chamber, where the cloud is produced.  $B$  was measured with a device based on the Hall effect. As it is not possible to set the device at the cloud position, i.e., inside the vacuum chamber, the device was placed at a distance  $d$  above the upper coil, where  $d$  is the vertical distance between the cloud and the upper MOT coil (this vertical distance coincides with the axis of the vertical MOT laser beams pair). In this configuration, the center of the upper coil is the midpoint between the cloud and the device positions, and the magnitude of the magnetic field measured by the device equals to the half of its value at the chamber center. The magnetic field is turned on at the instant  $t = -93$  ms and turned off at the instant  $t = -3$  ms, remaining on during 90 ms. The MOT loading takes place at the first 60 ms; the dark MOT phase, in the following 30 ms. Panel (b) shows how  $B$  decreases after the switch off. The probe beam is turned on at  $t = 0$ . We see that  $B$  is not completely extinguished at  $t = 0$ , meaning that the atoms might have their Zeeman levels split due to some residual  $B$ .

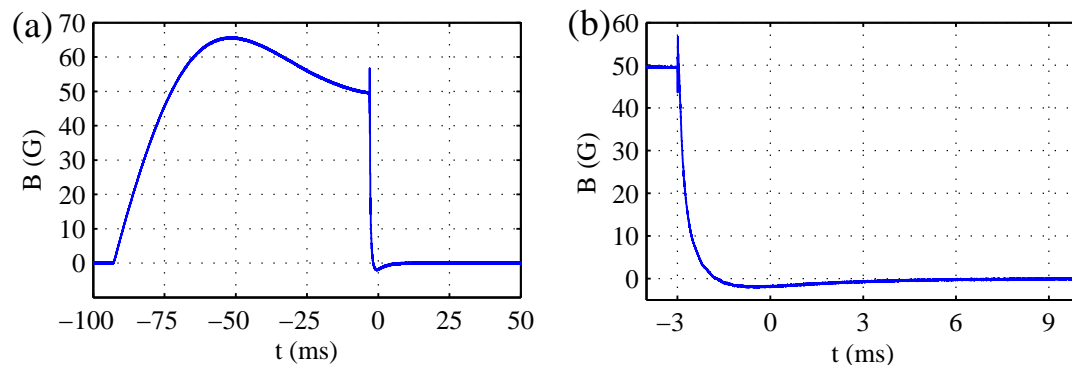


**Figure 2.12:** (a) Magnetic field at the MOT chamber center, measured with a device based on the Hall effect. The magnetic field is turned on at the instant  $t = -93$  ms and is switched off at  $t = -3$  ms. (b) Zoom of (a) around the switch off.

The data acquisition consists in sending the probe beam as a sequence of 12 pulses to the cloud, of duration  $30 \mu\text{s}$  and separation  $1.0 \text{ ms}$  (see Fig. 2.9). The cloud expansion allows us to have different values of  $b_0$  for each pulse, since the cloud size (and sometimes also the atom number  $N$ ) changes, for a fixed detuning  $\Delta$  and intensity  $I$  of the probe beam. After the pulse sequence, a waiting time of  $3.0 - 5.0 \text{ ms}$  is set and then the cycle restarts. The total number of cycles is  $\sim 500,000$ , which corresponds to  $\sim 14$  hours of acquisition.

During the cycles, the HPM averages the fluorescence emitted by the cloud. Also, the pulse amplitudes before and after the atoms are averaged, by means of the photodetectors Femto and MOT PD. The measurements are performed at a constant saturation parameter  $s(\Delta)$  for the probe beam, where  $s(\Delta)$  is the definition in Eq. 1.6 multiplied by  $g = 7/15$ . In Eq. 1.6, the probe beam intensity is  $I = 2P/(\pi w_0^2)$ , with  $w_0 = 5.7 \text{ mm}$  and  $P$  the probe beam power. For a given detuning  $\Delta$ ,  $P$  is set in order to have  $s(\Delta) = 1 \times 10^{-2}$ , but we can determine  $s(\Delta)$  experimentally since the pulses amplitudes are averaged with the main data.

After the acquisition of the main data, a calibration procedure is run in order to calculate  $b_0$  for each one of the pulses during the data acquisition. This calibration procedure uses the absorption imaging and the time of flight (TOF) techniques. In the three following subsections, we describe the absorption imaging, the TOF technique and then the calibration procedure.

## 2.2.5 Absorption imaging

The absorption imaging is a standard technique in cold atoms experiments which is used to measure some of the atomic cloud parameters, like: the atom number  $N$ , the RMS sizes  $R_x$ ,  $R_y$  and  $R_z$  in each direction, the temperature  $T$ , the density  $n_0$  at the center of the cloud, the optical thickness  $b(\Delta)$ , the resonant optical thickness  $b_0 = b(\Delta = 0)$ .<sup>2</sup> The atom number  $N$  and the RMS sizes  $R_{x,y,z}$  are the independent parameters of the cloud. They are related to the density and optical thicknesses by the expressions

$$n_0 \lambda^3 = \frac{(2\pi)^{3/2} N}{(k_0 R_x)(k_0 R_y)(k_0 R_z)} \quad (2.2)$$

$$b(\Delta) = \frac{b_0}{1 + 4\Delta^2/\Gamma^2} \quad (2.3)$$

$$b_0 = \frac{3N}{(k_0 R_x)(k_0 R_y)} \times g \quad (2.4)$$

(c.f. Eqs. 1.39, 1.43 and 1.42). Eq. 2.2 comes from the volumetric density definition  $N = \int n(x, y, z) dx dy dz$ , where

$$n(x, y, z) = n_0 \exp \left[ - \left( \frac{x^2}{2R_x^2} + \frac{y^2}{2R_y^2} + \frac{z^2}{2R_z^2} \right) \right] \quad (2.5)$$

---

<sup>2</sup> Additional cloud parameters are: the vapor pressure, the MOT loading time and the MOT loading rate.

is the Gaussian cloud density profile with  $\int_{-\infty}^{\infty} e^{-u^2/(2a^2)} du = \sqrt{2\pi}a$ . Eqs. 2.3 and 2.4 come from the Beer-Lambert law,

$$T = \frac{I_{\text{out}}}{I_{\text{in}}} = e^{-b} \quad (2.6)$$

where  $I_{\text{in}}$  is the intensity of an incident light on the cloud propagating and  $I_{\text{out}}$  is the transmitted intensity by the cloud. If  $I_{\text{in}}$  propagates along the  $z$  axis,  $b(\Delta)$  is by definition

$$b(\Delta) \equiv \sigma(\Delta) \int_{-\infty}^{\infty} n(x, y, z) dz \quad (2.7)$$

where  $\sigma(\Delta) = \sigma_0 f(\Delta)$  is the optical cross section,  $\sigma_0 = \sigma(\Delta = 0)$  is the resonant cross section and  $f(\Delta)$  is the atomic lineshape. For two-level atoms,  $\sigma_0 = g \times 3\lambda^2/(2\pi)$  [Foot 2005]. We assume only the natural atomic lineshape for the atoms in the cloud, so  $f(\Delta) = 1/(1 + 4\Delta^2/\Gamma^2)$ . The integration in Eq. 2.7 gives a function of  $x$  and  $y$ . By setting  $x = y = 0$ , i.e., at the center of the cloud, and replacing Eq. 2.2, we obtain Eq. 2.3 with  $b_0$  given by Eq. 2.4.

The absorption imaging technique consists in illuminating the atomic cloud with a weak probe beam of known detuning  $\Delta$ , and then in measuring the transmitted intensity by means of a CCD camera [Fig. 2.13(a)]. The analysis of the images collected by the camera allows us to determine  $b_0$  and  $R_{x,y,z}$ , and from them we obtain the related parameters. In our setup, we use a CCD camera from Point Grey, model GRAS-20S4M-C, pixel size 4.0  $\mu\text{m}$ . The cloud and the CCD camera were arranged in the called 2f-2f configuration with unit magnification. The images recorded by the CCD camera are analyzed with a program written in MATLAB [Fig 2.13(b)].

The CCD camera records a bi-dimensional image in its plane surface, which is set perpendicularly to the probe laser beam propagation axis. We choose  $z$  as the laser axis propagation and  $x, y$  the two orthogonal image axis lying on the camera plane, in a such way that  $x$  (and also  $z$ ) is horizontal to the plane of the optical table and  $y$  is vertical. After the phases *MOT loading*, *dark MOT*, *extinction of the magnetic field* and *optical hyperfine pumping* (see subsection 2.2.4), the probe beam is sent to the cloud as a sequence of two pulses of width 30  $\mu\text{s}$  and separation 70 ms. The first pulse goes through the cloud, so the CCD camera records the transmitted intensity  $I_{\text{out}}(x, y)$ . The second pulse is sent after the cloud expands completely, so there is no more cloud and the CCD camera records the incoming light intensity  $I_{\text{in}}(x, y)$ . Finally, after another 70 ms, no pulse is sent and the CCD camera records a third picture corresponding to the stray light intensity  $I_{\text{background}}(x, y)$ . Hence, from these three measured intensities, the transmission is calculated according to

$$T(x, y) = \frac{I_{\text{out}}(x, y) - I_{\text{background}}(x, y)}{I_{\text{in}}(x, y) - I_{\text{background}}(x, y)} \quad (2.8)$$

From the Beer-Lambert law  $T = e^{-b}$ , we obtain  $b = -\ln T$  as a function of  $x$  and  $y$ . A Gaussian fit is done on these two directions, which allows us to extract the maximum

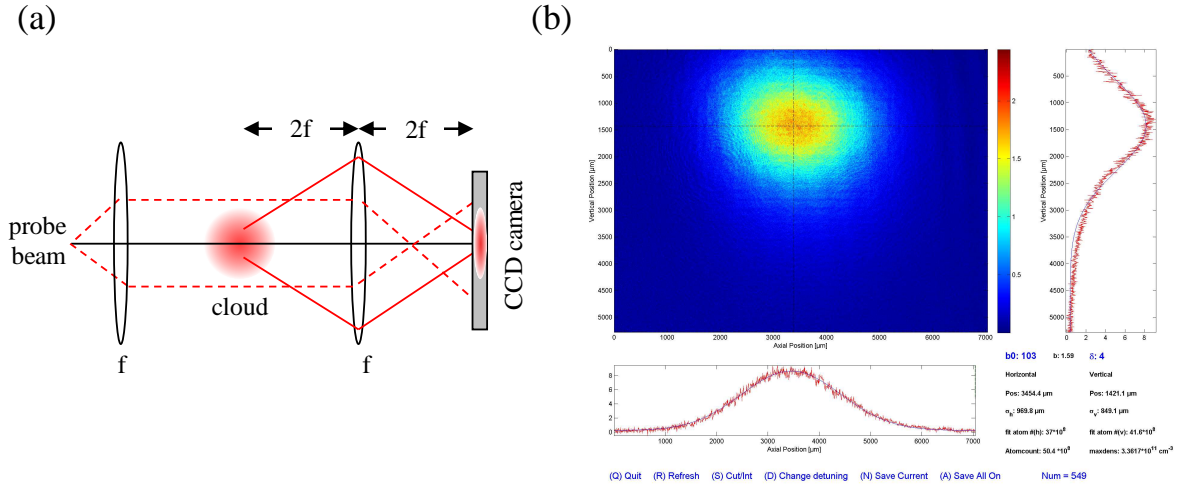


**Figure 2.13:** The absorption imaging setup. **(a)** The probe beam (dashed red line), the cloud shadow (continuous red line) and the CCD camera are in a  $2f$ - $2f$  configuration, where  $f = 100$  mm is the lens focal distance. **(b)** Interface of the imaging program written in MATLAB showing the parameters of the cloud after the analysis.

optical thicknesses  $b_x$  and  $b_y$  and also the cloud RMS sizes  $R_x$  and  $R_y$ , from the pixel size of the CCD camera image. Then, we use  $b = (b_x + b_y)/2$ , and  $b_0$  is calculated from Eq. 2.3, because  $\Delta$  is known. Hence,  $N$  can be determined from Eq. 2.4. Finally, for the density  $n_0\lambda^3$ , as there is no way to measure  $R_z$ , we assume that the cloud is quasi-spherical, so  $R_z$  is assumed to be equal to  $R_x$  or  $R_y$ . In our case,  $R_z = R_x$ , because the direction  $y$  contains the MOT coils and thus  $R_y$  is expected to be different. Hence,  $n_0\lambda^3$  is calculated with Eq. 2.2.

## 2.2.6 Time of flight (TOF)

Like the absorption imaging, the time of flight (TOF) is a standard technique in cold atoms experiments. Its goal is to measure the temperature  $T$  of the atomic cloud. To do this, during the ballistic expansion of the cloud, the absorption imaging technique (see subsection 2.2.5) is run for different time delays  $t_{TOF}$  between the switch off of the MOT and the first pulse of the two-pulses sequence of the probe beam. This allows us to obtain a set of cloud sizes  $R_x$  and  $R_y$  (and also  $b_0$ ,  $N$ , etc.) as a function of  $t_{TOF}$ . Then, a fit is done with the function

$$R(t_{TOF}) = \sqrt{R_0^2 + v_{\text{RMS}}^2 t_{TOF}^2} \quad (2.9)$$

where  $R_0$  is the initial RMS size and  $v_{\text{RMS}}$  is the atomic RMS velocity. Eq. 2.9 is derived from uniform motion,  $x_j(t_{TOF}) = x_{0j} + v_{xj}t_{TOF}$  for the atom  $j$  (and an analogous equation for the  $y$  direction), and the RMS size is defined by  $R_x^2 = \sum_{j=1}^N x_j^2/N \equiv \langle x_j^2 \rangle$ , so  $x_j(t_{TOF})^2 = (x_{0j} + v_{xj}t_{TOF})^2 = x_{0j}^2 + v_{xj}^2 t_{TOF}^2 + 2x_{0j}v_{xj}$  and hence  $\langle x_j(t_{TOF})^2 \rangle = \langle x_{0j}^2 \rangle + \langle v_{xj}^2 t_{TOF}^2 \rangle + 2 \langle x_{0j}v_{xj} \rangle$ . The term on the left-hand side gives  $R_x^2$ , the first term in the right-hand side gives  $R_0^2$ , the second term gives  $v_{\text{RMS}}^2 t_{TOF}^2$ , since  $v_{\text{RMS}}^2$  has an analogous

definition as  $R_x^2$ , and the third term vanishes because there is no correlations between the initial positions and velocities.

The fit with Eq. 2.9 allows to determine  $v_{\text{RMS}}$  for the directions  $x$  and  $y$ . Then, the temperature is extracted from the equipartition theorem [Salinas 2001]

$$\frac{k_B T}{2} = \frac{M v_{\text{RMS}}^2}{2} \quad (2.10)$$

and the cloud temperature is the arithmetic mean of the temperatures in the directions  $x$  and  $y$ .

Figure 2.14 below shows an example of a TOF measurement. The temperature obtained in this fit is  $T_x = 62.5 \mu\text{K}$  in the direction  $x$  and  $T_y = 74.5 \mu\text{K}$  in the direction  $y$ , which gives an average of  $T = 68.5 \mu\text{K}$ . An important remark is that in theory both temperatures  $T_x$  and  $T_y$  should be the same, and it is out of our comprehension why we have observed different values during all this work.

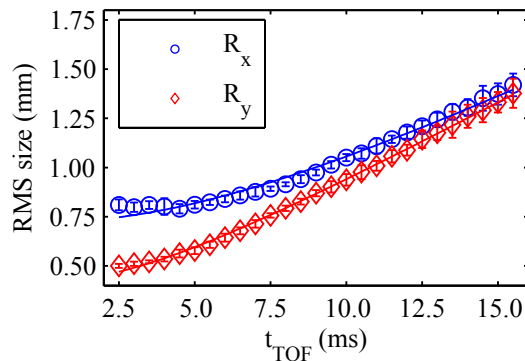


**Figure 2.14:** Example of TOF measurement for the superradiance data. Each value of the RMS size is averaged over 20 values. The continuous lines are the fits with Eq. 2.9, for the directions  $x$  and  $y$ .

### 2.2.7 Calibration of $b_0$

The calibration of  $b_0$  is a procedure developed in our laboratory in order to determine the values of  $b_0$  for the atomic cloud in the experimental measurements. As discussed in subsection 2.2.4, the experimental data are acquired by the HPM from a sequence of pulses exciting the atoms, and as the pulses are sent during the cloud expansion, this allows to vary  $b_0$  for a fixed detuning  $\Delta$  of the probe beam. However,  $b_0$  is not measured simultaneously with the data and has to be determined separately.<sup>3</sup>

From Eq. 2.4,  $b_0$  drops due to the increasing of  $k_0 R$  during the expansion. However, if the probe beam is largely detuned to the red, i.e.,  $\Delta < 0$  and  $\Gamma \ll |\Delta|$  (which is the case in some of our measurements), there is a non-zero probability of atomic decay to the

<sup>3</sup> In principle we can turn on the absorption imaging after the pulses sequence and then to measure  $b_0$ , however the disadvantages are longer cycles and total loss of atoms after the imaging, which results in few atoms for the MOT loading. Due to this, we decided to use *short cycles with recapture*, i.e., no absorption imaging and some remaining atoms after the pulses sequence. This allows to increase the number of cycles and to average more the detected intensity.

non-interacting state  $F = 1$  (see Fig. 2.15), which causes a decrease in  $N$ . Thus, for each pulse,  $b_0$  may also drop due to atom losses.

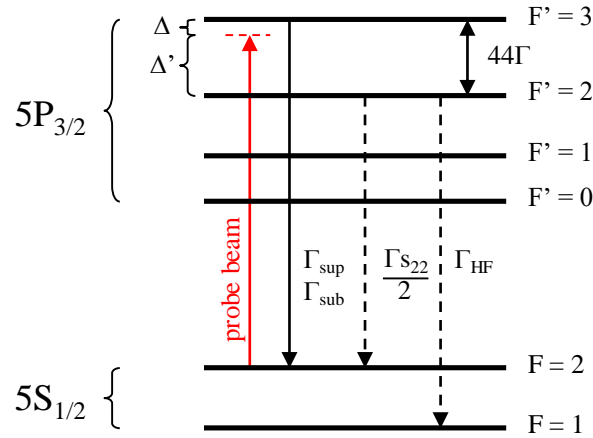


**Figure 2.15:** Probe beam excitation. The probe beam has a detuning of  $\Delta$  with respect to the transition  $F = 2 \rightarrow F' = 3$  and  $\Delta' = 44\Gamma - \Delta$  for the transition  $F = 2 \rightarrow F' = 2$ . For  $|\Delta| \gg \Gamma$ , the state  $F' = 2$  is occupied and decays to the states  $F = 2$  or  $F = 1$  with a rate of, respectively,  $\Gamma s_{22}/2$  and  $\Gamma_{\text{HF}}$ .

The atom number losses  $N(t)$  due to the decay from  $F' = 2$  to  $F = 1$  can be written as

$$N(t) = N(0) e^{-\Gamma_{\text{HF}} t} \quad (2.11)$$

where  $N(0)$  is the atom number at the first pulse of the pulses sequence,  $t$  is the time axis composed of the accumulated pulses duration (i.e.,  $t = 30, 60, 90, \dots \mu\text{s}$ ) and  $\Gamma_{\text{HF}}$  is the decay rate of the transition  $F' = 2 \rightarrow F = 1$ , also called *hyperfine depumping*.  $\Gamma_{\text{HF}}$  is equal to

$$\Gamma_{\text{HF}} = \frac{1}{2} \times \frac{\Gamma}{2} s_{22} \quad (2.12a)$$

$$s_{22} = \frac{1}{6} \times \frac{s(\Delta)}{1 + 4(44\Gamma + \Delta)^2/\Gamma^2} \quad (2.12b)$$

where in Eq. 2.12a  $s_{22}$  is the saturation parameter for the transition  $F' = 2 \rightarrow F = 2$  and the factor  $1/2$  is the decay probability of  $F' = 2 \rightarrow F = 1$  (the second factor  $1/2$  is due to the definition of scattering rate,  $\Gamma_{sc} = \Gamma s/2$ ).  $s_{22}$  is given by Eq. 2.12b, where:  $s(\Delta)$  is the saturation parameter for the transition  $F = 2 \rightarrow F' = 3$ ;  $1/6$  is the probability of excitation from  $F = 2 \rightarrow F' = 2$ ; and  $44\Gamma$  is the frequency separation between the levels  $F' = 2$  and  $F' = 3$  in such a way that  $\Delta' = 44\Gamma + \Delta > 0$  is the detuning from  $F = 2 \rightarrow F' = 2$ .

The change in  $b_0$  due to the cloud expansion can be determined by running a TOF measurement. A combination of Eqs. 2.4 and 2.9 allows to write (we simplify  $R_x \approx R_y$  since the cloud is quasi-spherical)

$$b_0(t_{\text{TOF}}) = \frac{b_0(t_{\text{TOF}} = 0)}{1 + ct_{\text{TOF}}^2} \quad (2.13)$$

where  $b_0(t_{\text{TOF}} = 0)$  is the value of  $b_0$  at the first pulse in the TOF measurement and  $c$  is a constant which depends on the atom RMS velocity. A fit of the measured  $b_0$  as a function of  $t_{\text{TOF}}$  with Eq. 2.13 allows us to extract  $b_0(0)$  and  $c$ .

Therefore, the values of  $b_0$  for the pulses sequence in the measurements can be written as

$$b_0(t) = \frac{3N(t)}{k_0^2 R(t)^2} = \frac{3N(0)e^{-\Gamma_{\text{HF}}t}}{k_0^2 R(t)^2} = \frac{b_0(0)}{1 + ct^2} e^{-\Gamma_{\text{HF}}t} \quad (2.14)$$

with  $b_0(0) = b_0(t_{\text{TOF}} = 0)$ .

It is also possible to measure the hyperfine depumping rate  $\Gamma_{\text{HF}}$  experimentally by repeating the data acquisition procedure without the cold atoms and with the repumper beams turned on during the pulse sequence. This is because, when performing the measurements, the repumper beams are off during the pulse sequence and the light recorded by the HPM contains also stray light from the vapor fluorescence and scattered light from the chamber windows. In practice, after the experimental data acquisition, we perform the followings auxiliary cycles:

- (1) *Data acquisition without the atoms.* The magnetic field is turned off, so the phases MOT loading, dark MOT, extinction of the magnetic field and optical pumping are run without the atoms. The HPM and the MOT PD record the light from the vapor in the chamber and some scattered light from the probe beam in the chamber windows. This acquisition is performed during  $\sim 40$  minutes. This cycle is to determine this amount of stray light.
- (2) *Data acquisition with the atoms and with the repumper beams.* The magnetic field is turned on and the repumper beams are turned on during the pulses sequence, which imposes  $N$  constant during the pulse sequence. The MOT PD averages the cloud fluorescence.  $b_0$  drops only due to the cloud expansion.
- (3) *Data acquisition without the atoms and with the repumper beams.* The magnetic field is turned off and the repumper beams are turned on, so the MOT PD measures the light from the vapor and chamber windows. This cycle is to determine the amount of stray light when the repumper beams are on.
- (4) *TOF measurement.* The TOF is run to measure the cloud expansion and temperature. Each value is averaged for 20 realizations.

From the main data and the sequences (1) to (3) above, the fluorescence level for each pulse is calculated by removing the minimum amplitudes after the pulses (due to dark count and stray light from the laboratory room). Then, the comparison of pairs of data with and without atoms allows us to remove the stray light from the vapor and chamber windows, resulting in fluorescence levels due only to the atoms. Next, the fluorescence

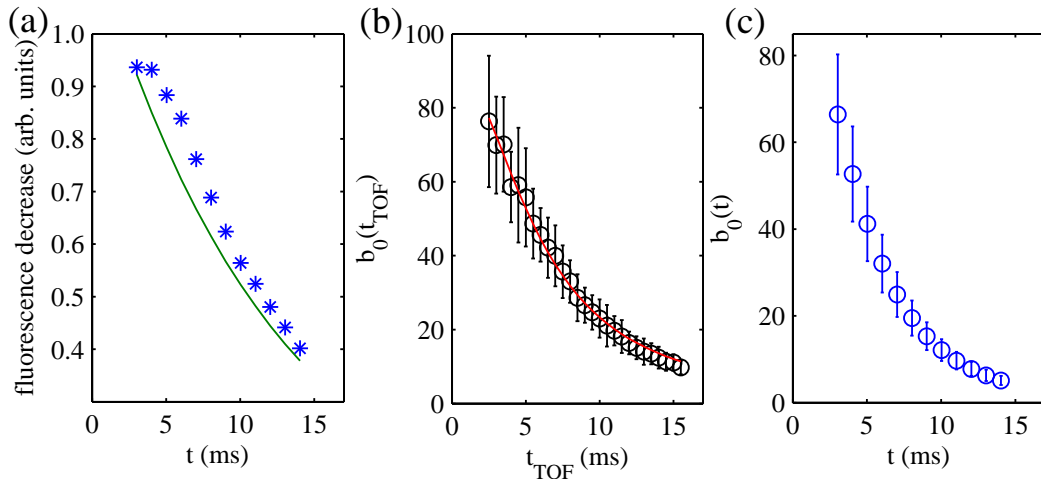


**Figure 2.16:** Example of calibration procedure. **(a)** Experimental fluorescence decrease (blue) due to atom losses only and theoretical decreasing (green) obtained from Eq. 2.11, where  $\Gamma_{\text{HF}}$  was calculated from Eqs. 2.12. The experimental saturation parameter is  $s(\Delta) = 0.92 \times 10^{-2}$ . **(b)** Experimental  $b_0$  decrease (black) due to the cloud expansion obtained from a TOF measurement and fitted  $b_0$  (red) from Eq. 2.13. **(c)** Calibrated  $b_0$  for each pulse in the main experimental data obtained from Eq. 2.14. The measured temperature is  $T = 68.5 \mu\text{K}$ . Data for superradiance,  $\Delta = -10\Gamma$ .

levels without repumper beams are divided by the ones with the repumper beams, yielding to Eq. 2.11, since the fluorescence levels are proportional to the atom number  $N$  for far-detuned data. The result of the division is fitted with Eq. 2.11 and allows us to extract  $\Gamma_{\text{HF}}$  (see Fig. 2.16). In practice, we have used this procedure only for a set of data at large detuning to calibrate  $s(\Delta)$  via Eq. 2.12. For other detunings, we have only used the theory already discussed.

## 2.3 Experimental results

In this section we discuss the experimental results for subradiance, obtained from the experimental setup and procedures described in the last section. All the subradiant data were acquired and analyzed by William Guerin, and for this reason a summarized discussion is presented in this thesis, without the technical adjustments and discussion for observation of first data. The reader is referred to [Guerin 2016] and its supplementary material as the main reference about the subradiance experiment and detailed discussion.

### 2.3.1 Detected intensities with $b_0$ and $\Delta$

The measured values of the saturation parameter of the probe beam and the temperature of the cloud were  $s(\Delta) \simeq 4.5 \times 10^{-2}$  and  $T \simeq 50 \mu\text{K}$ . This temperature is small enough to neglect Doppler effects and frequency redistribution, as already discussed (see Fig. 2.5).

Figure 2.17 shows some experimental normalized intensities, for constant detuning  $\Delta = -6\Gamma$  and several  $b_0$  [Fig. 2.17(a)] and for constant  $b_0$  and several  $\Delta$  [Fig. 2.17(b)], as well as the corresponding fitting curves in order to extract  $\Gamma_{\text{sub}}$ . The fitting interval was

set to be one decade above the noise level. As discussed in subsection 2.1, subradiance should not depend on  $\Delta$  (see Fig. 2.2), only on  $b_0$ . This is checked by the slopes of the emitted intensities in the slow range, which change with  $b_0$  and remain constant for different  $\Delta$ .

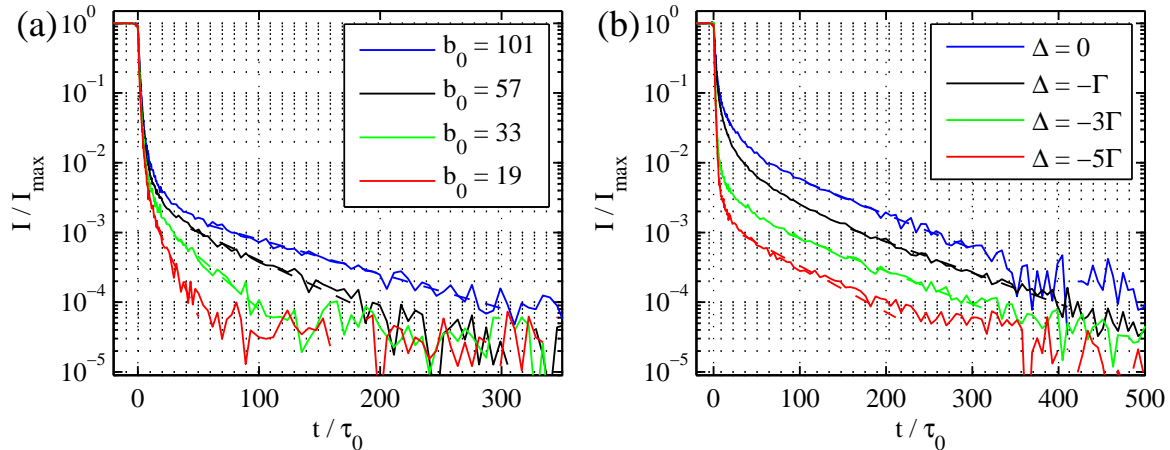


**Figure 2.17:** Subradiant experimental intensities measured with the HPM as a function of time, as well as fit curves in the slow part. **(a)** Intensities for several  $b_0 = 3N/(k_0R_x)(k_0R_y)$  for  $\Delta = -6\Gamma$ . **(b)** Intensities for several  $\Delta$  for  $b_0 = 3N/(k_0R_x)(k_0R_y) = 108 \pm 5$ .

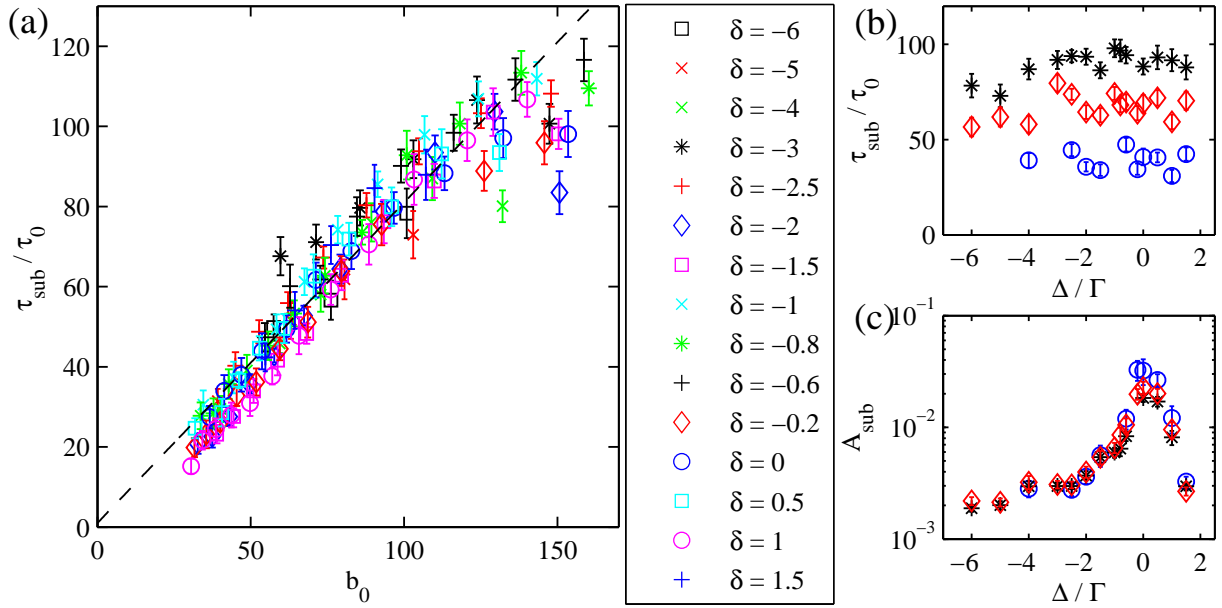
### 2.3.2 Subradiant decay rates *versus* $b_0$

Figure 2.18(a) shows experimental  $\tau_{\text{sub}}$  as a function of  $b_0$ , for several  $\Delta$ , obtained from the emitted intensities in Fig. 2.17. We see that all the values  $\tau_{\text{sub}}$  for different  $\Delta$  collapse into a single curve. The dashed line is a linear fit of the data in the form  $\tau_{\text{sub}}/\tau_0 = 1 + c b_0$ . Excluding the data for  $b_0 > 120$ , the fit gives  $c \simeq 0.8$ . By converting this  $b_0$  to the scalar definition (Eq. 1.40) to compare with the simulation data presented in Figs. 2.1(b) and 2.3, we have  $0.8 \times 3/2 = 1.2$ , which is almost two times more than the theoretical value of  $c = 0.53$ . However, as already mentioned, we do not expect any agreement with the theoretical data because the atoms used in the experiments are not a pure two-level system due to Zeeman states.

Figure 2.18(b) shows some of the data in (a) for a constant  $b_0$  for several  $\Delta$ . The fitted  $\tau_{\text{sub}}$  are constant, showing that the slow decay does not depend on  $\Delta$ , as expected from the simulations (see Fig. 2.2). In Fig. 2.18(c), the fit amplitudes  $A_{\text{sub}}$  are plotted for the same data in Fig. 2.18(b). The increasing of the amplitudes for the data close to resonance is what we see in Fig. 2.17(b), where the amplitude for the curve  $\Delta = 0$  is higher than for  $\Delta \neq 0$ . The numerical simulation simulations [see Fig. 2.4(c)] reproduces this same effect.

### 2.3.3 Subradiant decay rates *versus* laser intensity

Figure 2.19 shows  $\tau_{\text{sub}}$  [panel (a)] and  $A_{\text{sub}}$  [panel (b)] as a function of the saturation parameter  $s(\Delta)$ , where  $s(\Delta)$  vary in the limit  $s \ll 1$  to keep the linear optics regime.



**Figure 2.18:** (a) Experimental subradiant decay rates  $\tau_{\text{sub}}$  as a function of  $b_0 = 3N/(k_0R_x)(k_0R_y)$  for several detunings  $\delta = \Delta/\Gamma$ . The dashed line is a linear fit of the data. (b) Experimental  $\tau_{\text{sub}}$  as a function of  $\Delta$  for  $b_0 = 3N/(k_0R_x)(k_0R_y) = 50$  (blue circles), 80 (black asterisks) and 110 (red diamonds). (c) Experimental fit amplitudes  $A_{\text{sub}}$  as a function of  $\Delta$  for the same  $b_0$  value in (b).

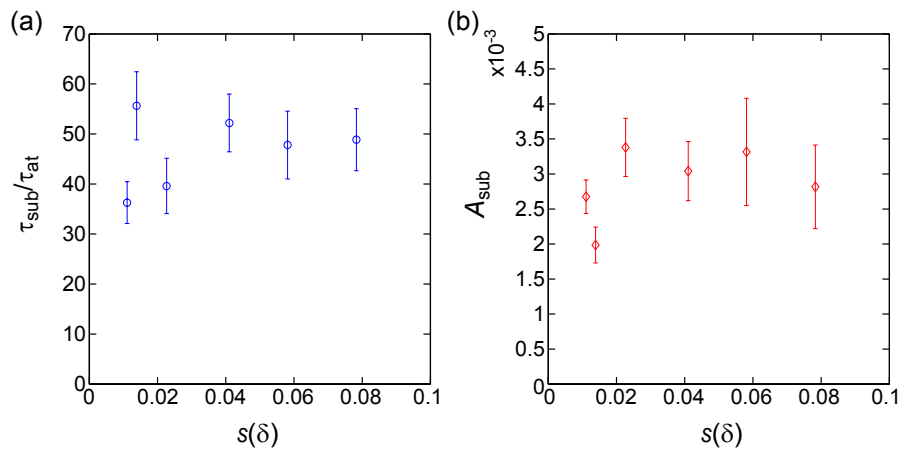


**Figure 2.19:** (a) Experimental subradiant time decay rates  $\tau_{\text{sub}}$  as a function of  $s(\delta)$ ,  $\delta = \Delta/\Gamma$ , for  $b_0 = 110 \pm 8\%$ . (b) Subradiant amplitudes  $A_{\text{sub}}$  as a function of  $s(\delta)$ .

Both the fitted  $\tau_{\text{sub}}$  and  $A_{\text{sub}}$  do not vary in the errorbar limits, as expected physically.

### 2.3.4 Possibility of radiation trapping in the subradiance data

The experimental results in the last three subsections show subradiance for a large set of particles, where an incident laser beam of large size compared with the atomic sample size excites all the atoms. The detuning  $\Delta$  of the incident beam was varied both for on- and off-resonance, and its intensity was set in the regime of single excitations. The obtained results are consistent with the theoretical predictions from the coupled-dipole model. The only parameter which allows to obtain the correct scaling law for the subradiant decay rates  $\Gamma_{\text{sub}}$  and  $\tau_{\text{sub}}$  is  $b_0$ , the resonant optical thickness of the cloud. This is true even for the data at resonance.

Another well-known phenomenon in physics about trapping of light in a medium is *radiation trapping*. Radiation trapping can be defined by the multiple scattering of a photon propagating in a medium of large optical thickness  $b(\Delta)$ . A physical picture is that the photon performs a random walk: after being absorbed by an atom, the photon is re-emitted in a random direction with a frequency which depends on the incident frequency of the photon and on the velocity of the atom. The photon is absorbed and emitted (i.e., scattered) until it leaves the medium, with a certain frequency in a certain direction. If the incoming laser beam is switched off, the time decay rate  $\tau_{\text{RT}}$  extracted from the output intensity is the time that the photon spent in the medium. If the medium is a cloud of cold atoms and if the incident field has a *small waist* compared with the cloud size, previous experimental work show that in the linear optics regime  $\tau_{\text{RT}}$  extracted at amplitudes  $\sim 10^{-1}$  scales with  $b(\Delta)^2$  for sufficiently low temperatures [Labeyrie 2003], meaning that, the higher  $b(\Delta)$  (i.e.,  $\Delta \sim 0$  or large  $b_0$ ), the stronger is the radiation trapping. Radiation trapping is also dependent very sensitively on the temperature, and even for small temperatures like some  $\mu\text{K}$ , the scaling  $\tau_{\text{RT}} \propto b(\Delta)^2$  is broken into linear-like dependence [Labeyrie 2003, Labeyrie 2005]. In addition, this phenomenon is incoherent, so there is no coherence created between the scatterers (absence of, e.g., the forward emission lobe in the steady state) [Chabé 2014].

We discuss radiation trapping in more detail in Chapter 4, under an experimental setup with a narrow beam exciting the sample. For the case of a large beam, the numerical results presented in this chapter show very well slow decay rates independent of  $\Delta$ , i.e., scaling with  $b_0$  only [Fig. 2.18]. Also, they are observed at amplitudes  $\sim 10^{-3} \ll 10^{-1}$  [Fig. 2.17] and independent of temperature (Fig. 2.5). Therefore, if there are some contribution from radiation trapping in these subradiant data, it is very small, even for the data with incoming beam at  $\Delta = 0$  [parallel slopes on Fig. 2.17(b)].

Since radiation trapping is very dependent on the temperature and the scaling law  $\tau_{\text{RT}} \sim b(\Delta)^2$  is valid only for low temperatures, it may be possible that, even for the data at  $\Delta \neq 0$ , resonant photons are created during the photon scattering such that they undergo multiple scattering and are emitted at resonance. However, for incoming far-detuned light, it is possible to show that the number of resonant photons created is negligible.

Indeed, there are at least three factors in the experimental setup which are not included in the theoretical model of coupled dipoles but may create resonant photons in the emitted

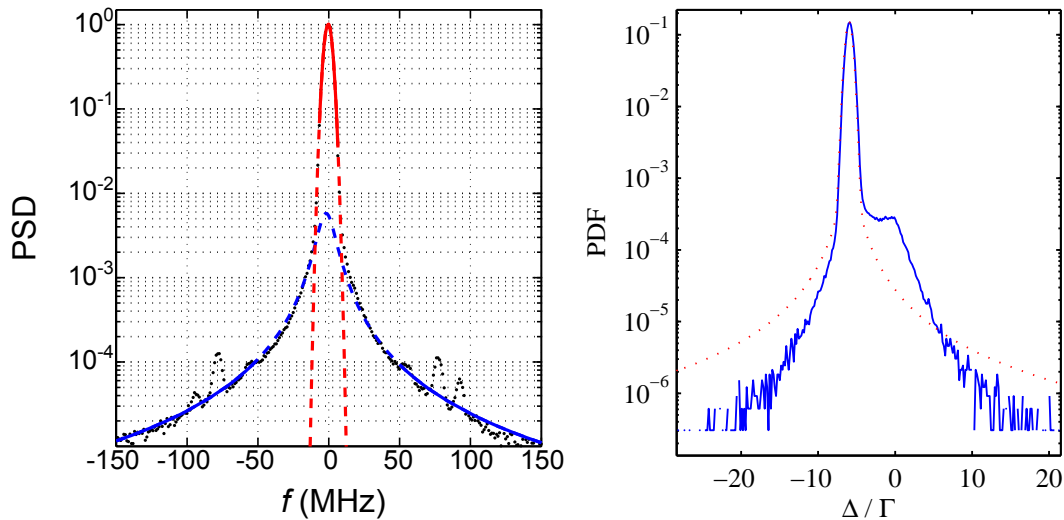


**Figure 2.20: Left:** Measured spectrum of the probe laser beam (black) and a Gaussian (red) and Lorentzian (blue) fits. **Right:** Fitted spectrum of the probe laser beam (red) at  $\Delta = -6\Gamma$  and the spectrum of the emitted light (blue), with frequency redistribution, calculated with a random-walk model. Parameters for the simulation:  $\Delta = -6\Gamma$ ,  $b_0 = 72.2$  ( $N = 10^9$  and  $R = 0.8$  mm),  $T = 55$   $\mu\text{K}$ .

intensity:

- (1) *Spectrum of the probe beam.* The probe laser beam is not perfectly monochromatic and, as discussed in subsection 2.2.2, its linewidth is  $\Delta\omega \sim 2\pi \times 3$  MHz. Ideally, in atomic physics experiments, the probe beam linewidth should be chosen to be very small compared to the natural decay rate of the chosen atomic species, i.e.,  $\Delta\omega \ll \Gamma$ . This is not the case, since  $\Gamma = 2\pi \times 6.066$  MHz, so there is a factor two between  $\Delta\omega$  and  $\Gamma$ . Also, there is the line broadening beyond this linewidth. This means that, even if the laser is set far from resonance, due to the large broadening of the laser source, there are resonant photons that may excite the atoms.
- (2) *The Mollow triplet.* For a single two-level atom interacting with a monochromatic laser beam at any detuning  $\Delta$ , the spectrum of its emitted intensity in general is not monochromatic [Cohen-Tannoudji 1992, Berman 2008]. In the particular case of  $\Delta \gg \Gamma$  and  $\Omega \ll \Gamma$ , i.e., low  $s(\Delta)$ , the spectrum of the emitted intensity has an elastic Dirac delta function component centered at  $\Delta$  and two sidebands with frequencies  $\Delta = 0$  and  $2\Delta$ , known as Mollow triplet [Mollow 1969]. The emitted photons in the sidebands, i.e., emitted at  $\Delta = 0$  and  $2\Delta$ , are due to inelastic scattering [Cohen-Tannoudji 1992]. It is possible to show that the ratio between the inelastic and elastic scattering rates is  $\Gamma_{\text{inel}}/\Gamma_{\text{el}} = s(\Delta)$ , so the arising of photons at  $\Delta = 0$ , i.e., resonant, in the emission spectrum is proportional to the saturation parameter of the incident light.
- (3) *Frequency redistribution.* After an absorption, the off-resonant photon is re-emitted with a frequency which depends both on the atomic natural lineshape and the atomic velocity spectrum. After a certain number of absorption and emission events, the

photon has its frequency shifted, even if initially out of resonance, and may leave the medium at resonance.

For (2), it is shown in the supplementary material of [Guerin 2016] that the amplitude for radiation trapping is negligible. For (1) and (3), Fig. 2.20 is a measurement of the spectrum of the incident probe laser beam (left panel) and a random walk simulation of the spectrum of the emitted photons by using the spectrum in (a) and the cloud temperature (right panel). We see that the ratio between the number of resonant photons and far-detuned photons is  $\sim 10^{-4}/10^{-1} = 10^{-3}$ , i.e., negligible.

## 2.4 Conclusions of this chapter

The main conclusions about this chapter is that we were able to measure subradiance in a sample of large number of particles. Both the experimental and theoretical results show a scaling of the subradiant decay rates only with the resonant optical thickness of the atomic cloud. Also, the measured subradiant decay rates are consistent with the predictions of the coupled-dipole model.

In the next chapter, we discuss the decay rates obtained with the same experimental setup, but for the fast decay, i.e., off-axis superradiance.

## Superradiance in cold atoms

In this chapter, we present the results obtained on off-axis superradiance. They include a numerical study, the description of the experimental setup for the probe beam, and the experimental results and discussion.

Superradiance in cold atoms in the single excitation regime has been studied extensively since M. O. Scully's work on single-atom superradiance [Scully 2006]. As discussed in Chapter 1, this cooperative emission is characterized by a strong emission in the forward direction with a decay rate  $\Gamma_{\text{sup}}$  faster than the natural atomic decay rate  $\Gamma$ . In the timed-Dicke approximation,  $\Gamma_{\text{sup}}$  was calculated to be  $\Gamma_{\text{sup}}/\Gamma = 1 + b_0/12$  [Courteille 2010] and takes place just after the switch off of the incoming exciting laser beam [Bienaimé 2012]. Concerning experimental works, recent experiments report a feature of superradiance, for instance: a superradiant laser [Bohnet 2012], single-photon superradiance in cold atoms in a multilevel scheme [de Oliveira 2014], and the observation of a superradiant flash in the forward direction [Kwong 2014], observation of superradiance and cooperative Lamb shift in the forward direction [Roof 2016]. Here, we discuss the off-axis superradiance, i.e., the observation of a fast decay in a direction out of the forward direction.

This chapter is divided in four sections. In section 3.1, we present the numerical results on superradiance, which consists mainly in off-axis superradiance and how it depends on the parameters of the system. In section 3.2, we describe the probe beam setup to measure superradiance and the data acquisition procedure. In section 3.3, we discuss the main experimental results. Finally, in section 3.4, we point out the conclusions of this chapter.

### 3.1 Numerical results

In the same way as subradiance, the numerical study on superradiance was performed by using the simulation procedure described in section 1.3. The superradiant decay rates  $\Gamma_{\text{sup}}$  and its corresponding time  $\tau_{\text{sup}} = 1/\Gamma_{\text{sup}}$  are extracted from an exponential fit in the emitted intensity  $I(\theta, t)$  given by Eq. 1.35, in a range where a fast decay is observed, just after the extinction of the incident field. The coefficients  $\beta_j$  are given by the differential equations Eqs. 1.15, which are solved numerically. The atomic cloud with  $N$  atoms is modeled as a Gaussian sphere with RMS size  $k_0 R$  and characterized by a resonant optical thickness  $b_0 \propto N/(k_0 R)^2$  and density  $n_0 \lambda^3 = (2\pi)^{3/2} N/(k_0 R)^3$ .  $b_0$  can be written in the scalar definition (Eq. 1.40) or in the vectorial definition (Eq. 1.41). The incident laser has

a detuning  $\Delta$  and the detector is placed at an angle  $\theta$  from the incident laser direction (see Fig. 1.2). We investigate how superradiance changes with respect to these parameters.

As discussed in Chapter 1, our approach is scalar, the atoms are excited by a pulse of duration  $\gg \tau_0$  and the incoming electric field is linearly polarized. A complete theoretical study on angular superradiance is reported in [Kuraptsev 2017], where the authors investigate the forward emission lobe and the superradiant decay rates with a vectorial model. The dependence of the results with the pulse duration, incoherent light and geometry of the sample are also discussed.

### 3.1.1 Off-axis superradiance

As discussed in subsection 1.3.2, when calculating the emission diagram  $I(\theta, t)$  in the steady state, a lobe in the forward direction is observed, attesting a strong emission of light [see Fig. 1.5(a)]. In its original context, superradiance was defined as a fast and strong emission in the forward direction [Dicke 1954, Scully 2006], where the superradiant decay rate is predicted to depend on  $b_0$  [Svidzinsky 2008c]. However, when calculating the temporal emitted intensity directionally, a fast decay is observed even for directions out of the forward lobe, what we have defined as off-axis superradiance.

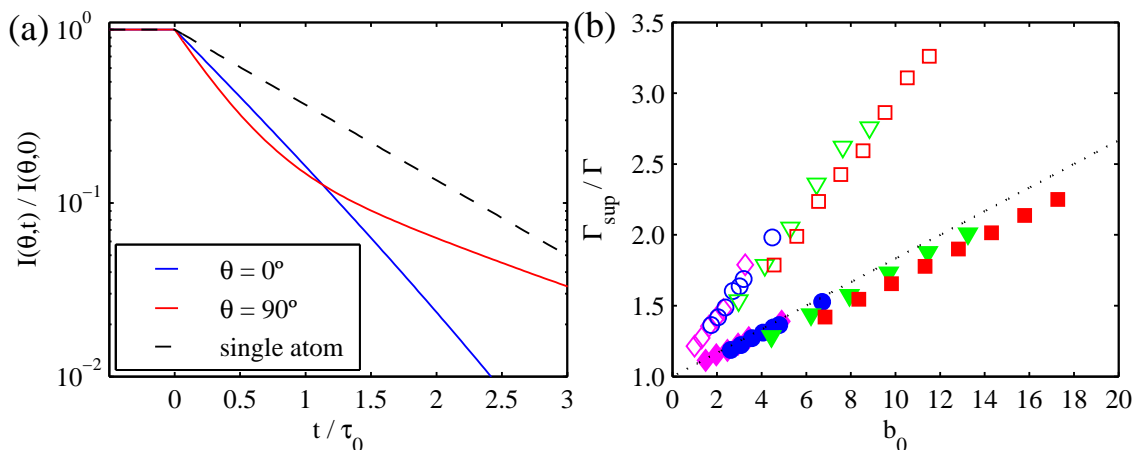


**Figure 3.1:** (a) Emitted intensities calculated from Eq. 1.35 for  $\theta = 0^\circ$  (blue) and  $\theta = 90^\circ$  (red) and comparison with the single atom decay (dashed line). Parameters:  $b_0 = 3N/(k_0R)^2 = 11.3$ ,  $n_0\lambda^3 = 4.6$  ( $N = 633$  and  $k_0R = 11.3$ ) and  $\Delta = 10\Gamma$ . (b) Superradiant decay rates  $\Gamma_{\text{sup}}$  as a function of the resonant optical thickness  $b_0$ , for  $\Delta = 10\Gamma$ ,  $n_0\lambda^3 = 0.5$  (magenta diamonds), 1.0 (blue circles), 2.5 (green triangles) and 4.6 (red squares), for  $\theta = 0^\circ$  (filled symbols) and  $\theta = 90^\circ$  (open symbols), and comparison with the law  $\Gamma_{\text{sup}}/\Gamma = 1 + b_0/12$  (black dotted line). The decay rates were obtained from a fit of the emitted intensity  $I(\theta, t)$ . Data averaged over 50 configurations of the atomic positions.

Figure 3.1(a) is a close-up of Fig. 1.5(b) in the fast decay range of the temporal emitted intensities, calculated in the forward direction ( $\theta = 0^\circ$ ) and in a perpendicular direction ( $\theta = 90^\circ$ ) with respect to the incident field. Both curves show a fast decay compared to the single atom decay and, maybe surprisingly, the off-axis decay is even faster than the

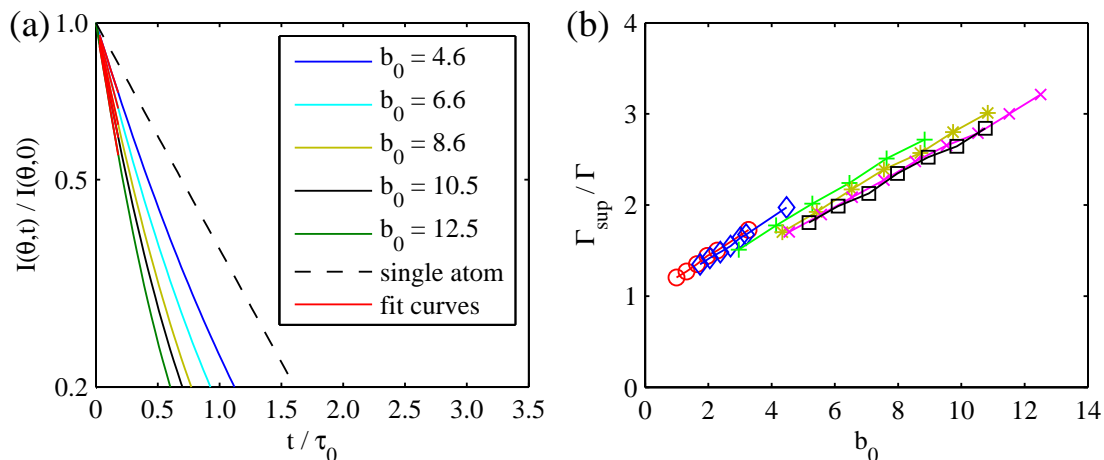
on-axis decay. We checked that intensities calculated for other values  $\theta \neq 0^\circ$ , for example,  $\theta = 45^\circ$  and  $\theta = 180^\circ$ , are similar to the curve for  $\theta = 90^\circ$ .

Figure 3.1(b) shows the fitted  $\Gamma_{\text{sup}}$  for several  $b_0$  and  $n_0\lambda^3$ , for the two directions in (a). The fit interval was set as  $t \in [0, 0.2]\tau_0$ , where the value  $0.2\tau_0$  was chosen in a such way that  $\Gamma_{\text{sup}}$  does not depend on the fit range. We compare these two sets of data with the analytic expression for  $\Gamma_{\text{sup}}$ , Eq. 1.22 (see subsection 1.1.3), obtained by [Courteille 2010] in the timed-Dicke approximation and rewritten below:

$$\frac{\Gamma_{\text{sup}}}{\Gamma} = 1 + \frac{b_0}{12}$$

where  $b_0$  is defined as  $b_0 = 3N/(k_0R)^2$  as in Fig. 3.1(b). We see that this law is valid only in the forward direction. The reference [Kuraptsev 2017] also finds this law valid for  $\theta = 0$  and for a short pulse of duration  $0.1\tau_0$ . Note that, despite most part of the light is emitted at  $\theta = 0^\circ$ , the off-axis contribution yields to  $\Gamma_{\text{sup}}$  significantly larger than those on-axis. A linear fit  $\Gamma_{\text{sup}}/\Gamma = 1 + c b_0$  for the off-axis data results in  $c \simeq 0.15$ , which is  $\simeq 1.8$  times larger than the constant  $1/12 \simeq 0.083$ , found for the forward direction. More features of this linear scaling of  $\Gamma_{\text{sup}}$  with  $b_0$  are discussed in the following subsection.

### 3.1.2 Scaling with $b_0$



**Figure 3.2:** (a) Emitted intensities for several  $b_0$ , for  $n_0\lambda^3 = 4.6$  and  $\Delta = 10\Gamma$ . The emitted intensity was calculated from Eq. 1.35 for  $\theta = 45^\circ$ . The red curves are exponential fits in the interval  $t \in [0, 0.2]\tau_0$ . (b) Superradiant decay rates  $\Gamma_{\text{sup}}$  as a function of the resonant optical thickness  $b_0 = 2N/(k_0R)^2$ , for  $\Delta = 10\Gamma$  and  $n_0\lambda^3 = 0.5$  (red), 0.9 (blue), 2.5 (green), 3.7 (dark yellow), 4.6 (magenta) and 5.3 (black). The decay rates were obtained from fits similar to those in (a). Data averaged over 100 configurations of the atomic positions.

In analogy to what was discussed in subradiance, Fig. 3.2(a) shows the same emitted intensities as in Fig. 2.1(a) in Chapter 2, but here the fits were done in the fast decay part. Fig. 3.2(b) shows  $\Gamma_{\text{sup}}$  extracted from the fits in (a), for several  $b_0$  and  $n_0\lambda^3$ . The intensities were calculated at  $\theta = 45^\circ$ , i.e., off-axis, and  $\Delta = 10\Gamma$ , i.e., far from resonance.

As for subradiance, a linear scaling with  $b_0$  is also observed, but for superradiance  $\Gamma_{\text{sup}} \propto b_0$ , whereas for subradiance  $\tau_{\text{sub}} = \Gamma_{\text{sub}}^{-1} \propto b_0$ . In addition, whereas  $\tau_{\text{sub}}$  does not vary for high values of  $n_0\lambda^3$ , the superradiance data for  $n_0\lambda^3 \geq 2.5$  deviate from those at smaller  $n_0\lambda^3$ . However, as discussed in section 1.3, experimental values of  $n_0\lambda^3$  are on the order of  $\sim 10^{-1}$  (more precisely  $n_0\lambda^3 \simeq 0.03$ ), so we do not expect such density effects in the experiment.

A linear fit  $\Gamma_{\text{sup}}/\Gamma = 1 + c b_0$  gives  $c \simeq 0.21$  for the data at low densities ( $n_0\lambda^3 = 0.5$  and  $0.9$ ), with  $b_0$  in the scalar definition. For  $b_0$  in the vectorial definition, the constant becomes  $c \simeq 0.14$ , exactly as obtained in Fig. 3.1(b) for  $\theta = 90^\circ$ . Also, as discussed for subradiance, we do not compare these values with the experiments due to the complexity of the atomic transitions in the latter.

### 3.1.3 Superradiance at resonance and for several detection directions

In the last subsection we discussed superradiance for far-detuned laser, i.e.,  $|\Delta| \gg \Gamma$ .  $\Gamma_{\text{sup}}$  was found to be larger at off-axis directions than at on-axis directions. In this subsection, we investigate  $\Gamma_{\text{sup}}$  at resonance and with respect to the detection directions.

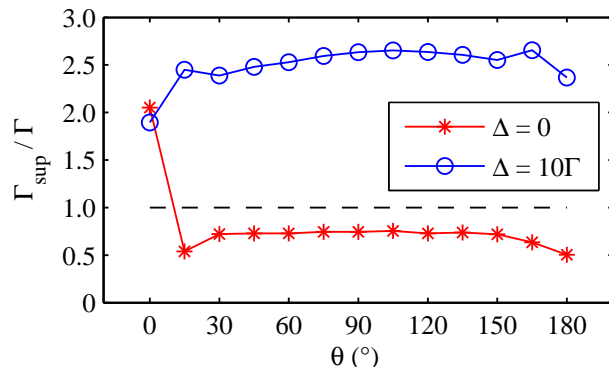


**Figure 3.3:** Angular dependence of  $\Gamma_{\text{sup}}$  for  $\Delta = 0$  (red) and  $\Delta = 10\Gamma$  (blue). The dashed line is the decay rate for a single atom. Parameters:  $b_0 = 12.8$  (vectorial definition),  $n_0\lambda^3 = 4.6$  ( $N = 921$ ,  $k_0R = 14.7$ ), averaged over 100 configurations on the atomic positions.

Figure 3.3 shows  $\Gamma_{\text{sup}}$  as a function of the direction  $\theta$ , for constant  $b_0$  and  $n_0\lambda^3$ , on- and off-resonance. We see that the off-resonant data (blue) confirms what was discussed in the last subsections:  $\Gamma_{\text{sup}}$  is larger for  $\theta \neq 0$  than for  $\theta \sim 0$ . On the other hand, at resonance (red data), superradiance is seen only for directions close to the forward direction ( $\Gamma_{\text{sup}}/\Gamma > 1$ ). For other directions,  $\Gamma_{\text{sup}}/\Gamma < 1$ , which is a signature of *radiation trapping*. As explained briefly in subsection 2.3.4, at resonance the photons are multiply scattered by the atoms before they escape, instead of single scattering. For subradiance, multiple scattering was shown to not suppress the subradiant states; however, concerning the fast decay, the red data in Fig. 3.3 show that superradiance is suppressed at resonance except in the forward direction. The reference [Chabé 2014] displays emission diagrams at resonance calculated with the coupled-dipole model and a pure radiation trapping model. The obtained diagrams are similar, except for a lobe in the forward direction, present only

for the coupled-dipole model. Therefore, resonant light has signatures of superradiance only in the forward direction.

As a last comment, the reference [Kuraptsev 2017] calculates  $\Gamma_{\text{sup}}$  for values of  $\theta$  inside the emission lobe. They are predicted to oscillate with  $\theta$ .

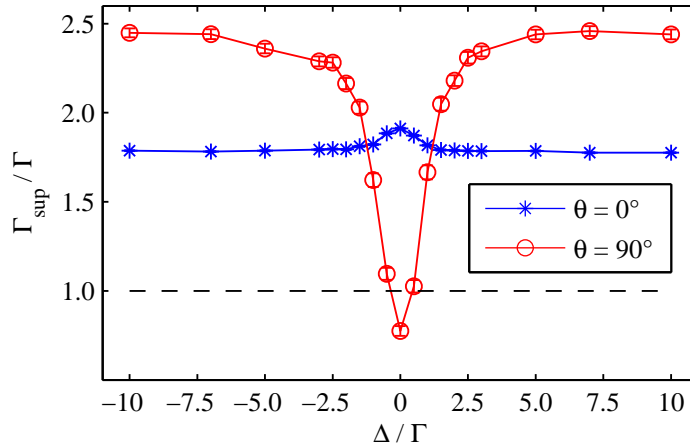


**Figure 3.4:** Superradiant decay rates  $\Gamma_{\text{sup}}$  as a function of the laser detuning  $\Delta$ , for  $\theta = 0^\circ$  (blue) and  $\theta = 90^\circ$  (red). The dashed line is the decay rate for a single atom. Parameters:  $b_0 = 3N/(k_0R)^2 = 12.8$ ,  $n_0\lambda^3 = 4.6$  ( $N = 921$  and  $k_0R = 14.7$ ), averaged over 50 configurations on the atomic positions.

Figure 3.4 is another way to see the effect of the detuning for the on- and off-axis superradiant emissions, where  $\Gamma_{\text{sup}}$  is plotted for varying  $\Delta$  for two fixed directions, on- and off-axis. By detecting the emitted intensity in the forward direction for several  $\Delta$  (blue data), where the peak of the emission lobe is present, superradiance is present both on- and off-resonance ( $\Gamma_{\text{sup}}/\Gamma > 1$ ); however,  $\Gamma_{\text{sup}}$  is larger at  $\Delta \sim 0$  than at  $\Delta \neq 0$ . On the other hand, the off-axis detection (red data) presents superradiance only far from resonance, as discussed in Fig. 3.3. The superradiant decay rate drops when  $\Delta$  becomes close to zero. Superradiance is completely suppressed for  $\Delta \simeq 0$ .

Finally, Fig. 3.5 shows  $\Gamma_{\text{sup}}$  as a function of  $b_0$  and  $b(\Delta)$  for several detunings of the incoming laser beam, at  $\theta = 45^\circ$ . This figure is similar to what will be discussed in the experimental results. Close to resonance [i.e.,  $\Delta \sim 0$  for panel (a) or large  $b(\Delta)$  for panel (b)],  $\Gamma_{\text{sup}}/\Gamma < 1$  for all  $b_0$ , attesting radiation trapping.  $\Gamma_{\text{sup}}$  becomes smaller for increasing  $b_0$  and  $b(\Delta)$  (large  $b_0$  and  $b(\Delta)$  increase the amount of multiple scattering events in the medium). For large detunings [or small  $b(\Delta)$ ],  $\Gamma_{\text{sup}}$  starts to increase with  $b_0$ , so superradiance appears. The linear scaling becomes completely independent of  $\Delta$  from  $\Delta \gtrsim 3\Gamma$  and  $b(\Delta) \ll 1$ .

The conclusion of these numerical study is that, contrary to subradiance, superradiance is strongly dependent on the laser detuning and the detection direction. Far from resonance, it is present both in and out of the forward directions, but on resonance only the forward direction contains superradiant emission. Also, superradiance is stronger off-axis than on-axis. Indeed, off-axis superradiance was observed in our first subradiant data, and this was our motivation to perform detailed simulations and to observe it experimentally.

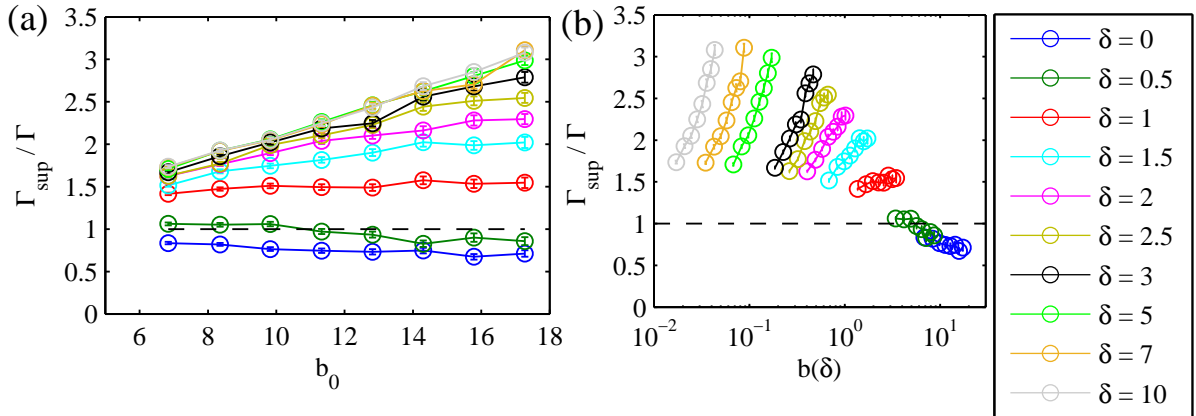


**Figure 3.5:** Superradiant decay rates  $\Gamma_{\text{sup}}$  as a function of **(a)** the resonant optical thickness  $b_0 = 3N/(k_0R)^2$  and **(b)** the optical thickness  $b(\delta) = b_0/(1 + 4\delta^2)$ , for several detunings  $\delta = \Delta/\Gamma$ . The values of  $\Gamma_{\text{sup}}$  were extracted from the intensity  $I(\theta, t)$  at  $\theta = 45^\circ$ . Parameters: same as in Fig. 2.3.

## 3.2 Experimental setup

The experimental setup for the superradiance experiment is the same as used for subradiance and it is described in section 2.2. We use a MOT of  $^{87}\text{Rb}$  atoms to produce the atomic sample, a sequence of laser pulses to excite the atoms and a hybrid photomultiplier (HPM) placed at an angle of  $\theta \approx 35^\circ$  from the incident probe beam to collect the emitted intensity. However, the setup for the probe beam was modified in order to accomplish the particular features of a superradiance experiment. In this section we describe the probe beam setup for superradiance.

### 3.2.1 Setup for the probe beam

For the subradiance experiment, as discussed in subsection 2.2.3, the probe beam setup was arranged in order to obtain a fast enough fall time and good extinction after its switch off, in order to observe a subradiant decay, which is late and small in amplitude. These conditions were accomplished with a setup of two AOMs in series where the laser beam is focused in the second AOM, which provides a fast fall time. The obtained extinction time was  $\sim 15$  ns. As Rb natural lifetime is  $\tau_0 = 26$  ns, we wish to measure  $\tau_{\text{sup}} < \tau_0$  as accurate as possible, so it is important to improve this extinction time in order to detect superradiance.

To do this, we decided to keep the AOM-focused-beam setup and, to improve this extinction time, we placed an electro-optic modulator (EOM) based on a Mach-Zehnder interferometer after the AOM output. In this type of EOM, the input beam is split in two paths, one to which a voltage is applied. A change in the voltage induces a phase shift for the beam passing through that path and, after the beams are recombined, the phase shift determines constructive or destructive interference for the recombined output beam.

The setup of both AOM and EOM is shown in Fig. 3.6. We used an EOM from EOspace, reference AZ-0K5-10-PFU-SFU-780. Also, the AOM and EOM are connected to a pulse generator from Stanford Research Systems, model DG535, which generates the

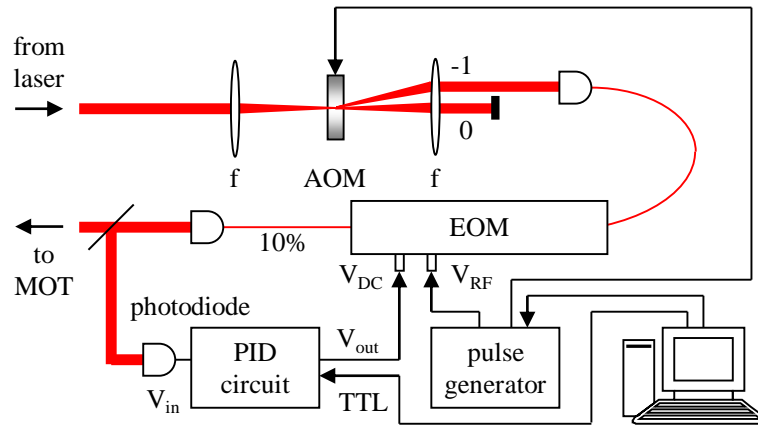


**Figure 3.6:** Setup for the probe beam for the superradiance experiment. An AOM and an EOM are set in series and controlled by the computer, pulse generator and a PID circuit. The laser beam between the two lenses is focused in the AOM. Its -1 order beam goes into the EOM.

pulse sequence. The voltage which induces the phase shift in the EOM is applied in the input  $V_{DC}$ , and its value is such as destructive interference takes place, making the EOM output to be minimum. As the output intensity might fluctuate due to drifts in the EOM itself, a PID circuit is set to stabilize the EOM emission in that minimum. Also, the EOM is placed in a box of polystyrene, in order to minimize thermal and mechanical vibrations.

The EOM  $V_{RF}$  input is connected to the pulse generator, which provides the pulse sequence for the EOM and also the AOM. The pulse sequence for both are the same and must be synchronized in the output in order to avoid delays between them. A TTL asks the PID circuit to hold its feedback during the measurements, and the computer controls the timing of the probe beam as follows: when the probe beam is on, the TTL turns on the  $V_{RF}$  input and  $V_{DC}$  is held, and then pulses are sent to the AOM and EOM. Emitted light is seen in the output, corresponding to the pulses amplitudes. When the probe beam is off, i.e., after the edge of each pulse, the TTL turns off the  $V_{RF}$  input and  $V_{DC}$  makes the extinction faster because of the destructive interference which takes place in the EOM. The EOM output beam goes to the MOT chamber to excite the atoms and the emitted fluorescence is collected by the HPM (see Fig. 2.9).

Figure 3.7 shows the pulses extinction after the EOM output, with and without the cold atoms in the MOT chamber. Both curves were recorded with the HPM. The curve without atoms (black) was recorded by placing a white paper after the MOT chamber to scatter the light to the HPM. It shows the pulse profile after it is extinguished. We observe a fast decay of  $\sim 1.5 - 2.0$  ns, measured from an exponential fit in amplitude between 10% and 90% of the maximum intensity. The fast decay is followed by an irregular profile due to the AOM response. The curve with atoms (red) is the emitted fluorescence for  $b_0 = 3N/(k_0R)^2 = 19$  and  $\Delta = -6\Gamma$ . Compared to the single atom decay (dashed line), the fluorescence decay is faster, i.e., off-axis superradiance.

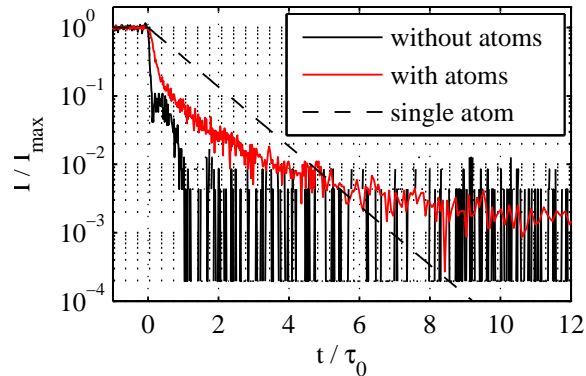


**Figure 3.7:** Probe beam extinction (black) and atomic fluorescence (red) for  $b_0 = 3N/(k_0R)^2 = 19$  and  $\Delta = -6\Gamma$ , measured by the HPM, after the probe beam setup for superradiance. The black dashed line is the single-atom decay. All data are normalized by their steady value.

### 3.3 Experimental results

From the experimental setup for the probe beam described in the last section, we can perform measurements on superradiance. The experimental procedure for preparing the sample and acquiring the data is the same as used for subradiance (see subsection 2.2.4): the MOT is loaded including a dark MOT and optical pumping phases, and then it is turned off, yielding to the cloud expansion. During the cloud expansion, a sequence of 12 pulses is sent and the emitted fluorescence is collected by the HPM. Each pulse has a duration of  $30 \mu\text{s}$  and separation  $1.0 \text{ ms}$ . The cloud expansion allows to vary  $b_0$  for each pulse, for a fixed saturation parameter  $s(\Delta)$  of the probe beam (fixed detuning  $\Delta$  and intensity  $I$ ). After the data acquisition, a calibration procedure is run (see subsection 2.2.7) in order to measure  $b_0$  for each pulse and the cloud temperature.

The first measured data showed no superradiance due to a large amount of background vapor light in the measured intensity. Hence, we decided to close completely the Rb valve of the vacuum system, in order to decrease the vapor amount. This is because the valve closure causes an immediate drop in the vapor pressure and an increase in the MOT loading time, but the atom number  $N$  and consequently  $b_0$  take some time to start to decrease. At the same time, the setup of the probe beam had to be checked, so  $b_0$  dropped significantly after some days, which led us to open again the valve by  $1/2$  of a turn. Then we waited four weeks for the stabilization and measurements.

#### 3.3.1 Fit procedure

Our method to extract  $\Gamma_{\text{sup}}$  from the experimental detected fluorescence is the same as in the simulations, i.e., an exponential fit just after the switch off, where the faster decay is observed. In the simulations, the fit range was set to be  $t \in [0, 0.2] \tau_0$ . However, in the experiment, the measured intensity does not contain only the emitted light from the atoms: as already mentioned in Chapter 2, in fact it is a sum of the fluorescence due to the cold atoms, light from the background vapor in the MOT vacuum chamber and scattered light due to the chamber walls.

Assuming that each fluorescence and the scattered light from the windows have a

characteristic decay rate after the probe beam extinction, we can write the measured fluorescence as

$$I(t) = A_s e^{-\Gamma_{\text{sup}} t} + A_v e^{-\Gamma t} + A_w e^{-\Gamma_{\text{ext}} t} \quad (3.1)$$

where  $\Gamma_{\text{sup}}$  is the superradiant decay rate we want to extract;  $\Gamma$  is the vapor decay rate, which decays as a single atom; and  $\Gamma_{\text{ext}} = 1/\tau_{\text{ext}}$ ,  $\tau_{\text{ext}} = 1.5 - 2.0$  ns, is the decay of the scattered light, which is the extinction time from the AOM and EOM setup. We measure values of  $\Gamma_{\text{sup}}$  such as  $\Gamma_{\text{ext}} > \Gamma_{\text{sup}} > \Gamma$ , which implies that the decay of  $I(t)$  is firstly governed by the EOM extinction, then by the superradiant decay and then by the background vapor decay. Also, the amplitudes  $A_s$ ,  $A_v$  and  $A_w$  determine the amount of vapor and windows scattered light in the total signal.

Each one of three amplitudes in Eq. 3.1 can be measured experimentally as follows. As a fluorescence signal without atoms is recorded during the calibration procedure (see subsection 2.2.7), it contains the scattered light only from the vapor and chamber walls, i.e.,

$$I_{\text{wo}}(t) = A_v e^{-\Gamma t} + A_w e^{-\Gamma_{\text{ext}} t} \quad (3.2)$$

so the ratio between the pulse amplitudes of  $I_{\text{wo}}(t)$  and  $I(t)$  gives  $I_{\text{wo}}(t=0)/I(t=0) = (A_v + A_w)/(A_s + A_v + A_w)$ , i.e., the amount of vapor and windows light together in the main signal. Then, by recording  $I_{\text{wo}}(t)$  at resonance (probe beam detuning  $\Delta = 0$ ) and far from resonance (by delocking the laser source and setting it very far from the Rb spectrum, which gives a frequency of some GHz), one can measure the contribution from the vapor and windows separately in  $I_{\text{wo}}(t)$ : the pulses amplitudes from the resonant  $I_{\text{wo}}(t)$  has both contributions, i.e.,  $A_v + A_w$ , and the pulses amplitudes from the detuned  $I_{\text{wo}}(t)$  contain only the scattered light from the windows, i.e.,  $A_w$ . The ratio  $A_w/(A_v + A_w)$  gives the amount of light from the windows and from it, as  $A_v + A_w = 1$ , we can determine  $A_v$ .

We observed that 70% of the total scattered stray light comes from the chamber windows and 30% comes from the Rb vapor. On the other hand, the ratio between the amplitudes for the fluorescence with and without atoms depends on the probe beam detuning and varies for each pulse.

In order to define a fit range to extract the superradiance decay rates  $\Gamma_{\text{sup}}$ , we considered the following analysis procedures:

- The subtraction of the signals with and without atoms, i.e.,  $S(t) = I(t) - I_{\text{wo}}(t) \propto e^{-\Gamma_{\text{sup}} t}$ . This gives a clear exponential decay, where an exponential fit can be done;
- An alternative fit method which consists in choosing a range fit of  $I(t)$  where the decays  $\Gamma_{\text{ext}}$  and  $\Gamma$ , from the windows and vapor, respectively, can be neglected. Hence, in this range the exponential fit gives  $\Gamma_{\text{sup}}$ .

The disadvantage of the subtraction method is the noise introduced when subtracting  $I_{\text{wo}}(t)$  from  $I(t)$ , specially for the data at large detunings, where we run out of enough probe beam intensity due to the alignment of the double-pass AOM. On the other hand,

as  $\Gamma_{\text{ext}} > \Gamma_{\text{sup}} > \Gamma$  in Eq. 3.1 and as the amplitudes  $A_s$ ,  $A_v$  and  $A_w$  can be determined, we use the alternative fit method where the fit range  $I(t)$  was set as follows:

- *The fit range starts at  $t/\tau_0 = 0.1$ .* The scattered light by the windows MOT chamber is the first one to decay, and becomes negligible when its amplitude decays to  $\sim 10\%$  of this initial value. Thus,  $0.10 I(t) = I(t) e^{-\Gamma_{\text{ext}} t}$ , which yields to  $t = -\ln(0.10) \tau_{\text{ext}} \approx 0.13 \tau_0 \approx 0.1 \tau_0$ . Therefore, for  $t \geq 0.1 \tau_0$  in the detected intensity, there is no more contribution from scattered light by the windows.
- *The fit range ends when the amplitude of  $I(t)$  decays to 20% of its initial value or when the vapor scattered light starts to contribute.* The 20% value comes from the standard definitions of fall time (pulse decay time), which is the time of decay of a signal calculated when its amplitudes decays from 80% to 20% (or from 90% to 10%) of its initial value. However, the vapor contribution in  $I(t)$  might be important earlier (the vapor decay follows the superradiant decay and has rate  $\Gamma$ ). By measuring the ratio between the pulse amplitudes  $I_{\text{wo}}(t)$  and  $I(t)$  for each pulse, and by multiplying it by 0.30, since 30% comes from the Rb vapor, we get the amplitude in  $I(t)$  where the vapor decay starts to dominate. This value is compared to the 20% value and the fit range goes until the larger one.

In addition, we discard the fit results where the number of points in the fit range is ten or when the statistical goodness of the fit  $R^2$  is smaller than 0.85. In the following, we present and discuss the experimental results.

### 3.3.2 Superradiant decay rates *versus* $b_0$

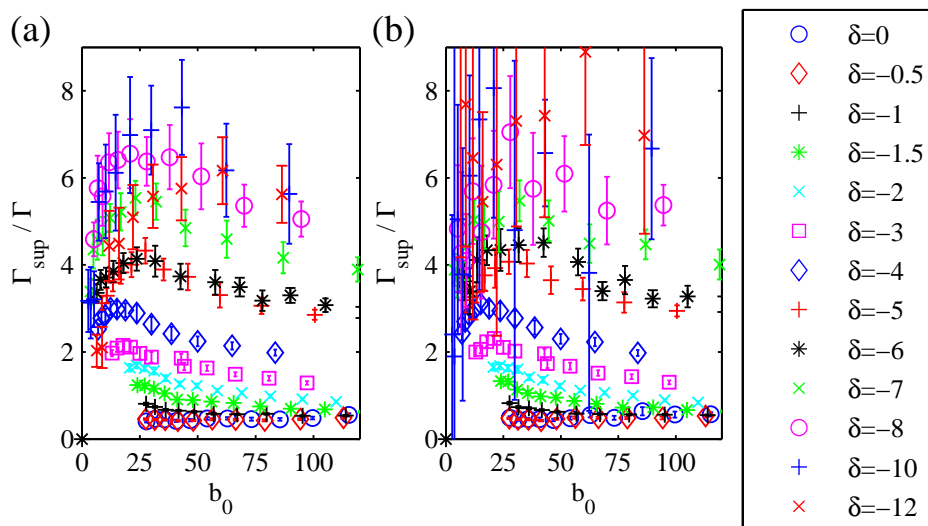


**Figure 3.8:** Experimental superradiant decay rates  $\Gamma_{\text{sup}}$  as a function of  $b_0 = 3N/(k_0 R_x)(k_0 R_y)$  for several detunings  $\delta = \Delta/\Gamma$ , extracted from an exponential fit from (a) the fit range method and (b) from the subtraction method.

After the acquisition of the data and after checking the measured temperatures and saturation parameter, we obtained the values  $T \simeq 50 \mu\text{K}$  (same for the subradiance data) and  $s = (2.2 \pm 0.6) \times 10^{-2}$ , which assures the linear optics regime. Fig. 3.8 is the

comparison between the two fit methods discussed in the previous subsection. Panel (a) shows  $\Gamma_{\text{sup}}$  extracted from the fit range method, whereas panel (b) displays  $\Gamma_{\text{sup}}$  extracted from the subtracted intensities with and without atoms. For low  $\Delta$ , we see similar values of  $\Gamma_{\text{sup}}$ . However, for large  $\Delta$ , the data from the subtraction method contain large errorbars. This is because for large detunings we need more intensity in the probe beam to balance the saturation parameter  $s(\Delta)$ , and our tapered amplifier (TA) does not provide it. Hence, the signal resulted from the subtraction is noisy. The conclusion is that the fit range method is satisfactory for our data analysis, leading to reliable values.

Figure 3.9(a) shows the same data as in Fig. 3.8(a) where the data at  $\delta = -8$ ,  $\delta = -10$  and  $\delta = -12$  were removed. This is because, due to the low intensity available in our probe beam for large detunings, those data yield to smaller values of the saturation parameter compared to the ones obtained for the other detunings.<sup>1</sup> Fig. 3.9(b) are the same  $\Gamma_{\text{sup}}$  in (a) but plotted as a function of  $b(\Delta) = b_0/(1 + 4\Delta^2/\Gamma^2)$ . the optical thickness of the cloud.

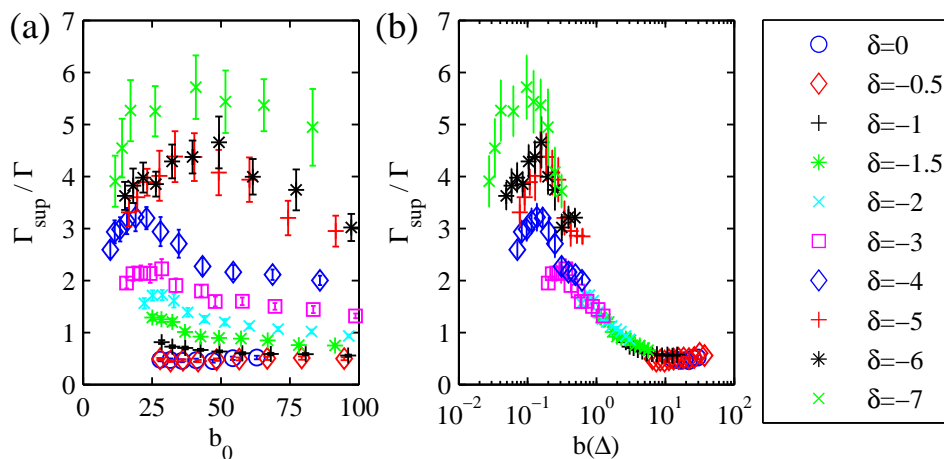


**Figure 3.9:** Experimental superradiant decay rates  $\Gamma_{\text{sup}}$  as a function of **(a)**  $b_0 = 3N/(k_0R_x)(k_0R_y)$  and **(b)**  $b(\delta) = b_0/(1 + 4\delta^2)$ , for several detunings  $\delta = \Delta/\Gamma$ .

We see that the measured  $\Gamma_{\text{sup}}$  increases with  $b_0$  for small  $b_0$  ( $b_0 \lesssim 20$ ) and large  $\delta$ , up to  $\Gamma_{\text{sup}}/\Gamma \sim 5 - 6$ , which is a significant measurement of  $\Gamma_{\text{sup}}$  for an off-axis direction. Also,  $\Gamma_{\text{sup}}$  do not collapse into a single curve as seen for subradiance [c.f. Fig. 2.18(a)], showing that superradiance is more sensitive to the detuning than subradiance. Indeed, for  $b(\Delta) > 0.1$ ,  $\Gamma_{\text{sup}}$  starts to decrease. This is a clear signature of *multiple scattering*, i.e., the photon is scattered more than one time before leaving the cloud. The superradiance appears for low  $b(\Delta)$ , showing that in this regime the scattering is predominantly single scattering. For  $\delta \sim 0$ , we see clearly that  $\Gamma_{\text{sup}}/\Gamma < 1$ , i.e., superradiance is suppressed at resonance.

### 3.3.3 Superradiant decay rates *versus* laser intensity

In analogy to what was done for subradiance, we performed measurements by changing the saturation parameter in order to check the validity of the prediction from the coupled-

<sup>1</sup> Indeed, since we are in the linear optics regime,  $\Gamma_{\text{sup}}$  does not depend on  $s(\Delta)$  (to be discussed in the next sub-subsection). Hence, no need to remove the data for large detuning.

dipole model that  $\Gamma_{\text{sup}}$  should not depend on  $s(\Delta)$  for  $s(\Delta) \ll 1$ . Fig. 3.10 shows the result of this measurement, for constant  $b_0$ . The saturation parameter was varied by changing the intensity of the probe beam for a fixed  $\Delta$ .  $\Gamma_{\text{sup}}$  practically does not change with  $s(\Delta)$  in the errorbars limit, which validates our measurements in the linear optics regime.

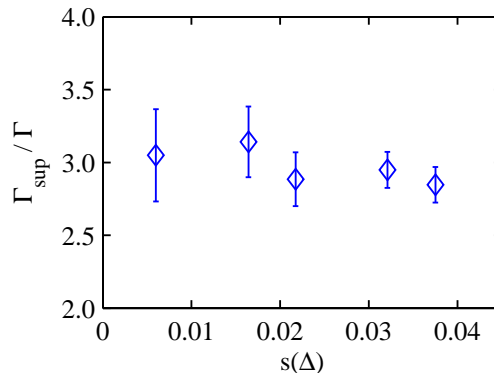


**Figure 3.10:** Experimental superradiant decay rates  $\Gamma_{\text{sup}}$  as a function of  $s(\Delta)$ , for  $b_0 = 3N/(k_0 R_x)(k_0 R_y) = 21 \pm 1$  and  $\Delta = -4\Gamma$ .

### 3.3.4 Superradiant decay rates for small $b_0$

As discussed in the previous subsection, we detected successfully superradiance *versus*  $b_0$  with a magnitude of  $\Gamma_{\text{sup}} = 5 - 6\Gamma$ . However, we decided to take more measurements in order to have more data for small  $b_0$  at resonance and to see  $\Gamma_{\text{sup}}$  tending to  $\Gamma$  for the far-detuned data.

In order to decrease  $b_0$  in the data acquisition procedure, we opted to decrease the MOT loading time. A small  $b_0$  implies a decrease of the measured intensity, which may decrease the signal-to-noise ratio when compared to the stray light. However, the obtained  $\Gamma_{\text{sup}}$  showed to be good due to their small errorbars. There are some ways to reduce the amount of stray light, like to close (partially or totally) the Rb valve in our vacuum system, and to use an iris to slightly decrease the probe beam waist. The former was not done because it takes a considerable time for stabilization, and the latter suppressed superradiance.

Figure 3.11 shows the measured  $\Gamma_{\text{sup}}$  for small  $b_0$ , for some detunings  $\delta = \Delta/\Gamma$ . We see that  $\Gamma_{\text{sup}}$  for  $\delta = -8, -10$  and  $-12$  seem to tend to  $\Gamma$ , but with large errorbars, which may be a noise effect. For the other detunings, the same discussion for Fig. 3.9 applies, i.e., multiple scattering for large  $b_0$ .

## 3.4 Conclusions of this chapter

We were able to observe superradiance for a large cloud of cold atoms out of the incident laser beam direction. We measure increasing superradiant decay rates with  $b_0$ . The experimental results are in agreement with the theory of coupled dipoles. The main results obtained are a theoretical scaling of the superradiant decay rates with the resonant optical thickness of the atomic cloud, the suppression of superradiance at resonance due

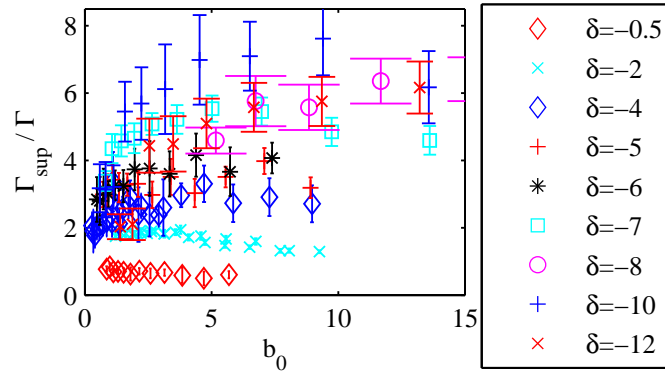


**Figure 3.11:** Experimental superradiant decay rates as function of  $b_0 = 3N/(k_0R)^2$ , for several detunings  $\delta = \Delta/\Gamma$ .

to multiple scattering, and larger superradiant decay rates for off-axis than on-axis. As a last comment, a similar experiment on superradiance was performed at the same year as ours in M. Havey's group on on-axis superradiance and detection of the cooperative Lamb shift [Roof 2016].

When presenting and discussing the results on subradiance and superradiance, we have found that at resonance multiple scattering is present. Superradiance is suppressed by multiple scattering, but subradiance is more robust. As both subradiant and multiple scattering decays take place at late times, we decided to study closely the interplay between subradiance and radiation trapping. This is the subject of the next chapter.



## Radiation trapping and subradiance

In the last chapters, we discussed the interaction of an atomic sample with a monochromatic plane wave by means of the coupled-dipole model. Cooperative effects like super- and subradiance were predicted by the coupled-dipole equations in the far-detuned field regime and were studied theoretically and experimentally. Whereas superradiance is a fast decay due to constructive interference, subradiance is the trapping of some remaining light due to destructive interference, emitted at late times.

In the particular case of the incident laser beam at resonance, the light may be multiply scattered in the medium, which characterizes radiation trapping, discussed briefly in the end of Chapter 2. Contrary to subradiance, which is a coherent effect due to destructive interference between the scattered light, radiation trapping is incoherent, i.e., the light imprisonment is due to the random walk performed by the photon. Radiation trapping was studied initially in hot vapors ( [Holstein 1947] and references therein), where Doppler and/or collisional broadening are taken into account because of the high temperature of the atomic samples. However, with the advent of laser cooling and cold atoms in the 1980 – 1990s, radiation trapping could be observed experimentally in a setup with a narrow beam exciting a cloud of cold atoms, firstly by [Fioretti 1998] and then by [Labeyrie 2003, Labeyrie 2005]. Its main features are its strong dependency with the detuning of the incident field and the temperature of the sample, even if it is in order of few  $\mu\text{K}$ . Radiation trapping is strong for high optical thickness and negligible far from resonance. Concerning super- and subradiance at resonance, and taking into account that the experimental setup discussed up to here is a plane wave exciting the atoms, we discussed in Chapters 2 and 3 that superradiance is suppressed at off-axis directions, but subradiance is robust: we showed with simulations that our observed late decay rates are indeed subradiance, and not radiation trapping.

In this chapter, we analyze in detail the slow and late trapping of light in cold atoms, in order to see the interplay between radiation trapping and subradiance. Our starting point is the experiment with a narrow and resonant beam exciting the atoms described in [Labeyrie 2003], but in our setup we can go to much lower amplitudes in the detected emitted intensity and we have the coupled-dipole model to take into account the interference between the scattered fields. As we will discuss, the key idea is to see where one phenomenon changes to the other phenomenon, by using as reference their dependence with the parameters of the system, like the detuning, optical thickness and temperature.

This chapter is divided in six sections. In section 4.1, we present the standard theory for radiation trapping in cold atoms, based on the *random walk and diffusion model*. It will be discussed the ideal case of no atomic motion and the real case treated in experiments. In sections 4.2 and 4.3, we discuss numerical simulations with the narrow beam setup, as well as the results obtained from the random walk model (incoherent) and the coupled-dipole model (coherent). In section 4.4, we present the modifications in our experimental setup in order to observe radiation trapping and subradiance, and in section 4.5 the obtained experimental results are presented and discussed. Finally, in section 4.6 we summarize the main conclusions.

## 4.1 Radiation trapping in cold atoms

### 4.1.1 Overview

Our current physical system consists in a medium modeled by a set of  $N$  identical two-level atoms at rest which interacts with a light beam modeled by a monochromatic electric field. We are in the *wave picture* (or semi-classical picture), since the light is described by a wave field. This allows us to take into account the interference between the fields scattered by each atom, during the scattering process, for single and multiple scattering. Therefore, the coupled-dipole model allows the description of the phenomena related with interference, like speckles, the emission lobe in the forward direction, coherent backscattering, Anderson localization, and the already discussed super- and subradiance.

Despite of this wave picture, maybe the most naive idea about propagation of light in a medium is the *corpuscular picture*, where the light is modeled as a punch of photons which are scattered by the atoms (Fig. 4.1). In each scattering event, the photon is absorbed (from the bottom level to an upper excited level) and then emitted by spontaneous emission (decay from the excited level to a lower level), in such a way that the photon is emitted in a random direction with a certain frequency  $\omega'$  and travels a distance  $x$  called *step size* before being absorbed by another atom. After  $N_{\text{diff}}$  scattering events, the photon leaves the medium in a certain direction and with a final frequency, and the time scale associated with the propagation is related to the time that the photon spent in the medium when performing the scattering.

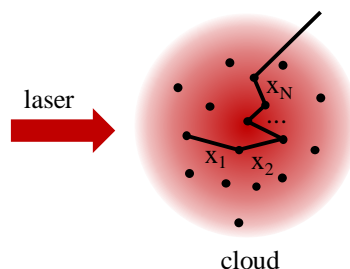


**Figure 4.1:** The physical mechanism for radiation trapping. A laser beam hits a medium modeled as a cloud of cold atoms at random positions. The distances  $x_1, x_2, \dots, x_N$  are the step sizes traveled by the photon between each scattering event.

The light scattering is thus seen as a sequence of collisions between the photons and the atoms, so the interference effects due to the scattered field are neglected. This light

scattering is called *multiple scattering* and explains the light propagation in fog, clouds, milk, etc. In the specific case where the photon frequency is close to the atomic resonance frequency, the multiple scattering is referred as *radiation trapping* and takes place in stars, light bulbs and gases.

Historically, initial description considered radiation trapping as a random walk described by a Brownian motion and diffusion, with constant attenuation coefficient [Compton 1922] and constant mean free path [Milne 1926]. Later, by restricting the problem to hot vapors with Doppler broadening, C. Kenty showed that the diffusion equation is not appropriate for a description of the photon propagation [Kenty 1932], so T. Holstein proposed a description with an integral equation [Holstein 1947]. He showed that, for a slab geometry with Doppler broadening, the emitted intensity  $I(t)$  in the steady state is a sum of exponentials  $I(t) \propto \sum_n \exp(-t/\tau_n)$  such that, at late times,  $I(t) \rightarrow \exp(-t/\tau_{\text{RT}})$ , where the radiation trapping decay rate  $\tau_{\text{RT}}$  is proportional to  $\tau_{\text{RT}} \propto b \sqrt{\ln(b/2)}$ ,  $b$  being the optical thickness of the sample. In cold atoms, the pioneering experiment was carried out by A. Fioretti *et al.* with Cs atoms [Fioretti 1998], but G. Labeyrie and collaborators showed that, in a experiment with narrow beam in a  $^{85}\text{Rb}$  cloud,  $\tau_{\text{RT}}$  scales with  $b^2$  for zero temperature and is slightly modified due to the low temperature in cold samples [Labeyrie 2003]. The scaling  $\tau_{\text{RT}} \propto b^2$  for cold atoms was calculated from a theory of elastic multiple scattering [Legendijk 1996, van Rossum 1999] adapted for cold atoms [Müller 2002]. Temperature effects and frequency redistribution in radiation trapping in cold atoms were observed in more detail in [Labeyrie 2005]. Later, R. Pierrat *et al.* proposed an integral equation description for low temperatures [Pierrat 2009].

The radiation trapping depends on the parameters of the medium and light. In atomic physics experiments, the light source is a coherent laser beam and the scattering media is a vapor, where the atoms move at low velocities (cold atoms) or high velocities (hot vapors). Some of the main regimes and features of radiation trapping are discussed below:

- *Macroscopic, mesoscopic and microscopic regimes.* The light scattering can be characterized by the mean free path  $l = \langle x \rangle$ , which is the average of all step sizes  $x$  during the scattering. The relation between  $l$  and the medium dimensions  $L$  determine the scattering regime [van Rossum 1999]. If  $l \ll L$ , we are in the macroscopic regime and the scattered intensity obeys the diffusion equation. If  $l \sim L$ , we are in the mesoscopic regime and the problem is described by the radiative transfer equation. If  $l \gg L$ , we are in the microscopic regime and the scattering is described by the quantum mechanics formalism, with scattering matrices, Born approximation and the Bethe-Salpeter equation.
- *Geometry of the medium.* Many works consider the medium as a slab of finite thickness and large transverse dimensions, in a such way that the photon, when leaving the medium, is emitted either at the same side of the incident light beam (diffuse reflection) or at the opposite side of the incident light (diffuse transmission). However, cold atoms experiments are generally carried out in anisotropic and quasi-spherical atomic clouds [Fioretti 1998, Labeyrie 2003, Labeyrie 2005]. It is shown in [Labeyrie 2004] that the diffuse transmission by a cloud of cold atoms excited by a narrow beam, detected close to the forward and backscatter directions, is analog

to, respectively, the diffuse transmission and diffuse reflection obtained in a slab geometry.

- *Atomic motion in the medium.* The atoms move in gaseous media like clouds of cold atoms or hot vapors. Hence, after each scattering event, the photon has a frequency which depends on the velocity of the atom. This phenomenon is called *frequency redistribution*, since the frequency is shifted for every scattering event due to the Doppler effect. In addition to the velocity, the frequency redistribution depends also on the collisions between the atoms, the atom lineshape and the spectrum of the incident photon (which is not monochromatic in experiments), as well as the number of scattering events (the more the photon is scattered, the more the frequency is shifted). For cold atoms, partial frequency redistribution occurs, due to the small temperatures in these samples [Labeyrie 2003, Labeyrie 2005, Pierrat 2009]. For hot atoms, complete frequency redistribution occurs [Holstein 1947] and the output photon frequency is completely uncorrelated from its initial value. The frequency redistribution can modify the photon step size distribution, from the standard exponential distribution to a Lévy distribution, also called Lévy flights of photons [Pereira 2004, Mercadier 2009, Chevrollier 2012].
- *Light beam size.* The ideal situation is to consider the incident photons as a beam of negligible size compared with the medium dimensions. This assures that the photons will suffer a high number of scattering events, instead of single scattering (one scattering event) which could take place at the borders of the medium. In [Labeyrie 2003], the laser beam size has a waist of 2 – 3 times smaller compared with the cloud size. Our experiment described in this chapter used a beam size of 4 – 5 times smaller than the cloud size. However, simulations with a large beam (infinite beam size) exciting the atoms was also considered [Chabé 2014].
- *Light spectrum.* No source of light is perfectly monochromatic, which means that the incoming photons have different frequencies. As the medium absorption coefficient depends on the light frequency, each incident photon will be scattered differently and the features of the output light might contain frequency redistribution. The spectrum of the incident photon may be the spectrum of the laser source itself, of a Doppler spectrum, which can be achieved if the output of a primary hot vapor cell is used to excite the main sample [Mercadier 2009].

## 4.1.2 Theory

We start by restricting the discussion to the most simplified possible case: two-level atoms at rest, and interaction with a monochromatic and infinitely narrow light beam. Also, we do not consider coherence, degeneracy, and inelastic scattering. The atoms are modeled as pure two-level systems, as before; however, here the light is modeled as a beam of photons. Under these assumptions, we have the *theory of multiple elastic scattering by resonant point scatterers* [Lagendijk 1996, van Rossum 1999, Müller 2002] for the description of radiation trapping in cold atoms.

To fix the ideas, we assume the physical system as follows:

- *Atoms*: a set of  $N$  motionless two-level systems, distributed in random positions  $\vec{r}_j$ ,  $j = 1, \dots, N$ , with two non-degenerate states  $|g_j\rangle$  and  $|e_j\rangle$ , resonance frequency  $\omega_0$ , natural decay rate  $\Gamma$ , natural lifetime  $\tau_0 = 1/\Gamma$  and natural Lorentzian lineshape  $f_L(\Delta) \propto 1/(1+4\Delta^2/\Gamma^2)$ . The geometry of the atomic sample is a sphere of Gaussian density and RMS size  $R$ , and it is characterized by a density  $n_0\lambda^3$ , resonant optical thickness  $b_0$  and optical thickness  $b(\Delta)$  defined by Eqs. 1.39, 1.41 and 1.43, respectively. Also, the cloud is dilute, i.e.,  $n_0\lambda^3 \ll 1$ , and characterized by a attenuation coefficient  $\alpha(\Delta)$ .
- *Light*: a set of  $N$  monochromatic photons with frequency  $\omega$  and detuning  $\Delta = \omega - \omega_0$ , such as  $\omega$  is close to  $\omega_0$  in order to have frequency dependence. Thus, the scattering is *resonant* and *multiple*, i.e., the photon undergoes several scattering events before leaving the cloud. The incident photons travel along an axis which passes through the cloud center of mass (see Fig. 4.1). The light beam has no transverse size, i.e., it is infinitely narrow, and has weak intensity, i.e., saturation parameter  $s(\Delta) \ll 1$ , to restrict the problem to linear optics. In these conditions *elastic scattering* occurs [Cohen-Tannoudji 1992], i.e., the frequency  $\omega'$  of the scattered photon is equal to the frequency  $\omega$  of the incident photon, so  $\omega' = \omega$ . There is no frequency redistribution. Also, the atoms are *point-like*, i.e., the effect of the atomic size during the scattering is neglected.

### Random walk and diffusion equation

When penetrating into the medium, the photon travels a distance  $x$ , and the incoming intensity  $I(x)$  is attenuated according to the Beer-Lambert law:

$$I(x) = I_0 e^{-b(\Delta)} = I_0 e^{-\alpha(\Delta)x} \quad (4.1)$$

where  $\alpha(\Delta) = 1/l(\Delta)$  [Rogers 2008] with  $l = \langle x \rangle$  the mean free path.

The Beer-Lambert law can be seen as a probability distribution for the photon step size, since each photon travels a distance  $x$ ,  $x \in (0, \infty)$ , before being absorbed, and the absorption depends on  $\Delta$ . Hence, the probability  $P(x)$  of the photon travels a certain distance  $x$  before being absorbed by an atom is

$$P(x) = \frac{1}{l} e^{-x/l} \quad (4.2)$$

On the other hand, as the photon emission is random, and as absorption and spontaneous emission occur several times, the photon performs a *random walk*. It can be shown that, in the one-dimensional case, the probability density function  $p(x, t)$  of the photon to be at a position  $x + dx$  at a time  $t + dt$ , where  $p(x, t)$  may be, e.g., the energy distribution or intensity distribution in the medium, obeys the equation

$$\frac{\partial p}{\partial t} = \frac{\langle x^2 \rangle}{2\tau} \frac{\partial^2 p}{\partial x^2} \quad (4.3)$$

for a homogeneous medium, where  $\tau$  is the time interval between two scattering events

and  $\langle x^2 \rangle$  is the mean square value of  $x$ . Eq. 4.3 is the *diffusion equation* [Butkov 1968], with diffusion coefficient

$$D = \frac{\langle x^2 \rangle}{2\tau} \quad (4.4)$$

The quantity  $\langle x^2 \rangle$  is defined by  $\langle x^2 \rangle = \int x^2 P(x) dx$ , where  $P(x)$  is the probability distribution of the step size. For  $P(x)$  given by Eq. 4.2, we obtain  $\langle x^2 \rangle = 2l^2$ . Also, by definition,  $\langle x \rangle = \int x P(x) dx$ , and  $\langle x \rangle = l$  for  $P(x)$  defined by Eq. 4.2.

The generalization for three dimensions gives  $p(x, t) \rightarrow p(\vec{r}, t)$  and Eq. 4.3 as

$$\frac{\partial p}{\partial t} = D \nabla^2 p \quad (4.5)$$

for a homogeneous medium. For a non-homogeneous medium,  $D = D(\vec{r})$  and

$$\frac{\partial p}{\partial t} = \nabla \cdot (D \nabla p) \quad (4.6)$$

Also, in three dimensions, Eq. 4.4 reads

$$D = \frac{l^2}{3\tau} \quad (4.7)$$

In addition, the solutions  $p(\vec{r}, t)$  of the diffusion equation are Gaussian functions and from it one can show that

$$\langle r^2 \rangle \propto 6Dt \quad (4.8)$$

where  $r = |\vec{r}|$ , i.e., the mean squared distance traveled by the photon is proportional to the traveled time  $t$ .

### Transport time and number of scattering events

As already mentioned, the time  $\tau$  is the time interval between two scattering events. It is called *transport time* and can be written as

$$\tau = \tau_W + \tau_{sc} \quad (4.9)$$

i.e., the sum of the interaction time  $\tau_W$ , called Wigner time, plus the photon propagation time  $\tau_{sc}$ . It can be shown that  $\tau_W \approx \tau_0$  [Weiss 2018], i.e., the interaction time is equal to the atomic lifetime  $\tau_0$ , and  $\tau_{sc} = l/v_g$ , where  $v_g$  is the group velocity, such as  $\tau_0 \gg l/v_g$ . Hence, the transport time is equal to

$$\tau \approx \tau_0 \quad (4.10)$$

in the diffusion equation.

If the photon is scattered  $N_{\text{diff}}$  times before leaving the cloud, its total time  $\tau_{\text{RT}}$  spent in the medium is

$$\tau_{\text{RT}} \simeq N_{\text{diff}} \tau_0 \quad (4.11)$$

In order to find the value of  $N_{\text{diff}}$ , we rewrite Eq. 4.11 as follows: since  $\tau_{\text{RT}}$  is the time scale that the photon spent in the cloud, we have  $\tau_{\text{RT}} \sim \langle r^2 \rangle / 6D$  from Eq. 4.8. The quantity  $\langle r^2 \rangle$  is in the order of the squared of the medium size  $R$ , so  $\langle r^2 \rangle \sim R^2$ , and  $D = l^2 / (3\tau_0)$  from Eqs. 4.7 and 4.10, so we obtain  $\tau_{\text{RT}} \sim (R^2 / l^2) \tau_0$ . By comparing this latter with Eq. 4.11, we have  $N_{\text{diff}} \propto (R/l)^2$ , and  $R/l \propto b(\Delta)$  from the Beer-Lambert law Eq. 4.1, because  $b = \alpha x \sim \alpha R = R/l$ , since  $x$  is in the order of the cloud size. Therefore,

$$\frac{\tau_{\text{RT}}}{\tau_0} \propto b(\Delta)^2 \quad (4.12)$$

i.e., the number of scattering events is proportional to the square of the optical thickness of the medium. The exact calculation gives [Labeyrie 2003]

$$\frac{\tau_{\text{RT}}}{\tau_0} \simeq \frac{3}{a\pi^2} b(\Delta)^2 \quad (4.13)$$

where  $a$  is a proportionality constant which depends on the geometry and density of the atomic sample. For a slab,  $a = 1$ . For a homogeneous sphere,  $a = 4$ . For a sphere with Gaussian density (our case), we have  $a = 5.35$ , so

$$\frac{\tau_{\text{RT}}}{\tau_0} \simeq \frac{3}{5.35\pi^2} b(\Delta)^2 \simeq 0.0568 b(\Delta)^2 \quad (4.14)$$

### Atomic motion

The result obtained in the last subsection for  $\tau_{\text{RT}}$  corresponds to the ideal case where the atoms do not move and the incoming field is monochromatic. This means that no redistribution frequency occurs. However, in experiments the light source is not monochromatic and even a sample of cold atoms has a Doppler motion which can influence the scattering.

The detuning  $\Delta'$  seen by the photon due to the atomic motion is equal to [Foot 2005]

$$\Delta' = \Delta - k_0 v \quad (4.15)$$

where  $k_0 = |\vec{k}_0|$  is the wave vector magnitude of the incoming light and  $v$  is the atomic velocity component in the direction of the photon, so the quantity  $k_0 v$  determines the amount of frequency redistribution that the photon will suffer. If

$$b(\Delta) k_0 v \ll \Gamma \quad (4.16)$$

we have partial frequency redistribution [Pierrat 2009], e.g., in cold atoms. If  $b(\Delta) k_0 v \gg \Gamma$ , total redistribution occurs, e.g., hot vapors.

The time  $\tau_{\text{RT}}$  can be measured from the intensity emitted by the cloud after the light-atoms interaction reaches a steady state and the incoming field is switched off, exactly as done when searching super- and subradiance signatures. This is indeed done

in [Labeyrie 2003], where radiation trapping was observed for a resonant laser beam in a cloud of cold atoms of  $^{85}\text{Rb}$ , for an incoming beam of diameter 2–3 times smaller than the cloud RMS diameter. The values of  $\tau_{\text{RT}}$  were extracted by exponential fits in the interval  $I(t)/I(0) \in [10^{-2}, 10^{-1}]$ , i.e., at amplitudes  $\sim 10^{-2}$  from the normalized emitted intensity. It was found that the quadratic law Eq. 4.14 breaks due to the cloud temperature, in order of  $\sim 80 \mu\text{K}$  [Labeyrie 2005], so simulations were performed to take into account the atomic velocities and to compare with the experimental data. The comparison between the experimental data and the simulations with frequency redistribution was successful.

## 4.2 Simulation methods with the small beam setup

The random walk and coupled-dipole models describe the propagation of light in a disordered medium, with the single difference that the random walk model neglects the interference in the scattering. On the other hand, the coupled-dipole model takes into account the coherence and interference between the atoms and the scattered field, and at resonance it describes a *coherent multiple scattering*, whereas the random walk model describes an *incoherent multiple scattering* [Chabé 2014]. As our setup here is a cloud excited by a narrow laser beam, it is important to run simulations with both models, in order to investigate radiation trapping and cooperative effects by means of the comparison between the results given by these two models.

In the following, we will discuss the simulation methods for an atomic cloud interacting with a narrow beam (see Fig. 4.1). We label “small beam” the setup with a narrow laser beam exciting the cloud, and “large beam” the setup with a plane wave exciting the cloud.

### 4.2.1 Coupled-dipole model

For the simulations with the coupled-dipole model, we have the coupled-dipole equations Eq. 1.15 for the amplitudes  $\beta_j(t)$  and the simulation procedure described in section 1.3: Gaussian spherical cloud of  $N$  atoms and RMS size  $R$  characterized by a resonant optical thickness  $b_0$  and density  $n_0\lambda^3$ , and atomic positions drawn under an exclusion volume condition to produce dilute cloud without close atomic pairs. However, to achieve the condition of small incoming field, we model it as a *truncated plane wave* of radius

$$w = \frac{R}{2}$$

i.e., the waist  $w$  of the incoming field is set to be the half of the cloud RMS size  $R$ . This makes  $\sim 10\%$  of the atoms in the cloud to be directly excited by the incoming field. Smaller waists decrease the number of driving atoms, and larger waists may break the small-beam assumption. Also, to make the simulations more reliable, we set the atom number to be  $N \sim 10^4$ , so 10% of this gives at least  $\sim 10^2$  atoms interacting directly with the truncated incoming beam.

By setting the driving beam on the  $z$  axis and the cloud center on the origin of the  $x$  and  $y$  axis (c.f. Fig. 1.2), and defining  $\rho_j = \sqrt{x_j^2 + y_j^2}$  the distance between the atom  $j$

and the cloud center lying on the  $xy$  plane (so  $\rho_j \perp \hat{z}$ ), the term  $\Omega$  in the coupled-dipole equations Eq. 1.15 is set as

$$\Omega = \begin{cases} \Gamma, & \text{if } \rho_j \leq w \\ 0, & \text{if } \rho_j > w \end{cases} \quad (4.17)$$

i.e., zero if the atom  $j$  is out of the laser “tube”, or  $\Gamma$  if the atom  $j$  is in the laser “tube”. This condition is checked for all the  $N$  atoms. Note that the incoming field is on to excite the atoms until a steady state is reached, such that after the switch off,  $\Omega = 0$  for all the atoms. Then, Eqs. 1.15 are solved numerically and the emitted intensities are calculated, totally in space (Eq. 1.29) or in a certain direction  $\{\theta, \phi\}$  (Eq. 1.34 or 1.35), where  $\theta$  and  $\phi$  are the angular spherical coordinates (see Fig. 1.2). Also, the intensities are calculated for several configurations of the atomic positions and then averaged, in order to remove spurious oscillations and noise.

### 4.2.2 Random walk model

The random walk simulations were done by William Guerin and consists in sending a given quantity of photons into a cloud defined by an optical thickness  $b = b(\Delta)$ . After the photon leaves the medium, its number of scattering events  $N_{\text{diff}}$  and its emission direction  $\{\theta, \phi\}$  are determined and then the scattered intensity as a function of the time can be plotted for a given direction.

The medium is modeled by a cloud with a given optical thickness  $b$  and Gaussian density  $n(r) = n_0 e^{-r^2/(2R^2)}$ , where the parameters  $n_0$  and  $R$  are written as a function of  $b$ . The incident photons have a frequency  $\Delta$ , i.e., they are monochromatic, and are sent at a fixed direction and position: for example, if the cloud center is at the origin of a Cartesian frame and if the photons travel along the  $z$ -axis, the incident photons will enter into the cloud at the position  $\{z = -R, \theta = \pi, \phi = 0\}$ . Thus, the incoming photons beam has zero waist, i.e., it is infinitely narrow.

Each photon enters into the cloud and travels a distance  $x$  before being absorbed, where  $x$  is set randomly from the probability law  $P(x)$  in Eq. 4.2. The value of  $l$  can be written in units of  $b$ . After setting the value of  $x$ , for a homogeneous cloud, the scattered photon is checked to be in or out of the cloud by comparing  $x$  with the cloud size  $R$ . However, for a Gaussian cloud, the comparison is not made: a calculation with integrals takes place to determine the photon position. If the photon is still in the cloud, one scattering event is counted and then the emission direction is calculated randomly, i.e.,  $\theta$  and  $\phi$  are set randomly by assuming isotropic emission in all space. A new value  $x$  is set randomly from  $P(x)$  and if the photon is still in the cloud a second scattering event is counted. A new emission direction is also set randomly. The procedure is repeated until the photon leaves the cloud, and then the output emission direction  $\{\theta, \phi\}$  and the performed number of scattering events  $N_{\text{diff}}$  are collected for this photon.

The procedure is repeated for many photons, set to be  $\sim 10^5$ , and they hit the cloud at the same position and direction. After they are all scattered, we have the values of  $\theta, \phi$  and  $N_{\text{diff}}$  for all the photons. If one takes into account the beam waist in the simulation, the photon input position is set randomly from a given waist  $w < R$  (truncated plane wave) or from a Gaussian distribution with waist  $w < R$  (Gaussian beam). If one takes

into account the incoming laser spectrum (i.e., non-monochromatic photons), the photon detuning  $\Delta$  is set randomly from a given frequency probability distribution. For the simulations with temperature, after the first absorption event, a velocity value is set randomly from a Gaussian distribution of given  $k_0v$ . Then, the detuning of the emitted photon is calculated as  $\Delta - k_0v$ , and the new value of  $x$  is set from  $P(x)$  where the value of  $l$  will depend on the new detuning.

In order to obtain the emitted intensity  $I$  as a function of the time, one plots the number of emitted photons as a function of  $N_{\text{diff}}$ , because  $N_{\text{diff}} = t/\tau_0$  from Eq. 4.11 and  $I$  is proportional to the number of emitted photons (e.g., if for 1000 photons, 110 performed zero scattering events, 350 performed one scattering event, 220 two scattering events, and so on, we have  $t/\tau_0 = \{1, 2, \dots\}$  and  $I = \{350, 220, \dots\}$ . The photons which performed zero scattering events are not included because in fact they were coherently transmitted.). Then, as the cloud-beam system is symmetric with the  $z$ -axis, it is enough to collect the emitted photons in a given direction  $\theta$  for all  $\phi$  (see subsection 1.2.2), so it is chosen only the photons which were emitted at a value of  $\theta$  we want. In order to have more photons and to improve the quality of the computed intensities, we set  $\theta = 45^\circ \pm 15^\circ$ , i.e., it was considered photons with  $\theta \in [30^\circ, 60^\circ]$ .

The advantage of the random walk simulations is that it takes much less time than the coupled-dipole simulations. Hence, it is even possible to use the parameters of the experiment for the cloud and laser size. For the simulations with temperature, the chosen parameters were like in the experiment. For the simulations without temperature,  $b$  is the single parameter, so the cloud atomic number, density or size are not defined.

Table 4.1 summarizes the parameters and assumptions for the simulation with small beam with the random walk and coupled-dipole models.

<i>Model</i>	<i>Coupled dipoles</i>	<i>Random walk</i>
optical thickness	$b \sim 10$	$b \sim 10$
cloud size	$R \sim 10/k_0$	not defined
atom number	$N \sim 10^4$	not defined
density	$n_0\lambda^3 \sim 10$	not defined
beam waist	$w = R/2$	zero
emission angle	$\theta = 45^\circ$	$\theta = 45^\circ \pm 15^\circ$

**Table 4.1:** Comparison between the parameters used in the simulations with the coupled-dipole model and the random walk model.

## 4.3 Numerical results

### 4.3.1 Emitted intensities *versus* time

The simulation results discussed in this section have as the main goal the comparison between the two models for propagation of light in the atomic cloud. As the coupled-dipole model takes into account interference and coherence, contrary to the random walk model, we can see that the former is more complete than the latter, in the sense that the random walk model will give only the contribution due to the radiation trapping, whereas the coupled-dipole model gives also the cooperative effects.

Figure 4.2 shows emitted intensities with the small beam setup, with the coupled-dipole and random walk models, for different values of  $b(\Delta)$ . In this simulation, the detuning  $\Delta$  was fixed at resonance, in a such way that  $b$  in the coupled-dipole simulation was varied with the atom number  $N$  and cloud size  $k_0R$ . For the random walk model, the values of  $b$  were chosen to be equal or close to the ones given from the coupled-dipole model.

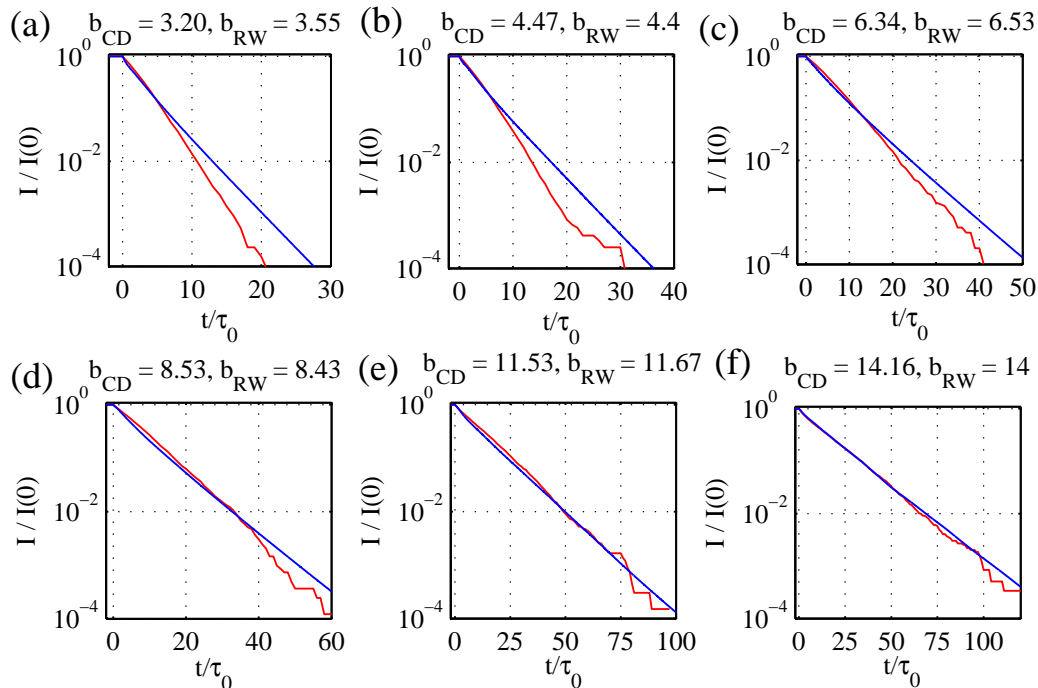


**Figure 4.2:** Emitted intensities calculated from the random walk (red) and coupled-dipole (blue) models, for small beam and several values of the optical thickness  $b$ . For the simulations with the coupled-dipole model, the values of  $b$  were calculated for  $\Delta = 0$  and by varying  $b_0$  by means of  $N$  and  $k_0R$  at  $n_0\lambda^3 = 4.6$ .  $I/I(0)$  are the normalized intensities at  $\theta = 45^\circ$  for the coupled-dipole model [ $I(\theta, t)$ , Eq. 1.35] and  $\theta = 45^\circ \pm 15^\circ$  for the random walk model.

We see that, for small  $b$  [panels(a) to (d)], the two intensities do not coincide for low amplitudes and late times, meaning that the contribution due to the random walk is weak compared with the coupled-dipole model. This can be interpreted that low  $b$  also decrease the number of scattering events, so the photons are not multiple scattered. In another words, the slow decay seen from the coupled-dipole curves are mainly due to the coherence and interference, i.e., subradiance. However, when  $b$  increases [panels (d) to (f)], the two curves become close to each other, collapsing completely for  $b \geq 10$  [panels (e) and (f)]. This means that the slow decay seen in the coupled-dipole model is in fact radiation trapping. On the other hand, the early decay of the intensity are the same in all panels, meaning that radiation trapping takes place in the early decay.

Figure 4.3 is the same as Fig. 4.2, but now  $b$  is varied by changing the detuning. This means that for the coupled-dipole simulations  $b_0$  is constant, i.e., constant  $N$  and  $k_0R$ . We see that, for high  $b$ , i.e., close to resonance [panel (a)], the two models are in agreement; however, when  $b$  decreases, i.e., increasing  $\Delta$  [panels (b) to (g)], the intensity from the random walk model decays faster than the intensity from the coupled-dipole

model. For very low  $b$  [panels (e) to (g)] we see clearly that the slow decay from the random walk model is practically negligible compared to the one from the coupled-dipole model. Also, the early decay of the intensity with the two models are the same, meaning that radiation trapping takes place at short times; however, for high  $b$  [panels (e) to (g)], the fast decay from the coupled-dipole model is faster than the one from the random walk model, meaning that we can see superradiance with the small beam setup at large  $b_0$  or  $\Delta$ .

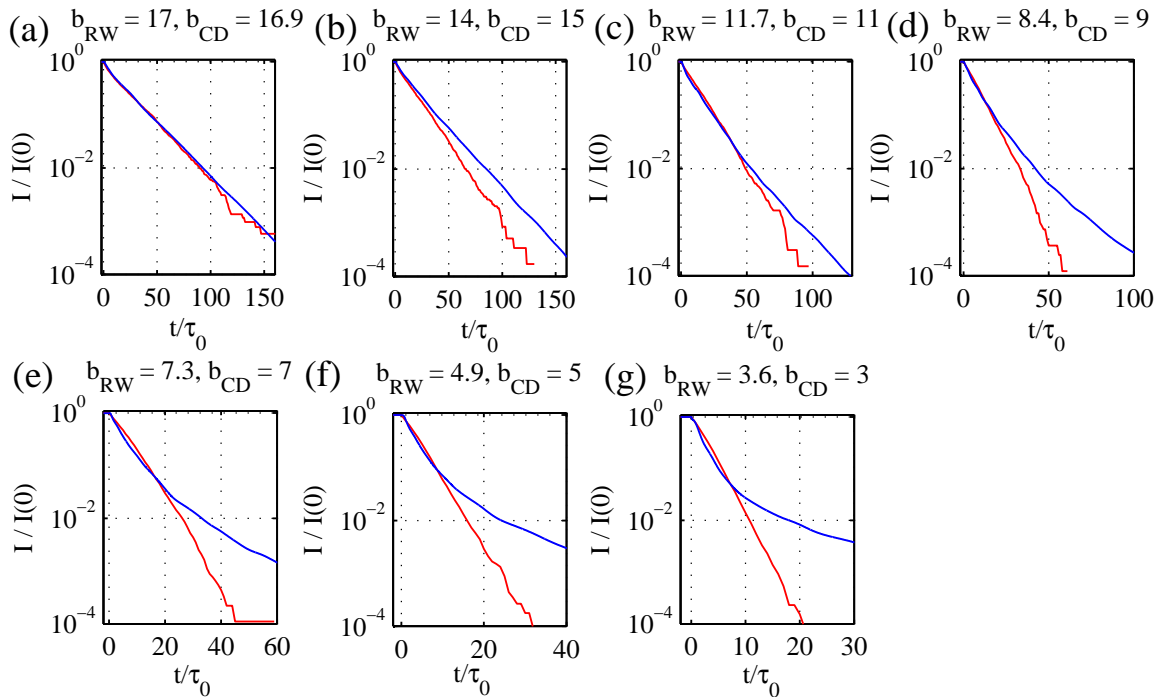


**Figure 4.3:** Emitted intensities calculated from the random walk (red) and coupled-dipole (blue) models, for small beam and several values of the optical thickness  $b$ . The values of  $b$  were calculated from constant  $b_0$  and by varying  $\Delta$ .  $I/I(0)$  are the normalized intensities at  $45^\circ$  for the coupled-dipole model [ $I(\theta, t)$ , Eq. 1.35] and at  $45^\circ \pm 15^\circ$  for the random walk model. Parameters:  $b_0 = 16.9$  and (a)  $\Delta = 0$ , (b)  $\Delta = 0.18\Gamma$ , (c)  $\Delta = 0.37\Gamma$ , (d)  $\Delta = 0.47\Gamma$ , (e)  $\Delta = 0.60\Gamma$ , (f)  $\Delta = 0.77\Gamma$  and (g)  $\Delta = 1.1\Gamma$ .

The main conclusions from these two figures is that, with the setup of small beam, at low  $b$  radiation trapping is negligible, meaning that the slow decay observed from the coupled-dipole model is subradiance. In another words, subradiance is present with the setup of small beam, and at the same range of amplitudes ( $\leq 10^{-2}$ ) as the ones observed with the large beam setup. On the other hand, radiation trapping takes place at short times, meaning that, after the switch off of the incoming beam, initially the emitted light is trapped by radiation trapping. The value of  $b$  determines if some remaining light will be trapped due to subradiance and emitted later.

### 4.3.2 Decay rates *versus* $b$

One can do an exponential fit in the slow part in all previous curves to characterize the slow decay. Initially our idea was to plot the fitted  $\tau_{\text{fit}}$  as a function of  $b$  and to see the quadratic scaling given by Eq. 4.14, however, we cannot go far in  $b$  in the coupled-dipole

model, and the plot for small  $b$  can be confused between quadratic and linear scaling.

Figure 4.4 shows the fit of the data in Fig. 4.3, where  $b$  was varied with the detuning for the data in the coupled-dipole model, in the range  $I/I(0) \in [10^{-3}, 10^{-2}]$ . We see that, for small  $b$ , more precisely  $b < 10$ ,  $\tau_{\text{fit}}$  from the coupled-dipole model is constant, i.e., subradiance ( $\tau_{\text{fit}} = \tau_{\text{sub}}$ ) showing that it does not depend on the detuning of the incoming beam. These rates correspond to subradiance. As  $b$  increases (near resonance), the  $\tau_{\text{fit}}$  from the coupled-dipole model tend to the  $\tau_{\text{fit}}$  from the random walk model, and they collapse for  $b \geq 10$ . This shows that the slow decay in this regime is radiation trapping ( $\tau_{\text{fit}} = \tau_{\text{RT}}$ ).

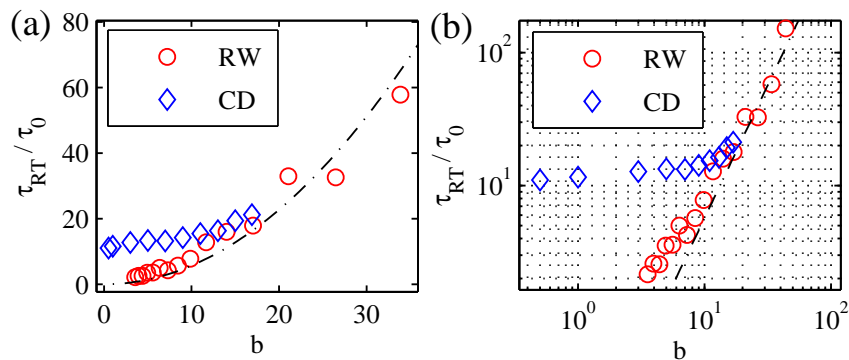


**Figure 4.4:** Slow decay rates  $\tau_{\text{fit}}$  as a function of the optical thickness  $b$ , in (a) linear and (b) logarithm scale, extracted from the intensities in Fig. 4.3 calculated with the random walk model (red circles) and coupled-dipole model (blue diamonds). The dashed line is Eq. 4.14. Parameters: same as in Fig. 4.3.

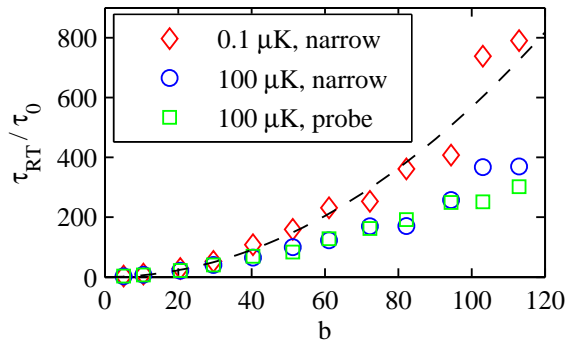
### 4.3.3 Comparison with the large beam setup

For the large beam setup, the simulations with the coupled-dipole model give subradiance independently of the detuning, as discussed in Chapter 2. At resonance both radiation trapping and subradiance take place, however the amplitude of radiation trapping in the emitted intensity for the large beam setup was calculated numerically and shown to be small [Guerin 2016], so we can conclude that radiation trapping is weak compared with subradiance in the setup of resonant large beam. On the other hand, at early times, superradiance is suppressed at off-axis directions, as shown in Chapter 3, however, the coherent transmitted light (forward direction) contains interference and superradiant features.

### 4.3.4 Effects of temperature and laser spectrum

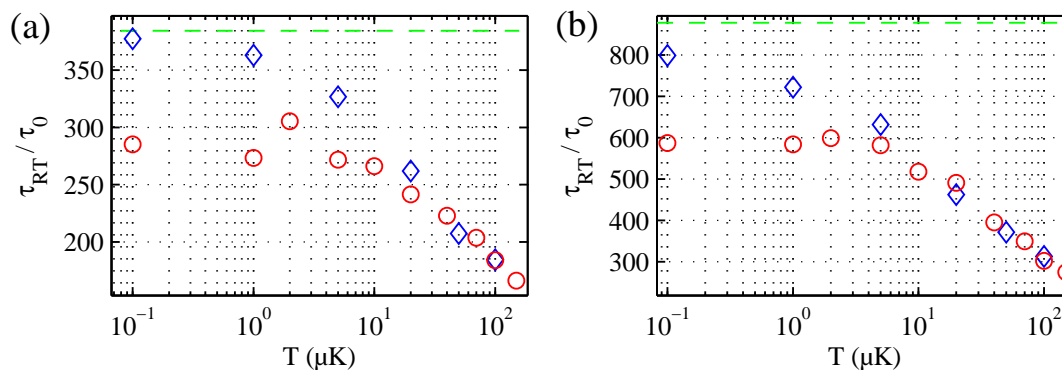
The random walk and coupled-dipole models are in agreement for large optical thicknesses in the ideal case, i.e., for monochromatic incident light and motionless atoms. However, as already described in section 4.2, we can include temperature and laser spectrum in the random walk model in order to investigate how they can impact the experiment.

Figure 4.5 shows  $\tau_{\text{RT}}$  as a function of  $b_0$  for three situations: both negligible temperature and laser spectrum (ideal case),  $T = 100 \mu\text{K}$  and negligible laser spectrum (experimental temperature with an ideal laser), and  $T = 100 \mu\text{K}$  and the actual probe



**Figure 4.5:** Radiation trapping decay rates  $\tau_{RT}$  as a function of  $b$  calculated by taking into account the temperature and the incident laser spectrum. In the legend, “narrow” stands for a Gaussian spectrum of width  $0.01\Gamma$  and “probe” stands for the spectrum in Fig. 2.20 left. The dashed line is Eq. 4.14. The values of  $b$  were calculated for  $\Delta = 0$ , so  $b = b_0 = 3N/(k_0R)^2$ , and  $b$  was varied by varying  $R$  for constant  $N$ . The values of  $\tau_{RT}$  were extracted from intensities at  $45^\circ \pm 15^\circ$ , in the interval  $I/I(0) \in [10^{-4}, 10^{-2}]$ . Parameters:  $N = 10^9$ ,  $\Delta = 0$ ,  $R \in [0.61, 3]$  mm,  $w = 300 \mu\text{m}$  with a Gaussian profile, for  $10^5$  incident photons.

beam spectrum in our experiment, displayed in Fig. 2.20 (experimental parameters). Also, the values of  $b$  were calculated from values of  $N$  and  $k_0R$  in the order of our experimental values, i.e.,  $N \sim 10^9$  atoms and  $R \sim 1$  mm (see section 1.3). We see that both negligible temperature and spectral width (red data) corresponds to the diffusion theory in the ideal case, showing that these fitted  $\tau_{RT}$  are due to radiation trapping. However, a temperature of some  $\mu\text{K}$  (blue data) and also a large laser spectrum (green data) break the theoretical prediction. In addition, the blue and green data collapse, meaning that the cloud temperature plays a more important role in radiation trapping than the laser width, at least at resonance.



**Figure 4.6:** Radiation trapping decay rates  $\tau_{RT}$  as a function of the temperature  $T$ , for (a)  $b = 82$  and (b)  $b = 124$ , calculated for incident laser light spectrum of narrow width 10 kHz (blue diamonds) and with the probe laser spectrum given in Fig. 2.20 left (red circles). The dashed green line is the prediction from Eq. 4.14.

Figure 4.6 shows how the slow decay rate is impacted by the temperature, for a constant value of  $b$  [ $b = 82$  in (a) and  $b = 124$  in (b)], with a negligible laser spectrum

(blue data) and the actual probe laser spectrum in our experimental setup (red data). We see that, for large  $T$ ,  $\tau_{\text{RT}}$  is the same with and without spectrum, which means that the radiation trapping is strongly impacted by the temperature. However, for low  $T$ ,  $\tau_{\text{RT}}$  without laser spectrum tends to the ideal value, whereas  $\tau_{\text{RT}}$  with laser spectrum saturates in a very low value compared with what is expected from the theory. Also, in panel (b),  $\tau_{\text{RT}}$  does not tend exactly to the ideal value as in (a). This can be explained by frequency redistribution due to the high value of  $b$ , which favors more scattering events.

We see how radiation trapping is modified when the cloud temperature and the laser spectrum are taken into account. Therefore, in order to perform a radiation trapping experiment in our laboratory, the experimental setup had to be modified to accomplish these two features.<sup>1</sup> This is discussed in the next section.

## 4.4 Experimental setup

The simulations with the random walk model showed that radiation trapping is very sensitive to the cloud temperature and the probe beam laser spectrum. About temperature, there are some experimental methods in order to decrease it, like adding a *molasses phase*, which can provide a decrease of the temperature until  $\sim 20 \mu\text{K}$ . The molasses phase consists in turning on only the six MOT laser beams after the MOT loading, dark MOT phase and extinction of the magnetic field (subsection 2.2.4), so the atoms will see a friction force  $F = \beta v$  (Eq. 2.1) and their velocities will be reduced. Another way to decrease the temperature is to check if the parameters of the dark MOT phase are optimized, since the dark MOT helps in the temperature decreasing due to the low intensity of the repumper beams.

In our experimental setup, as  $b_0$  is very large, in order of  $b_0 \sim 100 - 120$ , it is a very hard task to decrease the temperature until  $\sim 20 \mu\text{K}$  with the molasses technique. In addition, radiation trapping was observed at  $\sim 80 \mu\text{K}$  in [Labeyrie 2005], so we opted to keep the temperature and to replace the laser source to solve at least the laser linewidth problem. Also, we checked the parameters of dark MOT phase to see if they are already optimized.

In this section, we describe the changes made in the experimental setup in order to perform experiments with the small beam setup. The changes include: the setup of the new laser source, the optimization of the dark MOT phase, and the setup of the probe beam.

### 4.4.1 New laser source

In order to have a probe beam with small linewidth, we decided to replace the DFB laser source in our MOT setup (see subsection 2.2.2) by a laser from Toptica Photonics, references D1 pro and Sys DC 110, which has a linewidth of 200 kHz, much smaller compared with the Rb natural linewidth 6.067 MHz and the DFB laser linewidth  $\sim 2 - 3$  MHz. This laser was already available in our laboratories, in another experimental setup.

---

<sup>1</sup> In fact, as we will discuss in section 4.4, we could only replace the laser source in order to provide a narrower spectrum. We could not decrease the temperature of our atomic sample.

The setup of this new laser source in our experiment required some work due mainly to its mode hopping and temperature stabilization. Before placing it, we measured and wrote down the values of the cloud parameters (atom number,  $b_0$ , MOT loading time, vapor pressure), as well as the powers of the MOT laser beams, the emitted power at the DFB laser output and the power of the probe beam. Then, we placed the laser head on the optical table and its box control on a shelf. The laser head contains the diode laser and a diffraction grating; the box control contains the electronic controllers for temperature, current, frequency scan and the frequency stabilization circuits. After the laser output, we placed an optical isolator and then two mirrors in order to recover the whole original alignment by adjusting these mirrors.

After connecting the temperature, current and scan controls, we noticed that the laser was in the wrong emission wavelength  $\lambda$  by means of absence of fluorescence in the saturated absorption Rb cell. The correct value of  $\lambda$  was set by adjusting the diffraction grating in the laser head and by monitoring the output beam with an optical spectrum analyzer (OSA) from Yokogawa, reference AQ6370D, in a such way that the OSA displayed the values of  $\lambda$  for the DFB and the Toptica lasers. Another ways to measure  $\lambda$  are to use a wavemeter (which was not available in our laboratories) and to scan the laser current until a fluorescence in the Rb cell is observed (tried but not successful).

After adjusting  $\lambda$ , we tried to lock the Toptica laser with our homemade PID controller, whose input is the Rb saturated absorption spectrum at the crossover transition  $F = 2 \rightarrow F' = 2, 3$  (c.f. subsection 2.2.2). However, we noticed some noise in the generated error signal for the PID, due to the fact that the frequency modulation in our PID controller, 50 kHz, is much smaller compared with the required modulation frequency, 30 MHz, according to the user manual from Toptica. Also, the user manual suggests that the laser should be locked by means of two electronic boxes provided by the company itself, where one of them uses the Pound-Drever-Hall (PDH) technique [Drever 1983] to generate the error signal and the other is a PID controller. The PID box was included in the laser box control, but the PDH controller was not, so we ordered and installed it.

It is known that the frequency modulation with the PDH technique creates two sidebands separated by the modulation frequency from the desired (central) frequency. Also, the PDH output for modulation was supposed to be connected to the laser head, in order to modulate its current (the current modulation provides the frequency modulation, since the emitted frequency depends on the current sent to the diode laser). After setting the PDH and PID controllers in our laser source, we noticed that the sidebands could be a problem for the experiment, because beyond the central frequency, the atoms will see the sidebands frequency (separated by 30 MHz  $\simeq 5\Gamma$ ) and interact with them, specially for detuned frequencies (e.g., a detuning of  $-5\Gamma$  for the central frequency would bring one of the sidebands to resonance, so the atoms could interact with resonant photons). In order to solve this, we opted by using an EOM from Photonics Technologies, model EOM-02-20-V, in a such way that the PDH modulation output was connected to the EOM to modulate the laser phase, providing the sidebands only for the absorption saturation setup and not for the whole setup. Other ways of solving the sidebands problem are: to modulate Zeeman shifts in the absorption saturated Rb cell by setting a coil around it to generate a magnetic field [Shim 1999], and to set a Fabry-Pérot cavity to filter the sidebands frequencies before the beam is sent to the main setup. The former works well at low

modulation frequencies (not our case) and the latter requires a hard work for mechanical stabilization.

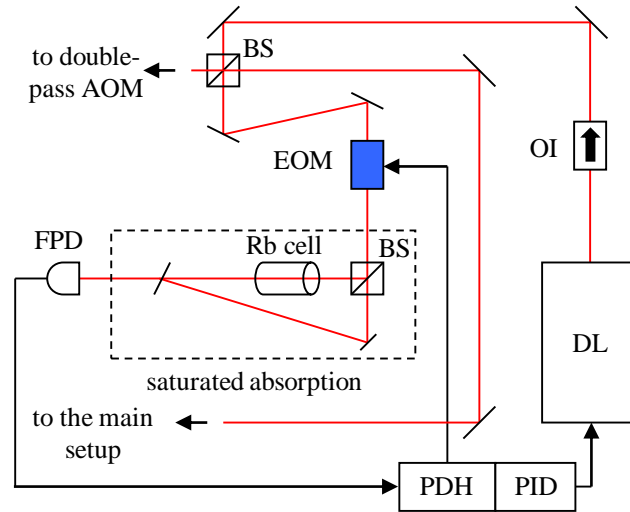


**Figure 4.7:** Scheme for the laser stabilization setup. Legend: BS: beam splitter, DL: diode laser, EOM: electro-optic modulator, FPD: fast photodiode, OI: optical isolator, PDH: Pound-Drever Hall controller, PID: proportional–integral–derivative controller.

Figure 4.7 is a scheme of our laser stabilization after the setup of the EOM. The laser beam is emitted at the laser head, where the laser diode and diffraction grating are, and then passes through an optical isolator and a beam splitter, where it is split in two. Most of the power goes to the double-pass AOM setup [McCarron 2007], and its output beam goes to the main setup, i.e., MOT and probe beam. A small power goes to the EOM and then to the saturated absorption setup, in order to stabilize the laser frequency by means of the detection of the signal with a homemade fast photodetector (FPD) and then modulation and locking with the PDH and PID controllers. Before the EOM was installed, the low power beam went directly to the saturated absorption setup and the PDH output, which sends the modulated signal, was connected to the diode laser, so the diode laser emitted light with the sidebands, which would be also present in the main setup. With the EOM installed, the PDH output is connected to the EOM, so only the light after the EOM output contains the sidebands. The light emitted by the laser head does not contain the sidebands: it contains only the central frequency and is already stabilized due to the PID correction sent to the diode laser. The output beam goes to the double-pass AOM setup and then to the main setup.

Figure 4.8 shows the connections between the laser head and its control box, as well as the connections with the FPD and EOM for the frequency stabilization. Once the laser head and its control box were placed on the optical table, we connected the laser head to the temperature and current controllers (inputs T and I) and then the piezoelectric scanner (output 1 to input A). The connections with the PDH and PID controllers were done as follows: the absorption saturated signal measured by the FPD is sent to the input of the PDH controller (fast output to input 4), then the signal is mixed with a modulating signal provided by an internal VCO. The modulating signal (with modulation frequency 30 MHz) is also sent to the EOM (output 3 to EOM) – before the EOM setup, the output 3 was connected to the AC modulating input current at the laser head (input B). The

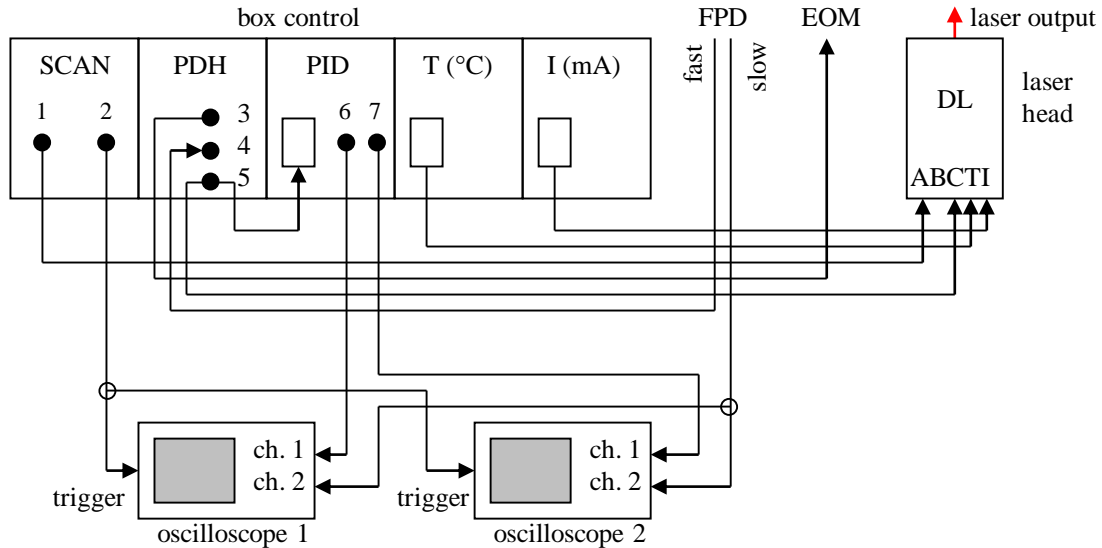


**Figure 4.8:** Scheme for the connections of the laser box control to the laser head and the fast photodiode. Legend: 1: piezo output, 2: trigger, 3: internal oscillator, 4: phase detector, 5: error output, 6: output, 7: monitor output, A: piezo input, B: AC modulation, C: DC modulation, T: temperature input, I: current input.

result of the electronic mixing is the derivative signal, which is sent to the PID controller (output 5 to the PID input). Then, the PID controller makes the correction and this is sent to the laser head (output 5 to input C). The saturated absorption signal can be displayed at an oscilloscope (output slow to channels 2 of oscilloscopes 1 and 2), by using the piezoelectric scanning as trigger (output 2 to oscilloscopes 1 and 2) as well as the derivative and correction signals (outputs 6 and 7, respectively). The parameters of the PDH and PID controllers, like modulation level, amplitude levels and gain, are adjusted with knobs at the control box by seeing the signals at the oscilloscope.

After the setup of laser stabilization and solving the mode hopping in frequency, we obtained the following values for the laser source parameters: temperature  $20.3^{\circ}\text{C}$ , current  $222\text{ mA}$ , output power after the optical isolator  $60\text{ mW}$ , power for the double-pass AOM  $51\text{ mW}$ , power for the saturated absorption setup  $3\text{ mW}$ , efficiency of the double-pass AOM setup  $60\%$  for detuning  $+\Gamma$ .

#### 4.4.2 Optimization of the dark MOT phase

As explained briefly in subsection 2.2.4, the dark MOT phase [Ketterle 1993] takes place after the MOT loading and its goal is to increase the density and decrease the temperature of the atomic cloud. For this, the intensity of the repumper beams is reduced, so the atoms do not interact with the MOT laser beams and repulsion between atoms due to scattering is reduced. Also, the detuning of the MOT laser beams is modified.

The MOT loading is a dynamical process, meaning that its parameters, like atom number, temperature, vapor pressure, etc., vary over time. This is because the amount of Rb atoms in the chamber changes, due to losses due to the chamber walls and the “pumping” due to the reservoir. For the super- and subradiance experiments, the temperature of the cloud was  $\approx 50\ \mu\text{K}$ , however, for the experiments with small beam, it increased

to  $\approx 100 \mu\text{K}$ , maybe due to a new opening of the valve of the Rb reservoir to increase  $b_0$  and  $N$  for the small beam measurements. Hence, as an attempt to recover the  $50 \mu\text{K}$  value, we decided to optimize the parameters for the MOT and repumper beams during the dark MOT phase. These parameters are the intensities and detunings for the MOT and repumper beams.

We ran several cycles with the phases MOT loading, dark MOT, extinction of the magnetic field and TOF (see subsections 2.2.4 and 2.2.6). In each cycle, a different value of the repumper beam intensity  $I_{\text{REP}}$  was set and the values of the repumper beams detuning, MOT beams detuning and MOT beams intensity were kept. The parameters for the MOT loading phase for all cycles were the same. For each cycle, we measured  $b_0$  and  $N$  before the cloud expansion and the temperature  $T$ . These three parameters can be plotted as a function of  $I_{\text{REP}}$ .

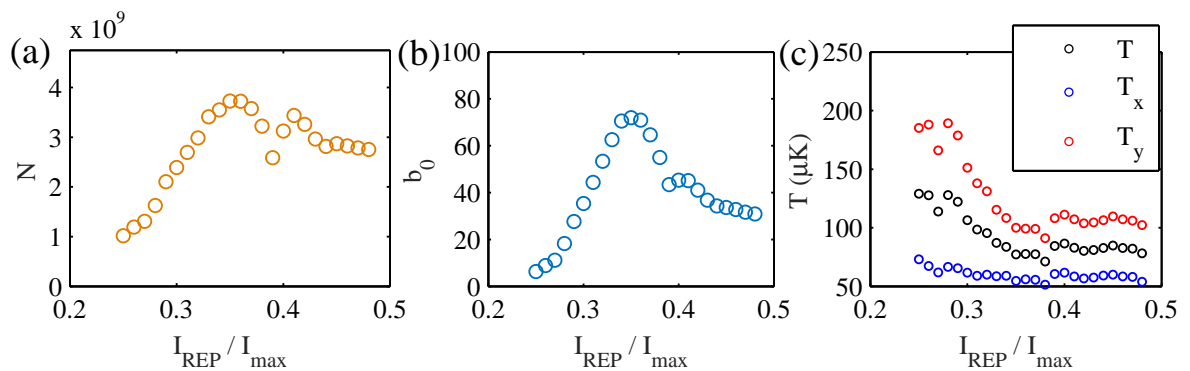


**Figure 4.9:** Measurement of the (a) atom number  $N$ , (b) resonant optical thickness  $b_0$  and (c) temperature  $T$  of the cloud as a function of the repumper beam intensity  $I_{\text{REP}}$  during the dark MOT phase, for  $\Delta_{\text{REP}} = -\Gamma$ ,  $\Delta_{\text{MOT}} = -5\Gamma$  and  $I_{\text{MOT}} = I_{\text{max}}$  during the dark MOT phase. In (c),  $T_x$  is the temperature measured at the horizontal direction perpendicular to the propagation probe beam axis,  $T_y$  is the temperature measured at the vertical direction (same direction as the MOT coils) and  $T = (T_x + T_y)/2$ .

Figure 4.9 shows  $N$ ,  $b_0$  and  $T$  as a function of  $I_{\text{REP}}$ . Physically, for low  $I_{\text{REP}}$ , many atoms stop interacting with the MOT beams, so  $N$  and consequently  $b_0$  drop. For high  $I_{\text{REP}}$ ,  $N$  is supposed to be constant, but the repulsions due to the high scattering rate increases and then  $b_0$  drops. Hence, there should be an intermediate value of  $I_{\text{REP}}$  where  $b_0$  and  $N$  are maximum. The maximum values for  $N$  and  $b_0$  occurs at  $I_{\text{REP}} = 0.35 I_{\text{max}}$ , for which the temperature is  $77 \mu\text{K}$ . Therefore, we set  $I_{\text{REP}} = 0.35 I_{\text{max}}$  in the control program during the dark MOT phase.

We repeated the measurement of Fig. 4.9 for another detuning of the repumper beams,  $\Delta_{\text{REP}} = -2\Gamma$ , because a more detuned beam in principle reduces the scattering rate. We obtained figures similar to the ones discussed, but the obtained maximum values of  $N$  and  $b_0$  were smaller.

#### 4.4.3 Setup of the probe beam

As done for super- and subradiance experiments, the setup of the probe beam was modified in order to perform the measurements with the small beam. Since radiation

trapping is a slow decay in time under excitation with a narrow beam, and since we want to perform subradiance measurements for comparison, also because the laser source was changed, the setup was arranged to accomplish these two features.

The probe beam setup was arranged in two steps: firstly we placed back the setup for subradiance (subsection 2.2.3), i.e., we removed the Mach-Zehnder EOM from the superradiance setup (3.2.1) and we set back the two AOMs in series. The single difference compared with the original subradiance setup is that now the AOMs were connected to the new pulse generator installed for the superradiance experiment. Also, as this pulse generator has two outputs which generates identical but inverted signals, the inversion connection in the two switches for the focused AOM was undone.

Then, a setup with lenses was imagined and simulated in MATLAB by means of the ABCD matrices theory for propagation of laser beams [Siegman 1986], in order to obtain a small probe beam compared with the atomic cloud dimensions. Also, we wanted to keep the original setup for the large probe beam for eventual comparison with subradiance, so a practical way to alternate between the large and small probe beam setups was also considered.

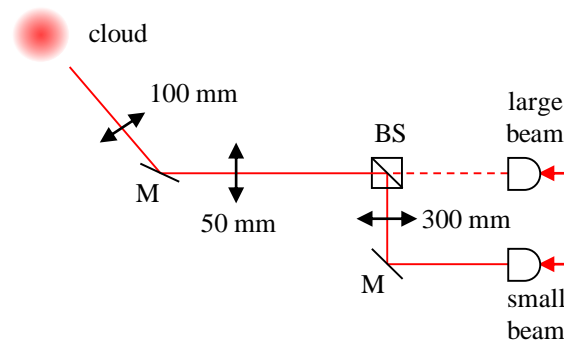


**Figure 4.10:** Setup for the probe beam for the radiation trapping and subradiance experiment. Two collimators allow to alternate between the small probe and large probe.

The setup was set as displayed in Fig. 4.10. The original setup with the large probe beam, for the super- and subradiance measurements, was as before, where the laser beam, coming from a monomode optical fiber, leaves the collimator and goes through two lenses before reaching the atoms. The two lenses are a telescope of magnification that serves to increase the beam waist to 5.7 mm, very large compared with the cloud RMS size,  $R \sim 1$  mm (see subsection 2.2.3). For the small probe beam, a second collimator from Thorlabs, reference F240APC-780, output waist  $750 \mu\text{m}$ , was set, followed by a mirror, a lens and a beam splitter, in a such way that the probe beam should reach the atoms by using the same propagation path as the large beam. This propagation path was aligned by adjusting the mirror and the collimator. The waist of the small beam at the cloud depends on the lens focal distance and the distance between the lens and the 50 mm lens. The alternance between the small and large beam setups is done by coupling the monomode optical fiber output to the corresponding collimator.

For a lens of focal distance 300 mm placed at a distance of 32.5 cm from the 50 mm lens, the laser beam, after leaving the collimator and arriving at the 300 mm lens, is focused before arriving at the 50 mm lens, in a such way that its focus is just before the 50 mm lens. Also, its waist is much smaller than the initial value. After the 50 mm

lens, the beam focuses just after it and then its waist increases a bit. After leaving the 100 mm lens, it focuses at the cloud position, with a waist of  $0.200 \text{ mm} = 200 \text{ }\mu\text{m}$ . In addition, the beam Rayleigh length is 16.1 cm, i.e., a large Rayleigh length, which assures that the beam waist is quasi-collimated around the cloud position. The beam waist was measured by deviating the beam with a mirror and by using a beam profiler based on the “knife-edge” technique.

## 4.5 Experimental results

The experimental procedure for preparing the atomic sample and acquiring the data is the same used for super- and subradiance, described in subsections 2.2.4 and 2.2.7: the MOT is loaded by including a dark MOT and optical pumping phases and then it is turned off, allowing the cloud to a free expansion. During its expansion, the probe beam is sent to the cloud as a sequence of pulses, and the emitted fluorescence is measured by the HPM. After the main measurements, a calibration measurement is run in order to measure  $b_0$  for each pulse.

The pulse separation was set as 1.0 ms, as for super- and subradiance experiments, however, the pulse duration was modified to  $10 \text{ }\mu\text{s}$ , i.e., three times shorter. This is because the temperature change in the cloud during the pulse excitation has to be negligible to avoid frequency redistribution. The temperature change  $\Delta T$  is given by

$$\Delta T \propto N_{\text{ph}} T_{\text{rec}} \quad (4.18)$$

where  $N_{\text{ph}}$  is the number of scattered photons and  $T_{\text{rec}}$  is the recoil temperature, which is equal to  $0.362 \text{ }\mu\text{K}$  for  $^{87}\text{Rb}$  in the considered transition [Steck 2001].  $N_{\text{ph}}$  is given by  $N_{\text{ph}} = \Gamma_{\text{sc}} \Delta t$ , where  $\Gamma_{\text{sc}} = \Gamma s(\Delta)/2$  is the scattering rate and  $\Delta t$  is the pulse duration. For  $s(\Delta) = 0.1$  and  $\Delta t = 30 \text{ }\mu\text{s}$ , we have  $N_{\text{ph}} = 57$  and  $\Delta T = 21 \text{ }\mu\text{K}$  per pulse, whereas for  $\Delta t = 10 \text{ }\mu\text{s}$  we get  $N_{\text{ph}} = 19$  and  $\Delta T = 6.9 \text{ }\mu\text{K}$  per pulse.

Our data acquisition started initially with the small probe beam setup only, without the replacement of the MOT DFB laser source, but only subradiance was observed. Then, the simulations with temperature and laser spectrum described in subsection 4.3.4 were run, so we decided to replace the laser source. We also opened the Rb reservoir valve by 1/4 of a turn to increase  $N$  and  $b_0$ . After optimizing the dark MOT phase, we checked the probe beam polarization with a polarimeter and also the magnification of the  $2f-2f$  setup for the cloud and CCD camera (see subsection 2.2.5). We also measured the linewidth at the output of the probe beam setup, to check the value 200 kHz, and we set a polarizing beam splitter at the input of the optical fiber after the AOMs setup (see Fig. 2.8) to correct intensity and polarization fluctuations due to the switch on and off of the  $-1$  order beam.

### 4.5.1 Data for large beam

The first measurement done was to see subradiance with this new setup, since the laser source was replaced and the probe beam has a new spectral broadening compared with the previous setup. Fig. 4.11 shows the emitted intensities for several  $b_0$  at  $\Delta = -3.15\Gamma$

[panel (a)] and the exponential fits done at the slow part, for several  $b_0$  and  $\Delta$  [panel (b)]. The fit interval was done at the same range as for subradiance discussed in Chapter 2, i.e., one decade above the noise level. We see in (a) that the slope increases for increasing  $b_0$ , and in (b) that the fitted decay rates collapse on the same line for several  $\Delta$ , a signature of subradiance. The solid line is a linear fit  $\tau_{\text{sub}}/\tau_0 = 1 + c b_0$  of the data, where the constant  $c$  was found to be  $c = 0.65$ . By converting this constant for the definition  $b_0 = 3N/(kR)^2$  in order to compare with the value  $c = 0.8$  obtained in Chapter 2, we have  $c = 0.65 \times 7/15 = 0.30$ , much smaller than those obtained initially.

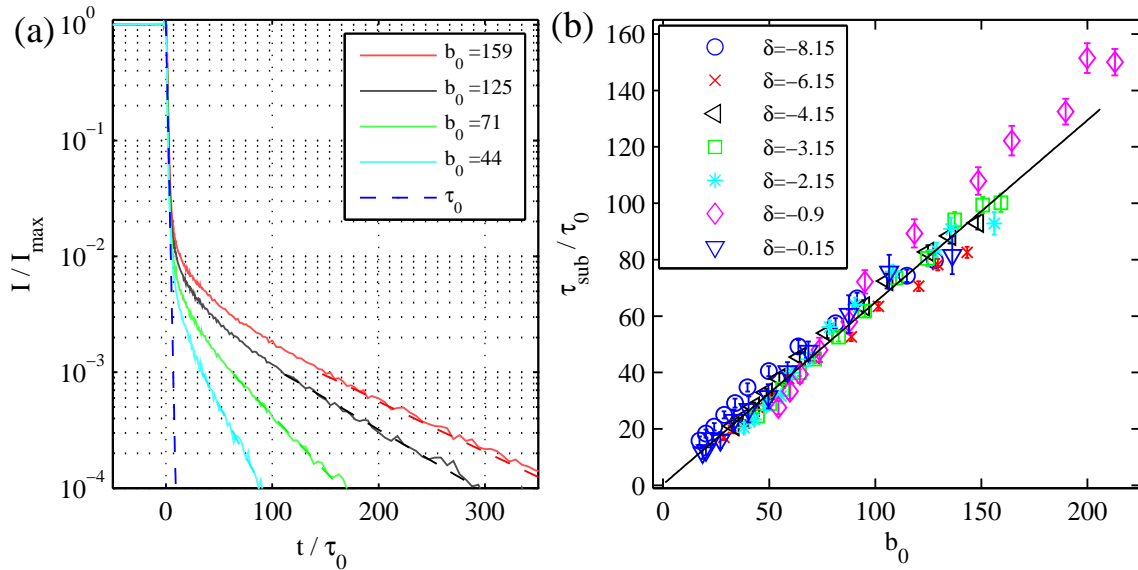


**Figure 4.11:** Experimental data obtained from the large beam setup. **(a)** Experimental emitted intensities as a function of time, for several resonant optical thicknesses  $b_0$  and  $\Delta = -3.15\Gamma$ , with the large probe beam. The dashed blue line is the decay for a single atom. **(b)** Experimental decay rates as a function of  $b_0 = 3N/(k_0R)^2 \times 7/15$  for several  $\Delta$ . The solid black line is a linear fit of the data. Parameters:  $s(\Delta) \approx 10^{-2}$ .

## 4.5.2 Data for small beam

For the data with the small beam setup, the saturation parameter was set initially to  $s(\Delta) = 0.1$ , i.e., ten times larger than for the super- and subradiance experiments. This is because a small size beam at resonance implies in a weak emitted intensity, which makes worse the signal-to-noise ratio, since the incoming beam is strongly attenuated when penetrating the cloud. From the definition of  $s(\Delta)$ , we have  $s(\Delta) = g \times s_0/(1 + 4\Delta^2/\Gamma^2)$  with  $g = 7/15$ ,  $\Delta = 0$ ,  $s_0 = I/I_s$ , where  $I = 2P/(\pi w_0^2)$ ,  $w_0 = 200 \mu\text{m}$  and  $I_s = 1.7 \text{ mW/cm}^2$ , so we obtain  $P = 229 \text{ nW}$ . This value is very small compared with the required power for the large beam setup. On the other hand, as the effective  $s(\Delta)$  seen by the atoms inside the cloud decreases as long as the incident beam propagates (shadow effect discussed in [Chabé 2014]), we decided to increase the value of  $s(\Delta)$  to 0.2, 0.5 and even 1.0, in order to improve the signal-to-noise ratio. The values of the fitted decay rates were compared for different  $s(\Delta)$  to check that there are only linear effects.

Figure 4.12 shows the temporal emitted intensities, acquired with the small beam setup, for several values of  $b_0$  and constant  $\Delta = -0.9\Gamma$ . We see that the intensities present

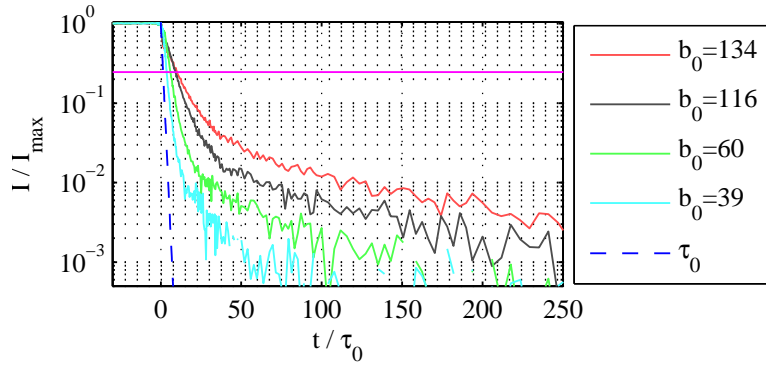


**Figure 4.12:** Experimental emitted intensities as a function of time, for several resonant optical thicknesses  $b_0$  and  $\Delta = -0.90\Gamma$ , with the small probe beam. The dashed blue line is the decay for a single atom.

two slow decay regimes compared with the single atom decay: an *intermediate* decay, around  $\sim [10^{-2}, 10^{-1}]$  in amplitude, and a *very late* decay, from amplitudes smaller than  $10^{-2}$ . The late decays seem to vary with  $b_0$  like the data for the large beam in Fig. 4.11(a) and the numeric data for small beam in Fig. 4.3, which may be a signature of subradiance. The intermediate decay takes place at the same amplitude range in [Labeyrie 2003], and may be radiation trapping.

In order to characterize these two decay regimes, we extracted the corresponding decay rates and plotted them as a function of  $b_0$  and  $b(\Delta)$ . For the late decay rate, we did an exponential fit in the same range as for the subradiance data for large beam, i.e., one decade above the noise level. For the intermediate decay, we set the decay rate  $\tau_{\text{RT}}$  equal to the time  $t$  where the intensity decays to  $1/e = 0.368$  of its value at  $t = 0$ .

Figure 4.13 displays the fitted decay rates, plotted as a function of  $b_0$  and  $b(\Delta)$ , for the intermediate decay [panels (a) and (b), labeled  $\tau_{\text{RT}}$ ] and the late decay [panels (c) and (d), labeled  $\tau_{\text{sub}}$ ]. In (a), we see that  $\tau_{\text{RT}}$  does not scale at all with  $b_0$ , but in (b) they scale well with  $b(\Delta)$ , which is a signature of radiation trapping. This should be compared with the data in [Labeyrie 2003], where radiation trapping was observed at the same amplitude range and showed to agree with simulations by taking into account the frequency redistribution.

For the late decay rates  $\tau_{\text{sub}}$ , [Labeyrie 2003] does not study them because his detector, a standard photomultiplier, measures only amplitudes  $\sim 10^{-2}$ , whereas in our setup, we use a hybrid photomultiplier able to reach amplitudes  $\leq 10^{-4}$  (c.f. Fig. 2.10). Also, in our setup we have a better extinction ratio and longer integration time, as discussed in Chapter 2. We see in panel (d) that  $\tau_{\text{sub}}$  do not scale at all with  $b(\Delta)$ . In (c), they vary linearly with  $b_0$ , but they do not collapse into a single line as well as the  $\tau_{\text{sub}}$  obtained from the large beam setup, represented by the dashed line. We attribute this to noise effect from the intensities measured with the small beam setup, due to the low power collected in the measured intensities.

As a last comment, numerical simulations with the random walk model by including the experimental temperature and the current laser spectrum were run in order to calculate  $\tau_{\text{RT}}$  versus  $b(\Delta)$  as in Fig. 4.13(c). Also, emitted intensities with the small beam setup were calculated for comparison with the experimental ones. All the obtained results

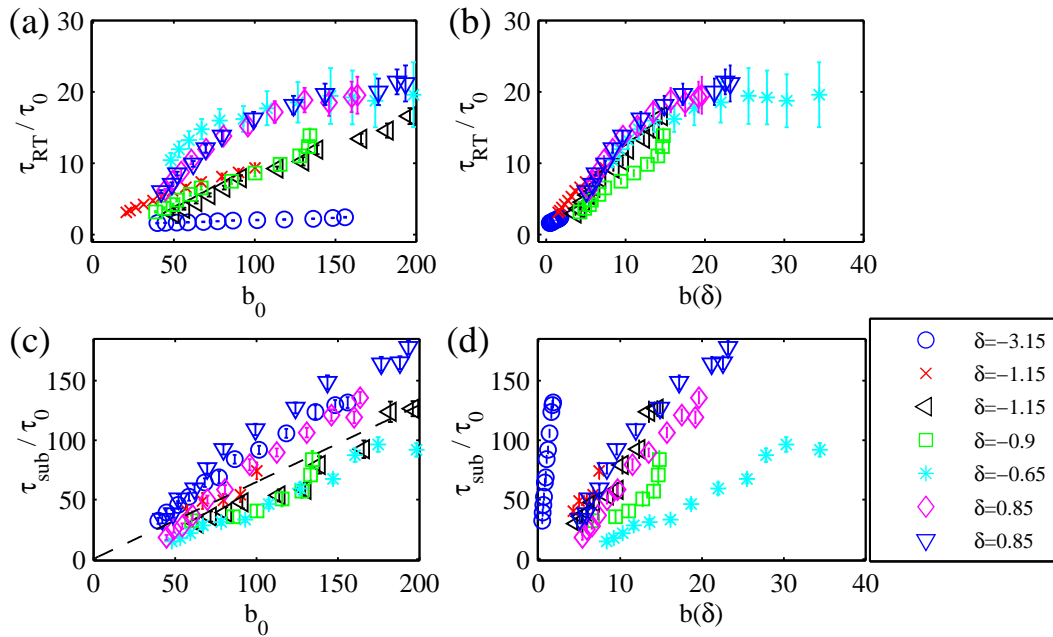


**Figure 4.13:** Experimental decay rates for the small beam setup, for several detunings  $\delta = \Delta/\Gamma$ . **(a)** Intermediate decay rate  $\tau_{RT}$  as a function of  $b_0 = 3N/(k_0R_x)(k_0R_y) \times 7/15$  **(b)** Intermediate decay rate as a function of  $b(\delta)$  **(c)** Late decay rate as a function of  $b_0 = 3N/(k_0R_x)(k_0R_y) \times 7/15$  **(d)** Late decay rate as a function of  $b(\delta)$ . The dashed black line in (c) is the linear fit in Fig. 4.11(b).

were shown to agree with the experiment. In addition, more simulations were run by considering possible anisotropy of the cloud and misalignment of the probe beam in the cloud center. These effects were shown to be negligible. The reader can find the detailed discussion in [Weiss 2018].

### 4.5.3 Attempt to decrease the temperature of the cloud

The experimental data shown in the two last subsections and their comparison with the theory show well the occurrence of radiation trapping and subradiance for the same sample in the emitted intensities, for certain values of  $b_0$  and  $\Delta$ . The cloud temperature was  $100 \mu\text{K}$ , a value optimized with the dark MOT phase. However, in our laboratory, after obtaining these experimental data, we wanted to use a molasses phase to control the temperature of the cloud in order to perform a systematic study of radiation trapping and subradiance as a function of temperature.

As already mentioned, the molasses phase was added after the MOT loading, dark MOT and extinction of the magnetic field, and its goal is to control the cloud temperature for the main measurements. It consists in turning on the MOT six beams and the two repumper beams during a time  $t_{mol}$ . Then, the TOF is run to measure  $b_0$  just after the molasses duration and the temperature. It is known from MOT theory that the cloud temperature varies as  $T \propto I_{MOT}/|\Delta_{MOT}|$  [Foot 2005], where  $I_{MOT}$  and  $\Delta_{MOT}$  are the intensity and detuning of the MOT beams, so  $T$  decreases if  $I_{MOT}$  decreases and/or  $\Delta_{MOT}$  increases to the red. Also,  $T$  decreases for increasing  $t_{mol}$  and reaches a constant value.

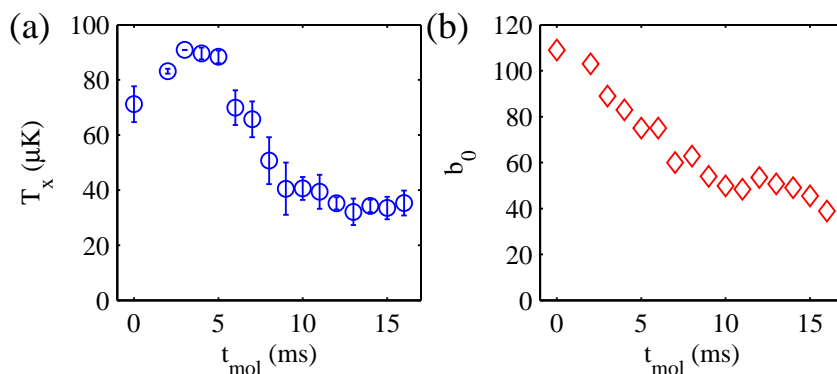
Before adding the molasses phase, we varied  $\Delta_{\text{MOT}}$  during the dark MOT phase (we had up to here  $\Delta_{\text{MOT}} = -5\Gamma$ ; see section 4.4.2). Also, we decided to vary  $\Delta_{\text{MOT}}$  smoothly by adding a *sweep* function  $R$ , i.e., to increase  $\Delta_{\text{MOT}}$  to the desired value from its value at the MOT loading phase, which is  $\Delta_{\text{MOT}} = -4\Gamma$ . For example, if we set  $\Delta_{\text{MOT}} = -5R\Gamma$ , this means that  $\Delta_{\text{MOT}}$  will increase linearly from  $-4\Gamma$  to  $-5\Gamma$  during the time duration of the dark MOT phase. This linear increasing is to avoid atom losses, compared if  $\Delta_{\text{MOT}}$  is set abruptly to  $\Delta_{\text{MOT}} = -5\Gamma$ . A comparison between  $\Delta_{\text{MOT}}$  with and without the sweep shows that we lose less atoms in the former.

Table 4.2 shows the temperatures and  $b_0$  measured for some values of  $\Delta_{\text{MOT}}$ . The value  $T = 98 \approx 100 \mu\text{K}$  is the value we had for the radiation trapping measurements. We see that  $\Delta_{\text{MOT}} = -6R\Gamma$  gives the largest  $b_0$  and a smaller temperature.

$\Delta_{\text{MOT}}/\Gamma$	$b_0$	$T$ ( $\mu\text{K}$ )
$-5R$	69	98
$-6R$	75	80
$-7R$	67	77
$-8R$	51	63

**Table 4.2:** Measurement of  $b_0 = 3N/(k_0R_x)(k_0R_y) \times 7/15$  and temperature  $T$  by changing the detuning  $\Delta_{\text{MOT}}$  of the MOT laser beams during the dark MOT phase. The symbol  $R$  at the  $\Delta_{\text{MOT}}$  values means that  $\Delta_{\text{MOT}}$  was varied linearly from  $\Delta_{\text{MOT}} = -4\Gamma$ . Other parameters:  $\Delta_{\text{MOT}} = -\Gamma$ ,  $I_{\text{MOT}}$  at its maximum value,  $I_{\text{REP}} = 0.39 I_{\text{REP max}}$ .

So, we modified  $\Delta_{\text{MOT}} = -6R\Gamma$  for the MOT beams during the dark MOT phase and then we turned on the molasses phase in order to decrease more this temperature. Firstly we set  $\Delta_{\text{MOT}} = -10\Gamma$  during the molasses phase ( $\Delta_{\text{MOT}}$  can be varied from  $-\Gamma$  to  $-11\Gamma$  in the double-pass AOM without power losses) and then we increased  $t_{\text{mol}}$ , for other parameters fixed. Naturally, as  $t_{\text{MOT}}$  increases,  $b_0$  drops due to the cloud expansion, so we also measured  $b_0$  to see how it drops.



**Figure 4.14:** Cloud temperature  $T_x$  along the  $x$  direction as a function of the molasses duration  $t_{\text{mol}}$ , for  $b_0 = 3N/(k_0R_x)(k_0R_y) \times 7/15$  and  $\Delta_{\text{MOT}} = -10\Gamma$ . Other parameters:  $\Delta_{\text{REP}} = -\Gamma$ ,  $I_{\text{MOT}}$  and  $I_{\text{REP}}$  at their maximum values.

Figure 4.14 shows  $T_x$  [panel (a)] and  $b_0$  [panel (b)] as a function of  $t_{\text{mol}}$ . The temperature was measured only along the direction  $x$  because in this measurement the fits along  $y$  direction were very bad, for reasons that we could not understand. In (a), we see that,

after a small increase,  $T_x$  starts to decrease and remains constant from  $t_{\text{mol}} \geq 13$  ms, with a value  $T_x \approx 34 \mu\text{K}$ . On the other hand, in (b),  $b_0$  drops from  $b_0 = 103$  to 51 for  $t_{\text{mol}} = 13$  ms and to  $b_0 = 39$  for  $t_{\text{mol}} = 16$  ms.

At this point, the following step is to repeat the measurement above with  $\Delta_{\text{MOT}}$  more detuned and by changing  $I_{\text{MOT}}$  and  $I_{\text{REP}}$  (maybe it will be not necessary because  $b_0$  may drop more). However, the tapered amplifier (TA) in our experimental setup (see Fig. 2.7), which provides the power for our MOT laser beams, broke and, as the substitution and new measurements would require some additional months, we decided to try to publish the experimental radiation trapping data already discussed. The systematic study of radiation trapping and subradiance as a function of temperature thus remains to be studied and is part of the next experiments to be performed on this work.

## 4.6 Conclusions of this chapter

The main conclusion about the interplay between subradiance and radiation trapping is that we could perform an improved experiment with a narrow beam exciting the atoms, concerning good extinction of the probe beam and better average in the measured signals. In the decay dynamics, radiation trapping is the first phenomenon to take place, and then subradiance comes later, at lower amplitudes. Also, the strongest dependence of radiation trapping with the detuning of the incoming beam suggests that one should consider only interactions close to resonance to see radiation trapping and subradiance at the same time. Therefore, both phenomena occurs, which shows the robustness of subradiance with the laser detuning and even with the laser beam size.

## Phased cloud and temperature effects

In the last chapters, we discussed super- and subradiance theoretically and experimentally in a cloud of cold atoms with the coupled-dipole model, our main tool for describing the response of  $N$  atoms after interacting with a plane wave, i.e., a large-sized field compared with the cloud dimensions. The interactions of all atoms with the field give rise to cooperative effects like super- and subradiance, discussed in Chapters 1 to 3. The discussion relies on the coupled-dipole equations for the dipole amplitudes  $\beta_j$ , Eqs. 1.15, rewritten below

$$\dot{\beta}_j = \left( i\Delta - \frac{\Gamma}{2} \right) \beta_j - \frac{i\Omega}{2} e^{i\vec{k}_0 \cdot \vec{r}_j} - \frac{\Gamma}{2} \sum_{j' \neq j} \frac{e^{ik_0 r_{jj'}}}{ik_0 r_{jj'}} \beta_{j'} \quad (5.1)$$

and the emitted intensity  $I(\theta, \phi, t)$  in Eq. 1.34, rewritten below

$$I(\theta, \phi, t) \propto \sum_j \sum_{j'} \beta_j(t) \beta_{j'}^*(t) e^{-ik_0(x_{jj'} \sin \theta \cos \phi + y_{jj'} \sin \theta \sin \phi + z_{jj'} \cos \theta)} \quad (5.2)$$

(also Eq. 1.35 depending on symmetry considerations and Eq. 1.29 for the total emitted intensity). In Chapter 4, the interaction field was modified to a truncated plane wave with a small size compared to the cloud size, which allowed us to discuss radiation trapping and its interplay with subradiance.

In this chapter, we modify the original setup of  $N$  atoms and light field in order to obtain new features in the emitted intensity and cooperative effects. More precisely, we discuss two specific setups: the *phased cloud*, which takes into account a plane wave with a phase difference in its spatial profile; and *temperature effects*, which investigates the impact of the atomic motion in the case of plane wave excitation. The former has as main result an increase of the subradiant amplitude level, which can be an improvement for its experimental detection. The latter suppresses the cooperative effects when the temperature becomes significantly large. Experiments will be run in the future in our laboratory in order to observe and characterize these predictions.

This chapter is divided in three sections. In section 5.1, we present and discuss the phased cloud setup. In section 5.2, we discuss the coupled-dipole model with temperature and the harmonic oscillator model as a procedure for our simulations, in order to simulate the atomic motion without cloud expansion, as well as its impact in the cooperative decay

rates. Finally, in section 5.3 we summarize the obtained conclusions.

## 5.1 Excitation with a phased cloud

### 5.1.1 Description

Super- and subradiance are cooperative effects related to the phase of the dipole oscillations, which plays a role on the decay rates due to the interference of the light fields scattered by the dipoles. For far-detuned light, both the amplitudes and the decay rates magnitudes are modeled by the cloud parameters, which determine the coherence strength created between the dipoles when interacting with the incident light field.

Based on [Scully 2015], which proposes a setup with two clouds excited by laser beams with a phase shift, we propose what we call a *phased cloud* setup (Fig. 5.1). Like in the Chapters 1 to 3, a monochromatic plane wave excites a cloud of  $N$  two-level atoms, with the difference that the incoming beam goes through a wave plate of different thicknesses before reaching the atoms. The thickness of the wave plate is built in a such way that half of the incoming beam is shifted to a phase of  $\pi$  with respect to the other half. By setting a Cartesian coordinate frame with the laser beam on the  $z$  axis and cloud center at the origin (c.f. Fig. 1.2), the setup is arranged such that the cloud side  $y > 0$  is excited by a phase  $\delta = \pi$  with respect to the side  $y < 0$ . Hence, the atoms in the respective halves are excited by a field with a phase difference of  $\pi$  with respect to each other.

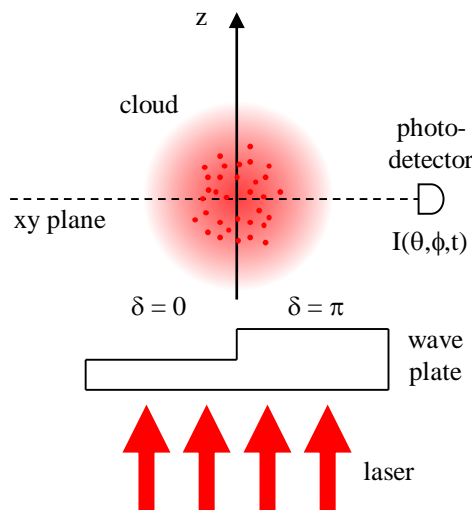


**Figure 5.1:** The phased cloud setup. A cloud of  $N$  identical and motionless atoms interacts with a laser beam and vacuum modes. The beam is set on the  $z$  axis and the wave plate has different thickness in a such way that half of the beam at the side  $y > 0$  suffers a phase shift of  $\delta = \pi$  with respect to the side  $y < 0$  ( $\delta = 0$ ). The detector measures the intensity  $I(\theta, \phi, t)$  given by Eq. 5.2. In the figure, the detector is placed on the  $xy$  plane, i.e.,  $\theta = 90^\circ$  and  $\phi \in [0, 2\pi]$ .

Due to the phase shift in each half of the cloud, the coupled-dipole equations, Eqs. 1.15, are written as

$$\dot{\beta}_j = \left( i\Delta - \frac{\Gamma}{2} \right) \beta_j - \frac{i\Omega}{2} e^{ik_0 z_j} - \frac{\Gamma}{2} \sum_{\substack{j'=1 \\ j' \neq j}}^{N'} \frac{e^{ik_0 |\vec{r}_j - \vec{r}_{j'}|}}{ik_0 |\vec{r}_j - \vec{r}_{j'}|} \beta_{j'} \quad (5.3a)$$

$$\dot{\beta}_j = \left( i\Delta - \frac{\Gamma}{2} \right) \beta_j - \frac{i\Omega}{2} e^{i(k_0 z_j + \pi)} - \frac{\Gamma}{2} \sum_{\substack{j'=N'+1 \\ j' \neq j}}^N \frac{e^{ik_0 |\vec{r}_j - \vec{r}_{j'}|}}{ik_0 |\vec{r}_j - \vec{r}_{j'}|} \beta_{j'} \quad (5.3b)$$

where Eqs. 5.3a are for the  $j' = \{1, \dots, N'\}$  atoms at the  $y < 0$  side (phase shift  $\delta = 0$ ), i.e., as before, and Eqs. 5.3b are for the  $j' = \{N' + 1, N' + 2, \dots, N\}$  atoms at the  $y > 0$  side (phase shift  $\delta = \pi$ ), i.e., a phase of  $e^{i\pi}$  in the second term. In words: each atom  $j$  sees the interaction with all the other  $N - 1$  atoms, as previous, but a phase term is present or absent in the driving field depending on which side the atom  $j$  lies.

As before, the incoming field excites the cloud during enough time that a steady state is reached, and then the emission dynamics is analyzed after the incident field is extinguished. We use Eq. 5.2 to compute the emitted intensity by the cloud, for a chosen direction  $\{\theta, \phi\}$ . In Eq. 5.2,  $\theta$  is the polar angle, measured from the  $z$  axis, and  $\phi$  is the azimuth angle, lying on the  $xy$  plane (see Fig. 1.2 for the definition of  $\theta$  and  $\phi$ ). Note that, as the phased cloud is not symmetric with respect to the  $z$  axis, we cannot use Eq. 1.35 to compute the emitted intensity (see subsection 1.2.2).

### 5.1.2 Simulation methods

The simulation procedure for the phased cloud setup is the same described in section 1.3: a Gaussian spherical cloud of RMS size  $k_0 R$  and atom number  $N$  has an resonant optical thickness  $b_0 \propto N/(k_0 R)^2$  and density  $n_0 \lambda^3 = (2\pi)^{3/2} N/(k_0 R)^3$ , and it is excited by a laser beam of detuning  $\Delta$ . The atomic positions  $\vec{r}_j$  are drawn randomly in space and then an exclusion condition is applied to restrict the simulations to dilute clouds without close pairs.

Equations 5.3 are solved numerically by means of the fourth order Runge-Kutta method, for a set of atomic positions and a value of the detuning  $\Delta$  of the incoming beam. Then, the solutions  $\beta_j(t)$  are obtained and substituted in Eq. 5.2, as well as the atomic positions, in order to obtain the emitted intensity for each instant  $t$ , for a given direction  $\theta$  and  $\phi$ . Then, as the intensity may present oscillations and spurious numerical effects, it is calculated for several configurations of the atomic positions and averaged. Finally, an exponential fit is done in an appropriate interval in order to extract the cooperative decay rates.

### 5.1.3 Numerical results

The study for the phased cloud was done only for far-detuned light and for a single value of  $b_0$  and  $n_0 \lambda^3$ , in order to make a qualitative study about the differences between the phased cloud setup compared with the standard setup discussed in the previous chapters. In the following, we label *normal cloud/normal excitation* the standard setup without phase shift, and *phased cloud/phased excitation* the phased cloud setup.

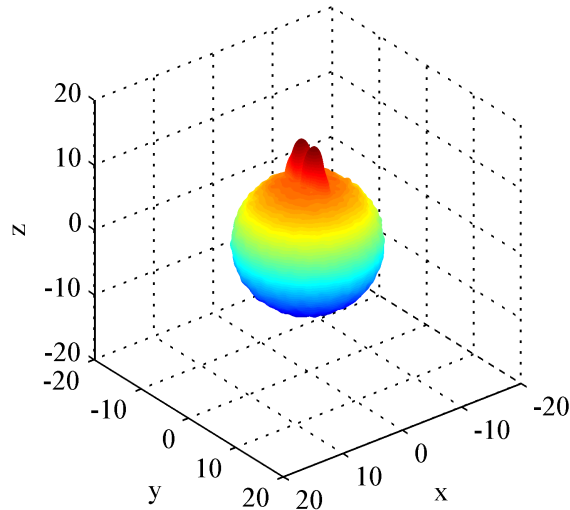


**Figure 5.2:** Emission diagram for the phased cloud in the steady state. Parameters:  $b_0 = 2N/(k_0R)^2 = 8.55$ ,  $n_0\lambda^3 = 4.6$  ( $N = 921$ ),  $\Delta = 10\Gamma$ , averaged over 100 realizations.

We start by presenting the emission diagram for the phased cloud. Fig. 5.2 shows the emission diagram in three dimensions, computed with Eq. 5.2 in the steady state for several values of  $\theta$  and  $\phi$ . We see that the forward lobe is divided in two, a remarkable difference with respect to the setup with no phase shift, where a single lobe is observed [c.f. Fig. 1.5(a)]. Thus, the phase difference seen by the two cloud halves has the net effect of separating the forward lobe in two, as if each half corresponded to two independent clouds with phase difference of  $\pi$ . A deviation in the emission forward lobe also due to a phase shift seen by the atoms in an atomic cloud was reported in [Máximo 2014], but in this case the phase shift is produced by an inhomogeneous magnetic field.

Due to this lobe separation, the maximum emission intensity is reached at an angle  $\theta$  slightly larger than zero, compared to the normal cloud where the lobe peak is exactly at  $\theta = 0$ . For  $\theta = 0$  in the phased cloud setup, the intensity has the same value as for those out of the lobe region, and this position is also the border between the two cloud sides. The two lobes are symmetric to each other. Also, the value of the intensity at the two peaks in the phased cloud is smaller than the value of the single peak in the normal cloud, meaning that the total intensity is only redistributed.

Now we turn to the emitted intensity from the steady state. Fig. 5.3(a) shows emitted intensities for the direction  $\{\theta = 90^\circ, \phi = 90^\circ\}$ , i.e., a detector placed orthogonally to the  $z$  axis and on the  $y$  axis in the positive side, i.e., the  $\delta = \pi$  side (like in Fig. 5.1). We see that the decay amplitude for the phased cloud has a higher amplitude compared to the normal setup, meaning an increase in the subradiance level. Also, we see that the two curves are practically parallel (same slope), showing that the decay rate is not impacted.

The ratio between the phased and normal intensities is plotted in Fig. 5.3(b), for all  $t$ . By choosing a range which corresponds to the subradiant part displayed in (a), e.g.,  $t \in [12, 115]\tau_0$ , we see that the ratio is equal to 6 – 8. This represents a significant gain in the subradiance amplitude in the phased cloud setup.

Figure 5.4 displays the ratio between the intensities for more detection directions in

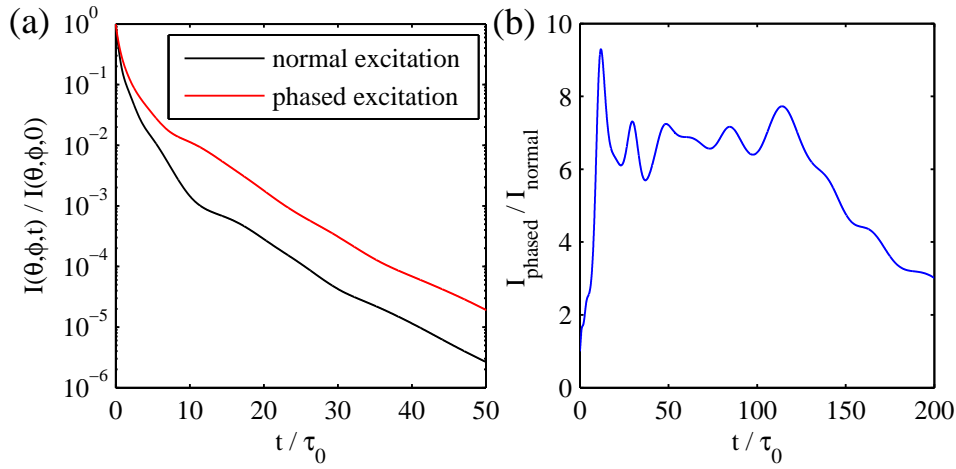


**Figure 5.3:** (a) Emitted intensities  $I(\theta, \phi, t)$  from Eq. 5.2 for the phased cloud (red) compared to a identical cloud with no phase excitation (black), calculated for  $\theta = 90^\circ$  and  $\phi = 90^\circ$ . (b) Ratio between the curves in (a), where  $I_{\text{phased}}$  and  $I_{\text{normal}}$  are the normalized intensities  $I(\theta, \phi, t) / I(\theta, \phi, 0)$  for the phased and normal clouds, respectively. Parameters: same as in Fig. 5.2.

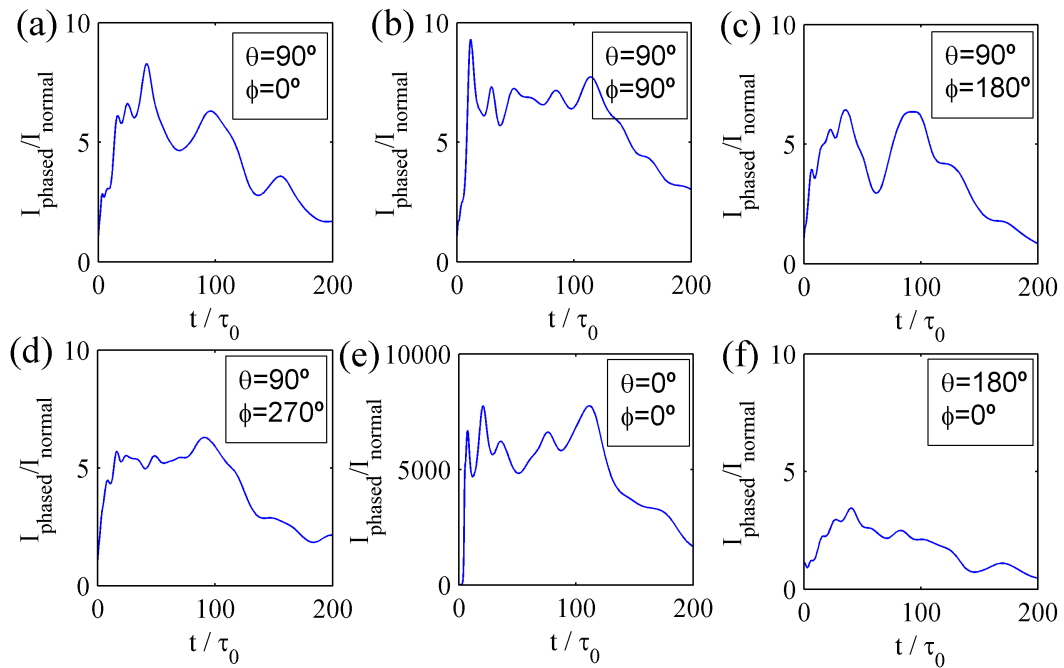


**Figure 5.4:** Ratio between the intensities  $I_{\text{phased}} / I_{\text{normal}}$  for several detection positions on the space. Parameters: same as in Fig. 5.2.

space. All of them were calculated similarly to Fig. 5.3(b), from intensities similar to the ones in 5.3(a). We see that, for the directions lying on the plane  $xy$  [panels (a) to (d)], the increase factor is  $\approx 5 - 8$  [the panel (b) is the Fig. 5.3(b) already discussed], meaning that on the  $xy$  plane, the enhancement in subradiance amplitude is the same. On the other hand, for the forward direction [ $\theta = 0$ ; panel (e)], the ratio is huge. This is because, as already discussed, at  $\theta = 0$  the normal cloud has its lobe and the maximum value, whereas the phased cloud has its intensity at the same value for directions out of its two lobes. The normalization makes the amplitudes for the normal cloud to go down, and the calculation  $I_{\text{phased}}/I_{\text{normal}}$  becomes high. Finally, for the backscattering direction [panel (e)], the ratio is not significant, meaning that there is no enhancement in the subradiant amplitude calculated in that direction.

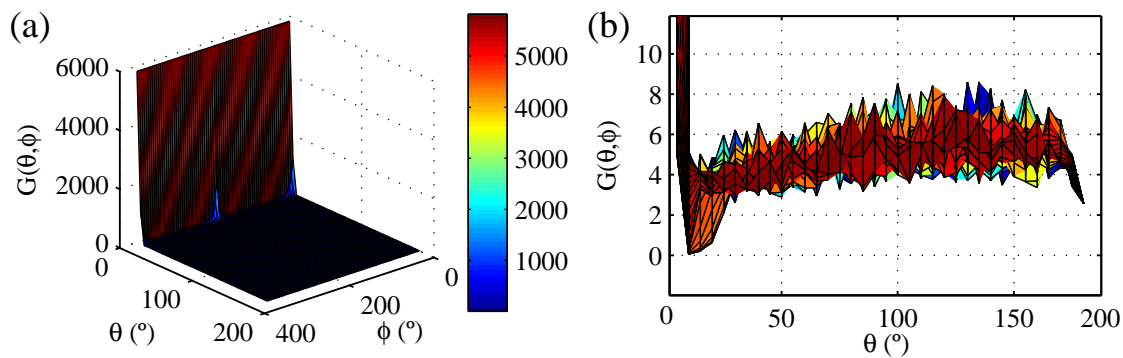


**Figure 5.5:** (a) Average ratio  $G(\theta, \phi)$  as a function of  $\theta$  and  $\phi$ , where  $G(\theta, \phi)$  is the average of the values of  $I_{\text{phase}}(t)/I_{\text{normal}}(t)$  in the interval  $t \in [25, 100]\tau_0$ . (b) Rotation of (a) in a such way that the  $\phi$  axis is perpendicular to the plane of the page, towards the reader. Parameters: same as in Fig. 5.2.

Another way to analyze the ratio between the intensities for the phased and normal clouds is to take the average value of  $I_{\text{phased}}/I_{\text{normal}}$  in a range where it is significantly enhanced, e.g.,  $t \in [25, 100]\tau_0$  [see Fig. 5.3(b), c.f. Fig. 5.4]. Labeling  $G(\theta, \phi)$  this average value, and repeating the simulation for more values of  $\{\theta, \phi\}$  in order to cover more detection positions, we obtain Fig. 5.5. In (a), we see that, for  $\theta \approx 0$  and all  $\phi$ ,  $G(\theta, \phi)$  is high like discussed in Fig. 5.4(e). For  $\theta \gtrsim 0$ ,  $G(\theta, \phi)$  decreases drastically and, from a given value of increasing  $\theta$ ,  $G(\theta, \phi)$  is roughly constant.

Figure 5.5(b) is a side view of (a), zoomed for small  $G(\theta, \phi)$  for a better visualization. We see that, except around the forward direction,  $G(\theta, \phi) \approx 6 - 8$  between  $\theta \in [50^\circ, 150^\circ]$ , meaning that the enhancement of subradiance is practically constant for all detection directions. This does not depend on the detector placement with respect to the cloud halves. Therefore, the subradiance amplitude level is improved practically for all directions in the phased cloud setup.

## 5.2 Temperature effects

### 5.2.1 The coupled-dipole model with temperature

So far we have discussed the coupled-dipole model for motionless atoms, which means zero temperature. In experiments, no real physical situation accomplishes total absence of motion and, as discussed in Chapters 2 to 4, the temperature of the atomic cloud in our experiments were 50 and 100  $\mu\text{K}$ . We had to show with numerical simulations that such temperatures do not play any significant role for cooperative effects (see Fig. 2.5), although for radiation trapping the temperature effects are more important in the decay dynamics. In this section, we discuss the details of the simulations with temperature for the standard cloud setup excited by a plane wave (setup of Chapters 1 to 3), and we will see that higher temperatures impact the super- and subradiant decays.

To include the temperature in the coupled-dipole model, the idea is to allow the atoms to move, so the atomic positions  $\vec{r}_j$  will be functions of the time  $t$ . Consequently, the second and third terms in the coupled-dipole equations, Eq. 5.1, are now functions of  $t$ :

$$\dot{\beta}_j = \left( i\Delta - \frac{\Gamma}{2} \right) \beta_j - \frac{i\Omega}{2} e^{i\vec{k}_0 \cdot \vec{r}_j(t)} - \frac{\Gamma}{2} \sum_{j' \neq j} \frac{e^{ik_0|\vec{r}_j(t) - \vec{r}_{j'}(t)|}}{ik_0|\vec{r}_j(t) - \vec{r}_{j'}(t)|} \beta_{j'} \quad (5.4)$$

After the steady state is reached and after the driving field is extinguished, the emitted intensity  $I(\theta, \phi, t)$  in a detection direction (Eq. 5.2, and also Eq. 1.35), as well as the total emitted power  $P(t)$  (Eq. 1.29 rewritten below)

$$P(t) \propto -\frac{d}{dt} \sum_j |\beta_j(t)|^2 \quad (5.5)$$

depend on these new  $\beta_j(t)$ s in Eqs. 5.4. Then, by setting a reference frame where the incoming laser travels along the  $z$  axis and the cloud center is at the origin of the  $x$  and  $y$  axis (see Fig. 1.2), we have  $\vec{k}_0 = k_0 \hat{z}$  and

$$|\vec{r}_j(t) - \vec{r}_{j'}(t)| = \sqrt{[x_j(t) - x_{j'}(t)]^2 + [y_j(t) - y_{j'}(t)]^2 + [z_j(t) - z_{j'}(t)]^2}$$

in the second and third terms of Eq. 5.4, respectively. Therefore, in order to solve Eq. 5.4, we need expressions for the position components  $x_j(t)$ ,  $y_j(t)$ ,  $z_j(t)$ .

### 5.2.2 The ballistic model

The atomic cloud is a vapor, so the atomic motion is about each atom having a velocity  $\vec{v}$ . When the MOT is turned off, the cloud performs a free expansion and the incoming laser beam is turned on to excite the cloud (see subsection 2.2.4). As discussed in section 1.3, the interaction is modeled as a square pulse of a given time duration, large enough to allow a steady state before the decay.

The velocity  $\vec{v}$  of each atom during the cloud expansion has constant magnitude and a given direction in space. The directions of all velocities are random, but its magnitude is given by the Maxwell-Boltzmann probability distribution [Salinas 2001]

$$P(v) = \frac{1}{\sqrt{2\pi}\sigma_v} \exp\left(-\frac{v^2}{2\sigma_v^2}\right) \quad (5.6)$$

where  $v$  is the magnitude of each one of the components  $\{v_x, v_y, v_z\}$  of  $\vec{v}$ , for each atom in the cloud. The parameter

$$\sigma_v = \sqrt{\frac{k_B T}{M}} \quad (5.7)$$

is the standard deviation of  $v$ , where  $T$  is the temperature of the sample,  $k_B$  is the Boltzmann constant and  $M$  is the atom mass. We can also write Eq. 5.7 in adimensional form as

$$\frac{k_0\sigma_v}{\Gamma} = \frac{k_0}{\Gamma} \sqrt{\frac{k_B T}{M}} \quad (5.8)$$

The parameter  $k_0\sigma_v/\Gamma$  is the parameter we will use to describe temperature effects. It is related to the temperature  $T$  by simply isolating  $T$  in Eq. 5.8:

$$T = \frac{M}{k_B} \left( \frac{k_0\sigma_v}{\Gamma} \times \frac{\Gamma}{k_0} \right)^2 \quad (5.9)$$

With Eqs. 5.8 and 5.9 we can determine the value of  $k_0\sigma_v/\Gamma$  for a known  $T$  and vice-versa. Some examples: for the temperatures 50 and 100  $\mu\text{K}$  we obtain  $k_0\sigma_v/\Gamma = 0.0146$  and 0.0207, respectively, so  $k_0\sigma_v/\Gamma \sim 10^{-2}$ ; for  $k_0\sigma_v/\Gamma = 0.1$  (10 times higher), we have  $T = 2.34$  mK. Also, the functional dependencies of these quantities are  $k_0\sigma_v/\Gamma \propto \sqrt{T}$  and  $T \propto (k_0\sigma_v/\Gamma)^2$ . The values of the constants  $M$ ,  $k_0$  and  $\Gamma$  depend on the atomic species. For  $^{87}\text{Rb}$  in the transition  $F = 2 \rightarrow F' = 3$  (see Chapter 2), the values are [Steck 2001]:  $\Gamma = 2\pi \times 6.066$  MHz,  $k_0 = 2\pi/\lambda$  with  $\lambda = 780$  nm, and  $M = 1.44 \times 10^{-25}$  kg.

When the cloud expands, each atom  $j = 1, \dots, N$  in the atomic cloud performs a linear motion with constant velocity, so their positions components evolve linearly in time:

$$\begin{aligned} x_j(t) &= x_j(0) + v_{xj}t \\ y_j(t) &= y_j(0) + v_{yj}t \\ z_j(t) &= z_j(0) + v_{zj}t \end{aligned} \quad (5.10)$$

for an initial  $t = 0$ . The velocities  $\{v_{xj}, v_{yj}, v_{zj}\}$  come from the distribution  $P(v)$  in Eq. 5.6 for a given  $k_0\sigma_v/\Gamma$ , so we have analytical expressions for the temporal positions and Eqs. 5.4 can be solved.

The cloud expansion due to the atomic ballistic motion implies in an increase of the cloud size  $R(t)$  with  $t$  according to

$$R(t)^2 = R(0)^2 + v_{\text{RMS}}^2 t^2 \quad (5.11)$$

(c.f. Eq. 2.9; see subsection 2.2.6), where  $v_{\text{RMS}} \approx \sigma_v$  for large atom number  $N$ . Eq. 5.11 can be written in adimensional form as

$$(k_0 R(t))^2 = (k_0 R(0))^2 + \left(\frac{k_0 \sigma_v}{\Gamma}\right)^2 (\Gamma t)^2 \quad (5.12)$$

During the pulse excitation, the cloud size  $R(t)$  indeed increases, however, in the experiment this increase is neglected. This is because typical experimental values of the cloud size are very high, in order of  $k_0 R(0) \sim 10^3$  (because  $R(0) \sim 10^{-3}$  and  $k_0 \sim 10^6 \text{ m}^{-1}$ ; see section 1.3 and subsection 2.2.4). Then, for a light excitation of duration  $\Gamma t \sim 10^3$  (because  $\Gamma \sim 2\pi \times 6.066 \text{ MHz}$  and  $t = 30 \mu\text{s}$  in the experiment) and, e.g.,  $k_0 \sigma_v / \Gamma = 0.1$ , the last term of Eq. 5.11 is equal to  $(k_0 \sigma_v / \Gamma)^2 (\Gamma t)^2 \sim 10^3$ , i.e., much smaller than  $(k_0 R(0))^2$ , so  $k_0 R(t) \approx k_0 R(0)$  and the cloud increase is practically negligible. However, in the simulations,  $k_0 R(0) \sim 10$ , i.e., much smaller than the experimental value, and a excitation duration of  $\Gamma t \sim 10^2$  leads to an increase of  $\sim 50\%$  in the cloud size  $k_0 R(t)$ , which is not negligible.

The increase of the cloud size makes the resonant optical thickness  $b_0$  drop during the atom-field interaction, in a such way that  $b_0$  after the pulse ends is different of its initial value. Fig. 5.6 shows  $b_0$  calculated at the end of a light pulse of duration  $\Gamma t = 100$ , for several values of  $k_0 \sigma_v / \Gamma$ , calculated with Eq. 5.11, for initial  $b_0 = 11.4$ . The larger  $k_0 \sigma_v / \Gamma$ , the larger  $k_0 R(t)$  after the pulse duration, so consequently the smaller  $b_0$ . We see that, when  $k_0 \sigma_v / \Gamma = 0.1$  ( $T \simeq 2 \text{ mK}$ ),  $b_0$  has dropped from 11.4 to 7.13, i.e., a decrease of 37.5% of its initial value.  $b_0$  drops completely to zero for  $k_0 \sigma_v / \Gamma \geq 1$ , i.e.,  $T \geq 234 \text{ mK}$ .

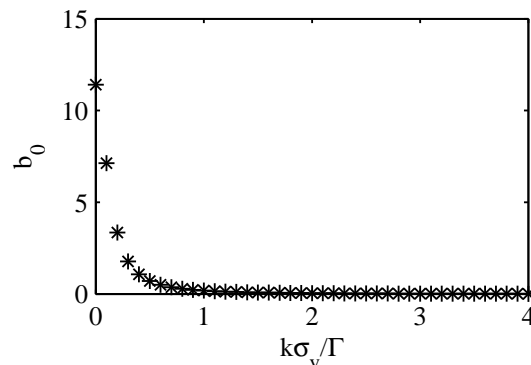


**Figure 5.6:** Resonant optical thickness  $b_0 = 3N/(k_0 R)^2$  as a function of  $k_0 \sigma_v / \Gamma$ , calculated with Eq. 5.11, for a light excitation of duration  $\Gamma t = 100$ . Parameters: initial  $b_0 = 11.4$ ,  $n_0 \lambda^3 = 4.6$  ( $N = 633$  and  $k_0 R = 12.9$ ).

We see that  $b_0$  varies during the light excitation, due to the values of the parameters in the simulations, meaning that after the interaction is switched off, the emitted light may also contain effects of the cloud expansion. Also, the cloud remains expanding after the field extinction. So, in order to analyze temperature effects, the cloud size must be kept constant, and to achieve that condition in the numerical simulations, we replace the ballistic model by the harmonic oscillator model, discussed in the following.

### 5.2.3 The harmonic oscillator model

In order to simulate the atomic motion without any changes in  $b_0$ , we decided to use the *harmonic oscillator model*, where each atom oscillates independently around its

initial position. Physically, this consists in adding a quadratic potential in space where its minimum coincides with the cloud center of mass. This can be achieved experimentally by a magnetic or optical trap [Foot 2005]. Although the quadratic potential introduces a potential energy and modifies the atomic motion compared to our experimental situation, where the cloud is free in space (zero potential energy), it impacts only the external dynamics of the atoms, so the internal dynamics, where the  $\beta_j(t)$  evolution comes from, is not impacted.

With the harmonic potential, the positions and velocities for each atom are given by

$$\begin{aligned} x_j(t) &= x_j(0) \cos(\omega t) + \frac{v_{xj}(0)}{\omega} \sin(\omega t) \\ v_{xj}(t) &= -\omega x_j(0) \sin(\omega t) - v_{xj}(0) \cos(\omega t) \end{aligned} \quad (5.13)$$

and similar equations for  $y_j(t)$ ,  $z_j(t)$  and  $v_{yj}(t)$ ,  $v_{zj}(t)$ . In Eqs. 5.13,  $\{x_j(0), y_j(0), z_j(0)\}$  are the initial atomic positions,  $\{v_{xj}(0), v_{yj}(0), v_{zj}(0)\}$  are the initial velocities (which come from the Maxwell-Boltzmann distribution) and  $\omega$  is the oscillation frequency.

The oscillation frequency  $\omega$  can be extracted from the equipartition theorem [Salinas 2001], which in our case gives

$$\frac{1}{2}M\sigma_v^2 + \frac{1}{2}M\omega^2 R^2 = 3k_B T \quad (5.14)$$

By extracting  $\omega$  above, we obtain

$$\omega = \frac{1}{R} \sqrt{\frac{k_B T}{M}} \quad (5.15)$$

so  $\omega$  depends on the temperature. In adimensional form, we have

$$\frac{\omega}{\Gamma} = \frac{k_0 \sigma_v / \Gamma}{k_0 R} \quad (5.16)$$

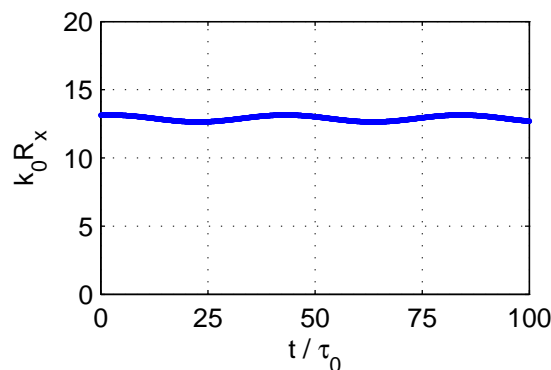


**Figure 5.7:** RMS cloud size  $k_0 R_x(t)$  in the  $x$  direction as a function of the time  $t/\tau_0 = \Gamma t$ , calculated from the definition of RMS value and Eq. 5.13. Parameters:  $k_0 R_x(0) = 13.1$  (in order to have the same  $b_0$  and  $N$  as in Fig. 5.6) and  $k_0 \sigma_v / \Gamma = 1$ .

Figure 5.7 shows the cloud size at the  $x$  direction as a function of the light excitation duration, calculated with the harmonic oscillator model for  $k_0 \sigma_v / \Gamma = 1$ . We see that, as all the atoms oscillates around their initial positions, the net effect is an oscillation

of the cloud size, however, this oscillation is small in amplitude, which makes the cloud size to be practically constant during the light interaction. The cloud size was calculated from its definition, i.e.,  $k_0 R_x(t) = \sqrt{\sum_j x_j(t)^2/N}$ , where  $x_j(t)$  were calculated with Eq. 5.13. The initial cloud size is  $k_0 R_x(0) = 13.13$ . Its maximum and minimum values are 13.14 and 12.6, respectively, and its mean value and standard deviation are 12.9 and 0.18, respectively.

### 5.2.4 Simulations methods

The simulation procedure for the coupled-dipole model with temperature is the same described in section 1.3. The starting point is to set randomly the initial atomic positions under a Gaussian sphere of RMS size  $k_0 R$  for  $N$  atoms, where  $N$  and  $k_0 R$  are calculated for given  $b_0$  and  $n_0 \lambda^3$ . The exclusion condition is checked in order to avoid atom pairs and to have dilute clouds.

The initial velocities  $v_{x,y,z j}(0)$  are also set randomly from a Gaussian distribution of size  $\sigma_v$  (or  $k_0 \sigma_v/\Gamma$ ), which is calculated with Eq. 5.8 for a given temperature  $T$ . Then,  $\omega$  is calculated with Eq. 5.15, with the detail that in the simulation the frequencies for each one of the directions  $x, y, z$  are set as

$$\begin{aligned}\omega_x &= \omega \times \pi/3 \\ \omega_y &= \omega \times 3/\pi \\ \omega_z &= \omega\end{aligned}\tag{5.17}$$

i.e.,  $\omega$  is multiplied by  $\pi/3$ ,  $3/\pi$  and 1 before being substituted in Eqs. 5.13 ( $\omega_x$  is for  $x_j$ ,  $v_{xj}$  and so on for the directions  $x$  and  $z$ ). This is to have incommensurable values, i.e., the trajectories of the atoms are set to be not closed paths, so the periodicity of the motion is slightly broken. Thus, possible oscillations in the emitted intensities due to the harmonic oscillator model are avoided.<sup>1</sup> Then, the positions and velocities in Eq. 5.13 are calculated for each value of  $t$  and replaced in Eqs. 5.4, with  $\Delta \gg \Gamma$  and

$$\Delta \gg k_0 \sigma_v\tag{5.18}$$

i.e., far detuned light and no resonant frequency seen by the atoms, respectively. If  $\Delta = 0$ , some atoms will be out of resonance due to their motion, so we discuss only the off-resonance case. Finally, Eqs. 5.4 are solved numerically and then replaced in Eqs. 5.5, 5.2 and 1.35 in order to calculate the emitted intensities. The result is averaged for several configurations on the atomic positions and velocities in order to avoid spurious oscillations in the result.

---

<sup>1</sup> We noticed later that by setting the same frequencies  $\omega$  for all positions and velocities, the result is not impacted.

### 5.2.5 Numerical results

In the simulations with temperature, it was noticed that the total emitted power  $P(t)$  is clean enough, however, the emitted intensity  $I(\theta, \phi, t)$  contains spurious oscillations. This is true even for high enough values of the configurations of the atomic positions and velocities (e.g., 50 configurations). Also, the intensities  $I(\theta, t)$  and  $I(\theta, \phi, t)$  were not equal (which is not understandable because even with the atomic motion the cloud-laser system is still symmetric with respect to the  $z$  axis). In addition, the simulations with temperature take much more time compared with the case  $T = 0$ , so the incoming pulse duration was reduced from  $100\tau_0$  to  $25\tau_0$ .

The reference [Bienaimé 2012] presents some of temperature effects, but, as already discussed in section 2.1, in this work all the simulations methods were improved. The main results here are the cooperative decay rates as a function of  $b_0$  and  $k_0\sigma_v/\Gamma$ , i.e., how the linear scaling is impacted in the former and how the rates evolve with the temperature in the latter for a fixed  $b_0$ . Also, due to the problem of oscillations observed in  $I(\theta, \phi, t)$ , the decay rates were extracted from  $P(t)$ , which technically is wrong for superradiance but correct for subradiance.

#### Cooperative decay rates *versus* $k_0\sigma_v/\Gamma$

Figure 5.8 shows the fitted decay rates  $\Gamma_{\text{fit}}$  obtained from the total emitted power  $P(t)$  calculated for several  $k_0\sigma_v/\Gamma$ , for two values of  $b_0$ . The values  $\Gamma_{\text{fit}}/\Gamma > 1$  (blue and red above the dashed line) were fitted in the range  $t \in [0, 0.2]\tau_0$ , i.e.,  $\Gamma_{\text{fit}} = \Gamma_{\text{sup}}$ , whereas the values  $\Gamma_{\text{fit}}/\Gamma < 1$  (blue and red below the dashed line) were fitted in the interval  $P(t)/P(0) \in [10^{-4}, 10^{-3}]$ , i.e.,  $\Gamma_{\text{fit}} = \Gamma_{\text{sub}}$ .

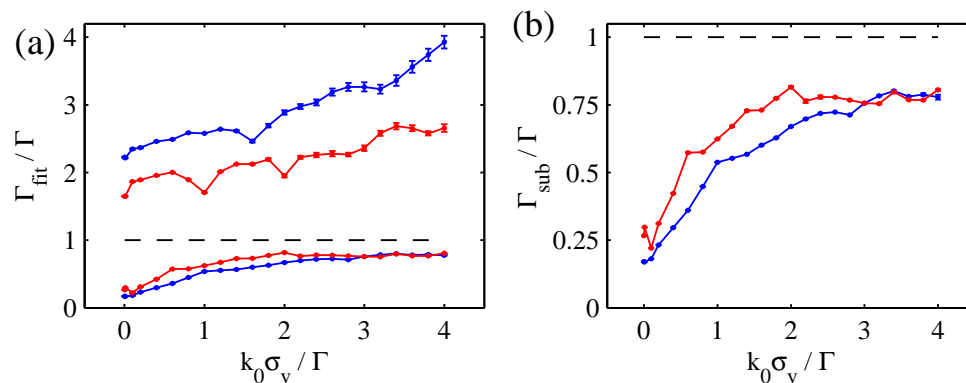


**Figure 5.8:** (a) Decay rates  $\Gamma_{\text{fit}}$  as a function of the parameter  $k_0\sigma_v/\Gamma$  for constant  $b_0 = 3N/(k_0R)^2 = 11.4$  (blue) and  $6.6$  (red), calculated from the normalized total emitted intensity  $P(t)/P(0)$ . (b) Close up of the  $\Gamma_{\text{sub}}$  displayed in (a). Parameters:  $\Delta = 20\Gamma$ , over 20 realizations on the atomic positions and velocities.

We see that, for the subradiant part, when  $k_0\sigma_v/\Gamma$  increases, the subradiant decay rates tend to  $\Gamma$ , showing that subradiance is suppressed for increasing temperature. For  $b_0 = 11.4$  (blue data), the initial value is  $\Gamma_{\text{sub}}/\Gamma = 0.17$ , for  $k_0\sigma_v/\Gamma = 0.001$  ( $T = 0.23 \mu\text{K}$ , i.e., negligible temperature). For  $k_0\sigma_v/\Gamma = 0.1$  ( $T = 2.3 \text{ mK}$ , i.e., few milikelvins is already the maximum than we can get in our experiment, in a  $^{87}\text{Rb}$  MOT; a  $^{88}\text{Sr}$  MOT

may provide a better detection due to its larger natural linewidth),  $\Gamma_{\text{sub}}/\Gamma = 0.18$ , i.e., a very non significant increase. A significant increase starts from  $k_0\sigma_v/\Gamma = 0.2$  ( $T \approx 9$  mK), where  $\Gamma_{\text{sub}}/\Gamma = 0.23$ , i.e., an increase of 36%. For  $k_0\sigma_v/\Gamma = 1$  ( $T = 233$  mK),  $\Gamma_{\text{sub}}/\Gamma = 0.54$ , and from  $k_0\sigma_v/\Gamma \geq 3$  ( $T = 2$  K),  $\Gamma_{\text{sub}}/\Gamma$  starts to increase more slowly, apparently tending to the unity for very large  $k_0\sigma_v/\Gamma$ . The values of  $\Gamma_{\text{sub}}$  for  $b_0 = 6.6$  (red data) present a similar behavior.

Concerning the superradiant part,  $\Gamma_{\text{sup}}$  increases with  $k_0\sigma_v/\Gamma$ , however we cannot trust these results because they were obtained from the total emitted fluorescence  $P(t)$ , where the angular dependence was washed out: superradiance is angular-dependent, as discussed in Chapters 1 and 3, so  $\Gamma_{\text{sup}}$  extracted from  $P(t)$  may be an ‘‘average’’ of the real  $\Gamma_{\text{sup}}(\theta)$ . Physically we expect a suppression of  $\Gamma_{\text{sup}}$  with increasing  $k_0\sigma_v/\Gamma$  like for  $\Gamma_{\text{sub}}$ .

### Cooperative decay rates *versus* $b_0$ for several temperatures

Figure 5.9 shows subradiant decay rates  $\tau_{\text{sub}}$  as a function of  $b_0$  for several temperatures, in order to see the impact of the atomic motion in the linear scaling already discussed. We see that, for low temperatures (50, 100 and 151  $\mu\text{K}$ ),  $\tau_{\text{sub}}$  is practically equal to the values for zero temperature, which shows that the temperature at this range does not impact subradiance. However, when  $T$  increases to some mK,  $\tau_{\text{sub}}$  decays abruptly, tending to  $\tau_0$  (no cooperative effects) for  $\sim 2K$ .

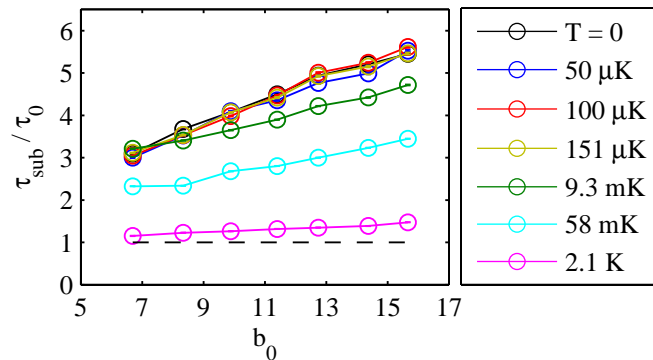


**Figure 5.9:** Subradiant decay rates  $\tau_{\text{sub}}$  as a function of  $b_0 = 3N/(k_0R)^2$  for different temperatures  $T$ . The values of the temperatures correspond to the following values of  $k_0\sigma_v/\Gamma$ , respectively: 0, 0.0146, 0.0207, 0.0254, 0.2, 0.5 and 3.  $\tau_{\text{sub}}$  were extracted from exponential fits of  $P(t)$ , range  $P(t)/P(0) \in [10^{-5}, 10^{-3}]$ . Parameters:  $n_0\lambda^3=4.6$ ,  $\Delta = 20\Gamma$ , averaged over 20 realizations.

An observation of suppression of super- and subradiance will be the subject for next experiments. More simulations will be needed, as well as physical understanding, to explain why subradiance is robust for increasing  $k_0\sigma_v/\Gamma$ .

## 5.3 Conclusions of this chapter

We have presented simulations on the coupled-dipole model by including a phase shift in the incident field and by considering the atomic motion in the cloud, to take into account temperature effects. The main obtained results are that the subradiance level can be increased for a phase shift of  $\pi$ , and subradiance is robust with temperature.

Changes and improvements in our experimental setup are in progress in order to observe these two phenomena in the future. In addition, new simulations may be performed. Some ideas are: the phased cloud with temperature, to see if the temperature plays any role in the subradiant gain; and how the subradiance decay rates scale empirically with  $k_0\sigma_v/\Gamma$ . Another idea come from the reference [Kwong 2014], where a cooperative flash was detected in the forward direction for a far-detuned probe laser exciting a cold sample of  $^{88}\text{Sr}$  at a temperature of  $k_0\sigma_v/\Gamma= 3.4$ .

# Conclusion

In this thesis, we presented an experimental study on super- and subradiance in a large cloud of cold atoms, as well as the interplay of subradiance and radiation trapping. We measured the intensity emitted by a dilute atomic cloud, after interacting with a weak laser beam. The emitted intensity is collected after the extinction of the incoming laser when the cloud-light system reaches a steady state. We extracted the super- and subradiant decay rates from the emitted intensity, for several resonant optical thicknesses and detunings of the incoming probe beam. Our main method for extracting these decay rates is an exponential fit in the region of interest: early times for superradiance, where a fast decay is observed; and late times for subradiance, where a slow decay is observed.

We have interpreted our experimental results by using a model of coupled dipoles for cold atoms, in the low-density regime (scalar approach) and by considering only single excitations (linear optics regime). This model describes the response of identical two-level atoms after interacting with a monochromatic plane wave and vacuum modes, and had been already developed and studied extensively in the literature. In the particular case of the super- and subradiant decay rates, a scaling of the decay rates with the resonant optical thickness was predicted.

In order to perform a detailed theoretical study, we improved the simulation methods and we obtained analytical expressions for the emitted intensities where the angular dependence is taken into account. We also added an exclusion volume in the simulations in order to avoid spurious pair physics effects, we averaged our results for several configurations on the atomic positions to remove speckles in the emitted intensity, and we used a quadratic trap model to simulate temperature effects without spurious expansion of the cloud, which in the simulations need to be rather modest in initial size. We showed that subradiance is very robust with temperature and angular direction, as well as the detuning of the probe laser, even at resonance. On the other hand, superradiance is observed mainly off-resonance. Superradiance was also shown to be completely suppressed at resonance, except in forward direction.

In order to detect these two phenomena experimentally, we had a  $^{87}\text{Rb}$  MOT available in our laboratory to produce large clouds of atoms, at high resonant optical thicknesses. To detect subradiance, we set the probe beam in a setup of two AOMs with a focused beam, in order to obtain a good extinction and short fall time. For superradiance, the probe beam setup was with a single AOM and a Mach-Zehnder EOM, in order to provide a fall time as short as possible. In addition, we set a hybrid photomultiplier to detect clearly the atomic decay without afterpulsing after the probe beam extinction. We performed systematic

measurements and all the experimental results were consistent with the coupled-dipole model, even when taking into account the laser spectrum, possible inelastic scattering and frequency redistribution in random walk simulations.

Since subradiance at resonance may be confused with radiation trapping, i.e., the simple random walk performed by a resonant photon, we revisited an experiment performed with a narrow beam exciting the cold atoms, in order to see the interplay between these two phenomena. Contrary to subradiance, radiation trapping is very dependent on the laser detuning and cloud temperature, being important at resonance and for low temperature and narrow laser spectra. Also, it is observed in amplitudes of order  $\sim 10^{-2}$ , whereas subradiance reaches decays low to  $\sim 10^{-4}$ . With our experimental setup of lower extinction and better acquisition average, we could observe that the two phenomena can be well observed simultaneously for certain values of the detuning and optical thickness, where radiation trapping comes first, followed by subradiance. These results are consistent with an incoherent model for random walk and also by taking into account laser spectrum, frequency redistribution and other effects.

Moreover, we observed experimentally signatures of off-axis superradiance and subradiance in a large and dilute cloud of cloud atoms, in the linear optics regime. We observed that the resonant optical thickness is the single observable to study cooperativity, and all results are consistent with the coupled-dipole model. Despite of some limitations of the coupled-dipole model compared with the experiment, like low atom number, higher densities and non-degenerate atoms, we expect that this model is a powerful tool to study experimentally other predictions related to super- and subradiance, like a setup where the incoming field has a phase shift, and for larger temperatures of the atomic cloud.

## Perspectives

As perspectives for future works, there are *a priori* two ideas, which are the experimental observation of the two theoretical predictions discussed in Chapter 5: the phased cloud setup, whose goal is to see the enhancement of the subradiance amplitude; and the effects of decoherence in subradiance by increasing the temperature of our atomic cloud. The experiment is now being carried out by the postdoctoral researcher Patrizia Weiss and the PhD student Ana Cipris. Up to now (October 2018), the experiment is under technical improvement and adjustment after installing a new tapered amplifier from Toptica and a new diode laser in the Topica laser source.

## Publications

Below we list the articles published in scientific journals throughout this thesis, in chronological order.

- [Guerin 2016] W. Guerin, M. O. Araújo and R. Kaiser. *Subradiance in a Large Cloud of Cold Atoms*. Physical Review Letters **116**, 083601 (2016).
- [Araújo 2016] M. O. Araújo, I. Krešić, R. Kaiser and W. Guerin. *Superradiance in a large and dilute cloud of cold atoms in the linear-optics regime*. Physical Review Letters **117**, 073002 (2016).

- [Araújo 2018] M. O. Araújo, W. Guerin and R. Kaiser. *Decay dynamics in the coupled-dipole model*. Journal of Modern Optics **65**, 1345 (2018).
- [Weiss 2018] P. Weiss, M. O. Araújo, R. Kaiser and W. Guerin. *Subradiance and radiation trapping in cold atoms*. New Journal of Physics **20**, 063024 (2018).



# Annex



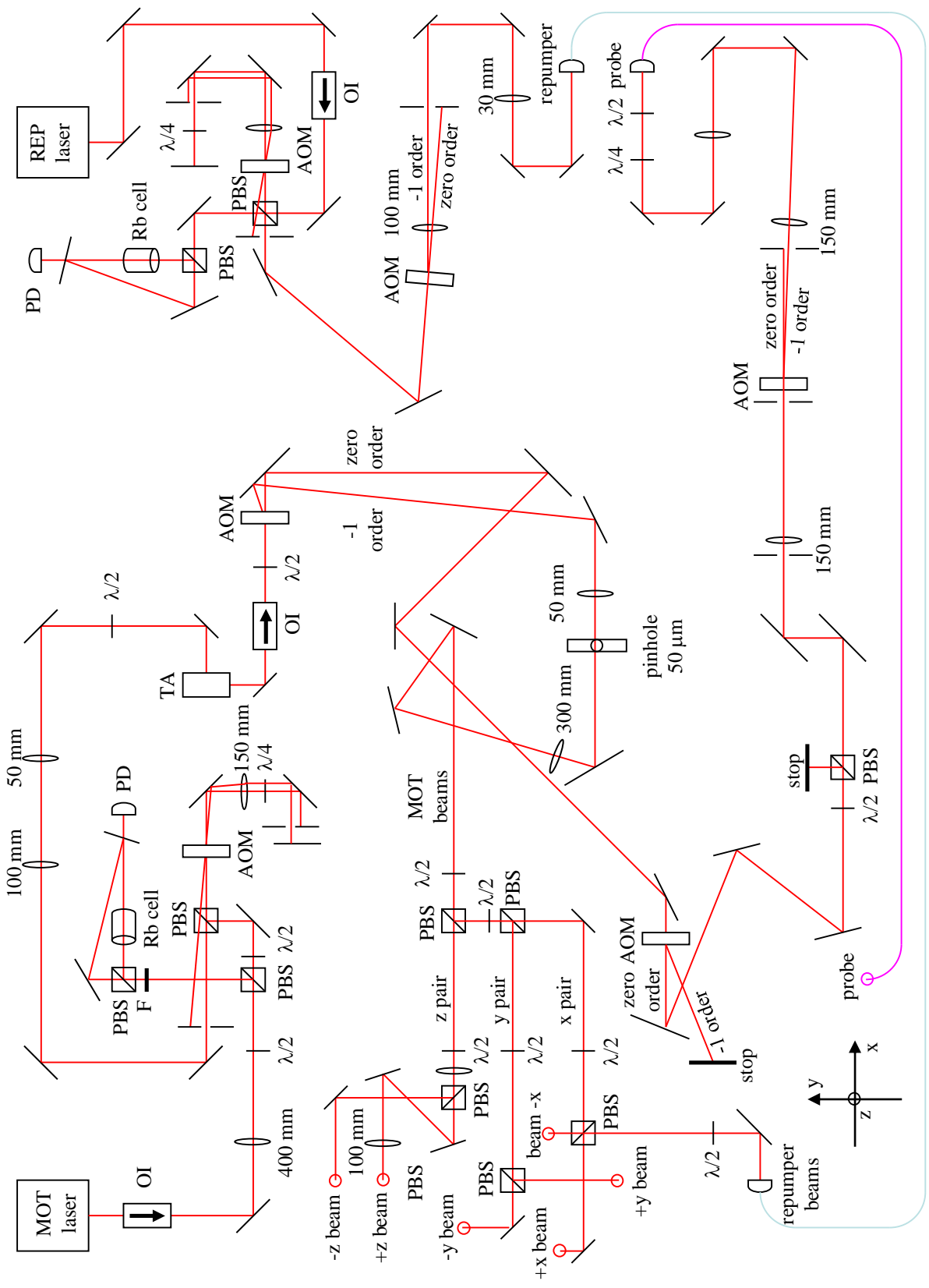
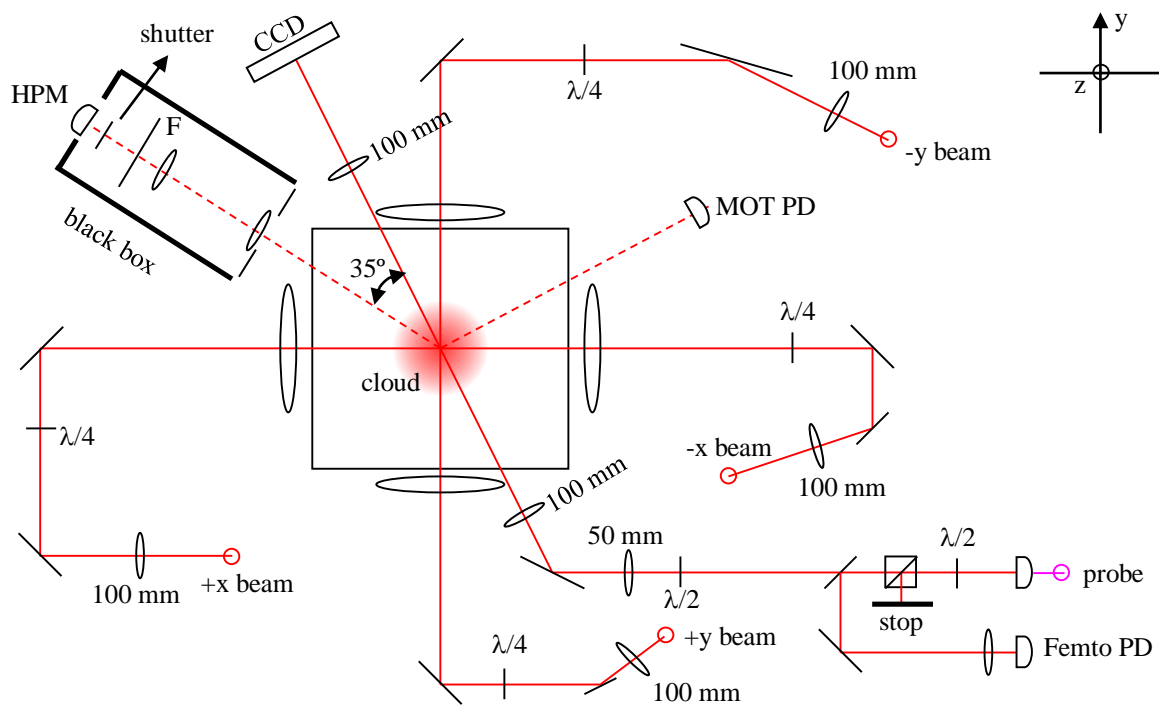
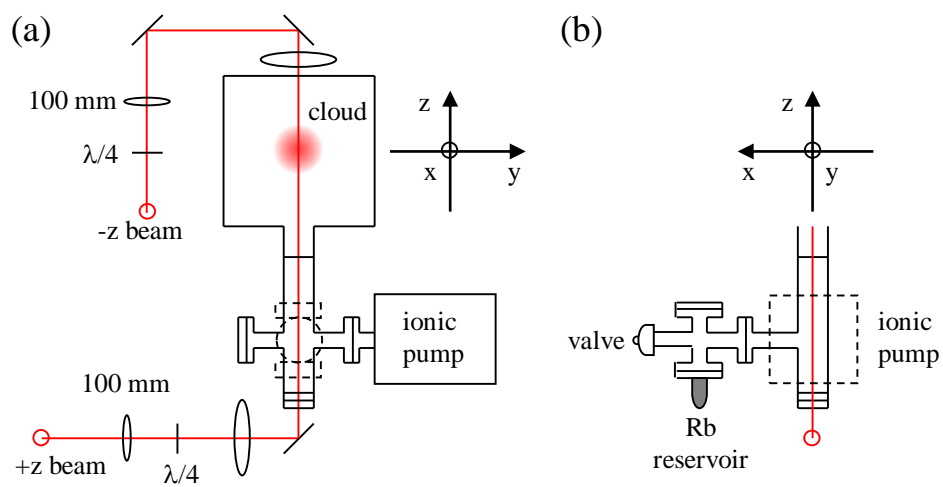


Figure 10: The complete experimental setup on the main table. Subradiance experiment.



**Figure 11:** Experimental setup for the MOT and probe beam. Subradiance experiment.



**Figure 12:** Scheme of the vacuum system and the vertical MOT beam pair.

# Bibliography

- [Araújo 2016] M. O. Araújo, I. Krešić, R. Kaiser, and W. Guerin. *Superradiance in a Large and Dilute Cloud of Cold Atoms in the Linear-Optics Regime*. [Physical Review Letters](#), Vol. **117**, p. 073002, Aug 2016.
- [Araújo 2018] M. O. Araújo, W. Guerin, and R. Kaiser. *Decay dynamics in the coupled-dipole model*. [Journal of Modern Optics](#), Vol. **65**, No. 11, p. 1345–1354, 2018.
- [Arpornthip 2012] T. Arpornthip, C. A. Sackett, and K. J. Hughes. *Vacuum-pressure measurement using a magneto-optical trap*. [Physical Review A](#), Vol. **85**, p. 033420, Mar 2012.
- [Bachelard 2011] R. Bachelard, N. Piovella, and P. W. Courteille. *Cooperative scattering and radiation pressure force in dense atomic clouds*. [Physical Review A](#), Vol. **84**, p. 013821, Jul 2011.
- [Bachelard 2012] R. Bachelard, P. W. Courteille, R. Kaiser, and N. Piovella. *Resonances in Mie scattering by an inhomogeneous atomic cloud*. [Europhysics Letters](#), Vol. **97**, No. 1, p. 14004, 2012.
- [Bachelard 2016] R. Bachelard, N. Piovella, W. Guerin, and R. Kaiser. *Collective effects in the radiation pressure force*. [Physical Review A](#), Vol. **94**, p. 033836, Sep 2016.
- [Bellando de Castro 2013] L. Bellando de Castro. *Localisation de la lumière et effets coopératifs dans des nuages d’atomes froids*. PhD thesis, Université Nice Sophia Antipolis, Nov. 2013.
- [Bellando 2014] L. Bellando, A. Gero, E. Akkermans, and R. Kaiser. *Cooperative effects and disorder: A scaling analysis of the spectrum of the effective atomic Hamiltonian*. [Physical Review A](#), Vol. **90**, p. 063822, Dec 2014.
- [Bender 2010] H. Bender, C. Stehle, S. Slama, R. Kaiser, N. Piovella, C. Zimmermann, and P. W. Courteille. *Observation of cooperative Mie scattering from an ultracold atomic cloud*. [Physical Review A](#), Vol. **82**, p. 011404, Jul 2010.
- [Berman 2008] P. R. Berman. *Light scattering*. [Contemporary Physics](#), Vol. **49**, No. 5, p. 313–330, 2008.

- [Biella 2013] A. Biella, F. Borgonovi, R. Kaiser, and G. L. Celardo. *Subradiant hybrid states in the open 3D Anderson-Dicke model*. [Europhysics Letters](#), Vol. **103**, No. 5, p. 57009, 2013.
- [Bienaimé 2010] T. Bienaimé, S. Bux, E. Lucioni, P. W. Courteille, N. Piovella, and R. Kaiser. *Observation of a Cooperative Radiation Force in the Presence of Disorder*. [Physical Review Letters](#), Vol. **104**, p. 183602, May 2010.
- [Bienaimé 2011a] T. Bienaimé, M. Petruzzo, D. Bigerni, N. Piovella, and R. Kaiser. *Atom and photon measurement in cooperative scattering by cold atoms*. [Journal of Modern Optics](#), Vol. **58**, No. 21, p. 1942–1950, 2011.
- [Bienaimé 2011b] T. Bienaimé. *Effets coopératifs dans les nuages d’atomes froids*. PhD thesis, Université Nice Sophia Antipolis, Dec. 2011.
- [Bienaimé 2012] T. Bienaimé, N. Piovella, and R. Kaiser. *Controlled Dicke Subradiance from a Large Cloud of Two-Level Systems*. [Physical Review Letters](#), Vol. **108**, p. 123602, Mar 2012.
- [Bienaimé 2013] T. Bienaimé, R. Bachelard, N. Piovella, and R. Kaiser. *Cooperativity in light scattering by cold atoms*. [Fortschritte der Physik](#), Vol. **61**, No. 2-3, p. 377–392, 2013.
- [Bienaimé 2014] T. Bienaimé, R. Bachelard, J. Chabé, M. T. Rouabah, L. Bellando, P. W. Courteille, N. Piovella, and R. Kaiser. *Interplay between radiation pressure force and scattered light intensity in the cooperative scattering by cold atoms*. [Journal of Modern Optics](#), Vol. **61**, No. 1, p. 18–24, 2014.
- [Bohnet 2012] J. G. Bohnet, Z. Chen, J. M. Weiner, D. Meiser, M. J. Holland, and J. K. Thompson. *A steady-state superradiant laser with less than one intracavity photon*. [Nature](#), Vol. **484**, No. 7392, p. 78, 2012.
- [Bromley 2016] S. L. Bromley, B. Zhu, M. Bishof, X. Zhang, T. Bothwell, J. Schachenmayer, T. L. Nicholson, R. Kaiser, S. F. Yelin, M. D. Lukin, et al. *Collective atomic scattering and motional effects in a dense coherent medium*. [Nature Communications](#), Vol. **7**, p. 11039, 2016.
- [Butkov 1968] E. Butkov. *Mathematical Physics*. Addison-Wesley, 1968.
- [Bux 2010] S. Bux, E. Lucioni, H. Bender, T. Bienaimé, K. Lauber, C. Stehle, C. Zimmermann, S. Slama, P. W. Courteille, N. Piovella, and R. Kaiser. *Cooperative scattering by cold atoms*. [Journal of Modern Optics](#), Vol. **57**, No. 19, p. 1841–1848, 2010.
- [Chabé 2014] J. Chabé, M.-T. Rouabah, L. Bellando, T. Bienaimé, N. Piovella, R. Bachelard, and R. Kaiser. *Coherent and incoherent multiple scattering*. [Physical Review A](#), Vol. **89**, p. 043833, Apr 2014.
- [Chevrollier 2012] M. Chevrollier. *Radiation trapping and Lévy flights in atomic vapours: an introductory review*. [Contemporary Physics](#), Vol. **53**, No. 3, p. 227–239, 2012.

- [Chomaz 2012] L. Chomaz, L. Corman, T. Yefsah, R. Desbuquois, and J. Dalibard. *Absorption imaging of a quasi-two-dimensional gas: a multiple scattering analysis*. [New Journal of Physics](#), Vol. **14**, No. 5, p. 055001, 2012.
- [Cohen-Tannoudji 1992] C. Cohen-Tannoudji, J. Dupont-Roc, and G. Grynberg. *Atom-photon interactions: basic processes and applications*. Wiley-Interscience publication. J. Wiley, 1992, ISBN 9780471293361.
- [Compton 1922] K. T. Compton. *Theory of Ionization by Cumulative Action and the Low Voltage Arc*. [Physical Review](#), Vol. **20**, p. 283–299, Oct 1922.
- [Corman 2017] L. Corman, J. L. Ville, R. Saint-Jalm, M. Aidelsburger, T. Bienaimé, S. Nascimbène, J. Dalibard, and J. Beugnon. *Transmission of near-resonant light through a dense slab of cold atoms*. [Physical Review A](#), Vol. **96**, p. 053629, Nov 2017.
- [Cottier 2018] F. Cottier, R. Kaiser, and R. Bachelard. *Role of disorder in super- and subradiance of cold atomic clouds*. [Physical Review A](#), Vol. **98**, p. 013622, Jul 2018.
- [Courteille 2010] P. W. Courteille, S. Bux, E. Lucioni, K. Lauber, T. Bienaimé, R. Kaiser, and N. Piovella. *Modification of radiation pressure due to cooperative scattering of light*. [The European Physical Journal D](#), Vol. **58**, No. 1, p. 69–73, May 2010.
- [Das 2008] S. Das, G. S. Agarwal, and M. O. Scully. *Quantum Interferences in Cooperative Dicke Emission from Spatial Variation of the Laser Phase*. [Physical Review Letters](#), Vol. **101**, p. 153601, Oct 2008.
- [de Oliveira 2014] R. A. de Oliveira, M. S. Mendes, W. S. Martins, P. L. Saldanha, J. W. R. Tabosa, and D. Felinto. *Single-photon superradiance in cold atoms*. [Physical Review A](#), Vol. **90**, p. 023848, Aug 2014.
- [DeVoe 1996] R. G. DeVoe and R. G. Brewer. *Observation of Superradiant and Subradiant Spontaneous Emission of Two Trapped Ions*. [Physical Review Letters](#), Vol. **76**, p. 2049–2052, Mar 1996.
- [Dicke 1954] R. H. Dicke. *Coherence in Spontaneous Radiation Processes*. [Physical Review](#), Vol. **93**, p. 99–110, Jan 1954.
- [Drever 1983] R. W. P. Drever, J. L. Hall, F. V. Kowalski, J. Hough, G. M. Ford, A. J. Munley, and H. Ward. *Laser phase and frequency stabilization using an optical resonator*. [Applied Physics B](#), Vol. **31**, No. 2, p. 97–105, Jun 1983.
- [Eberly 2006] J. H. Eberly. *Emission of one photon in an electric dipole transition of one among  $N$  atoms*. [Journal of Physics B: Atomic, Molecular and Optical Physics](#), Vol. **39**, No. 15, p. S599, 2006.
- [Fano 1961] U. Fano. *Effects of Configuration Interaction on Intensities and Phase Shifts*. [Physical Review](#), Vol. **124**, p. 1866–1878, Dec 1961.

- [Feng 2014] W. Feng, Y. Li, and S.-Y. Zhu. *Effect of atomic distribution on cooperative spontaneous emission*. *Physical Review A*, Vol. **89**, p. 013816, Jan 2014.
- [Fioretti 1998] A. Fioretti, A. Molisch, J. Müller, P. Verkerk, and M. Allegrini. *Observation of radiation trapping in a dense Cs magneto-optical trap*. *Optics Communications*, Vol. **149**, No. 4, p. 415 – 422, 1998.
- [Fleischhauer 1999] M. Fleischhauer and S. F. Yelin. *Radiative atom-atom interactions in optically dense media: Quantum corrections to the Lorentz-Lorenz formula*. *Physical Review A*, Vol. **59**, p. 2427–2441, Mar 1999.
- [Foot 2005] C. J. Foot. *Atomic physics*, volume 7. Oxford University Press, 2005.
- [Friedberg 2008a] R. Friedberg and J. T. Manassah. *Effects of including the counterrotating term and virtual photons on the eigenfunctions and eigenvalues of a scalar photon collective emission theory*. *Physics Letters A*, Vol. **372**, No. 14, p. 2514 – 2521, 2008.
- [Friedberg 2008b] R. Friedberg and J. T. Manassah. *Reply to: “Comment on: ‘Effects of including the counterrotating term and virtual photons on the eigenfunctions and eigenvalues of a scalar photon collective emission theory’ [Physics Letters A 372 (2008) 2514]” [Physics Letters A 372 (2008) 5732]*. *Physics Letters A*, Vol. **372**, No. 35, p. 5734 – 5740, 2008.
- [Friedberg 2010] R. Friedberg and J. T. Manassah. *Cooperative Lamb shift in an ellipsoid*. *Physical Review A*, Vol. **81**, p. 063822, Jun 2010.
- [Griffiths 2005] D. J. Griffiths. *Introduction to Quantum Mechanics*. Pearson Education, 2005.
- [Gross 1982] M. Gross and S. Haroche. *Superradiance: An essay on the theory of collective spontaneous emission*. *Physics Reports*, Vol. **93**, No. 5, p. 301 – 396, 1982.
- [Guerin 2016] W. Guerin, M. O. Araújo, and R. Kaiser. *Subradiance in a Large Cloud of Cold Atoms*. *Physical Review Letters*, Vol. **116**, p. 083601, Feb 2016.
- [Guerin 2017a] W. Guerin, M. T. Rouabah, and R. Kaiser. *Light interacting with atomic ensembles: collective, cooperative and mesoscopic effects*. *Journal of Modern Optics*, Vol. **64**, No. 9, p. 895–907, 2017.
- [Guerin 2017b] W. Guerin and R. Kaiser. *Population of collective modes in light scattering by many atoms*. *Physical Review A*, Vol. **95**, p. 053865, May 2017.
- [Hecht 2002] E. Hecht. *Optics*. Addison Wesley, 2002.
- [Holstein 1947] T. Holstein. *Imprisonment of Resonance Radiation in Gases*. *Physical Review*, Vol. **72**, p. 1212–1233, Dec 1947.
- [Jackson 1998] J. D. Jackson. *Classical electrodynamics*. John Wiley & Sons, 1998.

- [Jenkins 2016] S. D. Jenkins, J. Ruostekoski, J. Javanainen, R. Bourgain, S. Jennewein, Y. R. P. Sortais, and A. Browaeys. *Optical Resonance Shifts in the Fluorescence of Thermal and Cold Atomic Gases*. [Physical Review Letters](#), Vol. **116**, p. 183601, May 2016.
- [Jennewein 2016] S. Jennewein, M. Besbes, N. J. Schilder, S. D. Jenkins, C. Sauvan, J. Ruostekoski, J.-J. Greffet, Y. R. P. Sortais, and A. Browaeys. *Coherent Scattering of Near-Resonant Light by a Dense Microscopic Cold Atomic Cloud*. [Physical Review Letters](#), Vol. **116**, p. 233601, Jun 2016.
- [Jennewein 2018] S. Jennewein, L. Brossard, Y. R. P. Sortais, A. Browaeys, P. Cheinet, J. Robert, and P. Pillet. *Coherent scattering of near-resonant light by a dense, microscopic cloud of cold two-level atoms: Experiment versus theory*. [Physical Review A](#), Vol. **97**, p. 053816, May 2018.
- [Kenty 1932] C. Kenty. *On Radiation Diffusion and the Rapidity of Escape of Resonance Radiation from a Gas*. [Physical Review](#), Vol. **42**, p. 823–842, Dec 1932.
- [Ketterle 1993] W. Ketterle, K. B. Davis, M. A. Joffe, A. Martin, and D. E. Pritchard. *High densities of cold atoms in a dark spontaneous-force optical trap*. [Physical Review Letters](#), Vol. **70**, p. 2253–2256, Apr 1993.
- [Kuraptsev 2017] A. S. Kuraptsev, I. M. Sokolov, and M. D. Havey. *Angular distribution of single-photon superradiance in a dilute and cold atomic ensemble*. [Physical Review A](#), Vol. **96**, p. 023830, Aug 2017.
- [Kwong 2014] C. C. Kwong, T. Yang, M. S. Pramod, K. Pandey, D. Delande, R. Pierrot, and D. Wilkowski. *Cooperative Emission of a Coherent Superflash of Light*. [Physical Review Letters](#), Vol. **113**, p. 223601, Nov 2014.
- [Labeyrie 2003] G. Labeyrie, E. Vaujour, C. A. Müller, D. Delande, C. Miniatura, D. Wilkowski, and R. Kaiser. *Slow Diffusion of Light in a Cold Atomic Cloud*. [Physical Review Letters](#), Vol. **91**, p. 223904, Nov 2003.
- [Labeyrie 2004] G. Labeyrie, D. Delande, C. Müller, C. Miniatura, and R. Kaiser. *Multiple scattering of light in a resonant medium*. [Optics Communications](#), Vol. **243**, No. 1, p. 157 – 164, 2004.
- [Labeyrie 2005] G. Labeyrie, R. Kaiser, and D. Delande. *Radiation trapping in a cold atomic gas*. [Applied Physics B](#), Vol. **81**, No. 7, p. 1001–1008, Nov 2005.
- [Lagendijk 1996] A. Lagendijk and B. A. van Tiggelen. *Resonant multiple scattering of light*. [Physics Reports](#), Vol. **270**, No. 3, p. 143 – 215, 1996.
- [Lehmberg 1970] R. H. Lehmberg. *Radiation from an N-Atom System. I. General Formalism*. [Physical Review A](#), Vol. **2**, p. 883–888, Sep 1970.
- [Li 2012] Y. Li, J. Evers, H. Zheng, and S.-Y. Zhu. *Collective spontaneous emission beyond the rotating-wave approximation*. [Physical Review A](#), Vol. **85**, p. 053830, May 2012.

- [Li 2013] Y. Li, J. Evers, W. Feng, and S.-Y. Zhu. *Spectrum of collective spontaneous emission beyond the rotating-wave approximation*. [Physical Review A](#), Vol. **87**, p. 053837, May 2013.
- [Lucioni 2008] E. Lucioni. *Realization of a dipole trap for ultracold atoms of rubidium and study of the collective effects*. MSc thesis, Università degli Studi di Milano, 2008.
- [Manassah 2012] J. T. Manassah. *Cooperative radiation from atoms in different geometries: decay rate and frequency shift*. [Advances in Optics and Photonics](#), Vol. **4**, No. 2, p. 108–156, Jun 2012.
- [Mandel 1995] L. Mandel and E. Wolf. *Optical coherence and quantum optics*. Cambridge University Press, 1995.
- [Máximo 2014] C. E. Máximo, R. Kaiser, P. W. Courteille, and R. Bachelard. *Atomic lighthouse effect*. [Journal of the Optical Society of America A](#), Vol. **31**, No. 11, p. 2511–2517, Nov 2014.
- [Mazets 2007] I. E. Mazets and G. Kurizki. *Multiatom cooperative emission following single-photon absorption: Dicke-state dynamics*. [Journal of Physics B: Atomic, Molecular and Optical Physics](#), Vol. **40**, No. 6, p. F105, 2007.
- [McCarron 2007] D. J. McCarron. *A Guide to Acousto-Optic Modulators*. Dec 2007.
- [Mercadier 2009] N. Mercadier, W. Guerin, M. Chevrollier, and R. Kaiser. *Lévy flights of photons in hot atomic vapours*. [Nature Physics](#), Vol. **5**, No. 8, p. 602, 2009.
- [Metcalf 1999] H. J. Metcalf and P. van der Straten. *Laser cooling and trapping. Graduate texts in contemporary physics*. Springer, New York, 1999.
- [Milne 1926] E. A. Milne. *The Diffusion of Imprisoned Radiation Through a Gas*. [Journal of the London Mathematical Society](#), Vol. **s1-1**, No. 1, p. 40–51, 1926.
- [Milonni 1974] P. W. Milonni and P. L. Knight. *Retardation in the resonant interaction of two identical atoms*. [Physical Review A](#), Vol. **10**, p. 1096–1108, Oct 1974.
- [Mollow 1969] B. R. Mollow. *Power Spectrum of Light Scattered by Two-Level Systems*. [Physical Review](#), Vol. **188**, p. 1969–1975, Dec 1969.
- [Morice 1995] O. Morice, Y. Castin, and J. Dalibard. *Refractive index of a dilute Bose gas*. [Physical Review A](#), Vol. **51**, p. 3896–3901, May 1995.
- [Müller 2002] C. A. Müller and C. Miniatura. *Multiple scattering of light by atoms with internal degeneracy*. [Journal of Physics A: Mathematical and General](#), Vol. **35**, No. 47, p. 10163, 2002.
- [Ott 2013] J. R. Ott, M. Wubs, P. Lodahl, N. A. Mortensen, and R. Kaiser. *Cooperative fluorescence from a strongly driven dilute cloud of atoms*. [Physical Review A](#), Vol. **87**, p. 061801, Jun 2013.

- [Pavolini 1985] D. Pavolini, A. Crubellier, P. Pillet, L. Cabaret, and S. Liberman. *Experimental Evidence for Subradiance*. [Physical Review Letters](#), Vol. **54**, p. 1917–1920, Apr 1985.
- [Pellegrino 2014] J. Pellegrino, R. Bourgain, S. Jennewein, Y. R. P. Sortais, A. Browaeys, S. D. Jenkins, and J. Ruostekoski. *Observation of Suppression of Light Scattering Induced by Dipole-Dipole Interactions in a Cold-Atom Ensemble*. [Physical Review Letters](#), Vol. **113**, p. 133602, Sep 2014.
- [Pereira 2004] E. Pereira, J. M. G. Martinho, and M. N. Berberan-Santos. *Photon Trajectories in Incoherent Atomic Radiation Trapping as Lévy Flights*. [Physical Review Letters](#), Vol. **93**, p. 120201, Sep 2004.
- [Pierrat 2009] R. Pierrat, B. Grémaud, and D. Delande. *Enhancement of radiation trapping for quasideviant scatterers at low temperature*. [Physical Review A](#), Vol. **80**, p. 013831, Jul 2009.
- [Pucci 2017] L. Pucci, A. Roy, T. S. do Espirito Santo, R. Kaiser, M. Kastner, and R. Bachelard. *Quantum effects in the cooperative scattering of light by atomic clouds*. [Physical Review A](#), Vol. **95**, p. 053625, May 2017.
- [Rehler 1971] N. E. Rehler and J. H. Eberly. *Superradiance*. [Physical Review A](#), Vol. **3**, p. 1735–1751, May 1971.
- [Rogers 2008] G. L. Rogers. *Multiple path analysis of reflectance from turbid media*. [Journal of the Optical Society of America A](#), Vol. **25**, No. 11, p. 2879–2883, Nov 2008.
- [Roof 2016] S. J. Roof, K. J. Kemp, M. D. Havey, and I. M. Sokolov. *Observation of Single-Photon Superradiance and the Cooperative Lamb Shift in an Extended Sample of Cold Atoms*. [Physical Review Letters](#), Vol. **117**, p. 073003, Aug 2016.
- [Rouabah 2014] M.-T. Rouabah, M. Samoylova, R. Bachelard, P. W. Courteille, R. Kaiser, and N. Piovella. *Coherence effects in scattering order expansion of light by atomic clouds*. [Journal of the Optical Society of America A](#), Vol. **31**, No. 5, p. 1031–1039, May 2014.
- [Salinas 2001] S. R. A. Salinas. *Introduction to Statistical Physics*. Springer New York, 2001.
- [Samoylova 2014] M. Samoylova, N. Piovella, R. Bachelard, and P. Courteille. *Microscopic theory of photonic band gaps in optical lattices*. [Optics Communications](#), Vol. **312**, p. 94 – 98, 2014.
- [Schilke 2011] A. Schilke, C. Zimmermann, P. W. Courteille, and W. Guerin. *Photonic Band Gaps in One-Dimensionally Ordered Cold Atomic Vapors*. [Physical Review Letters](#), Vol. **106**, p. 223903, Jun 2011.
- [Scully 1997] M. O. Scully and M. S. Zubairy. *Quantum Optics*. Cambridge University Press, 1997.

- [Scully 2006] M. O. Scully, E. S. Fry, C. H. R. Ooi, and K. Wódkiewicz. *Directed Spontaneous Emission from an Extended Ensemble of  $N$  Atoms: Timing Is Everything*. [Physical Review Letters](#), Vol. **96**, p. 010501, Jan 2006.
- [Scully 2007] M. O. Scully. *Correlated spontaneous emission on the Volga*. [Laser Physics](#), Vol. **17**, No. 5, p. 635–646, May 2007.
- [Scully 2009] M. O. Scully. *Collective Lamb Shift in Single Photon Dicke Superradiance*. [Physical Review Letters](#), Vol. **102**, p. 143601, Apr 2009.
- [Scully 2015] M. O. Scully. *Single Photon Subradiance: Quantum Control of Spontaneous Emission and Ultrafast Readout*. [Physical Review Letters](#), Vol. **115**, p. 243602, Dec 2015.
- [Shim 1999] U. Y. Shim, J. A. Kim, and J. W. Ho. *Saturated absorption spectroscopy in the presence of a longitudinal magnetic field*. [Journal of the Korean Physical Society](#), Vol. **35**, No. 3, p. 222–225, 1999.
- [Siegman 1986] A. E. Siegman. *Lasers*. University Science Books, 1986.
- [Steck 2001] D. A. Steck. *Rubidium 87 D line data*. 2001.
- [Stephen 1964] M. J. Stephen. *First-Order Dispersion Forces*. [The Journal of Chemical Physics](#), Vol. **40**, No. 3, p. 669–673, 1964.
- [Sutherland 2017] R. T. Sutherland and F. Robicheaux. *Degenerate Zeeman ground states in the single-excitation regime*. [Physical Review A](#), Vol. **96**, p. 053840, Nov 2017.
- [Svidzinsky 2008a] A. Svidzinsky and J.-T. Chang. *Comment on: “Effects of including the counterrotating term and virtual photons on the eigenfunctions and eigenvalues of a scalar photon collective emission theory” [Physics Letters A 372 (2008) 2514]*. [Physics Letters A](#), Vol. **372**, No. 35, p. 5732 – 5733, 2008.
- [Svidzinsky 2008b] A. Svidzinsky and J.-T. Chang. *Cooperative spontaneous emission as a many-body eigenvalue problem*. [Physical Review A](#), Vol. **77**, p. 043833, Apr 2008.
- [Svidzinsky 2008c] A. A. Svidzinsky, J.-T. Chang, and M. O. Scully. *Dynamical Evolution of Correlated Spontaneous Emission of a Single Photon from a Uniformly Excited Cloud of  $N$  Atoms*. [Physical Review Letters](#), Vol. **100**, p. 160504, Apr 2008.
- [Svidzinsky 2009] A. A. Svidzinsky and M. O. Scully. *Evolution of collective  $N$  atom states in single photon superradiance: Effect of virtual Lamb shift processes*. [Optics Communications](#), Vol. **282**, No. 14, p. 2894 – 2897, 2009.
- [Svidzinsky 2010] A. A. Svidzinsky, J.-T. Chang, and M. O. Scully. *Cooperative spontaneous emission of  $N$  atoms: Many-body eigenstates, the effect of virtual Lamb shift processes, and analogy with radiation of  $N$  classical oscillators*. [Physical Review A](#), Vol. **81**, p. 053821, May 2010.

- [van Rossum 1999] M. C. W. van Rossum and T. M. Nieuwenhuizen. *Multiple scattering of classical waves: microscopy, mesoscopy, and diffusion*. [Reviews of Modern Physics](#), Vol. **71**, p. 313–371, Jan 1999.
- [Weiss 2018] P. Weiss, M. O. Araújo, R. Kaiser, and W. Guerin. *Subradiance and radiation trapping in cold atoms*. [New Journal of Physics](#), Vol. **20**, No. 6, p. 063024, 2018.